Characterisation of Mechanical Loss in Fused Silica Ribbons for use in Gravitational Wave Detector Suspensions

Alastair W. Heptonstall, B.Sc.

Department of Physics and Astronomy,

University of Glasgow

Presented as a thesis for the degree of Ph.D.

in the University of Glasgow, University Avenue,

Glasgow G12 8QQ.

August 2004

To Ruth

Sad, cheerless, broken-hearted,

The night's gloomy shades, cloudy, dark, o'ercast my sky:

But when she charms my sight,

In pride of Beauty's light-

When thro' my very heart

Her burning glories dart;

'Tis then-'tis then I wake to life and joy!

Robert Burns

Table of Contents

List of Figures

Acknowledgements

Firstly I would like to thank my supervisor Geppo Cagnoli without whose support, guidance and encouragement the work presented in this thesis would not have been possible. My second supervisors, Ken Strain and Norna Robertson have also provided much needed input into parts of this thesis, and again I wish to thank them for this. I would also like to thank Jim Hough for many helpful discussions during the course of my research and for his dedication to helping make experiments work. I would like to thank Phil Willems for the period of ten weeks I spent working with him at the California Institute of Technology. The contribution of Jim Faller to the design of the experiments in this thesis should also be acknowledged as without his help much time and energy would have been spent without cause. I would also like to thank Sheila Rowan and Alastair Grant for their helpful discussions on a variety of topics throughout this period. I would like to thank Stephen McIntosh for his help in laboratory work at the start of my research.

Thanks go also to Morag Casey, David Crooks and Stuart Reid who suffered the fate of sharing an office with me over the course of the past three years with all the humour imaginable.

I would like to thank Colin Craig, Steven Craig, Alan Latta, Neil Robertson and all the members of the Physics and Astronomy department workshop for technical assistance during my research.

On a personal note I would like to thank my mother and father for their continual support over the course of my education and also my brother Barrie.

sister Mary and other close family. I would also like to thank my close friends, Ewan, Neil and Magic for being there for me over the years.

Finally I would like to give my thanks to my fiancée Ruth, whose love and support I have been so fortunate to have.

Preface

This thesis is an account of the work carried out between October 2000 and June 2003 on characterising losses in fused silica ribbon fibres for use as suspensions elements for the test masses of future gravitational wave detectors.

Chapter 1 contains a brief description of the nature of gravitational waves along with potential sources and detection schemes. A discussion of the limiting noise sources is also given along with current sensitivities of the LIGO and GEO600 detectors. This work is derived from current published literature.

Chapter 2 gives an introduction to the issue of thermal noise within detectors. Using the fluctuation dissipation theorem, losses in the suspensions are linked directly to displacement noise. The sources of thermal noise are discussed along with potential methods for reducing its effects at detection band frequencies. The material given in this chapter is derived from published literature.

Chapter 3 contains a discussion on the design of silica fibres for use in the Advanced LIGO detector. The effects on seismic noise, vertical bounce frequency, thermoelastic damping and thermal noise are discussed with an emphasis placed on reducing noise at detection band frequencies. The theory presented in this chapter is derived from published literature. Experimental work on silica blades was carried out by the author in conjunction with Dr. G.Cagnoli and Dr. G.Losurdo.

Chapter 4 gives details of the production of silica fibres from stock material. A variety of systems using hydrogen-oxygen flames were used to produce both round and rectangular cross section fibres. Work on the production of round fibres was carried out by the author in conjunction with Dr. G.Cagnoli, Dr. P.Willems, Mr. S.McIntosh and Dr. D.Crooks. Work on producing fibres of rectangular cross section was carried out by the author with advice from Dr. G.Cagnoli. Current research on use of CO_2 lasers is being performed by Dr. D.Crooks.

Chapter 5 details the measurement of loss in the violin modes of a fibre held in tension. Sources of excess loss are characterised and the material loss of the fused silica fibres is measured. Experimental data is fitted to a model of expected loss and a discussion on measured dilution levels given. Work on designing the support frame was carried out by the author with advice from Dr. G.Cagnoli and Dr. J.Faller with Solidworks drawings produced by the author and Mr. R.Jones. Construction of the silica pendulums and characterisation of the recoil loss was performed by the author in conjunction with Dr. G.Cagnoli. Experimental measurements were carried out by the author.

Chapter 6 details the measurement of loss of the linear pendulum mode of a monolithic fused silica pendulum. The contributions of sources of excess loss are calculated and a material loss found from the theoretical dilution factor. Construction of the pendulum was carried out by the author with advice from Prof. J.Hough. The optical readout was developed by the author with advice from Prof. K.Strain. Software used in data acquisition was written by the author. Analysis of data was performed with advice from Prof. J.Hough, Prof. K.Strain and Dr. G.Cagnoli.

Chapter 7 describes an experiment designed to look for stress dependence of the loss in fused silica by measurement of the vertical bounce mode of a suspension. Work on production of the suspension and frame was carried out

by the author and Dr. P.Willems. Measurements and analysis were performed by Dr. P.Willems with some fitting of data being performed by the author.

Chapter 8 gives a discussion of the strength of fused silica fibres along with experimental measurements of breaking strengths and long term testing of strength. The discussion of aging of fibres and surface crack propagation is derived from published literature. AFM images were produced by the author with Mr. C.How and Ms. A.Kundrotaite. All experimental measurements were carried out by the author with contributions from Dr. G.Cagnoli.

Chapter 9 details the construction techniques used in producing monolithic suspensions along with a proposed method for producing the Advanced LIGO suspensions. The proposed attachment solution was devised by Dr. G.Cagnoli with some discussion with the author. Construction of pendulums in this thesis was performed by the author in conjunction with Dr. G.Cagnoli and Dr. P.Willems. Discussion of the construction of the GEO600 suspensions is derived from published literature. All other discussions are the result of work performed constructing test pendulums and are the work of the author.

Chapter 10 presents the conclusions drawn from work given in this thesis.

Appendix A gives a derivation of the beam equation along with a solution for the boundary conditions of a fibre fixed at both ends and under tension. The derivation was made using current literature. Calculation of the solution for the above boundary conditions was performed by Dr. G.Cagnoli and the author.

Appendix B describes the use of a three segment model to calculate the force and torque at the end of a bending fibre and compares the results gained with the exact results from the beam equation. Work on this derivation was performed by Dr. G.Cagnoli.

Appendix C gives a calculation of the coefficients for the expression of the potential energy stored in a bent beam as a function of transverse

displacement and rotation of the end of the beam. This derivation was calculated by Dr G.Cagnoli.

Appendix D gives a derivation of the effects of recoil on both the pendulum and violin mode measurements. The calculation for the pendulum mode was performed by the author in conjunction with Dr. G.Cagnoli and Prof. J.Hough. The derivation of the ratios of energy stored in measured fibre and isolation fibre for the violin mode experiment was performed by Dr. G.Cagnoli.

Appendix E gives a discussion on the operation of electrostatic drives. This work followed a discussion with Dr. G.Cagnoli.

Appendix F gives a discussion of the design of the support frame for the violin mode experiment. This design followed discussions with both Dr. G.Cagnoli and Dr. J.Faller. The solidworks design was produced by the author with rendering and dimensioning being performed by Mr. R.Jones. The finite element analysis of stiffness was performed by the author with Maple analysis by Dr. G.Cagnoli.

Appendix G gives a derivation of the loss associated with residual gas damping of a pendulum. This work is based on current literature with some derivation work performed by the author.

Summary

In Albert Einstein's 1916 general theory of relativity the propagation of localised fluctuations in gravity was predicted to occur as ripples in the curvature of space time known as gravitational waves, moving at the speed of light. While there is currently only indirect evidence of their existence, based on the measured rate of inspiral of a binary system by Hulse and Taylor, research toward direct detections continues which will give insights into the large scale astrophysical events which produce gravitational radiation.

Gravitational waves, which are quadrupole in nature, produce a tidal strain in space. They interact only weakly with matter, causing them to be both difficult to detect and less likely to be attenuated over long distances than electromagnetic radiation. The strains expected for gravitational waves amenable to detection on Earth (within the frequency range of a few Hz to a few kHz) are of the order 10^{-21} to 10^{-22} for the most violent sources. The detection scheme currently most likely to detect these strains is long baseline laser interferometry.

A number of interferometric detectors are now under construction world wide. The Institute for Gravitational Research at the University of Glasgow, working in collaboration with the Albert Einstein Institute, the Max-Planck-Institut für Quantenoptik and the University of Wales, are working towards a 600m arm length interferometer known as GEO600 at Ruthe near Hannover. The commissioning of this detector is now complete and the sensitivities continue to move closer to the design predictions as excess noise sources are identified. It has recently taken part in scientific data runs with the 4km arm

length LIGO detectors in America which are similarly moving closer to design performances and these measurements will be used to set upper limits on gravitational emissions from a variety of sources. The VIRGO detector in Italy is now nearing the completion of commissioning while the TAMA detector in Japan is now operational with work beginning on a cryogenically cooled detector. A space based detector known as LISA is planned for launch in 2013.

The noise source limiting sensitivities at between 50Hz and 200Hz for GEO600 is predicted to be thermal noise arising from thermally induced displacement of the face of the test masses. The monolithic fused silica suspensions employed by GEO600 are designed to give lower thermal noise contributions than the wire loop and silica mass systems used in LIGO. The level of thermal noise is related to the mechanical loss factors of the suspensions with the limit to sensitivity for GEO600 at 50Hz predicted to be $2\times10^{-22}/\sqrt{Hz}$. The LIGO detectors, gaining increased sensitivity from arm lengths around six times larger than GEO600, are scheduled to have their suspensions upgraded in 2006. The single wire loop suspensions with fused silica masses will be replaced with quadruple suspensions using quasi-monolithic final stages. The possible use of sapphire masses, whose material losses are lower than fused silica is under investigation. These masses will be suspended using fused silica fibres.

The fused silica fibres used to suspend the test masses for Advanced LIGO must achieve higher performance levels than those currently used in GEO600 in order to stop their thermal noise limiting the sensitivity of the detectors, requiring higher working loads and lower mechanical losses for the pendulum.

The majority of work contained in this thesis involves characterisation of the mechanical losses in fused silica ribbon fibres to determine their potential for use in suspending the 40kg test masses for Advanced LIGO. The design of fibres is discussed here, demonstrating the advantages of rectangular cross

sections over the circular cross sections already used in GEO600, with experimental work used to show the viability of this suspension scheme.

The losses of a number of modes of oscillation of fibres were investigated using different suspension designs to reduce excess loss mechanisms. Measurements made of the material loss of the fused silica, using cantilever bending modes of a fibre held at one end, gave values slightly higher than those used in the design of noise curves for Advanced LIGO. The measurements also showed a reduced thermoelastic damping effect from that theoretically calculated from which an altered value for the Young's modulus of the fibres was found compared to the value for bulk fused silica.

Measurements performed using the violin modes and pendulum modes of the fibres showed that, while excess loss mechanisms were characterised and in the case of the violin mode measurement shown to be negligible, the level of dilution of loss calculated theoretically was not achieved. The source of increased loss is thought to be due to the energy being concentrated closer to lossy welded regions of the fibre. The losses measured for the linear pendulum were the lowest ever measured.

Measurements of the vertical bounce mode of a small mass suspended between two fibres has shown clear evidence that there is no intrinsic stress dependence of the material loss of fused silica and has given further evidence that the majority of loss in the fibres comes from a thin highly dissipative layer on the surface.

The strength of ribbon fibres has been shown to be sufficient to carry the working load of the Advanced LIGO masses, with a 20kg test suspension being created, however there was a wide variation in measured fibre breaking strengths thought to be due to bending in the fibre coupling longitudinal force into shear stress. Issues regarding thermal stress at welds are discussed with suggested solutions for construction of Advanced LIGO suspensions.

Chapter 1

Gravitational Wave Detection

1.1. Introduction

When, in 1916, Albert Einstein published his Theory of General Relativity [1], the idea of gravity as a force acting instantly at a distance, as described through Newtonian mechanics, was to become redundant. His description of the effects of gravity, in which mass causes the curvature of space time, showed us that objects travelling through this space-time simply move along the straightest path possible, described by the geodesics of space-time. The 'action at a distance' description of gravity was to be replaced by one in which propagation of the gravitational field was at a finite speed; one which it also shares with light. The solutions of the linearised Einstein Field Equations show that this propagation is in the form of a wave.

In 1974 the pulsar known as 1913+16 was discovered by Russell Hulse and Joseph Taylor [2]. Subsequent measurements of the radio wave emissions showed that there was a modulation of the pulse rate of approximately 7.75 hours due to the Doppler shift as the pulsar moved about the centre of mass of a binary system. Further to this it was discovered that the pulsar was creeping gradually ahead of the orbital position expected if its period was constant. with the discrepancy increasing quadratically in time. This is due to the inspiral of the two neutron stars in this binary system, which increases their orbital rate. The energy lost in this inspiral is in the form of gravitational wave emission. When the calculated inspiral rate due to this emission was compared to the observed inspiral the values matched to around 1%, within the accuracy of the experiment [3]. These measurements therefore provide us with evidence of the existence of gravitational waves.

The quest for direct detection of gravitational waves was begun by Joseph Weber in the 1960s with his development of resonant bar detectors [4]. Work has continued to increase sensitivities of detectors, which are now around 10,000 times more sensitive than those original bar detectors of Weber. Despite Einstein's own lack of confidence that gravitational waves would ever be detected it now appears that just such a detection may be seen in the near future. Detection of gravitational waves will not only confirm aspects of general relativity but will also be the beginning of a new form of astronomy, able to look directly at some of the largest interactions to occur such as the creation and merger of black holes and may allow us to look further back to the beginning of the universe.

A world-wide network of detectors is now being put in place with collaboration between a large number of countries and institutions. Many first generation ground based interferometers such as GEO600 [5] and LIGO[6] are now nearing completion and are taking part in joint test runs. These first generation detectors may indeed be the first to directly detect gravitational waves, yet it is likely that only a small number of sources will be visible to them. The planned upgrading of detectors to give what is known as advanced or mature detectors will improve sensitivities further and greatly improve the

number of potential sources for detection. In particular the work shown in this thesis is directed toward the upgrading of LIGO to Advanced LIGO[7].

In this chapter the nature of gravitational waves is discussed along with the proposed methods of detection, potential sources of noise in detectors and the current status of the GEO600 and LIGO projects.

1.2. The Nature of Gravitational Waves

Gravitational waves are produced by the acceleration of mass. They may be considered as ripples or waves in the curvature of space time and hence produce a time varying tidal strain in space. Sources of gravitational radiation must be at least quadrupole in nature since conservation of mass precludes monopole radiation and conservation of angular momentum precludes dipole radiation. This therefore implies that only non-axisymmetric accelerations of mass will produce gravitational waves [8].

The waves which we may detect on Earth come from distant sources and are the superposition of two independent polarisations of amplitude h_+ and $h_\times$. Figure 1 shows the effect that the passage of each of these polarisations has on a circular ring of test particles if the incident waves are normal to the page. The ring of particles whose initial diameter is L are extended by ΔL in one direction while being compressed by a similar amount in the orthogonal direction. The amplitude of the gravitational wave is then given in terms of the strain it produces in space:

$$h = \frac{2\Delta L}{L} \qquad (1)$$

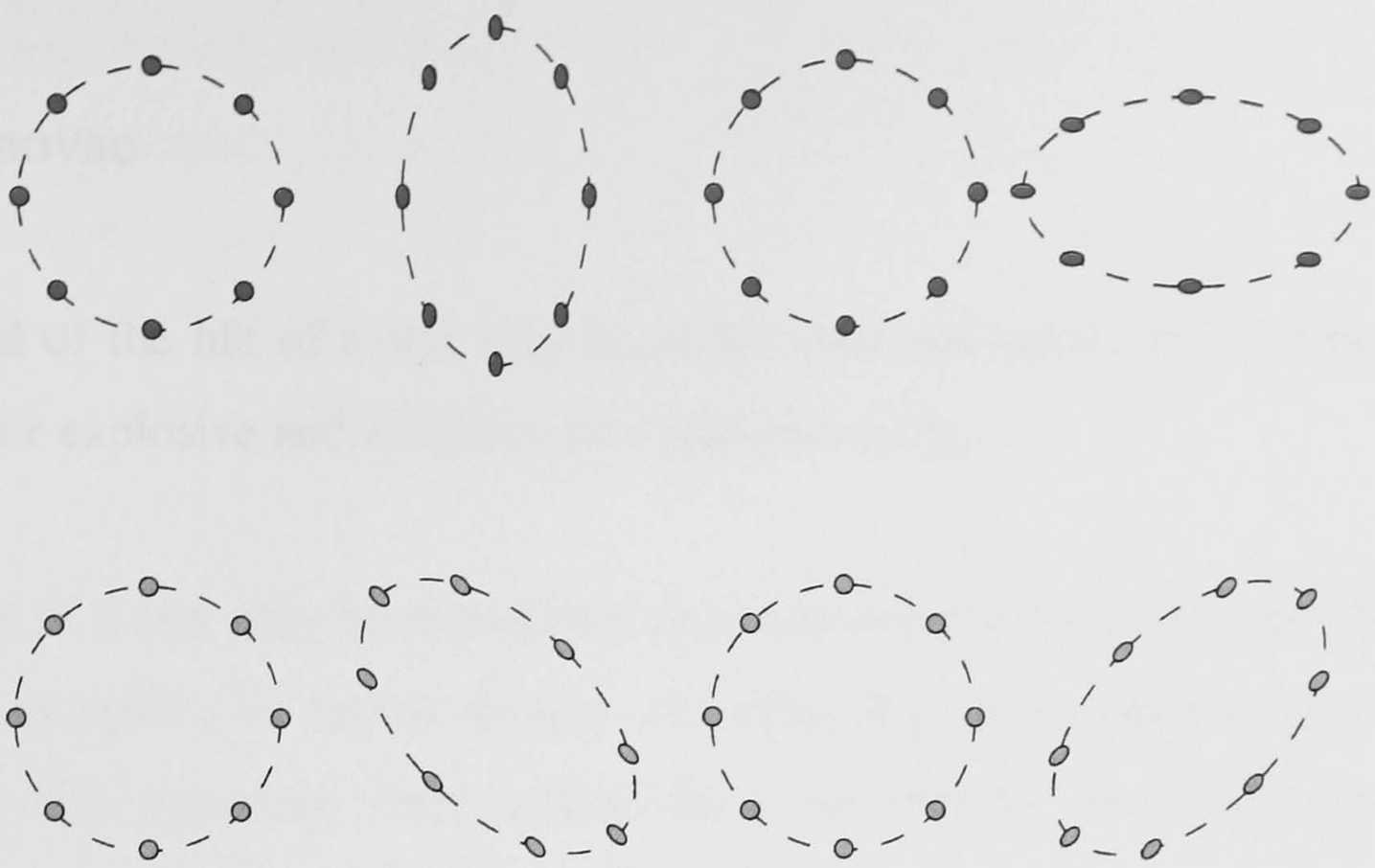

Figure 1: The effect of the two polarisations of gravitational waves incident upon a ring of test particles. The h_+ polarisation is incident upon the red particles while the $h_\times$ polarisation is incident upon the blue test particles

As gravity is the weakest of the four forces of nature it is impractical to construct a source of gravitational radiation in a lab. Indeed if we consider the thought experiment described by Saulson [8] in which two 1 tonne weights are held two meters apart and spun at a frequency of 1kHz about their centre of mass, the strain amplitude produced is only $h \approx 10^{-38}$ at a distance one wavelength from the source. Thus we must look instead to astrophysical sources where accelerations and densities may be extremely high.

1.3. Sources of Gravitational Waves

Discussed below are sources of gravitational radiation which occur in the frequency band of a few Hz to a few thousand Hz, this being the region in which ground based detectors will be most sensitive due to noise sources discussed later in this chapter.

1.3.1. Burst Sources

Burst sources emit gravitational radiation for only a very short amount of time. They are caused by large scale events such as those discussed below.

Supernovae

The end of the life of a star may be either dark and quiet, as a cooling white dwarf, or explosive and luminous as a supernova [9].

The life of a star may be considered as a continuous battle between the force of gravity pulling its matter inward, and opposing forces holding the star out. Initially this opposing force comes from the energy created by fusion of hydrogen in a self regulating process. When the temperature at the core is high enough helium begins to fuse, creating oxygen and carbon. The next stage of the process depends on the size of the star.

In a smaller star, less than approximately five solar masses $(5M_{\Theta})$, as this fuel runs out the temperature at the core is not high enough for further fusion reactions to occur, causing the core to collapse to the point where electron degeneracy pressure due to the Pauli exclusion principle maintains the size. This is known as a white dwarf. If the mass is below the Chandrasekhar limit $(1.4M_{\Theta})$ it will settle and cool unless accreting mass from a companion, usually a larger diffuse star which does not have a strong gravitational grip on matter in its outer most layers, or unless it merges with a companion.

A larger star goes on to fuse carbon and oxygen to produce neon, sulphur and silicon which in turn may fuse to form an iron core. As the iron core does not produce energy through fusion it shrinks and is supported by electron degeneracy pressure until its mass exceeds the Chandrasekhar limit.

When electron degeneracy can no longer support the core it quickly collapses. Electrons, squeezed tightly against the nucleus, join protons to form neutrons, thus reducing the electron degeneracy pressure and accelerating the process. The collapse continues until neutron degeneracy pressure can support the core, forming a neutron star, or if the mass is sufficiently high the collapse continues until a black hole is formed. During the collapse the outer regions

are blown off in a spectacular explosion known as a supernova. Although only a small amount of the energy is released as light, the vast majority being neutrinos, the luminosity is still around one billion times that of the sun. The collapse of the core of a white dwarf due to accretion is known as a Type I supernova, and it is identified by its light spectrum which does not include the hydrogen line. If this collapse is due to a merger with another dense companion star such as another white dwarf the core will be greatly deformed by the increased mass and angular acceleration resulting in the emission of large quantities of gravitational radiation. Collapse of a white dwarf core due to slower accretion of matter will result in a much smaller emission of gravitational radiation.

The collapse of the core of larger mass stars is known as a Type II supernovae and its spectral lines do include hydrogen. If this collapse is non-axisymmetric then gravitational radiation will be produced.

An estimate of the strain amplitude expected from a supernovae calculated by Schutz [10] is:

$$h \approx 5\times10^{-22}\left(\frac{E}{10^{-3}M_{\Theta}c^{2}}\right)\left(\frac{15Mpc}{r}\right)\left(\frac{1kHz}{f}\right)\left(\frac{1ms}{\tau}\right)^{\frac{1}{2}} \qquad (2)$$

where E is the total energy radiated at a frequency f, over timescale τ, at a distance r from the detector.

The typical event rate calculated for such supernovae out to a distance of 15Mpc, where the Virgo cluster occurs, is several per month[11].

Coalescing Compact Binaries

A system of two stars orbiting about a common centre of mass is known as a binary system. Most stars form part of a multiple star system, with the binary being the most common. If the stars have a high density this is known as a

compact binary system. There are three types of compact binary systems, neutron star / neutron star (NS/NS), black hole / black hole (BH/BH) and neutron star / black hole (NS/BH). An example of a compact binary system which has already been mentioned is PSR1913+16 whose orbital frequency increases with time as the two neutron stars inspiral. The energy lost from inspiral is emitted as gravitational radiation. As the two close in upon each other the frequency of this radiation will increase. The frequency is too low during most of the inspiral for it to be measured using ground based detectors, however it will be within the detection band of space based detectors. In the last few seconds before coalescing the frequency will be high enough to be measurable with terrestrial detectors, finally ending with a strong burst emission known as a 'chirp'.

The estimated strain amplitude for a coalescing binary system of NS/NS is calculated by Schutz [12] to be :

$$h \approx 1\times10^{-23}\left(\frac{100Mpc}{r}\right)\left(\frac{M_B}{1.2M_\Theta}\right)^{\frac{5}{3}}\left(\frac{f}{200Hz}\right)^{\frac{2}{3}} \qquad (3)$$

where $M_B = (M_1 M_2)^{\frac{3}{5}} / (M_1 + M_2)^{\frac{1}{5}}$, M_1 and M_2 are the masses of the two stars, the distance to the source is r and the emitted gravitational radiation is at a frequency f .

While the fraction of compact binary systems involving black holes is thought to be smaller than for neutron stars, the greater mass gives a higher amplitude to the gravitational radiation and makes it more likely we shall detect these.

1.3.2. Periodic Sources

While binary systems will emit gravitational radiation continuously during inspiral, the frequency when their separation is still reasonably large is too low to put such a source within the detection band of a ground based detector.

However other stably rotating sources may appear within such a frequency band. By using long integration times the signal to noise ratio when measuring emissions from a continuous source may be improved and a detection may be made using a single detector assuming the noise is random. Potentially detectable continuous sources are discussed below.

Pulsars

Neutron stars which spin non-axisymmetrically will emit gravitational radiation. If a neutron star is created from the collapse of a spinning core which has a large diameter, then in order to conserve angular momentum the neutron star must have a high rotation speed. In addition the accretion of mass from a companion may increase the angular momentum. The non-axisymmetric motion may be due to irregularities in the surface of the pulsar or may occur due to the pulsar precessing due to accretion from its companion. The degree of non-symmetry is given by the star's equatorial ellipticity, ε, with an estimated strain amplitude for gravitational emissions given by [13]:

$$h \approx 6\times10^{-25}\left(\frac{f_{rot}}{500Hz}\right)^{2}\left(\frac{1kpc}{r}\right)\left(\frac{\varepsilon}{10^{-6}}\right) \tag{4}$$

This frequency of gravitational wave emission is twice that of the rotation of the pulsar since there can be no monopole or dipole gravitational wave emission.

The Crab pulsar, the remnant of a supernova documented by Chinese astronomers in 1054 to have been seen in daylight for weeks, is expected to be a source of gravitational radiation. As one of the fastest spinning pulsars it has a rotational frequency of 30.3Hz and is therefore expected to emit gravitational waves of frequency 60.6Hz and gives an estimated strain amplitude of $h \sim 10^{-24}$ [13].

Wagoner Stars

If a neutron star is caused to spin up due to accretion from a companion it may reach a limit known as the Chandrasekhar-Friedman-Schutz instability point beyond which it will become non-axisymmetric. The additional angular momentum may then be lost as gravitational waves as first described by Wagoner [14]. Such a source is expected to produce a strain amplitude [8]:

$$h \approx 3\times10^{-27}\left(\frac{330Hz}{f_{rot}}\right)^{\frac{1}{2}}\left(\frac{1kpc}{r}\right)\left(\frac{L_\gamma}{10^{-11}Jm^{-2}s^{-1}}\right)^{\frac{1}{2}} \quad (5)$$

where L_γ is the x-ray flux which is used as an indicator of the rate of accretion.

1.3.3. Stochastic Sources

A final source of gravitational waves whose amplitude may be high enough to be detectable, known as stochastic background, comes from the superposition of signals from many sources. Due to the noise like nature of the stochastic background two or more detectors are required to make measurements of it as the results must be correlated. Otherwise it is indistinguishable from other noise sources in a detector.

One potential source which will appear as a part of the stochastic background may come from gravitational waves produced as a result of an inflationary period following the big bang. A prediction for the magnitude of h, using the cosmic string scenario for the creation of galaxies, is given by [15]:

$$h \approx 1.8\times10^{-25}\left(\frac{H_0}{100kms^{-1}Mpc^{-1}}\right)\left(\frac{\Omega_{GW}}{10^{-8}}\right)^{\frac{1}{2}}\left(\frac{f}{100Hz}\right)^{-\frac{3}{2}}\left(\frac{B}{2Hz}\right)^{\frac{1}{2}} \quad (6)$$

for a bandwidth B, taken about the frequency f, where H_0 is Hubble's constant and with Ω_{GW} being the energy density per logarithmic frequency interval required to close the universe.

Figure 2 shows a chart, produced by Kip Thorne [16], of the predicted strain amplitude and frequency distribution of sources that are likely to be detected by advanced detectors along with the sensitivities such detectors may achieve.

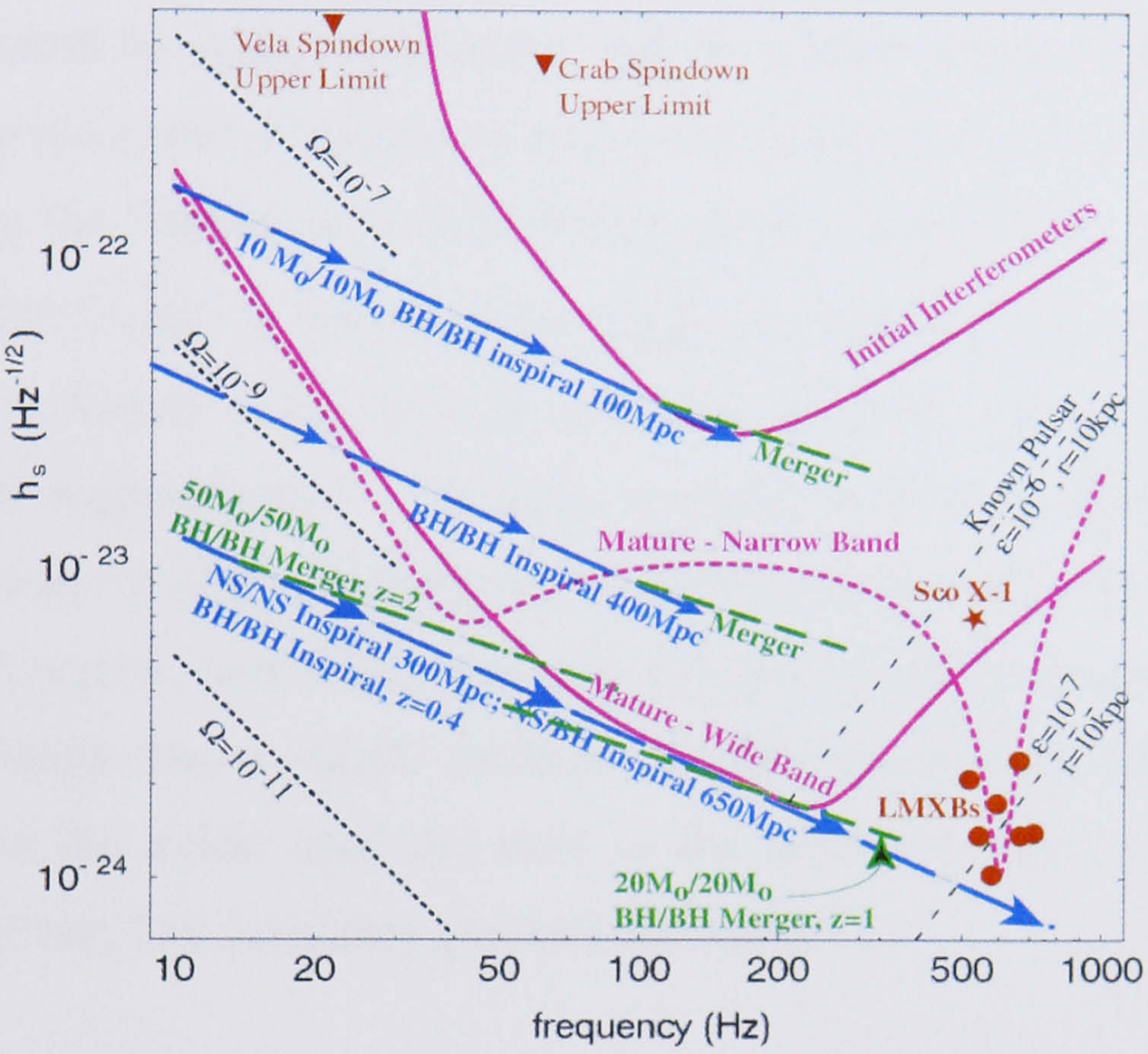

Figure 2: Predicted sources of gravitational waves of interest to ground based systems along with the design sensitivity curves for initial and advanced LIGO detectors. Graph created by Kip Thorne

1.4. Methods of Detection

The strain in space which sources of gravitational waves induce is, as we have seen in the previous section, extremely small. Any potential detector must therefore be extremely sensitive to small strains. Currently there are two types of detector being developed for ground based measurements, these being resonant bars and laser interferometers.

The long baseline interferometers are expected to have a detection band from a few Hz to a few kHz. Space based detectors would not be subject to the same gravity gradient noise, discussed in Section 1.4.3, and hence would be capable of high sensitivity at even lower frequencies.

Other detection methods for gravitational waves include Doppler tracking of spacecraft and pulsar timing. The relative separation of a spacecraft and the earth will be affected by the strain of a passing gravitational wave, which may be measured by using the Doppler shift of a radio signal, which is used to track the spacecraft, measured against a very stable clock [17]. Measurements made by the Ulysses joint ESA/NASA project have set an upper limit of $h \sim 3\times10^{-15}/\sqrt{\mathrm{Hz}}$ in the frequency region of millihertz [18]. The CASSINI mission to Saturn should improve upon this sensitivity by approximately two orders of magnitude [19]. The limits to sensitivity of these measurements are the precision of clock used and any fluctuations in the medium through which the radio waves travel which may alter the speed of electromagnetic radiation. Pulsar timing uses a similar technique to Doppler tracking. Here the radio signals of the pulsar itself are used as the reference clock to look for the effects of very low frequency gravitational waves.

1.4.1. Resonant Bar Detectors

At the start of the 1960s Joseph Weber began work on a type of detector now known as the resonant bar detector[4]. Built around a massive metal core of low mechanical loss material to reduce the effects of thermal noise, a typical bar detector works by excitation of the longitudinal mode of a cylinder of either aluminium or niobium, by a passing gravitational wave. This motion is then measured using a transducer highly sensitive to motion of the bar.

A claim in 1969 by Weber that he had seen coincident signals in two bar detectors has since been essentially discredited as more sensitive instruments have failed to reproduce such an event as upper limits on gravitational emissions are reduced.

The main difficulties in producing a usable instrument are high susceptibility to thermal noise, and low bandwidth.

While limits to sensitivity due to seismic noise and acoustic noise are dealt with by suspending the bar from vibration isolation stages and placing it under vacuum, thermal noise presents a larger problem. In order to reduce its effects most bar detectors now operate at cryogenic temperatures with some using operating temperatures as low as $\sim 0.2\mathrm{K}$. Such a detector may achieve a strain sensitivity of order $10^{-19}/\sqrt{\mathrm{Hz}}$ [20, 21]. Currently there are four resonant bar detectors achieving a strain sensitivity of this order, these being AURIGA, EXPLORER, NAUTILUS and NIOBE.

With bandwidth being restricted by the resonant nature of this type of detector, work is now being done to produce spherical detectors which will have a highly improved bandwidth due to their multiple resonant frequencies and the ability to determine direction and polarisation of the wave. Also the increased mass of a spherical detector of similar resonant frequency gives a lowered thermal noise with proposed detectors such as 'Mario Schenberg' detector in Brazil having a design sensitivity of around $h \sim 10^{-21}/\sqrt{\mathrm{Hz}}$ and a bandwidth of $3.0-3.4\mathrm{kHz}$ [22]. Another such detector named MiniGRAIL in Holland will shortly be operational [23].

1.4.2. Ground Based Laser Interferometric Detectors

A Michelson interferometer, with its orthogonal arms, provides an excellent basis for a detector due to the quadrupole nature of gravitational waves. If we look at the effect, shown in Figure 1, that the passage of a gravitational wave has on a ring of test particles we may see that using an interferometer, such as that shown in Figure 3, for a correctly aligned gravitational wave, the path length of one arm would increase while the other would decrease.

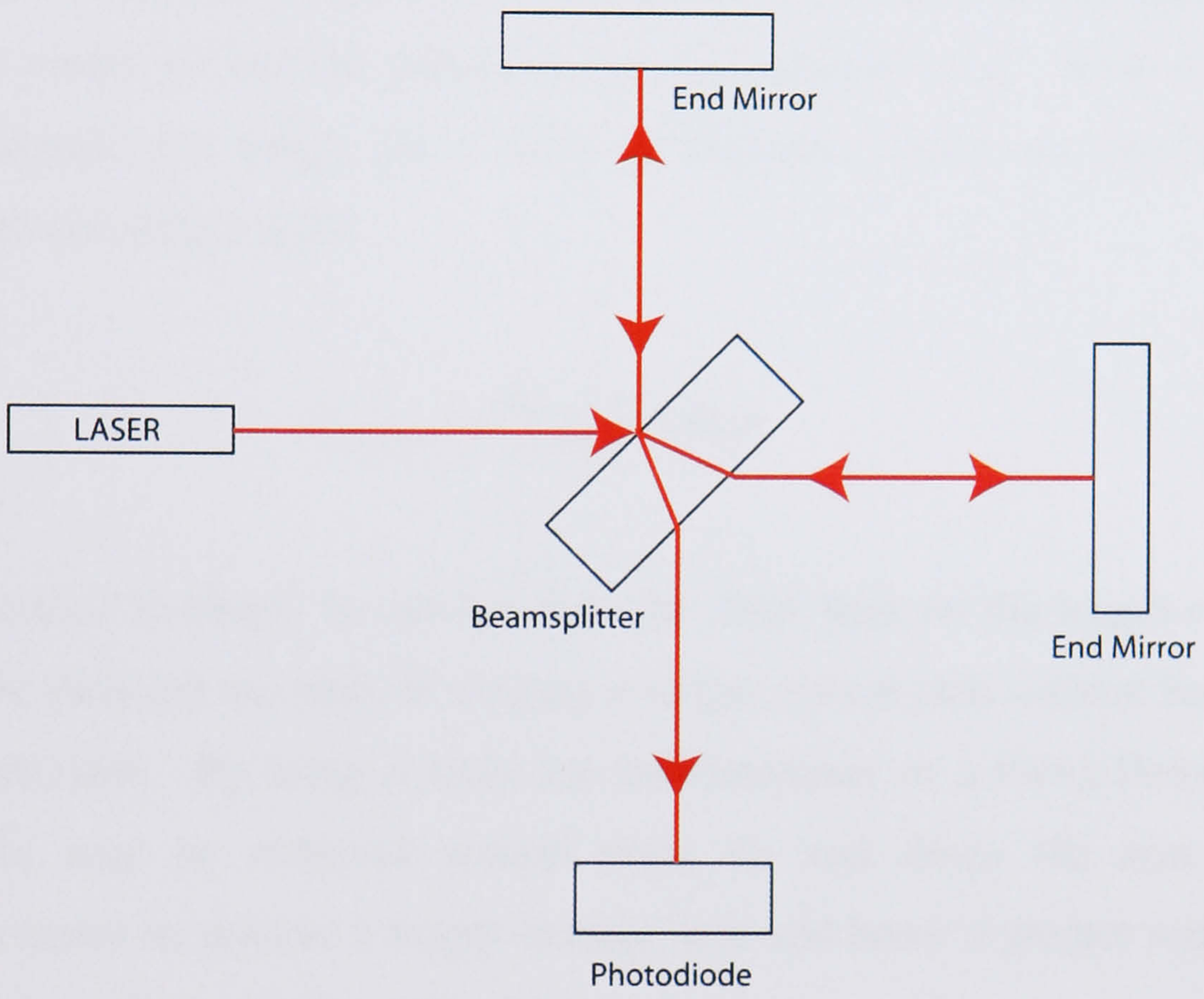

Figure 3: Schematic of a simple Michelson interferometer

A Michelson interferometer works by splitting the light of an incident laser using a beam splitter and sending the beams down orthogonal arms each of similar length. The reflected light is then recombined by the beam splitter with an interference pattern being seen at the output, in this case a photodiode detector. As the relative arm lengths changes due to motion of the mirrors the interference pattern is altered due to the change in relative path length travelled by the light. The mirrors are suspended as pendulums to isolate them from seismic noise and are operated under vacuum to remove the interactions of air molecules.

In practice interferometers are designed to hold the output steady on a dark fringe by acting back to one of the mirrors with a force proportional to the output signal, thus the output is often taken from this feedback signal.

The incidence of a gravitational wave produces a fractional change in the arm length, $\partial l / l$, hence the signal strength is directly proportional to the length of arm. However the curvature of the earth provides a practical limit to the size of detector that can be built, this being around 4km. The interferometer achieves its maximum sensitivity when the light is stored in the arms of the interferometer for half the period of the gravitational wave. If we calculate the optimum arm length for a wave of frequency 1kHz we find that the optimum arm length is [8]:

$$L_{optimum} = \lambda_{gw} / 4 \approx 75\text{km} \tag{7}$$

This distance is clearly far greater than the 4km limit on the length of arms, however there are methods of creating a longer optical path without building a larger detector. By using a delay line interferometer or a Fabry-Perot cavity the light may be reflected several times up and down the arm of the interferometer to achieve a longer storage time and hence a greater sensitivity. These two designs are discussed next.

Delay Line Interferometers

In a delay line interferometer, shown in Figure 4, two additional mirrors are added close to the beam splitter. These are known as the inboard mirrors and are used to reflect light returning from the end mirrors back along the arm, thus increasing the storage time. In one arrangement the laser light enters the arm through a hole in the inboard mirrors and then travels up and down the arm with the beams not overlapping due to the curved surface of the mirrors. This design of interferometer was first proposed by Weiss in the early 1970s

[24], with a variation on this design, the 30m delay line prototype at Garching achieving a strain sensitivity of $h \sim 10^{-19} / \sqrt{\text{Hz}}$ by 1988 [25].

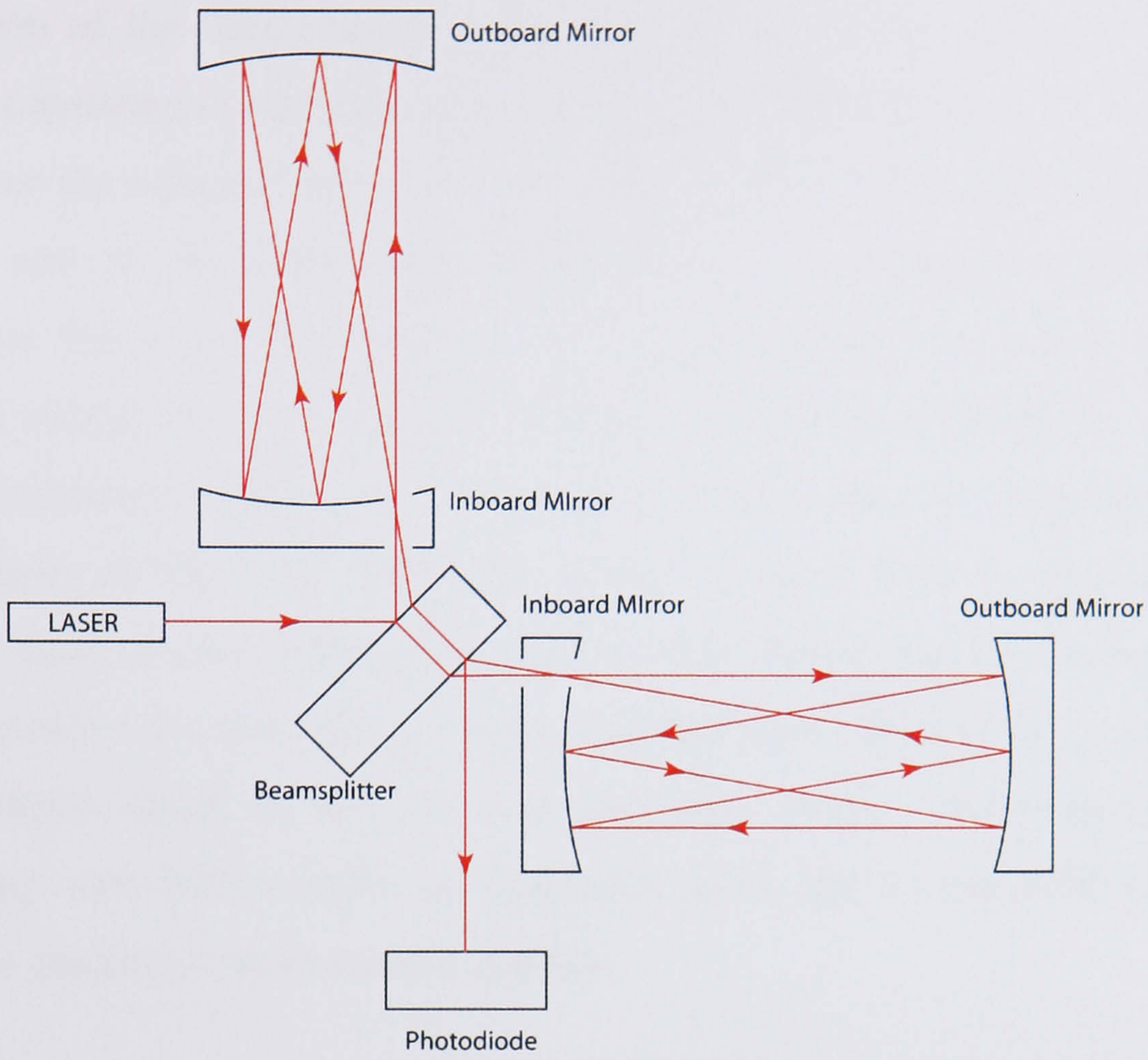

Figure 4: Schematic of a delay line interferometer in which the optical path length of the arms is increased using multiple bounces of light in the arms using non-overlapping beams

With its non-overlapping beams the delay line interferometer also provides a simple way of considering the issue of a storage time limit. As the light travels back and forth down the arms of the interferometer the phase change due to an incident gravitational wave builds up. As the storage time starts to exceed one half of the time period of the gravitational wave the phase starts to move back again as the wave enters the second half of its cycle, thus reducing the overall phase change seen at the photodetector and hence the sensitivity.

Fabry-Perot Interferometers

An alternative system for increasing the path length of the arms is to use Fabry-Perot cavities. Developed in Glasgow in the early 1980's [26], this

method provides some advantages over the delay line techniques discussed above and is the design used in the LIGO detectors.

Each arm of the interferometer, shown in Figure 5, contains a Fabry-Perot cavity, consisting of one fully and one partially reflecting mirror. Unlike in a delay line the reflected beams in the arm lie on top of each other allowing the mirror size to be significantly smaller than in a delay line system. In operation the cavity must be held on resonance, where its length, L, is an integral number of wavelengths of the laser. In a process known as 'locking' the interferometer, the cavity of one arm is held on resonance by altering the wavelength of the laser, while the second cavity is held on resonance by feeding back to one of the cavity mirrors, thus maintaining the output of the interferometer at a dark fringe. A gravitational wave signal is then encoded in the feedback signal for the laser and secondary cavity. The requirement of operating with both cavities on resonance gives rise to the need for some complex electronic servo control systems.

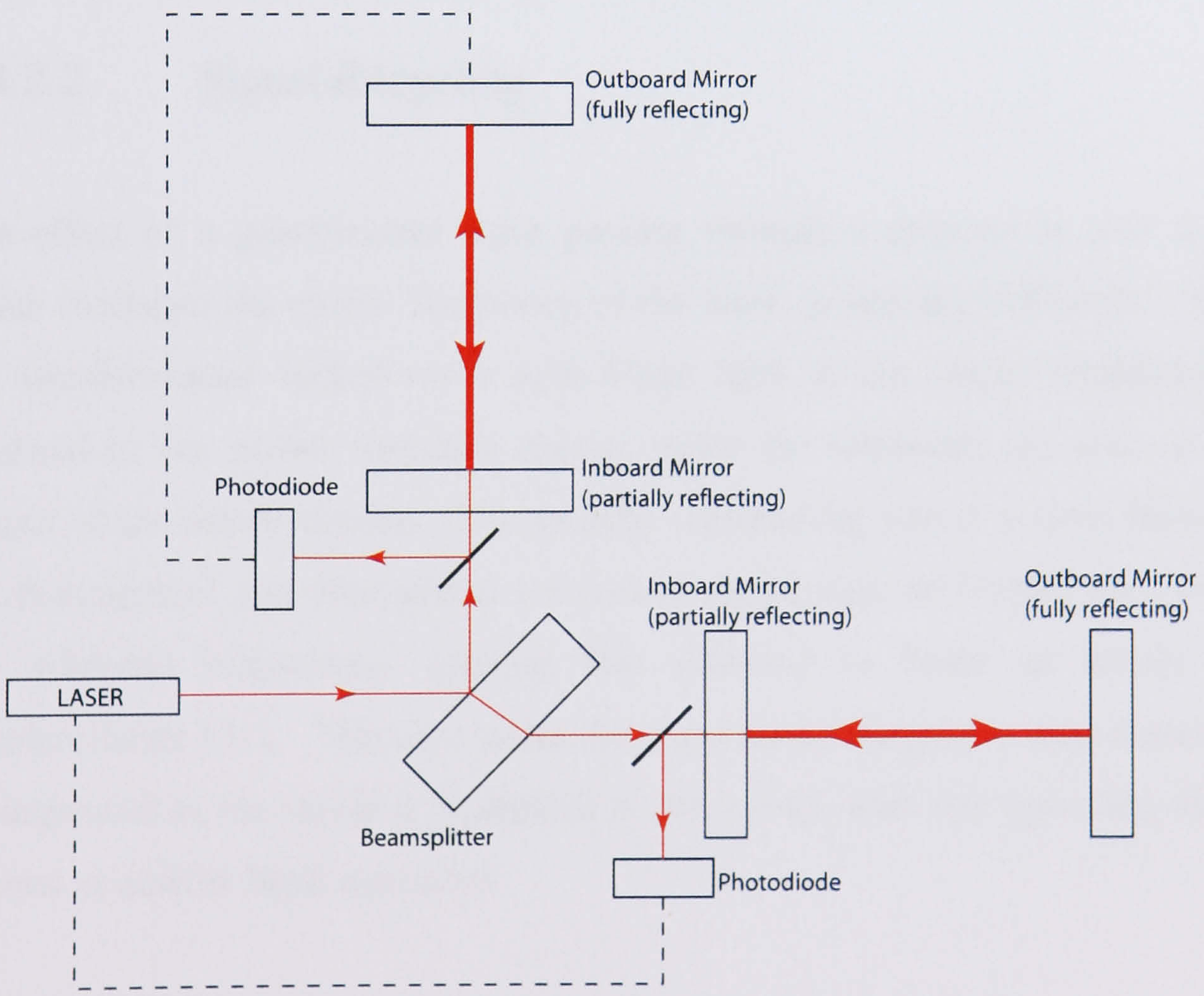

Figure 5: Schematic of a simple Fabry-Perot interferometer in which the optical path length of the arms is increased by storing the light in cavities using a partially reflecting inboard mirror and overlapping beams.

The prototype detectors at the University of Glasgow (10m) and also at California Institute of Technology (40m). both Fabry-Perot designs. have achieved strain sensitivities of the order of $10^{-19}/\sqrt{\text{Hz}}$ [27-29].

1.4.2.1. Power Recycling

With the interferometer operated such that the output is held on a dark fringe. the light exiting the interferometer will head back toward the laser. with the interferometer acting like a mirror. If a partially reflecting mirror is then placed between the laser and the beamsplitter it is possible to form a resonant cavity with the interferometer acting as the second mirror [30]. Thus the power within the interferometer will build up. The increase in power expected in GEO600 will of the order of 2000 times, with an increase in sensitivity in frequency regions that are shot noise limited of a factor of $\sqrt{2000}$.

1.4.2.2. Signal Recycling

The effect of a gravitational wave passing through a detector is such as to phase modulate the carrier frequency of the laser, producing sidebands. With the interferometer locked on a dark fringe light at the carrier frequency is returned to the power recycling mirror, while the sidebands are seen at the output of the interferometer. If a partially transmitting mirror is used between the beamsplitter and photodiode a resonant cavity may be formed for one of the sideband frequencies, causing this sideband to build up within the interferometer [31]. The shot noise for a particular frequency may therefore be improved as the signal is multiplied in this cavity. with this operating mode known as narrow band operation.

1.4.2.3. Current Ground Based Interferometric Detectors

A number of ground based interferometric detectors are currently being built or are moving closer toward their design sensitivities through continued development. The distribution of these is shown in Figure 6.

Figure 6: Global distribution of current ground based interferometric detectors

The GEO 600 detector at Ruthe near Hannover in Germany is a joint German/British project with a 600m arm length and is a delay line interferometer . It has taken part in the collaborative detection runs in order to set upper limits and although a smaller detector than others its advanced optical configuration allows it to achieve high sensitivities [32]. This detector is discussed further in Section 1.6.

The detectors that form LIGO are based in Livingston (Louisiana) and Hanford (Washington). Both have arm lengths of 4km with the Hanford detectors beam tubes also being shared with a 2km detector [6]. These detectors have also taken part in the recent science runs achieving sensitivities $4\times10^{-22}/\sqrt{\text{Hz}}$ at 100Hz as shown in Figure 9. In the near future a large scale upgrade is planned for LIGO to create what will be known as Advanced LIGO. The upgrade to these detectors is discussed further in Section 1.7.

The VIRGO group, an Italian/French collaboration, is currently constructing a 3km arm length interferometer in Cascina near Pisa in Italy [33]. The infrastructure for this detector is currently in place with operation expected to be late in 2004. An upgraded detector is planned called Advanced VIRGO. It will use monolithic suspensions, signal recycling and a 200W YAG laser. A cryogenic detector called EGO has recently been discussed among European groups [34].

A Japanese detector called TAMA is already completed in Tokyo with an arm length of 300m [35]. This is a Fabry-Perot interferometer using power recycling and has reached sensitivities of $8\times10^{-19}/\sqrt{\text{Hz}}$ with a duty cycle of 81%. A second interferometer is already planned named CLIO based in the Kamioka mine which will use cryogenically cooled test masses to reduce thermal noise and will be built underground to reduce seismic and gravity gradient noise [36].

The ACIGA group plans to construct a 4km arm length detector at Gingin in western Australia where an 80m prototype is currently being constructed [37].

1.4.3. Space Based Interferometric Detectors

With ground based detectors fundamentally limited at low frequency by gravity gradient noise, work is now being carried out on a planned space based interferometer known as LISA [38]. It will observe gravitational waves at frequencies down to 0.1mHz, where continuous sources such as binary stars with large separations may be detected. The Laser Interferometer Space Antenna is a joint project between NASA and ESA, with a launch planned for 2013.

LISA will consist of three space craft, each providing a drag free environment for their test masses, which will form an equilateral triangle of side $5\times10^{9}\,\text{m}$.

Space based interferometers do not provide an alternative to ground based detectors but instead will be used to compliment them, with observations being made at far lower frequencies.

1.5. Sources of Noise

The sensitivity of a laser interferometric detector is limited at different frequencies by a number of sources of noise. We shall now discuss these sources of noise and what may be done to limit their effect on the detector and hence maximise the sensitivity.

1.5.1. Photon Shot Noise

Photon shot noise arises from fluctuations in the vacuum level. If N photons reach the photodiode then from Poisson statistics the uncertainty in the measurement will be $\sqrt{N}$. This gives a fluctuating noise against which a signal has to be detected. The photon shot noise sensitivity limit for a delay line type interferometer may be given by [15]:

$$h_{shot}(f) = \left(\frac{\pi \hbar \lambda}{2\varepsilon P_{in} c}\right)^{1/2} \frac{f}{\sin(\pi f \tau)} \quad \text{per } \sqrt{\text{Hz}} \tag{8}$$

where $\hbar$ is the reduced Plank's constant, λ is the wavelength of the laser, ε is the quantum efficiency of the photodiode, P_{in} is the power of the laser, c is the speed of light, f is the frequency of an incident gravitational wave and τ is the length of time the light is stored. From this equation we see that the length of storage time may be set to minimise the effects of shot noise. This occurs when τ is equal to half the period of the gravitational wave and hence $f\tau = \frac{1}{2}$. Also we see that the shot noise may be improved by increasing the power of the laser. Shot noise is expected to be the dominant noise source at frequencies close to a few hundred Hz.

1.5.2. Radiation Pressure Noise

Radiation pressure noise originates from fluctuations in the number of photons impacting upon the surface of the test masses. When a photon hits a test mass and is reflected momentum is transferred. Hence any fluctuation in the number of photons will cause a fluctuating force on the mirror. The limit to sensitivity this sets for a delay line type interferometer is given by [8]:

$$h_{rp} = \frac{N}{mf^2 L}\sqrt{\frac{2\hbar P_{in}}{\pi^3 c\lambda}} \quad \text{per}\sqrt{\text{Hz}} \tag{9}$$

where m is the mirrors mass, L is the arm length and N is the number of times the light in one arm travels a distance $2L$. We see that radiation pressure noise falls off at higher frequencies and increases with laser power.

Radiation pressure and photon shot noise contribute to what is called optical or quantum noise, this being given as the quadrature sum of these two noise sources. We see from equations 8 and 9 that while at low frequency radiation pressure noise is the dominant part of the optical noise while at high frequency photon shot noise dominates. Also we find that while one increases with laser power the other decreases, thus there exists some power at which, for a given detection frequency, the combined noise is a minimum. This occurs when $h_{shot}(f) = h_{rp}(f)$ and sets a noise level known as the standard quantum limit (SQL). The quantum limit comes as a result of the Heisenberg uncertainty principle and may be considered as follows. If we wish to accurately measure the position of our test masses then in order to improve shot noise we must increase the laser power which in turn increases the radiation pressure. The momentum of the masses is now less well known and at some subsequent point in time a measurement of the position will be less accurate as a result of this.

Research is now being carried out on quantum non demolition (QND) systems which may make measurements below the standard quantum limit [39]. One

type of potential QND system is the Sagnac interferometer in which the output signal is proportional to the relative speed of the test masses rather than position [40]. In this type of system light is passed in opposite directions round a ring formed by mirrors, with both light beams reflecting from the same mirrors and the relative phase being measured at the output. Radiation pressure noise does not contribute to the overall noise of the detector in this scheme as the light travelling in the interferometer bounces off all mirrors giving rise to a similar momentum transfer to each. Moreover we may see that this system does not limit us to the SQL as the momentum is a QND observable. However this system is still susceptible to photon shot noise as it is still optically sensed, and hence will require large amounts of laser power to be circulating in the interferometer. A further problem arises due to the thermal lensing that this light will cause for example at the beam splitter. A solution to this is to use all reflective optics with low absorption coatings and which have high thermal conductivities to dissipate any heat that is generated through absorption. The beam splitter used will be a diffractive grating.

It has also been realised that signal recycled Michelson interferometers should be capable of performing below the SQL over a very narrow frequency band [41]. The effect of radiation pressure, in moving a mirror, is to cause a change in the phase of photons reflected. The amplification of sidebands at a particular frequency, due to the signal recycling, will then effectively couple this phase modulation into a phase and amplitude modulation. The effect is such that an optical spring is set up. At the resonant frequency of this optical spring the interferometer can perform below the SQL although this is only over a very narrow bandwidth.

1.5.3. Seismic Noise

Indirectly Coupled

Another important source of noise to consider is displacement of the test masses through direct coupling of ground motion. This ground motion may

come from natural phenomena, such as the motion of oceans, or from manmade sources such as movement of traffic and is dependant on site location and may vary from day to day. The mirrors of the interferometer must be isolated from seismic noise at detection band frequencies and for this reason they are mounted as part of a pendulum suspension. As discussed in Chapter 3 a pendulum attenuates this displacement by a factor of approximately $\left(f_0/f\right)^2$ where f_0 is its resonant frequency and f is the frequency at which it is driven [8]. This is effective in the horizontal direction where the resonant frequency is low and the mass may be suspended from a series of pendulums each giving this factor of isolation. However in the vertical direction this is not effective due to the higher resonant frequency. With vertical motion coupling in to horizontal displacement at some low level this vertical noise will dominate [42]. A more detailed description of the suspensions will be given in Chapter 3.

Another stage of passive isolation is given by suspending the pendulum from vibration isolation stacks. These consist of alternating layers of rubber and steel and give isolation in all directions above their resonant frequencies. Additionally, due to the lossy nature of rubber there is little amplification of noise at the resonant frequency of the stack. The resonances of the pendulums below will become excited however they are far less lossy and active control systems are used to damp out their resonances.

Finally a system of active isolation is also often used whereby geophones pickup ground motion and are coupled to piezo actuators which actively move the suspension to cancel out seismic motion.

Directly Coupled

Also known as gravity gradient noise this arises when test masses couple directly to seismic noise due to local fluctuations in the gravitational field [43]. The use of pendulums and vibration isolation systems has no effect on

this source of noise as it affects the mass directly through gravitational field coupling when large amounts of mass are moved in proximity to the test masses. This source of noise sets a challenging limit to low frequency detection on earth, one which may be reached with the coming generation of advanced detectors.

1.5.4. Thermal Noise

The thermally excited motion of atoms in the test masses and suspensions of an interferometer combines to give rise to a source of displacement noise known as thermal noise [8]. According to the equipartition theorem the mean value of energy for each quadratic term in the expression for the total energy is $\frac{1}{2}k_BT$ joules. While it is not possible to reduce the total energy associated with this form of noise unless we reduce the temperature by cryogenic cooling of the suspension, it is possible to alter or shape the spectral distribution of this noise such that its effects are reduced at detection band frequencies. This is done by using high Q materials which concentrate the energy into narrow bands around their resonant frequencies, thus reducing the noise off resonance. The resonant frequencies of the suspension fibres will be within the detection band, though at known frequencies and may thus be removed using notch filters. The resonant modes of the test masses occur at frequencies above the detection band and may therefore be dismissed.

In current detectors the off resonance thermal noise of the internal modes of test masses is one of the major sources of noise at mid-detection band frequencies (~50 to 500Hz). As such a large amount of experimental work is currently under way to reduce the thermal noise associated with the masses and mirror coatings, with investigations looking at materials including fused silica and sapphire. The off resonance thermal noise associated with the modes of the suspension fibres is expected to be below that due to other sources of noise.

Thermal noise will be discussed in greater depth in Chapter 2.

1.5.5. Thermorefractive Noise

The temperature dependence of the refractive indices of the mirror coatings of test masses and of the bulk material of the beam splitter gives rise to a source of noise known as thermorefractive [44]. Localised fluctuations in temperature may therefore alter the refractive index of the material leading to an altered phase of transmitted or reflected light, ultimately leading to phase noise in the recombined beam of an interferometer.

Thermorefractive noise is expected to be one of the dominant noise sources at mid-band frequencies in the GEO600 interferometer.

1.5.6. Other Noise Sources

While the noise sources discussed in the previous sections are the main ones to limit the sensitivity of the detector there are other noise sources which are of interest to briefly discuss. These are mostly concerned with the laser and its stability as well as control electronics for the suspensions and are not expected to be dominant at any frequencies in the detection band.

The frequency and intensity of the laser may both vary giving rise to noise. Frequency noise is reduced by frequency stabilising using a reference cavity while the intensity noise is moved to a frequency at which it is not the dominant noise source by use of modulation. Variations in the orientation position and shape of the laser may also introduce noise and are minimised by using a mode cleaning cavity or a single optical fibre [45].

Any light that is scattered in the interferometer will have a random phase relative to the main beam and may therefore contaminate it giving rise to another source of noise. This may be reduced by use of baffles to absorb stray beams.

Two sources of noise may occur due to fluctuations in the vacuum. The first is an increase in thermal noise due to viscous damping by residual gas molecules. Secondly such fluctuations in vacuum will affect the refractive index inside the tanks and arms and give rise to noise in a similar manner to the thermorefractive noise discussed above. Neither of these sources of noise will be dominant if the vacuum is kept below approximately 10^{-8} mbar which is achievable [8].

Electronic noise in the systems which are used to damp parts of the suspension may also cause motion of the test masses and hence may be a source of noise.

The expected noise performance of Advanced LIGO is given in Figure 7, showing the constituent noise sources.

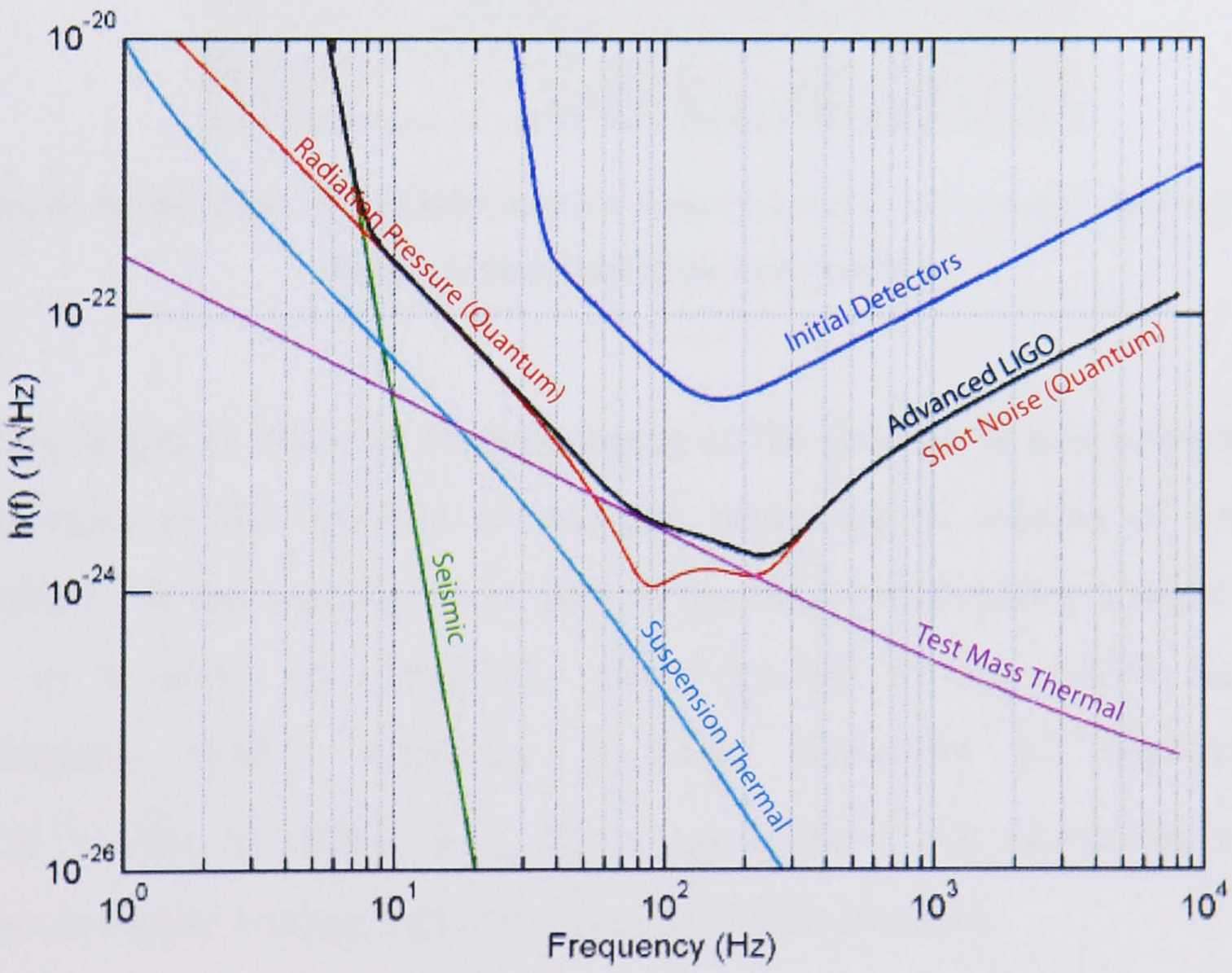

Figure 7: Predicted noise performance of the Advanced LIGO detector (black line) along with constituent noise sources [46].

1.6. GEO600

GEO600 is a delay line interferometer, shown in Figure 8, using both power recycling and signal recycling. The detector is a collaboration of groups from the University of Glasgow, the University of Wales (Cardiff), the Max Planck Institut für Quantenoptik (Garching, Germany), the Albert Einstein Institute (Hannover) and Laser Zentrum (Hannover).

Figure 8: Aerial photo of GEO600 detector near Hannover in Germany showing the two 600m vacuum tube arms and buildings.

Having begun in 1995 the commissioning of the detector is now complete and sensitivities of the detector are steadily improving as sources of noise are identified. It has recently taken part in the third collaborative science run as part of a series of coincident runs organised by the LIGO Scientific Community (LSC), achieving a strain sensitivity of approximately $2\times10^{-21}/\sqrt{\text{Hz}}$ at 100Hz and a duty cycle of 98%. The sensitivity curve is shown in Figure 9 along with those for the LIGO detectors.

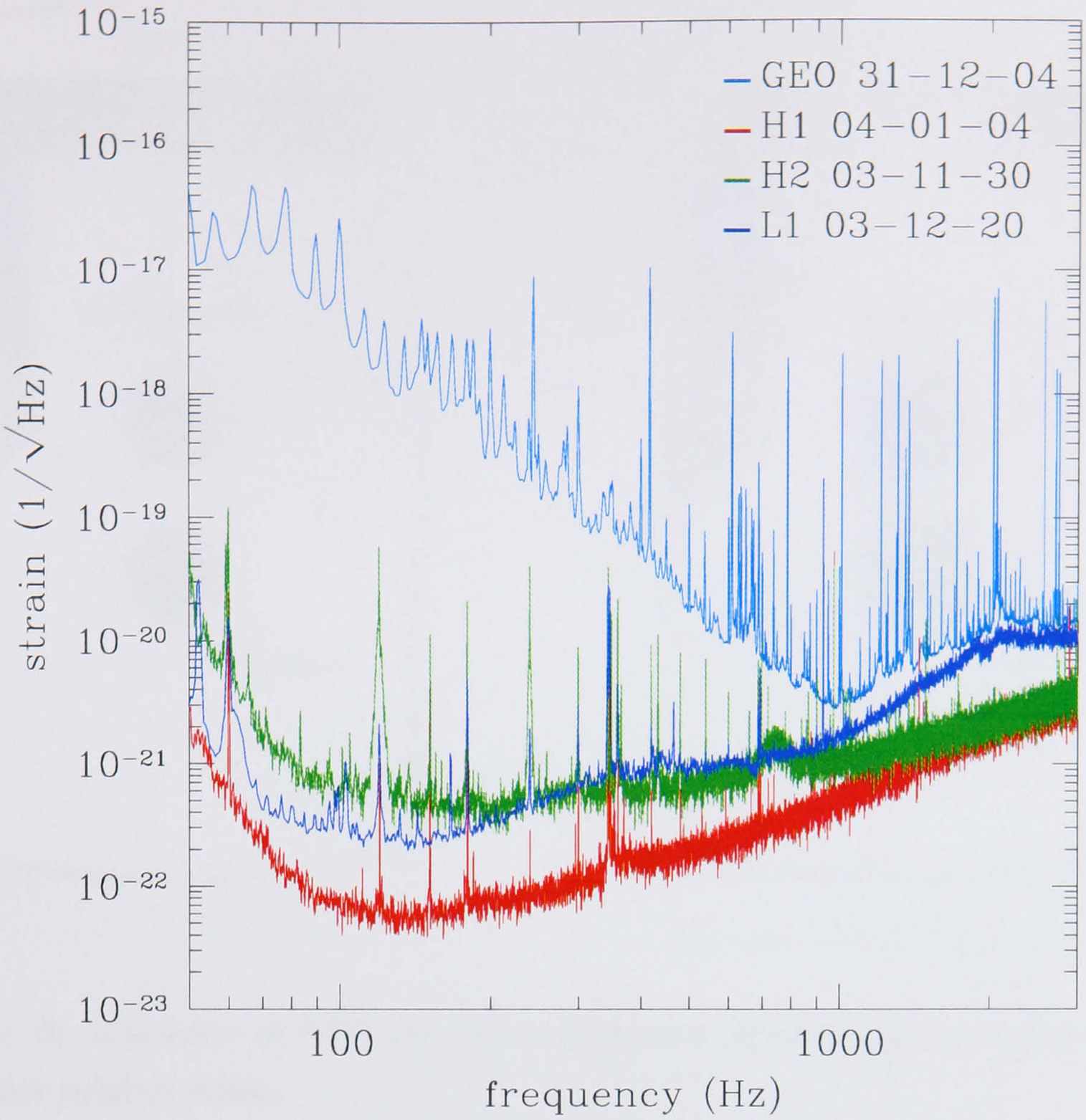

Figure 9: Sensitivity results from the third LSC science run. The LIGO detector sensitivities shown are Hanford 4km (red, H1), Hanford 2km (green, H2) and Livingston 4km (dark blue, L1). The GEO600 detector sensitivity is shown in light blue (GEO).

The laser used is an injection locked laser diode pumped Nd:YAG system giving an output power of 12W, which is passed through two modecleaners, to improve the geometry of the beam [47], and a power recycling mirror before being split at the beam splitter and travelling out to the end test masses. The test masses are suspended as triple pendulums, as shown in Figure 10, in order to improve the horizontal isolation from seismic noise, which in turn is suspended from passive and active vibration isolation stacks. Vertical isolation is improved by used of cantilever blades.

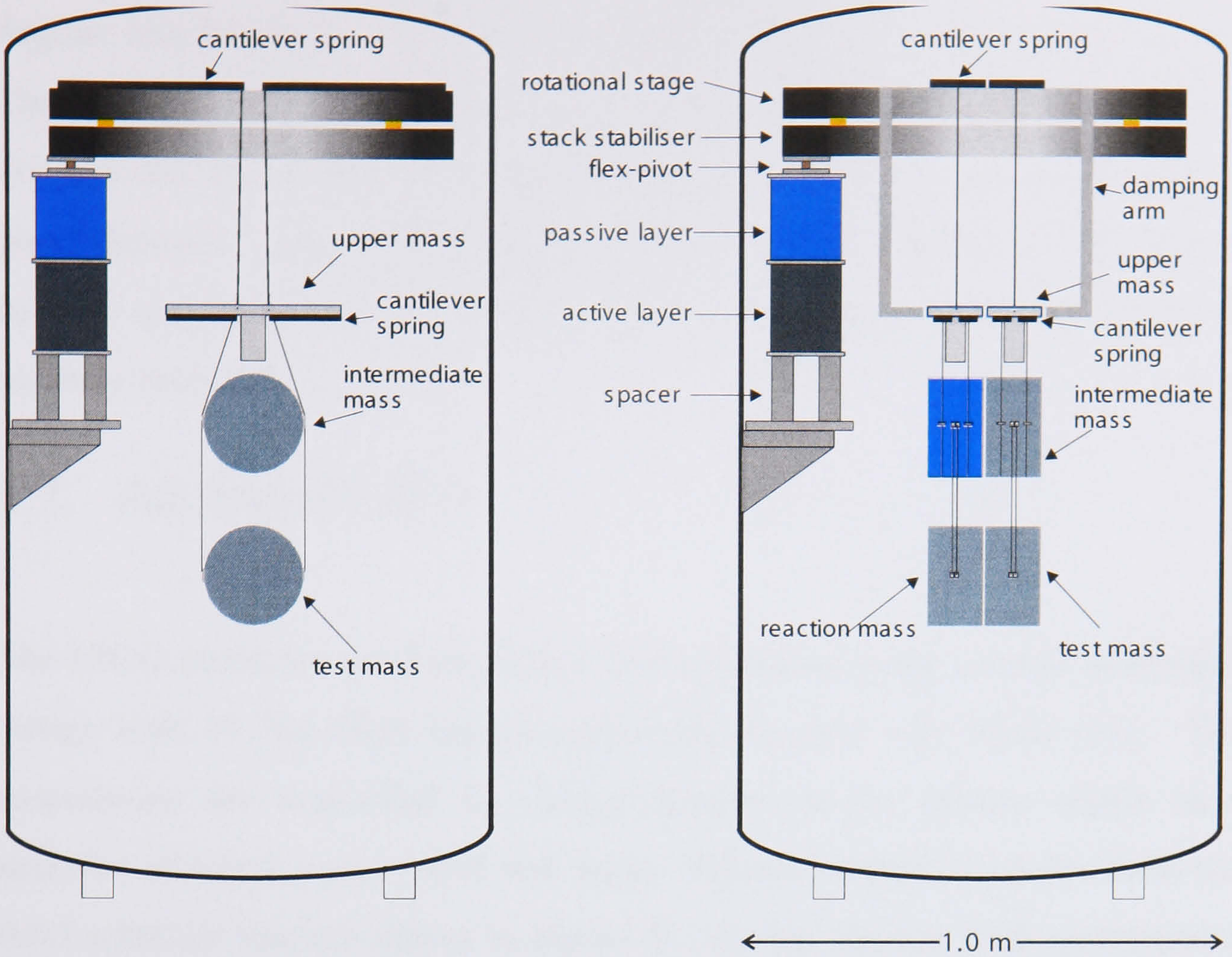

Figure 10: Schematic of GEO test mass suspensions showing triple pendulums and vibration isolation stacks.

The last stage of the pendulum is quasi-monolithic fused silica in order to reduce the thermal noise, discussed further in Chapter 2. The 6kg fused silica test mass with a dielectric mirror coating and the intermediate mass have small silica attachments bonded to them using hydroxide catalysis bonding [48, 49]. The test mass is then suspended from the intermediate mass using fused silica fibres which are welded in place between the masses.

A reaction pendulum, shown in Figure 10, hangs a few millimetres behind the main pendulum and is used as an isolated stage from which to act upon the masses using electrostatic force.

With the upgrades to LIGO already planned which will be well beyond GEO600's expected sensitivity the GEO600 detector will require further development in order to have a future role to play. The arm length of GEO600, which is approximately seven times shorter than LIGO, will make it hard to match Advanced LIGO sensitivities unless an alternative approach is taken. Currently research is being directed at altering the detector to create a

Sagnac interferometer which will be highly sensitive at high frequency [50]. The laser power stored in the arms will be of the order of 10MW in order to improve the shot noise. This higher power requires the test masses to have good thermal conductivity properties as even a small absorption will lead to heating and hence lensing effects. Hence these will either be silicon or sapphire masses.

1.7. Advanced LIGO

The LIGO detectors are Fabry-Perot interferometers using a single pendulum design with 10.7kg silica masses suspended on steel wire loops [51]. The suspensions are controlled by acting directly on the masses which have magnets attached to the sides and back. Recent sensitivity results from the third scientific run are shown in Figure 9. As has already been mentioned a planned upgrade to Advanced LIGO is currently scheduled for 2006 and will make the following changes to suspension and optical design [46, 52].

Figure 11: Aerial photograph of the site of the Livingston LIGO detector in Louisiana

The mirror suspensions will be replaced by quadruple pendulums which will use quasi-monolithic suspensions, with 40kg sapphire or silica masses and silica suspension fibres. The damping of low frequency modes of the pendulum will be done by acting on the highest stage of the pendulum. The

positional control of the masses required to operate the interferometer is expected to be done by acting on the mass using electrostatic force.

The optical layout of the detector will be modified by use of a signal recycling mirror placed at the output. During the upgrade the laser will also be replaced by a 200W unit.

1.8. Conclusions

With GEO600 and LIGO detectors now being tested and moving toward their design sensitivities we are now closer than ever to a direct detection of gravitational waves. A worldwide network of detectors including GEO600, LIGO and VIRGO is now under construction which will give positional information on burst sources.

The upgrading of LIGO to Advanced LIGO which will occur in the near future will improve sensitivities by a factor of around 10-15 and increase the number of potentially detectable sources. GEO600 is intended to follow with an upgrade designed to produce a detector capable of high sensitivities at higher frequency in order to search for known pulsar emissions.

The LISA mission which is scheduled to fly within the next ten years will open up the low frequency band to detections impossible on Earth.

Chapter 2

Thermal Noise

2.1. Introduction

According to the equipartition of energy theorem, in a classical system the mean value of each quadratic term in the expression of the total energy of the system is $\frac{1}{2}k_BT$ joules, through application of the Boltzmann distribution for energy [53]. This thermal energy is stored in the translation, vibration and rotation of the atoms in the system. In a multimode mechanical oscillator, such as the mirror suspensions in an interferometer, this energy will combine to produce the effect of thermally induced motion of the test mass and suspension modes, causing a form of displacement noise on the front face of the mass, hence we have a thermally induced source of noise.

One potential route to reducing thermal noise is to reduce the thermal energy of the system, using cryogenic techniques. Such use of cryogenics is not

uncommon in the field of gravitational wave detection as it is already used in most resonant bar detectors [20] and work is now being done to implement this in future interferometers [54].

However, as previously mentioned, even without cryogenics it is possible to reduce the effects of thermal noise by using materials of low mechanical loss or high Q.

2.2. Brownian Motion

In 1827 Robert Brown, a botanist by training, observed that pollen grains allowed to float freely on the surface of water move in a vigorous and irregular manner. While Brown observed that the motion was similar to that seen in micro-organisms, this motion was also seen in both organic and inorganic matter [55]. Brown's own interpretation, that this motion came from the action of a 'vital force' within the particles, was superseded when in 1905 Einstein showed that it was in fact the fluctuation in number of collisions with water molecules that caused the pollen to move [56].

Einstein showed that the impacts resulted in the pollen losing kinetic energy as it travelled through the water, thus linking the fluctuation and dissipation within the system. The random fluctuations in number of impacts seen at a microscopic level cause a dissipation described by the viscosity of the water. This was later to be developed by Callen et al into the Fluctuation-Dissipation Theorem [57, 58], giving a general form of the relationship between the fluctuation and dissipation of a system.

2.3. The Fluctuation-Dissipation Theorem

The fluctuation dissipation theorem relates the power spectral density of the thermal driving force $S_f(\omega)$ of a system to the dissipative (or real) part of the mechanical impedance $Z(\omega)$ as follows:

$$S_f(\omega) = 4k_B T \Re[Z(\omega)] \tag{10}$$

Where the mechanical impedance Z is defined as $Z = F/V = F/i\omega X$ where F, V and X are the Fourier components of the external force f, the speed v, and the displacement x respectively.

The fluctuation dissipation theorem can then be rewritten in terms of the power spectral density of displacement, $S_x(\omega)$ using the definition of impedance:

$$S_x(\omega) = \frac{4k_B T}{\omega^2} \Re[Y(\omega)] \tag{11}$$

Where $Y = 1/Z$ is the admittance.

Thus the fluctuation dissipation theorem allows us to calculate the thermal noise contribution from the dissipative properties of the system.

If we look again at the example of viscous dissipation observed by Brown we can calculate the thermal noise contribution of such a source of dissipation on an oscillator. The frictional force of the water is viscous and as such can be given as:

$$F_{fric} = -b\dot{x} \tag{12}$$

The equation of motion of the system as driven by an external force F_{ext}. excluding the fluctuating force, is then given by:

$$m\ddot{x} = -kx - b\dot{x} + F_{ext} \tag{13}$$

for some spring constant k. Once the previous equation has been rewritten in the frequency domain the impedance of the oscillator is:

$$Z = \frac{F_{ext}}{V} = b + i\omega m - \frac{ik}{\omega} \tag{14}$$

where V is the Fourier component of the velocity v.

We can see that the real part of Z is simply b and so we have:

$$S_f(\omega) = 4k_B Tb \tag{15}$$

From this we find that the power spectral density of displacement is given by:

$$S_x(\omega) = \frac{4k_b Tb}{\omega^2\left(b^2 + \left(\omega m - k/\omega\right)^2\right)} \tag{16}$$

An interesting point arising from this is that we can see that in frequency regions below and above the resonance condition, $\left(\omega m - k/\omega\right) = 0$, the denominator is dominated by k and m respectively. In these regions a lower dissipation value will give a reduced thermal noise level. However at resonance these terms cancel and b^2 becomes the dominant term. Thus, on resonance, the lower the dissipation the larger the resonance peak. The equipartition of energy theorem tells us that the mean square fluctuation cannot be affected by reducing the dissipation as we are not altering the number of degrees of freedom in the system, but this still holds as the integral of the displacement power spectrum over all frequencies is independent of

dissipation [8]. The fluctuation-dissipation theorem gives instead the distribution of this across the frequency spectrum.

2.4. Sources of Dissipation

A system with very low thermal noise levels requires that all possible sources of dissipation, both internal and external, be minimised. In a system such as the mirror suspensions used in an interferometer there are many sources of dissipation of which a brief account will be given.

2.4.1. External Sources of Dissipation

Possible sources of external dissipation include:

- Friction at the point of suspension. For example this might include the friction at the point where a wire is used to hang a test mass or point of clamping of a mass.
- Eddy current damping
- Magnetic hysteresis
- Motion of a pendulum causing the supporting structure to recoil (though this does not contribute significantly to thermal noise of the detector)
- Damping from collisions with residual gas molecules

2.4.2. Internal Sources of Dissipation

If the external dissipative sources have been reduced to a low level then the dominant source of loss will become the internal dissipation of the suspension due to friction within the material.

When a solid body has a force applied to it, it does not react instantaneously and elastically but instead continues to alter after its initial response. It achieves its move to a new equilibrium state only after an interval of time

known as the 'relaxation time'. This process is known as anelastic relaxation and is a source of dissipation caused by imperfections in the solid such as shifting defects.

A perfectly elastic oscillator can be described by a restoring spring constant in Hooke's law as follows:

$$F_R = -kx \tag{17}$$

Here we see no time lag between the force being applied and the final equilibrium position. Anelasticity can be described by adding just such a time lag to this equation, which in the frequency domain appears as a phase lag [59].

$$F_R(\omega) = -k(1 + i\phi(\omega))x(\omega) \tag{18}$$

where $\phi(\omega)$ is the loss angle.

We can now look at the equation of motion for this oscillator when subject to an internal thermal driving force:

$$m\ddot{x} = F_R(\omega) - k(1 + \phi(\omega))x \tag{19}$$

or in velocity terms

$$i\omega mv = F_R(\omega) + i\tfrac{k}{\omega}(1 + i\phi(\omega))v \tag{20}$$

In order to calculate the thermal noise from this source of dissipation we must rewrite this in terms of the impedance:

$$Z = \frac{F}{v} = i\omega m - i\frac{k}{\omega}(1 + i\phi(\omega))$$
$$= i\left(\omega m - \frac{k}{\omega}\right) + \phi(\omega)\frac{k}{\omega} \qquad (21)$$

Then the admittance is given by:

$$Y(\omega) = \frac{1}{Z(\omega)} = \frac{\omega}{k\phi(\omega) + i(\omega^2 m - k)}$$
$$= \frac{1}{\frac{k}{m}\phi(\omega) + i(\omega m - \frac{k}{\omega})} \bullet \frac{\frac{k}{m}\phi(\omega) - i(\omega m - \frac{k}{\omega})}{\frac{k}{m}\phi(\omega) - i(\omega m - \frac{k}{\omega})} \qquad (22)$$
$$= \frac{\frac{k}{m}\phi(\omega) - i(\omega m - \frac{k}{\omega})}{\left[\frac{k}{m}\phi(\omega)\right]^2 + (\omega m - \frac{k}{\omega})^2}$$

If we now substitute the real part of the admittance into the fluctuation -- dissipation theorem (equation 16) then we can obtain an expression for the power spectral density of thermal motion of the form:

$$S_x(\omega) = \frac{4k_B T}{\omega^2} \frac{\frac{k}{m}\phi(\omega)}{\left[\frac{k}{m}\phi(\omega)\right]^2 + (\omega m - \frac{k}{\omega})^2} \qquad (23)$$

which we can then simplify by substituting $k = \omega_0{}^2 m$:

$$S_x(\omega) = \frac{4k_B T}{\omega} \frac{\phi(\omega)\omega_0{}^2}{m\left[\omega_0{}^4\phi(\omega)^2 + (\omega_0{}^2 - \omega^2)^2\right]} \qquad (24)$$

We see that at frequencies well below ω_0 we can simplify this to:

$$S_x(\omega) \approx \frac{4k_B T\phi(\omega)}{m\omega\omega_0{}^2(\phi^2(\omega) + 1)} \qquad (25)$$

which assuming $\phi^2(\omega) \langle\langle 1$ simplifies to :

$$S_x(\omega) \approx \frac{4k_B T}{m\omega_0^2}\left(\frac{\phi(\omega)}{\omega}\right) \tag{26}$$

Similarly in the frequency region well above the resonance we can, by making the same assumptions, simplify to:

$$S_x(\omega) \approx \frac{4k_B T\omega_0^{\,2}}{m}\frac{\phi(\omega)}{\omega^5} \tag{27}$$

At the resonant frequency we can simplify to:

$$S_x(\omega_0) \approx \frac{4k_B T}{m\omega_0^3}\left(\frac{1}{\phi(\omega_0)}\right) \tag{28}$$

Consequently we see once more that at frequencies far below or above the resonant frequency a low loss angle gives a lower level of thermal noise while on resonance a low loss angle corresponds to a high power spectral density of noise. The high Q of the suspensions may cause problems for the locking of the interferometer, with the energy in the modes taking a long time to be damped out. To solve this issue the monolithic suspensions of the GEO600 interferometer use selective damping of violin modes using Teflon coating on the fibres. The proposed solution for future detectors is to use electrostatic force to actively damp the suspension fibre modes. The upper stages of suspension are also actively damped using magnetic actuators.

2.4.3. The Form of Internal Dissipation

Experimental evidence suggests that we may closely model the loss factor associated with internal dissipation as being approximately constant with frequency [60]. The form of structural damping, which arises from relaxation processes within the solid body such as dislocation movement, point defect movement and transitions between metastable states, is an example of this. A body may have many internal loss mechanisms, each with its own resonant

peak at some characteristic frequency. The distribution of energy within a body may also cause one single relaxation process to give rise to multiple peaks as the characteristic relaxation times will differ. This gives a range of resonant peaks spanning many decades of frequency. Although at frequencies close to these resonances there is a frequency dependence to the loss, in the regions in between, where the bandwidth for detectors will lie, the tails of these peaks combine to give an effectively constant loss factor over several decades of frequency [61].

There is however one source of thermal noise that may have a peak within the detection band. This is thermoelastic damping, which is discussed in Section 2.7.

2.5. Measurement of Internal Loss

With materials commonly used in pendulums exhibiting extremely low levels of loss it is very difficult to measure them at frequencies of interest for gravitational wave detection since the dynamics do not depend on the loss to a high degree. This however is not true at resonance and so instead a method is used where the loss is measured at resonance as follows. The Q, or quality factor, of an oscillator is a dimensionless measure of dissipation at the resonant frequency [8].

$$Q(\omega_0) = 2\pi \frac{E_{stored}}{E_{lostpercycle}} \tag{29}$$

For a pendulum where $F_R = -kx$ we have, at maximum amplitude of swing, a stored potential energy given by:

$$E = \tfrac{1}{2} kA^2 \tag{30}$$

To find the energy lost per cycle we then add in the dissipation in the spring constant:

$$\begin{aligned} F_R &= -k(1+\phi)x = -Ae^{i\omega t}ke^{i\phi} = -Ake^{i(\omega t+\phi)} \\ &= -Ak[\cos(\omega t+\phi)+i\sin(\omega t+\phi)] \end{aligned} \tag{31}$$

We can then integrate the real part of this to find the work done:

$$\begin{aligned} W.D. &= \int F_R dx = \int -Ak\cos(\omega t+\phi)dx \\ &= \int_0^T kA\cos(\omega t+\phi)A\omega\sin(\omega t)dt \\ &= -\tfrac{1}{2}k\omega A^2 T\sin\phi \end{aligned} \tag{32}$$

Thus $Q(\omega_0)$ can be given as:

$$Q(\omega_0) = \frac{2\pi\,\frac{1}{2}kA^2}{\frac{1}{2}k\omega_0 A^2 T\sin\phi(\omega_0)} = \frac{1}{\sin\phi(\omega_0)} \approx \frac{1}{\phi(\omega_0)} \tag{33}$$

Hence we can measure the loss of the pendulum at its resonant frequency and, then assuming it is approximately frequency independent use this to approximate the loss at other frequencies.

2.6. The Dilution Factor

We have mentioned in Section 1.4.2 that the pendulum suspensions perform a role in vibration isolation of our test mass mirrors but this is not the only benefit we can receive from them. A pendulum is also a smart choice of oscillator for the purposes of further reducing thermal noise. As will be demonstrated this is due to its ability to store most of the energy in the non-dissipative gravitational field.

To look at this effect we can think of a simple pendulum consisting of a wire with a mass at one end. With the mass attached to the bottom of the wire it will extend until the elastic restoring force matches the mass's weight. If the mass were now to be excited vertically the frequency of simple harmonic motion would be determined by the spring constant of the stretched wire.

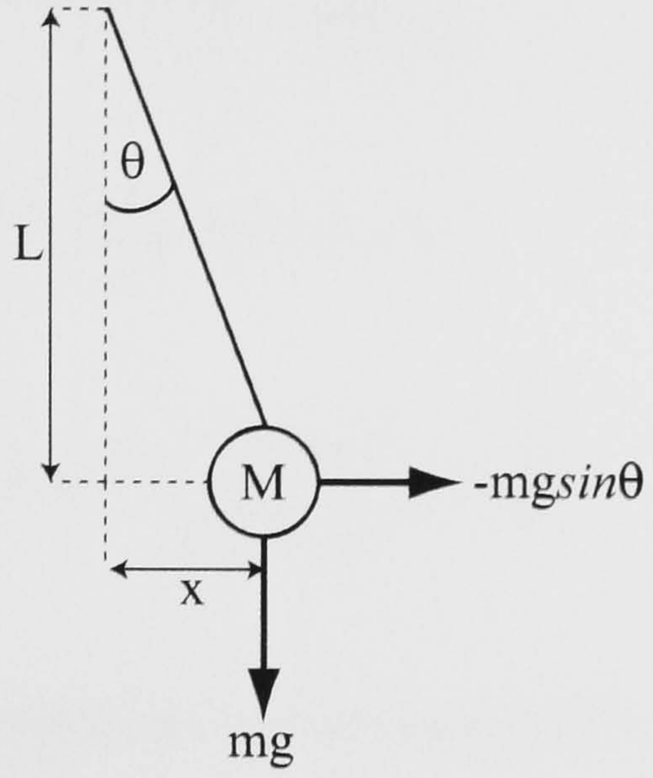

Figure 12: Action of gravity as a restoring force in a simple pendulum.

If however the mass were displaced horizontally the restoring force comes not only from the spring constant of the wire but also from the gravitational effect on the mass. As can be seen from Figure 12, the restoring force for the gravitational field gives a spring constant of:

$$k_{grav} = \frac{mg}{L} \tag{34}$$

We can now use this to calculate the effect on the loss for such a pendulum. The energy stored in the bending of the wire is given by:

$$E_{stored_{wire}} = \frac{1}{2} k_{wire} x^2 \tag{35}$$

where k_{wire} is the spring constant of the wire for such a bending process. If we now assume that some fraction (χ) of this energy is dissipated per cycle:

$$E_{lostpercycle} = \frac{1}{2}\chi k_{wire} x^2 \tag{36}$$

Hence by using a description of loss as:

$$\phi(\omega_0) = \frac{1}{Q} = \frac{E_{lostpercycle}}{2\pi E_{stored}} \tag{37}$$

we can calculate the loss of the material to be:

$$\phi_{mat}(\omega_0) = \frac{\frac{1}{2}\chi k_{wire} x^2}{2\pi \frac{1}{2} k_{wire} x^2} = \frac{\chi}{2\pi} \tag{38}$$

Adding in the energy stored in the gravitational field we have:

$$E_{stored_{pendulumj}} = \frac{1}{2}(k_{wire} + k_{grav})x^2 \tag{39}$$

Hence:

$$\phi_{pendulum}(\omega_0) = \frac{\frac{1}{2}\chi k_{wire} x^2}{2\pi \frac{1}{2}(k_{wire} + k_{grav})x^2} = \frac{\chi k_{wire}}{2\pi(k_{wire} + k_{grav})} \tag{40}$$

If we then divide this through by the loss of the material:

$$\frac{\phi_{pendulum}(\omega_0)}{\phi_{mat}(\omega_0)} = \frac{k_{wire}}{k_{wire} + k_{grav}} \tag{41}$$

and if we then assume $k_{grav} >> k_{wire}$ then :

$$\phi_{pendulum}(\omega_0) \approx \phi_{mat}(\omega_0)\frac{k_{wire}}{k_{grav}} \tag{42}$$

It is therefore found that due to $k_{grav} >> k_{wire}$ the loss of the pendulum is reduced by the factor given above, known as the dilution factor.

If our suspension were to be suspended at the centre of the sides by n wires instead of just one then the elastic spring constant is given by [59]:

$$k_{wires} = \frac{n\sqrt{TEI}}{2L^2} \tag{43}$$

where T is the tension in each wire, E is the Young's modulus of the wire material and I is the moment of cross-sectional area. The moment of cross-sectional area for a round wire is given by $I = \pi r^4/4$ [62]. For a fibre with a rectangular cross-section this moment is given by $I = ba^3/12$ [63] where a is the thickness of the fibre in the direction of bending and b is the width in the direction perpendicular to this. This then gives a total pendulum loss of:

$$\phi_{pendulum}(\omega_0) \approx \phi_{mat}(\omega_0)\frac{n\sqrt{TEI}}{2mgL} \tag{44}$$

thus the dilution factor is given by:

$$D = \frac{2L\sqrt{T}}{n\sqrt{EI}} \tag{45}$$

2.7. Thermoelastic Damping

There exists another source of damping, known as thermoelastic damping, which does exhibit a frequency dependence. If one were to think of a beam that is deflected, one side would be in compression while the other is in tension. The side that is in compression will increase in temperature while

that in tension will cool. With a thermal gradient thus set up we then observe a heat flow across the beam until thermal equilibrium is achieved. This heat flow is a source of loss that has a characteristic frequency associated with it relating to the relaxation time to reach the new equilibrium.

If one thinks now of the beam being undeflected, local temperature fluctuations will cause motion of the beam as a result of the expansion or contraction caused by the thermal expansion coefficient of the material. This expansion coefficient can be described by:

$$\alpha = \frac{1}{l}\frac{dl}{dT} \tag{46}$$

Unsurprisingly the characteristic frequency for heat transfer is related to both the thermal conductivity and specific heat capacity of the material as well as the thickness and shape of the body. Shown below is the characteristic frequency of a round beam of diameter d [61, 64].

$$\begin{aligned} f_{char} &= \frac{1}{2\pi\tau} \\ &= 2.16\frac{\kappa}{\rho C d^2} \end{aligned} \tag{47}$$

where κ is the thermal conductivity, C is the specific heat capacity and ρ is the density .

This can also be given for a rectangular cross section beam of thickness t as:

$$f_{char} = \frac{\pi\kappa}{2\rho C t^2} \tag{48}$$

It should be noted that only the thickness in the direction of heat transfer is needed here. This means that if a fibre of rectangular cross section is used in a pendulum only the dimension of the fibre normal to the surface of the mirror

will give a contribution to the thermoelastic damping in this direction. This then allows the tension to be set independently of the characteristic frequency of thermoelastic damping and hence the level of thermal noise resulting from this.

The loss associated with this damping mechanism can be given as [64]:

$$\phi(\omega) = \Delta \frac{\omega\tau}{1+(\omega\tau)^2} \tag{49}$$

where

$$\Delta = \frac{Y\alpha^2 T}{\rho C} \tag{50}$$

However this assumes a Young's modulus that is approximately temperature independent. For many materials this approximation cannot be made [65]. We can now introduce a parameter, β, called the thermal elastic coefficient which bears a close resemblance to the thermal expansion coefficient in its definition:

$$\beta = \frac{1}{E}\frac{dE}{dT} \tag{51}$$

This thermal elastic coefficient is in itself not enough to cause a change in strain and hence will not give any contribution to thermal noise unless there is a static stress σ_0 in the beam. This stress coupled to a changing Young's modulus will give a thermal expansion like parameter α':

$$\alpha' = \beta \frac{\sigma_0}{E} \tag{52}$$

Thus we can give a modified expansion coefficient term to include this temperature dependant Young's modulus:

$$\alpha_{effective} = \alpha - \alpha' = \alpha - \left(\frac{1}{E}\frac{dE}{dT}\right)\frac{\sigma_0}{E} \tag{53}$$

Hence the loss can be given by:

$$\phi(\omega) = \Delta_T \frac{\omega\tau}{1+(\omega\tau)^2} \tag{54}$$

where:

$$\Delta_T = \frac{YT}{\rho C}\left[\alpha - \left(\frac{1}{E}\frac{dE}{dT}\right)\frac{\sigma_0}{E}\right]^2 \tag{55}$$

We can see that this new effective thermal expansion coefficient can be set to zero for a material with a positive dE/dT and given a certain stress which would then cause the thermoelastic loss to be cancelled out by the effects of the temperature dependence of Young's modulus. It therefore of particular interest that silica is one such unusual material that has a positive dE/dT.

A similar mechanism for loss exists in the test masses [66]. The low thermal conductivity of silica makes the effect negligible in first generation detectors. However with sapphire being the proposed test mass material for Advanced LIGO due to its low intrinsic loss and silicon masses also being proposed for future detectors where cryogenics or high laser powers are used, these being high conductivity materials in comparison to silica, the effects of test mass thermoelastic noise are expected to become important. Hence research is currently being performed examining the loss mechanisms in these materials.

2.8. Resonant Modes of a Typical Interferometer Suspension

As we have now shown that in a low loss oscillator the majority of thermal noise is concentrated in the resonant modes, it is of interest to briefly summarise the main modes of a suspension of the type common to interferometric gravitational wave detectors.

The resonant modes can be grouped as either internal modes of the test mass or suspension modes.

2.8.1. Internal Modes of a Test Mass

These are the vibrational modes of a test mass if we consider the centre of mass to be fixed, allowing the test mass itself to alter shape. In principle some modes will contribute to the thermal noise in the detector while others will not, depending on whether the centre of the front face of the mass is displaced.

The resonant frequencies associated with the test masses tend to be in the region of tens of kHz and as such are well above the detection band of the detector. The losses associated with the test mass may be increased through coating and bonding processes.

2.8.2. Suspension Modes

If we now imagine the mirror to be a rigid body we can look at the other resonant modes in the suspension. Those with thermal noise contributions will cause the centre of mass of the test mass to alter. The following modes may occur in such a suspension:

2.8.3. Pendulum Mode

The pendulum mode of a suspension will couple directly into the signal in the interferometer as it will directly cause a displacement of the centre of mass of test mass, thus altering the path length of the laser light in that arm.

However the frequency of this mode should be well below the detection band although this must be designed into the suspension by keeping the fibres long and their cross section thin (other factors such as strength and thermoelastic damping frequency will also be taken into consideration when determining the dimensions of fibres used).

The loss of the pendulum mode is decreased by the effect of the dilution factor as energy is stored in the gravitational field as well as in the bending of the fibres.

2.8.4. Violin Modes (or transverse vibrational modes)

The transverse vibrational modes of the suspension fibres form a slightly anharmonic series which lie within the detection band. The first mode of oscillation in this series will have a loss that is twice that of the pendulum mode as twice the bending occurs in the fibre. As with the pendulum mode, the loss associated with the violin modes is reduced by the dilution factor.

Although the resonant frequencies lie within the detection band, the fact that the loss is low will concentrate the energy into narrow peaks at the resonant frequencies, allowing these to be notched out of the data.

2.8.5. Other Modes

Thermal noise associated with the vertical mode of the suspension will couple into horizontal displacement. For GEO 600 a conservative estimate of ~0.1% was used in design with the largest contributing factors being the folding of

the optical path and the curvature of the earth. Other mechanical imperfections such as non-uniformity of suspension fibres/wires, stiffness of support structure and imperfect mass distribution during mounting of the test masses will also contribute to coupling though these are more difficult to quantify [42].

The thermal noise contributions of the tilting and torsional modes will also couple into horizontal displacement, though this coupling can be kept to a low level by ensuring that the incident laser beam hits the centre of the test mass.

2.9. Calculation of Combined Thermal Noise Sources in a Detector

While the above methods can be used to determine the thermal displacement of the face of the test mass in one suspension it is of interest to calculate the total thermal noise contribution from a number of mirrors in a detector; in this example we will use a simplified version of the optical layout from the GEO600 detector as shown in Figure 13.

The beam from the laser is split and sent down the two arms which are of the same length ($x_2 = x_4$ and $x_3 = x_5$) with the returned beam being recombined and sent to the detector. As the detector measures the relative path changes of the two arms, any noise from thermal displacement of the test masses must also affect the relative path lengths; for this reason any alteration to lengths x_1 and x_6 will give no contribution to the total thermal noise as they affect both paths equally.

If we first consider the displacement of the end test mass in one arm, such as Δ_{ETM} of the end test mass in the north arm, we see that the total beam path length is altered by $+\Delta_{ETM}$. A similar effect is seen on the path length of the east arm if its end test mass is displaced.

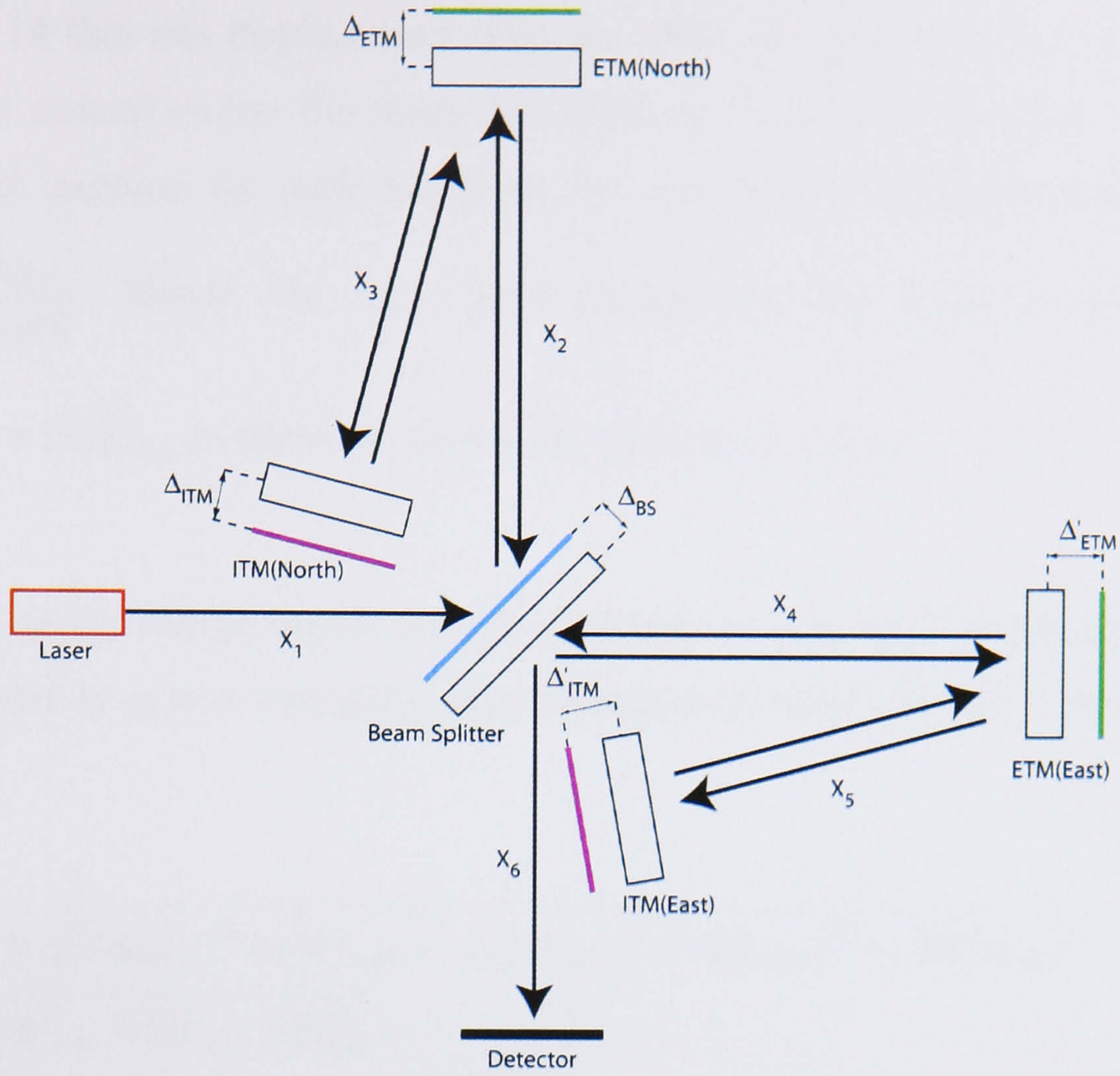

Figure 13: Simplified optical layout of the GEO600 detector

Next we consider a displacement of an inboard test mass such as Δ_{ITM} in the north arm. Here the total change to the path length is only $2\Delta_{ITM}$ as the beam only bounces once from its surface.

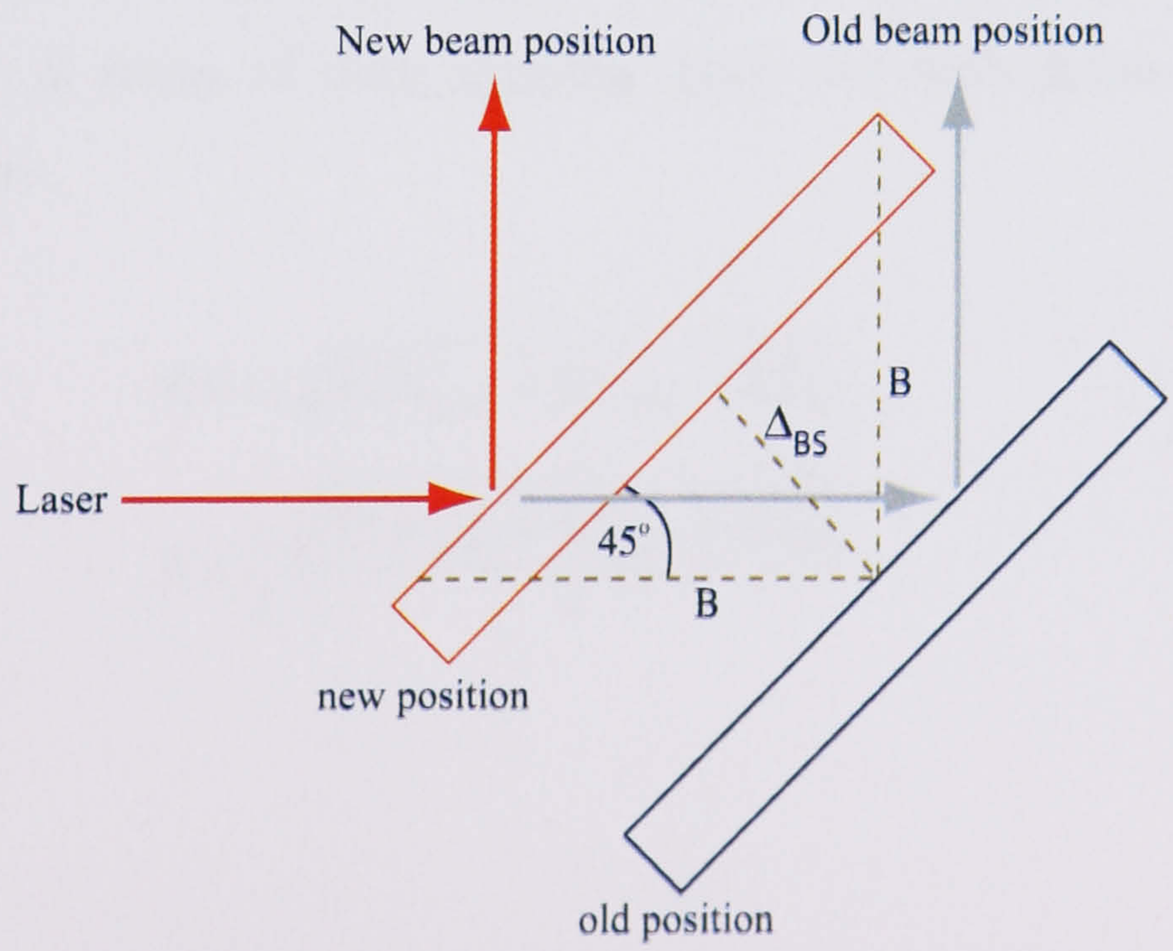

Figure 14: Effect of displacement of the beam splitter

Finally we consider a displacement of the beam splitter. We can see from Figure 14 that this displacement does not affect the path length of the north arm but instead moves the beam perpendicular to the arm direction. It does however increase the path length of the east arm by an amount B, where $B = \frac{\Delta_{BS}}{\cos 45}$. Hence the total path change for the beam is given by $\frac{2\Delta_{BS}}{\cos 45} = 2\sqrt{2}\Delta_{BS}$ as the beam travels the distance x_2 twice.

Finally, as the displacements are uncorrelated, we sum these displacements in quadrature to give a total path length change from displacement of the masses of:

$$\begin{aligned}\Delta_{Total} &= \sqrt{(4\Delta_{ETM})^2 + (4\Delta_{ETM})^2 + (2\Delta_{ITM})^2 + (2\Delta_{ITM})^2 + (2\sqrt{2}\Delta_{BS})^2} \\ &= \sqrt{32\Delta_{ETM}^2 + 8\Delta_{ITM}^2 + 8\Delta_{BS}^2}\end{aligned} \tag{56}$$

It is now of interest to consider how this would appear in terms of h. The effect of a gravitational wave of strain h is to alter the length of each arm by $\Delta l = hl/2$ with one arm increasing in length and the other decreasing. This therefore causes a path length change in each arm of $4\Delta l = 2hl$ assuming that the inboard test masses are very close to the beam splitter. The total path length difference is then $8\Delta l = 4hl$. Thus we can give the total thermal displacement in terms of h by equating these two descriptions of the total length change:

$$4hl = \sqrt{32\Delta_{ETM}^2 + 8\Delta_{ITM}^2 + 8\Delta_{BS}^2} \tag{57}$$

$$h = \frac{1}{l}\frac{\sqrt{32\Delta_{ETM}^2 + 8\Delta_{ITM}^2 + 8\Delta_{BS}^2}}{4} \tag{58}$$

2.10. Conclusion

Thermal noise is one of the most significant limitations to detector sensitivity. In this chapter it has been shown that, through application of the fluctuation-dissipation theorem, the level of thermally induced motion as a function of frequency in a system can be obtained through understanding its loss. This loss can be found by measuring the Q of the system at resonance. Thus by experimentally finding the Q of the modes in a mirror suspension we may calculate the level of thermally induced displacement. We have also seen how it is possible to combine the displacement of a number of mirrors in a detector to find the total level of thermal noise.

Methods for reducing thermal noise within the detector bandwidth have also been discussed. By careful design of suspension some resonant modes will occur outwith the detection band while those within it are notched out of the signal. By using low loss materials the thermal displacement at frequencies above and below resonance is kept at a low level.

Thermoelastic noise from the suspension fibres may have its peak value within the detection band. A method for removing this noise source is given, in which the expansion of the material, from localised fluctuations in temperature, is exactly cancelled by the effects of a static stress on a material with a temperature dependant Young's modulus.

Chapter 3

Silica Fibre Design

3.1. Introduction

The design of fibres to be characterised in this thesis was based on the requirements for Advanced LIGO. With work on installation of the monolithic suspensions at GEO600 now completed, the higher level requirements of the Advanced LIGO suspensions must now be considered. Here we propose a solution using rectangular cross section fibres to increase the compliance of the suspension in the direction of measurement, compared to a suspension using round fibres of similar cross sectional area.

When considering the design of the final stage of the pendulums the main objective is to reduce the overall noise contribution at detection band frequencies. The two sources of noise dealt with here are seismic and

thermal. As seismic noise will dominate the lower end frequencies, for reasons we will shortly examine, we shall look at this first.

3.2. Seismic Noise

Seismic noise originates from ground motion at the site of the detector, with contributions to it relating not to some fundamental noise source (such as thermal motion of atoms) which cannot be reduced, but to sources that could be reduced (for example by putting a detector in space as the planned LISA detector shall be) and which in densely populated areas are primarily from human activity.

In order to reduce this noise source we seek to isolate our test mass from any motion that will be normal to the face of the mass by suspending it as a pendulum. The pendulum acts as a low pass filter for motion with a resultant transfer function, assuming there is no finite damping, given by [8, 42]:

$$\frac{x}{x_g} = \frac{f_0^2}{f_0^2 - f^2} \tag{59}$$

where x is the displacement of the mass, x_g is the displacement of the ground, f_0 is the resonant frequency of the pendulum and f is the frequency of motion of the ground.

We can now look at this in the limit where $f \rangle\rangle f_0$ and approximate:

$$\frac{x}{x_g} \approx \frac{f_0^2}{f^2} \tag{60}$$

At these high frequencies the inertia of the mass means that the motion induced is small in the period of time before the force switches direction.

At frequencies $f \langle\langle f_0$, well below the resonant frequency the approximation becomes:

$$\frac{x}{x_g} \approx \frac{{f_0}^2}{{f_0}^2} = 1 \tag{61}$$

where we now see that the spring acts as a rigid coupling to the mass. The transfer function of a pendulum with resonant frequency 1Hz is shown in Figure 15.

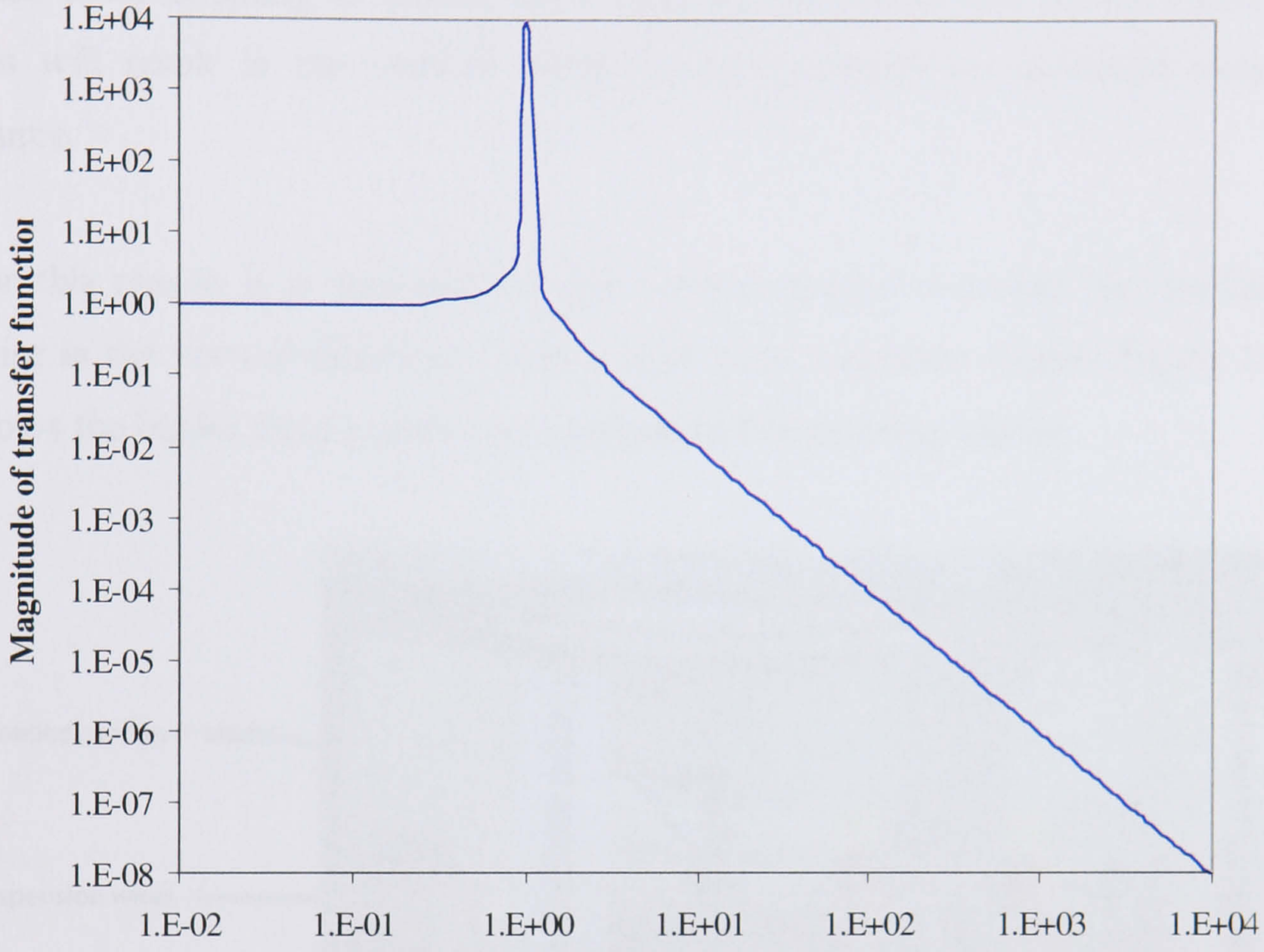

Figure 15: Transfer function of a 1Hz pendulum. Below the resonant frequency the pendulum acts as a rigid coupling. Above the resonant frequency the pendulum attenuates the motion as like a low pass filter.

It is then also possible to enhance this effect further by using a multiple pendulum design, where the lower pendulum stage is suspended from another pendulum. This achieves isolation in the horizontal direction, at frequencies well above the resonant frequency, of:

$$\frac{x}{x_g} \approx \left(\frac{{f_0}^2}{f^2} \right)^N \tag{62}$$

for N pendulums. At these frequencies the inertia of the mass is dominant.

This is however not as effective for the vertical isolation of the test mass. Due to the higher spring constant in the vertical direction, a result of the lower

compliance of the suspension fibres, the resonant frequency will be at around 10Hz. With the transfer function relating to the square of the resonant frequency this will give $1/100^{th}$ of the isolation. If we then suspend N pendulums in a cascade, the transfer function in the vertical direction will become 100^N times greater than that for the horizontal direction. Even with a small cross coupling of around 0.1% between horizontal and vertical modes this will result in the vertical seismic noise becoming the dominant noise source.

For this reason it is necessary to use vertical springs to reduce the seismic noise in the vertical direction. This is done using cantilever blades; Figure 16 shows the blades from a prototype suspension before being loaded.

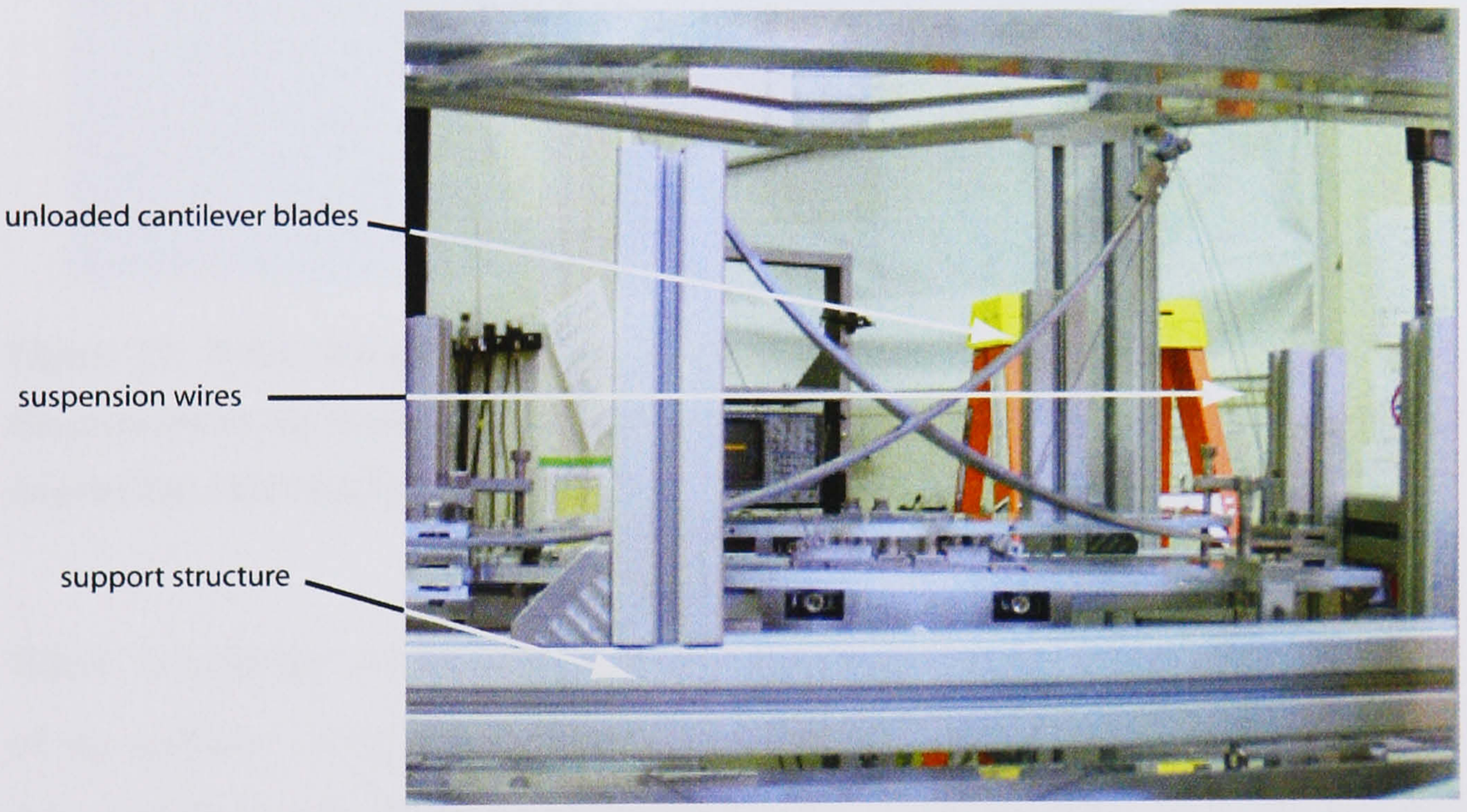

Figure 16: Unloaded cantilever blades in prototype quad suspension. When loaded the blades are deflected to horizontal.

Figure 17 shows a diagram of the four level (quad) suspensions planned for Advanced LIGO [67]. This incorporates not only four pendulum stages but also three vertical isolation stages of cantilever springs as well. The support for the pendulum is also isolated actively.

Clearly it is advantageous to have to have the resonant mode of the pendulum at as low a frequency as possible to attenuate the seismic noise and to move

the resonance peak down below the detection band. This then sets our first criterion for the design of the last stage of suspension.

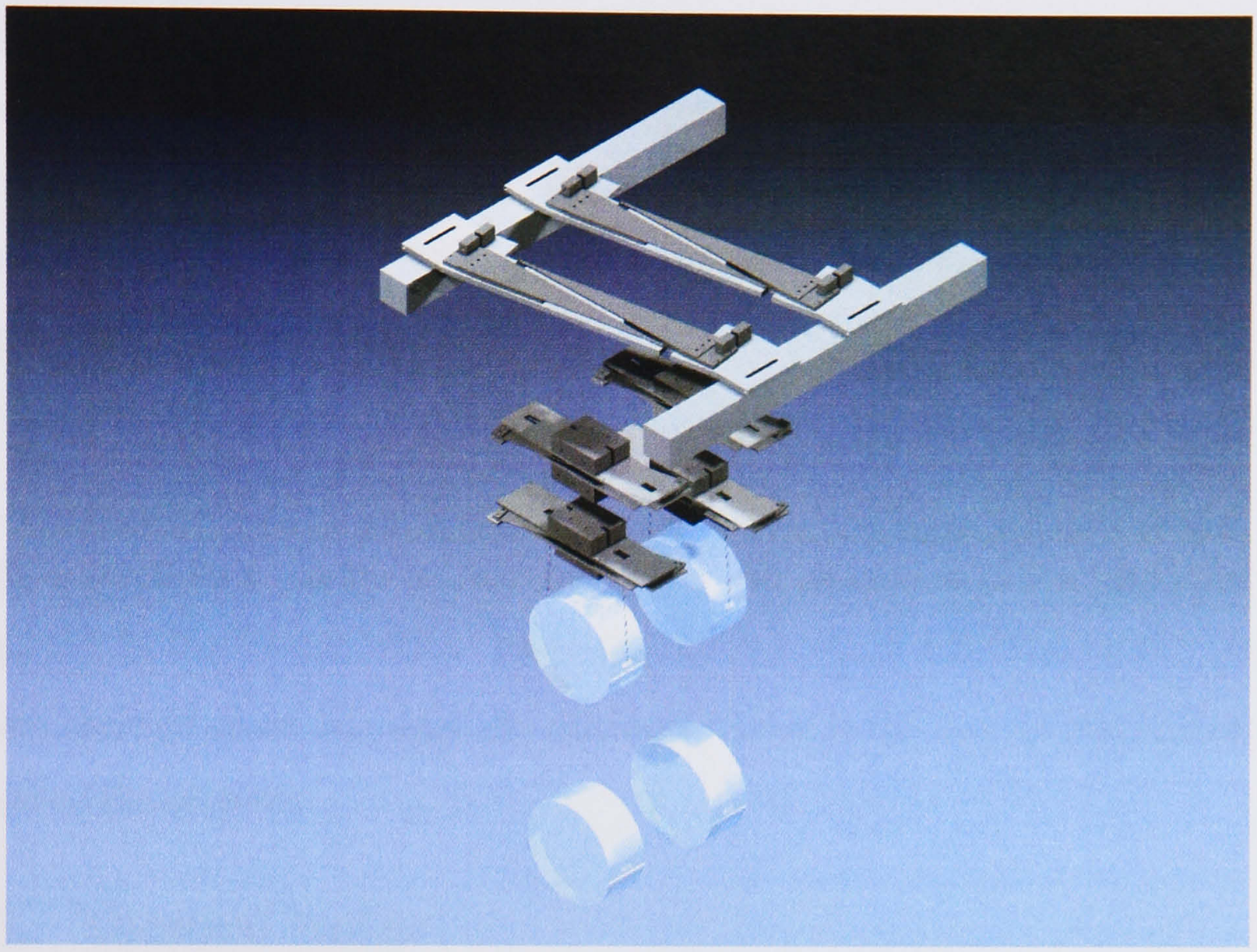

Figure 17: Solid Works Rendering of Quad Suspension for Advanced LIGO. The diagram shows the three stages of cantilever blades as well as the quasi-monolithic lower suspensions with sapphire masses[67].

When calculating the pendulum mode frequency we must consider the effect of the stiffness of the fibre. This causes a shortening of the effective length of the pendulum and affects not only the spring constant of the fibre but also the gravitational spring constant (as the mass is not lifted as high for a given force). The new pendulum spring constant is given by [68]:

$$k_{pendulum} = \frac{T}{L}\left[1+\sqrt{\frac{EI}{TL^2}}\right] \tag{63}$$

where T is the tension, L is the fibre length, E is the Young's modulus and I is the moment of inertia of the cross section of the fibre which is given as $I = {ba^3}/{12}$ for a rectangular cross section fibre [63] whose thickness in the

direction of bending is a and whose width in the direction perpendicular to this is b. This shortening of the fibre affects the pendulum frequency at around the 0.04% level. This therefore means that there is little difference to the pendulum frequency by using round or rectangular fibres. The most significant way of reducing the pendulum frequency is to increase the length of the fibre. Unfortunately the total length of the pendulum must be limited by the size of tanks used in the vacuum system and hence a limit of 0.6m has been put on the fibres. We can then calculate that this gives a pendulum frequency of $f_0 = 0.65\text{Hz}$.

With a pendulum mode at this frequency the seismic noise is expected to dominate in the region below 10Hz for the Advanced LIGO detector, above which thermal noise becomes the dominant issue in the low to mid frequency range of the detector.

3.3. Thermal Noise

The main aspects of thermal noise have already been dealt with in chapter 2. We have seen that it is possible to reduce the levels of thermal noise away from the frequencies of modes of the suspension by using low loss material such as silica or sapphire and that the effect of suspending the mass as a pendulum is to give an even lower loss through the dilution factor. Thus it is clear that not only do we need a high Q suspension but also we require the dilution factor to be large. These form the next two requirements of our pendulum.

3.3.1. Dilution Factor

The dilution factor is given by equation 45. In the frequency regions well above and below resonance the power spectral density of thermal motion can be approximated as being directly proportional to the loss of the pendulum and hence to the dilution factor. In order to increase the dilution factor we

must either decrease fibre thickness or increase the mass. Clearly there is a limit to this, which is the strength of the fibres, adding in some working margin of strength as it is obviously unwise to work too close to the breaking stress limit. For this reason a loading of above 1GPa is unwise (see Chapter 8 for a discussion of strengths). For a ribbon of $0.1mm^2$ cross sectional area, comprising of 1mm breadth and 0.1mm thickness with a 10kg loading per fibre, we therefore have a dilution factor of 4899.

Using a fibre with a round cross section also of $0.1mm^2$ we achieve only a dilution factor of 1585, which gives a thermal noise contribution 3.09 times higher in power at frequencies well away from resonance.

3.3.2. Vertical Mode

It has been noted that, while a low level of dissipation in a suspension causes the thermal noise levels away from resonance to decrease, the energy is transferred to the levels at resonance with the width of the resonance peak being dependant on the Q of the mode of oscillation. The vertical resonant mode, occurring at the lower end of the detection band, is not affected by dilution. This is because gravity does not act as a restoring force but instead provides a constant force in one direction. The restoring force here comes instead from the longitudinal tension in the fibre which will have both lossless and lossy components relating to the real and imaginary parts of the Young's modulus. As such its loss will be 4899 times larger than for the violin modes (when using a rectangular fibre). Although this only couples to horizontal motion at around 0.1% the height of the resonance peak from the vertical mode will still be large due to the lack of any dilution effect. It will also have a wider resonant peak due to the low Q of this mode. For this reason we wish to push it to as low a frequency as possible.

The frequency of the vertical mode of a rectangular fibre is given by:

$$f_0 = \frac{1}{2\pi}\sqrt{\frac{k}{m}} \tag{64}$$

where the spring constant k is given by:

$$k = E\frac{wt}{l} \tag{65}$$

where E is the Young's modulus, w is the width, t is the thickness and l is the length. Thus to reduce the frequency we must reduce the cross section. increase the length or increase the mass. Again the strength of the fibres and the length of suspension limit these factors. By using rectangular fibres here we do not gain compared with a round fibre of similar cross sectional area. For a fibre of cross section $0.1mm^2$, 0.6m length and a 10kg mass we then have a vertical resonant mode at 9.18Hz which cannot be improved upon without stressing fibres more highly or increasing the suspension length. One potential solution would involve using soft, cantilever style, vertical springs to reduce the vertical spring constant for the final stage of the pendulum. This must of course not increase the loss and so a low loss material such as silica would be required. Initial testing of fused silica blades has been performed to look at the viability of such a design. A fused silica blade was produced from a glass slide by cutting along a diagonal and was then shaped by heating over a curved silica tube using a hydrogen-oxygen flame. This is shown in Figure 18 under tension from a welded fibre. The blade was loaded to over 0.5kg before breaking with the failure being almost certainly due to thermal stresses at the welds.

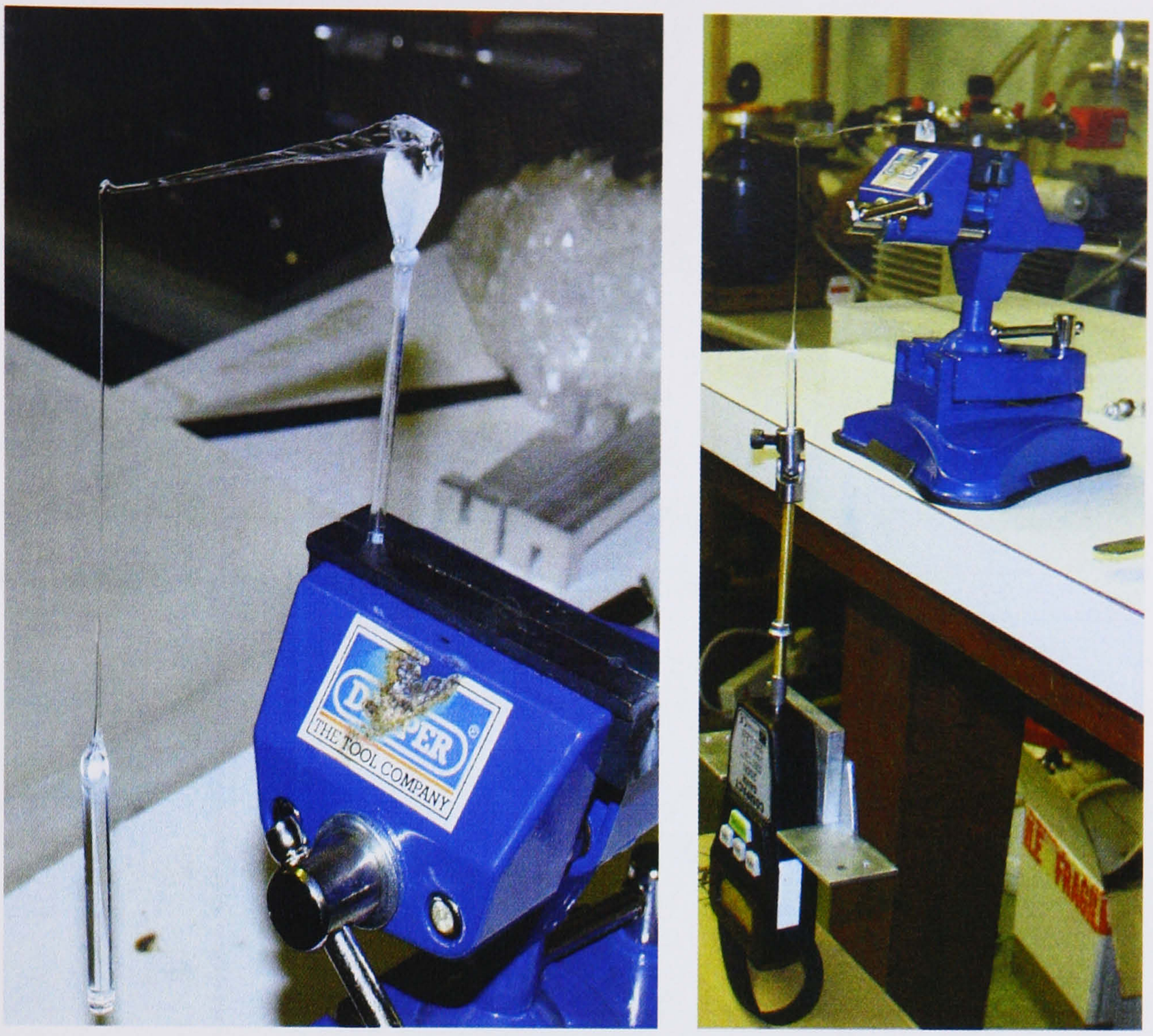

Figure 18: Silica blade with fibre attached to tip (Left, close up image. Right, under tension with force meter attached). The only silica blade to have been tested, this broke at over 5N loading despite being only 1mm thick.

The transverse vibrational modes of the suspension fibres will also occur within the detection band (at a few hundred Hz) however due to their high Q these will cover only a very narrow frequency band and will be notched out of the data.

3.3.3. Thermoelastic Peak

The thermoelastic peak may also occur at detection band frequencies and hence it is of interest to look at how its effects can be reduced through careful design. Its resonant frequency for a round fibre is calculated using Equation 47, which is repeated here [65]:

$$f_{char} = \frac{1}{2\pi\tau} = 2.16\frac{\kappa}{\rho C d^2}$$

where κ is the thermal conductivity, C is the specific heat capacity, d is the diameter of fibre and ρ is the density . For a round silica fibre of 0.1mm this would give a resonance at 8.8Hz. For a rectangular fibre the resonant frequency is given by Equation 48, which is repeated here:

$$f_{char} = \frac{\pi\kappa}{2\rho C t^2}$$

where t is the thickness of the fibre. Again using a 0.1mm thick ribbon we have a resonant frequency of 20.3Hz. A graph showing the thermoelastic loss as a function of frequency is shown in Figure 19.

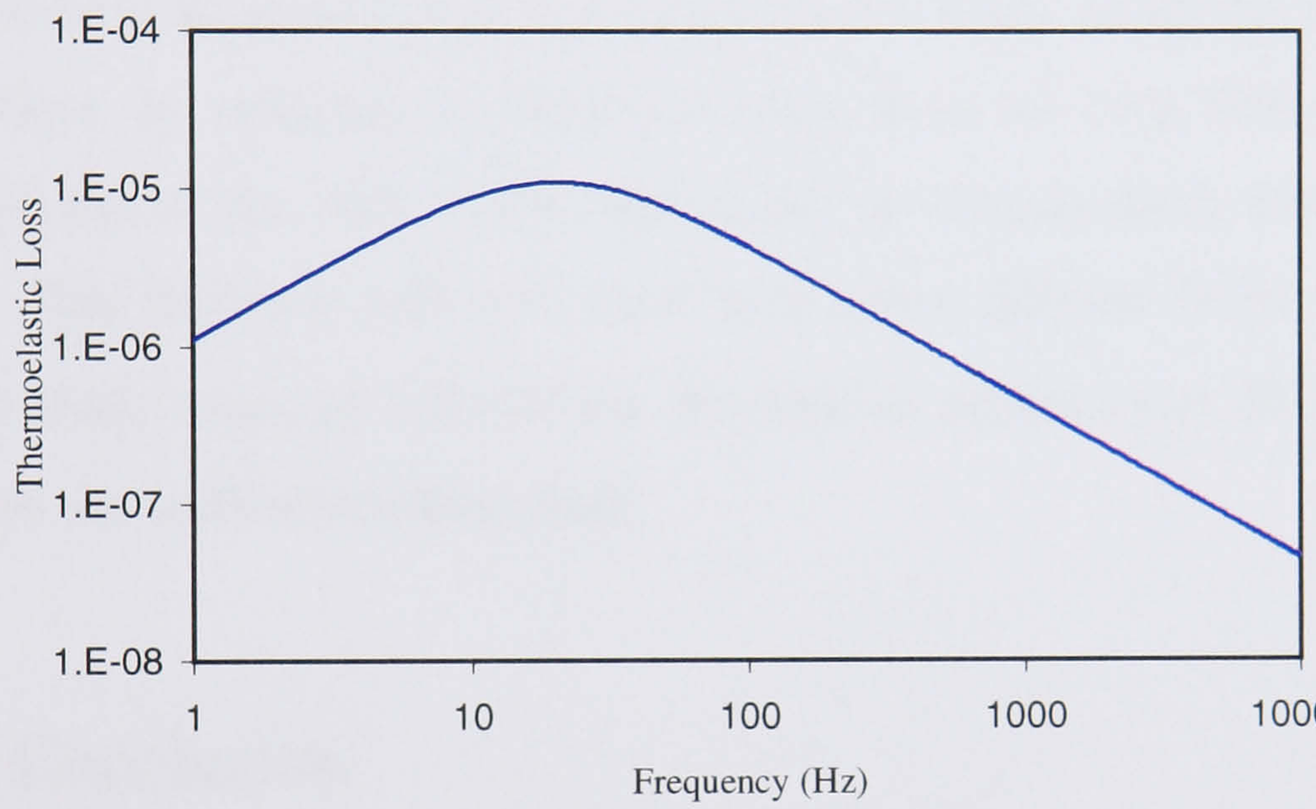

Figure 19: Calculated frequency dependence of thermoelastic loss in a 0.1mm thick fused silica ribbon with no static stress using Equations 54 and 55.

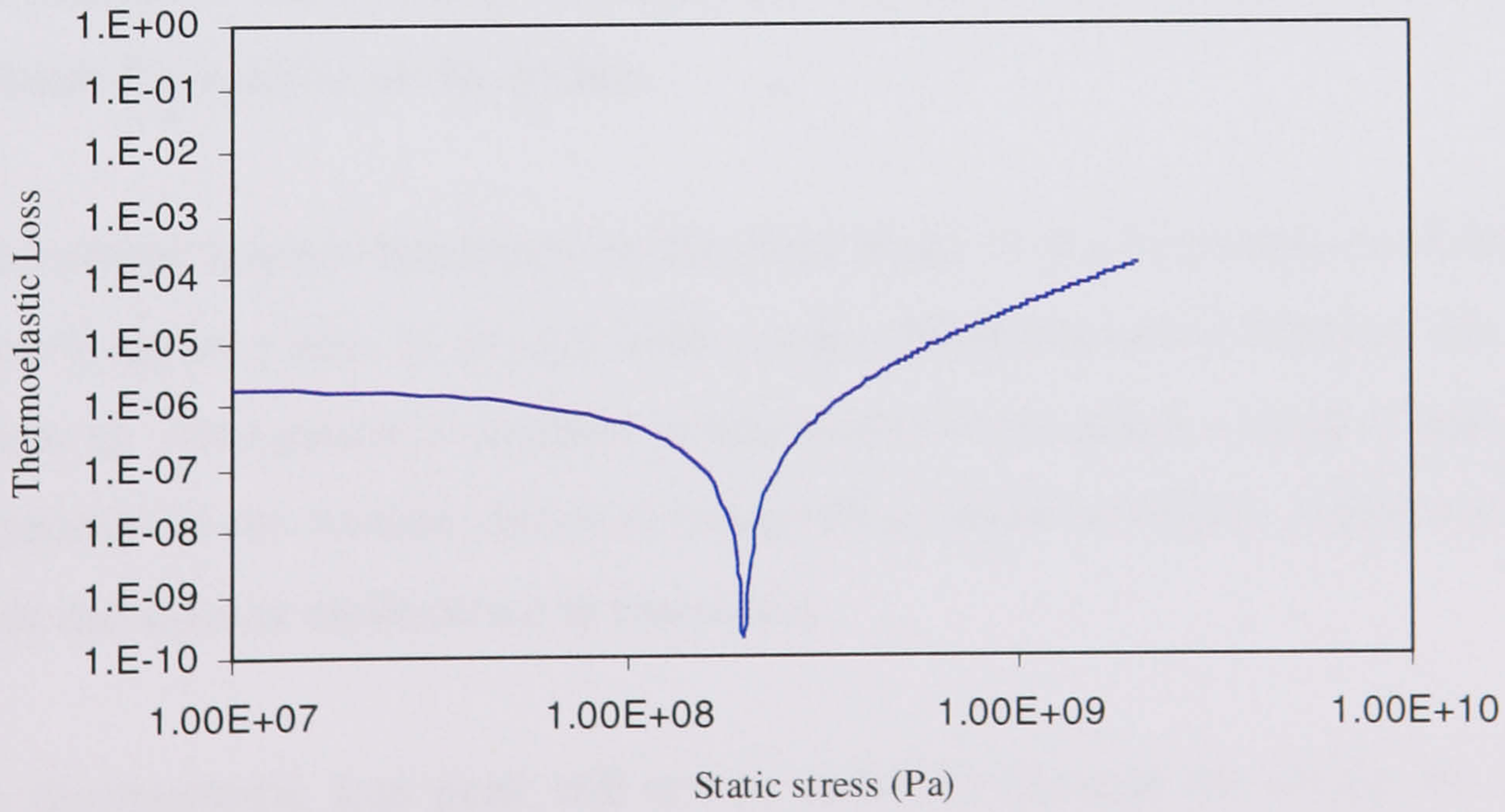

Figure 20: Calculated stress dependence of thermoelastic loss in a 0.1mm thick fused silica ribbon using Equations 54 and 55.

The technique described in Chapter 2 for using the static strain in the fibre to cancel out the thermoelastic effect would mean a strain of approximately $2\times10^{8}\,\mathrm{Nm}^{-2}$ be applied for the ribbon discussed here. A graph showing the dependence of loss on static strain at the characteristic thermoelastic loss frequency is shown in Figure 20. However this strain is lower than the $9.8\times10^{8}\,\mathrm{Pa}$ planned for Advanced LIGO and would give a lower dilution factor of 2213. It would also push the vertical frequency up from 9.18Hz to 20.32Hz. It may be possible using a tapered fibre to get around the problems of the vertical frequency, which depends on the shape along the whole length of the fibre, by reducing the thickness away from the ends [69], while using the thickness of the ends of the fibre to set the thermoelastic loss to the null point. This however will still result in a lower dilution factor. Using the planned static strain of $3.9\times10^{9}\,\mathrm{Pa}$ the limit to sensitivity at 20.3Hz will still be due to the vertical resonant peak.

3.4. Conclusion

Toward the lower end of the detection frequency band the limiting noise source will be seismic in origin, with the use of multiple stage suspensions and cantilever blade springs reducing the effects of seismic noise above the resonant frequencies of the springs.

The vertical bounce frequency of the final stage of the suspension will set a lower frequency limit of around 10Hz on the Advanced LIGO detector due to its low Q. One potential solution to this would be to create a more compliant suspension in the vertical direction using silica cantilever blades, which would move the vertical mode down in frequency.

The thermoelastic loss peak will not be removed through the design for the Advanced LIGO detector. The requirement of a $2\times10^{8}\,\mathrm{Pa}$ static stress to

allow operation at the thermoelastic null point would give a dilution factor a factor of two lower as well as pushing the vertical mode up to 20.32Hz.

Therefore in order to minimise the effects of the vertical bounce mode and to increase the Q of the suspension we wish the suspension fibres to be as long as possible and with as small a cross section as possible, with rectangular fibres giving an increased dilution effect over round fibres. The limits of the vacuum tank dimensions and the working load on fibres have led to the decision to propose 60cm ribbon fibres with a cross section of 1.13mm by 0.13mm.

Chapter 4

Silica Fibre Production

4.1. Introduction

Silica fibres are produced by a variety of methods, though all follow a common theme. The thin fibres are drawn from a thicker stock material by heating until molten and pulling. Once produced the thin fibres must not be touched, as even a soft touch with a piece of tissue paper will affect the strength, and they are manipulated by holding the thicker stock material at the ends. Here we will look at a number of different methods that have been used to produce fibres used for measurements made in this thesis and used previously for mounting monolithic suspensions in GEO600. The first techniques described here were developed at the University of Glasgow and use a vertically mounted piece of stock material heated uniformly about the centre and then pulled uniformly at both ends in order to achieve a high degree of uniformity. The fibres used in the vertical Q measurements.

described in Chapter 7, however used a glass working lathe with one surface mix burner using a feed and pull system allowing longer fibres to be produced.

The most important characteristics of a system for producing fibres are that it produces them in a reproducible manner and that the strength of the fibres is high. The strength can be damaged through contamination of the flame, thermal stresses, non-uniformity (leading to regions of high mechanical stress) and damage to the surface of the fibres.

We will begin by looking at the simplest way in which a fibre can be produced.

4.2. Pulling Fibres by Hand

It is possible to create a round fibre by using only a hydrogen-oxygen flame and the stock material. The stock material, usually 3mm or 5mm diameter silica rod, is heated in the middle while it is rolled between thumb and forefinger to ensure a more uniform heating. Once it is glowing white hot it is quickly removed from the flame and the two ends pulled apart. The advantage of using this technique is that fibres can be produced quickly to a variety of thicknesses without the need for more complex apparatus. Also there is no reason why fibres with high Q cannot be produced in this manner as long as high quality stock and a clean flame are used. The disadvantages however are substantial. There is little or no ability to reproduce the same dimensions of fibre and, with each fibre being unique, a suspension such as the monolithic suspensions in GEO600 that requires a number of near identical fibres cannot be produced. Also it is difficult to produce fibres that are uniform and they usually display substantial ellipticity.

4.3. Pulling Fibres Using a Rig

In order to gain more control over the uniformity of heating and the direction in which the ends of the stock material are pulled a rig was used which is shown in Figure 21.

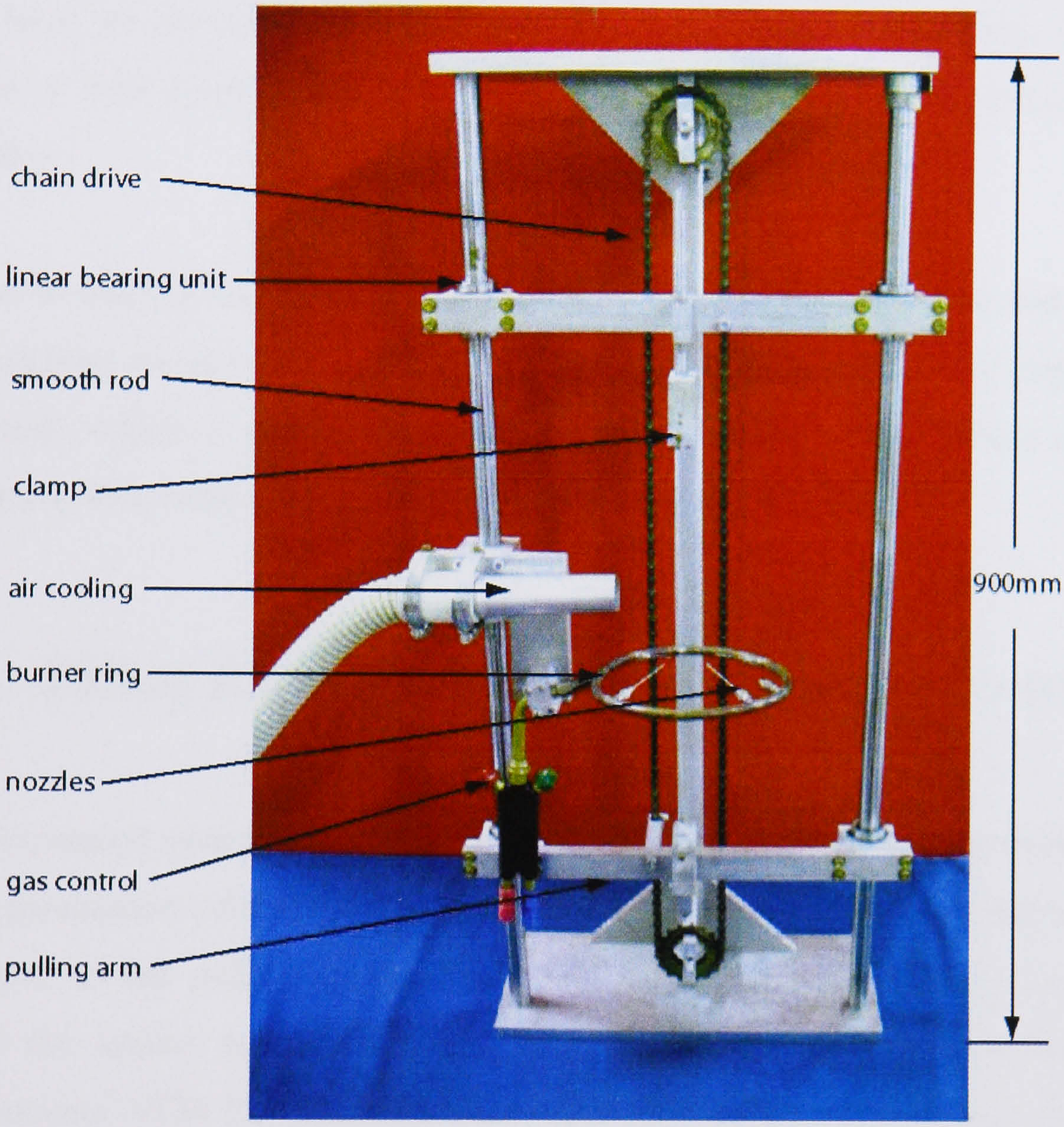

Figure 21: Hand pulling rig for producing round fibres. Stock material is clamped between the two arms which are linked by a chain to produce equal force on each. Needle burners mounted on a circular ring give a well shaped neck region.

The gas now flows not through one nozzle but through four, which are evenly distributed around the stock material to give a uniform heating. The ends of the stock material are clamped to horizontal arms, which slide vertically on two linear bearing tracks. The two arms are linked through a chain drive, which ensures that when one is moved they both move, but in opposite

directions and with the same velocity in order to create uniform shaping of the ends. By pulling the fibre vertically the effects of gravity on the shape are minimised (when pulled horizontally this causes fibres to sag). A fan unit is used to blow cold air at the upper clamp to ensure it does not expand sufficiently to release the rod. Using this rig fibres can be produced which are far more uniform and with a little practise they can be produced to approximately the same lengths (within 1cm) of up to 60cm. However we still have no precise control over heating times, flame temperature, pulling speed or final length, all of which have an impact on the final dimensions of the fibre.

When producing the fibres it is common practise to pull the thicker rod down to a slightly thinner section first. This gives a longer tapered 'neck' region at the ends, which is often used when welding the fibre. The thinner central section is then reheated and the fibre pulled from this material.

4.4. Pulling Round Fibres Using an Automated System

An automated system for producing round fibres was constructed in order that fibre production could be made more reproducible. The outline of the system is based on the pulling rig discussed above however a number of alterations allow the system to be controlled using a Labview script with a National Instruments ATM IO 16 XE-50 data acquisition board which gives a number of analogue and digital inputs and outputs.

The motion of the arms, causing the fibre to be pulled, is controlled using a motor with a feedback controller. This takes a control voltage from the DAC board of between 0V and 10V to set the speed of the motor, with the power supply coming from a separate 30V supply.

The supply of hydrogen and oxygen to the flame is controlled by using two sets of valves; one set is used to preset the gas mixture while the other is used

to turn the gas on and off. This then gives a reproducible flame temperature on each run. Five burners are mounted at evenly spaced intervals on a movable platform, which allows the flame to be lit before being moved into position. The platform is sprung such that it would pull the flame away from the silica rod but during the heating cycle it is held in place using an electromagnet, which takes a power of around 0.1A and a voltage of 12V through a power transistor controlled by the DAC. Two fans are mounted on the platform to cool the clamps and are not controlled by Labview but have a separate 24V supply. An example of this arrangement can be seen in Figure 23.

Positional information is given to the Labview programme using micro switches that switch the ADC inputs between 4v and ground. Analogue inputs are used to allow the operating voltages to be easily set and a switching point of 3V was chosen. Three such micro switches are used: the platform switch senses when the burner platform is pushed into place, the end of run switch senses when the pulling arms have reached their final position after extruding the fibre and the reset switch senses when the pulling arm positions have been reset to their starting positions. Figure 26 shows a similar control system but with the power transistor now controlling the fan and solenoid valves instead of the platform magnet.

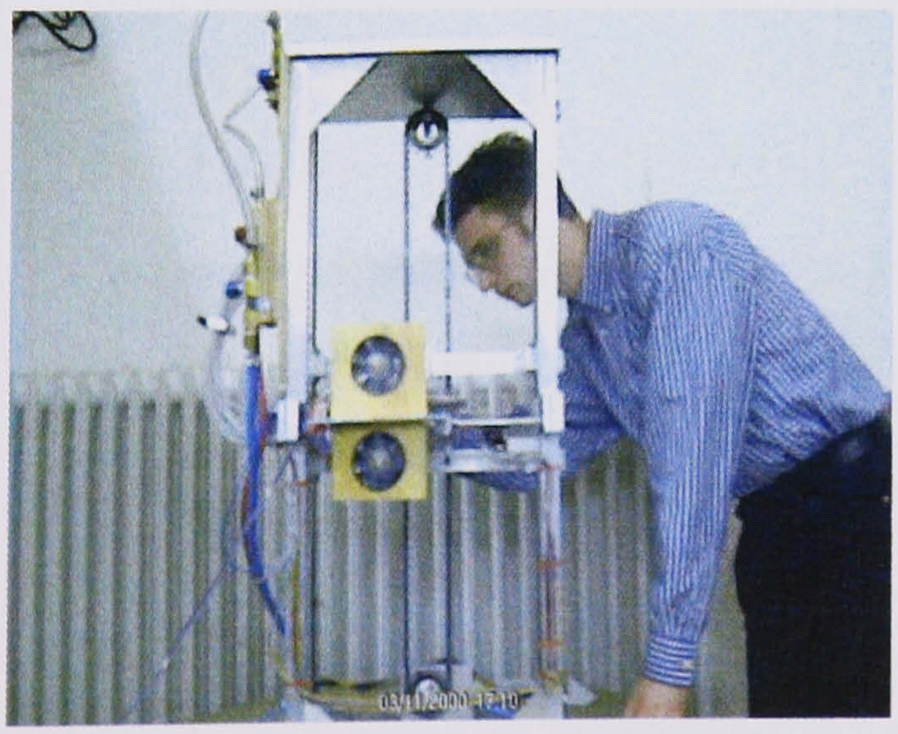

Figure 22: Production of the round fused silica fibres for the GEO600 monolithic suspensions

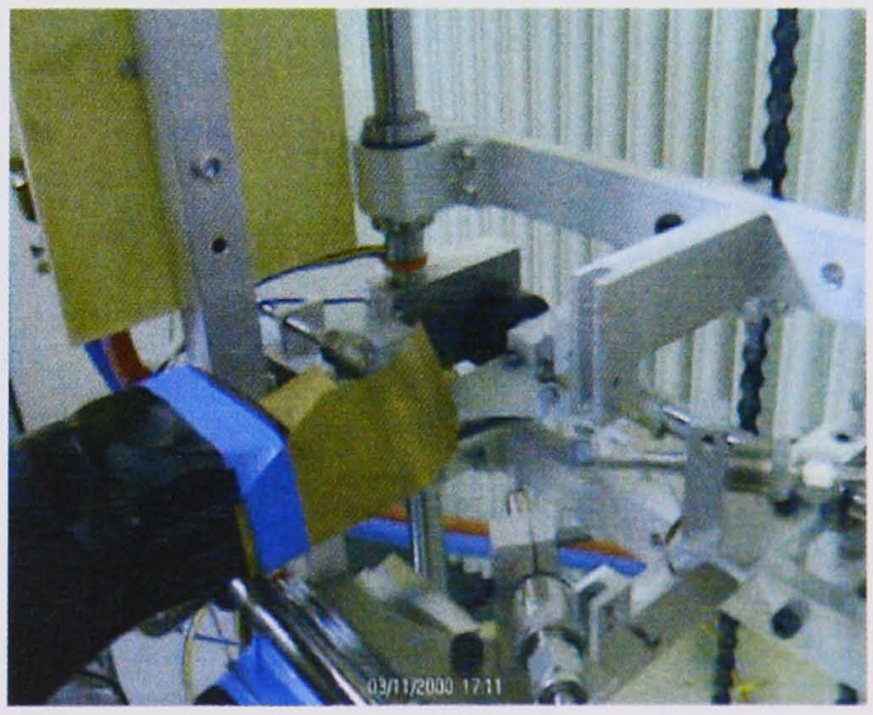

Figure 23: Close-up of burner platform showing five burners arranged in a ring. Fan shown is used to cool upper clamp.

Thus one run of the process, in which the stock material is heated and pulled twice in order to produce a neck region, would be as follows:

- A piece of rod is clamped into place between the two pulling arms.
- With the burner platform away from the fibre and the fans turned on the gas is lit with the levels being preset.
- The burner platform is pushed into place to heat the silica. This switches the platform switch and gives a high signal to Labview. The Labview programme then turns on the platform magnet to latch the burners in position.
- The silica is now heated for a length of time set in the Labview script.
- The electromagnet is turned off by Labview and the platform springs away from the rod. At the same time the arms are pulled to produce the neck region which is approximately 1cm long. The speed and time of pull, set in the Labview programme, are slow and short respectively as we are not pulling the fibre section here.
- Once this has cooled the platform is pushed into place again. This time when the platform switch is tripped it causes Labview to go onto the second phase of the cycle in which we will pull the thin section of the fibre. Again the electromagnet is used to hold the platform in place for a preset length of heating.
- Labview turns off the electromagnet at the end of the heating time again allowing the platform to spring away from the rod. The speed of pull this time is faster, around 0.6 seconds, to pull a thinner, longer fibre of approximately 40cm. The end of run micro switch controls the length of pull.
- With the gas supply turned off the cooled fibre can then be removed from the clamps, held by the end of the stock material.

Figure 22 shows a system of this sort used to produce fibres for the GEO600 suspensions. An identical copy of it was constructed before being adapted to produce ribbon fibres.

4.5. Pulling Ribbon Fibres Using an Automated System

Most work presented in this thesis involves the use of fibres with a rectangular cross section, the benefits of which are discussed in the previous chapter. As such the development work that was done on this system will be given in detail here.

For the production of fibres with a rectangular cross section the burner arrangement used above would be unsuitable. Most alterations that were made to the system stem from the need to move the burner positions as will be explained. A diagram of the system can be seen below.

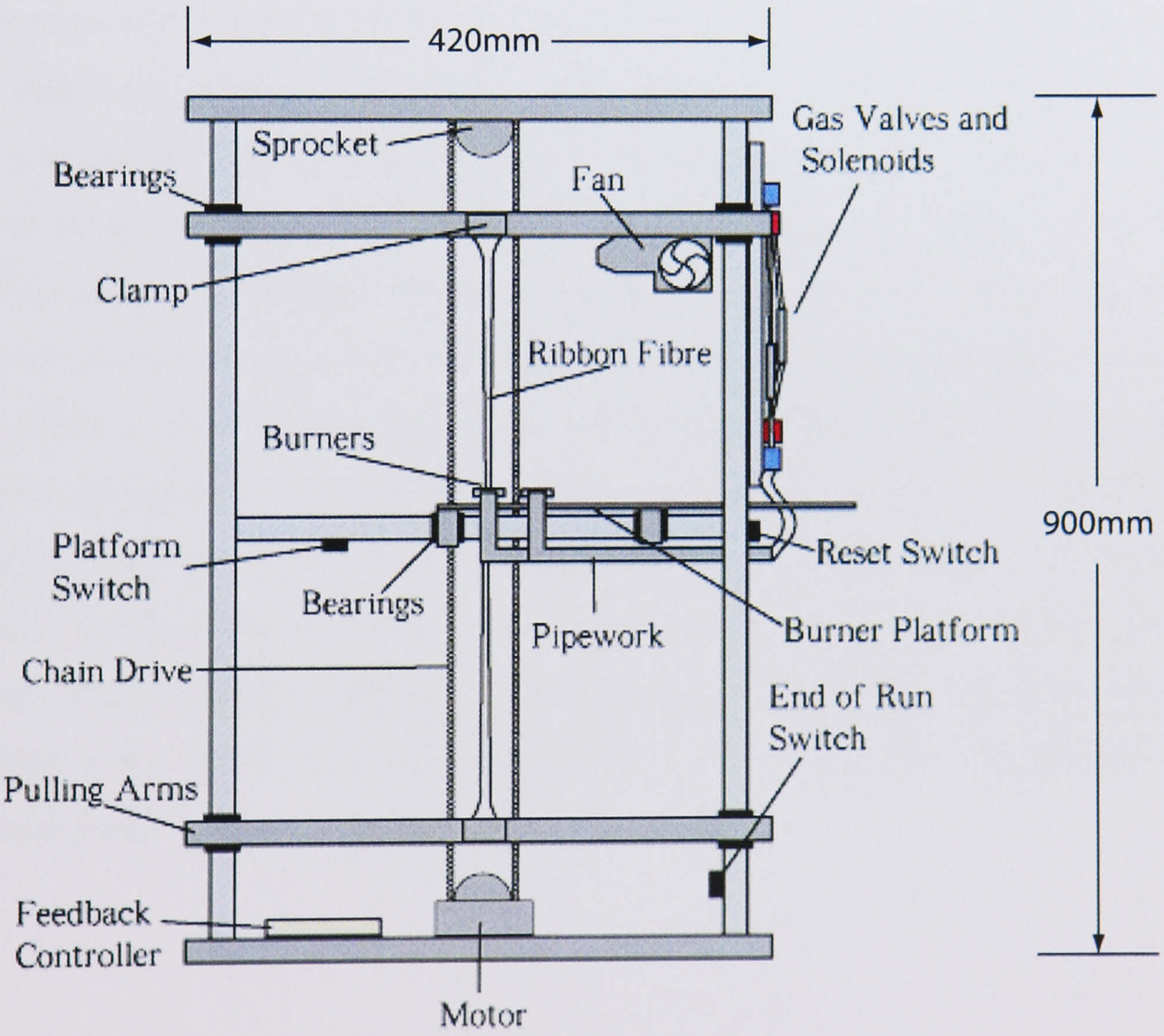

Figure 24: Diagram of ribbon pulling system. This 'heat and pull' system uses a chain drive to pull the heated stock material evenly at both end.

To give an even heating of the thin quartz slides (11mm x 1mm cross section) from which ribbon fibres are to be extruded, four burners are used in an arrangement of two pairs of burners facing each other, slightly inclined upwards, using sprung adjusting screws underneath, to stop heating of the nozzle opposite. The position of the burners was then aligned carefully such that even heating of a glass slide was achieved. A horizontal rail was used to allow the burners to be lit away from the clamped glass and then moved into place. This then meant that the burners needed to be aligned at right angles to the direction of motion of the rail as seen in Figure 25. As a consequence of positioning the burners in this way the fans cooling the clamps also needed to be moved. The two fans were replaced by one, as only the upper clamp required cooling. A brass duct was made to allow the direction of air flow to be controlled. It can be seen from the diagram that when the burner platform is moved back out of position the air current from the fan will still flow in the direction of the silica. This would cause differential cooling of the silica as it is pulled and would be a cause of non-symmetry in the fibre. For this reason it was decided that the platform should no longer spring back to remove the heat from the silica but that instead the fans and gas supplies should be turned off as part of the cycle controlled by Labview. Also the fan was now attached to the pulling arm to ensure that as it slowed to a stop any air current would continue to flow toward the clamp, not the fibre being pulled. The clamps were redesigned to hold the silica slides. Despite the use the fan to cool the upper clamp problems were still encountered with it expanding due to heating and a spring washer was then used in the clamp to give a more constant force even after expansion. Shims of paper were used to distribute the force of the clamp more evenly over the surface of the silica which otherwise tended to crack easily.

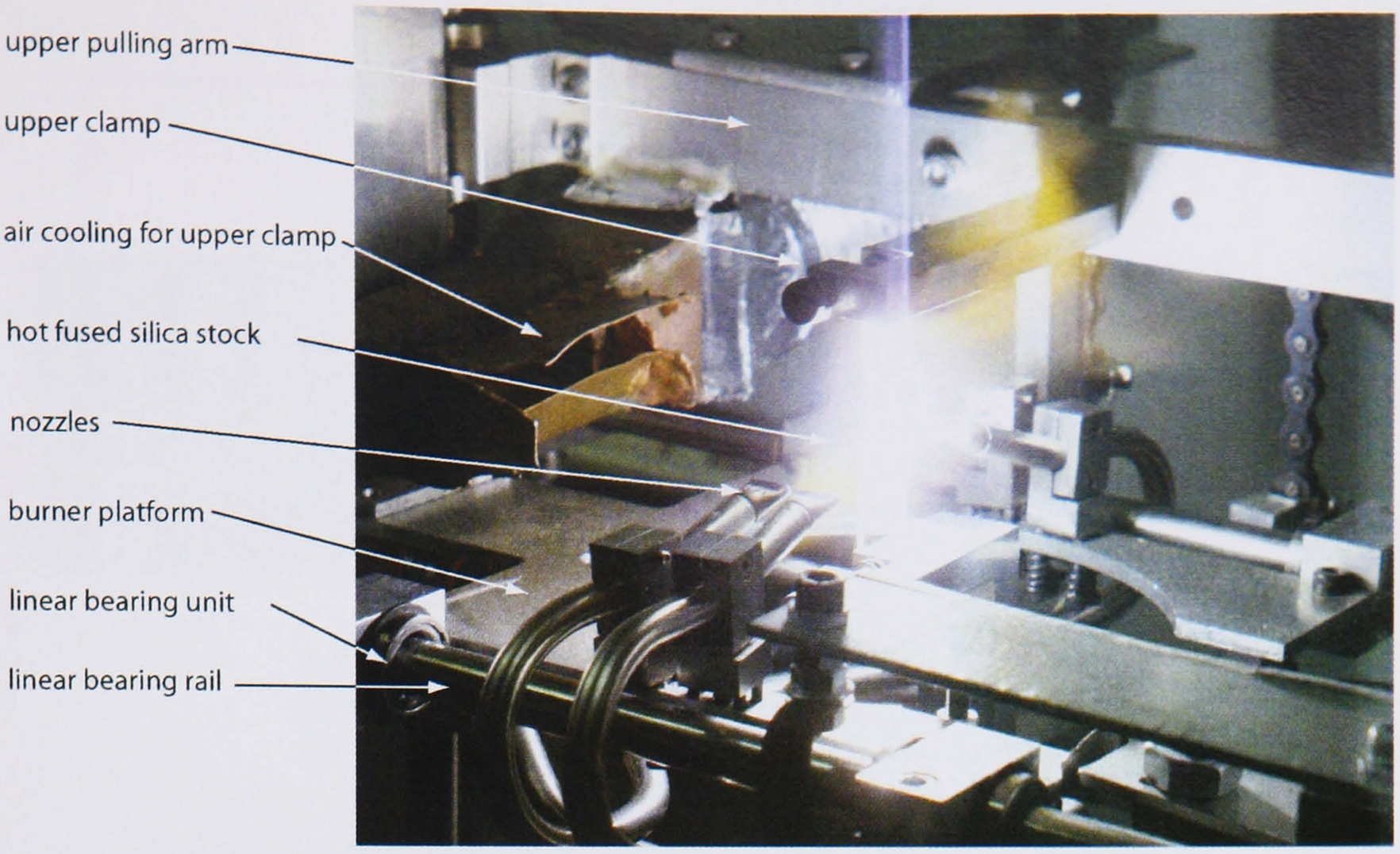

Figure 25: Photo of fused silica being heated in a hydrogen-oxygen flame by ribbon pulling machine prior to pulling.

The electromagnet used to hold the platform during heating was replaced with a fixed magnet and the DAC channel used to control this was used instead as the control for the fan and gas supplies. Power to the fans was controlled by a relay while solenoid valves now controlled the gas. The solenoid valves operate with a compressed air supply to power the valve and are switched electrically. A delay of 0.5 seconds was incorporated using a capacitor and variable resistor between switching the oxygen and fan off and switching off the hydrogen supply in order to follow the common practise of turning the oxygen supply off first. For safety reasons a flashback arrestor was incorporated in the section of pipeline that carries the mixed gas and a footswitch, requiring a constant pressure to operate, was installed to give a cut-off switch for the solenoid valves. Figure 26 shows the control scheme used with the data acquisition board.

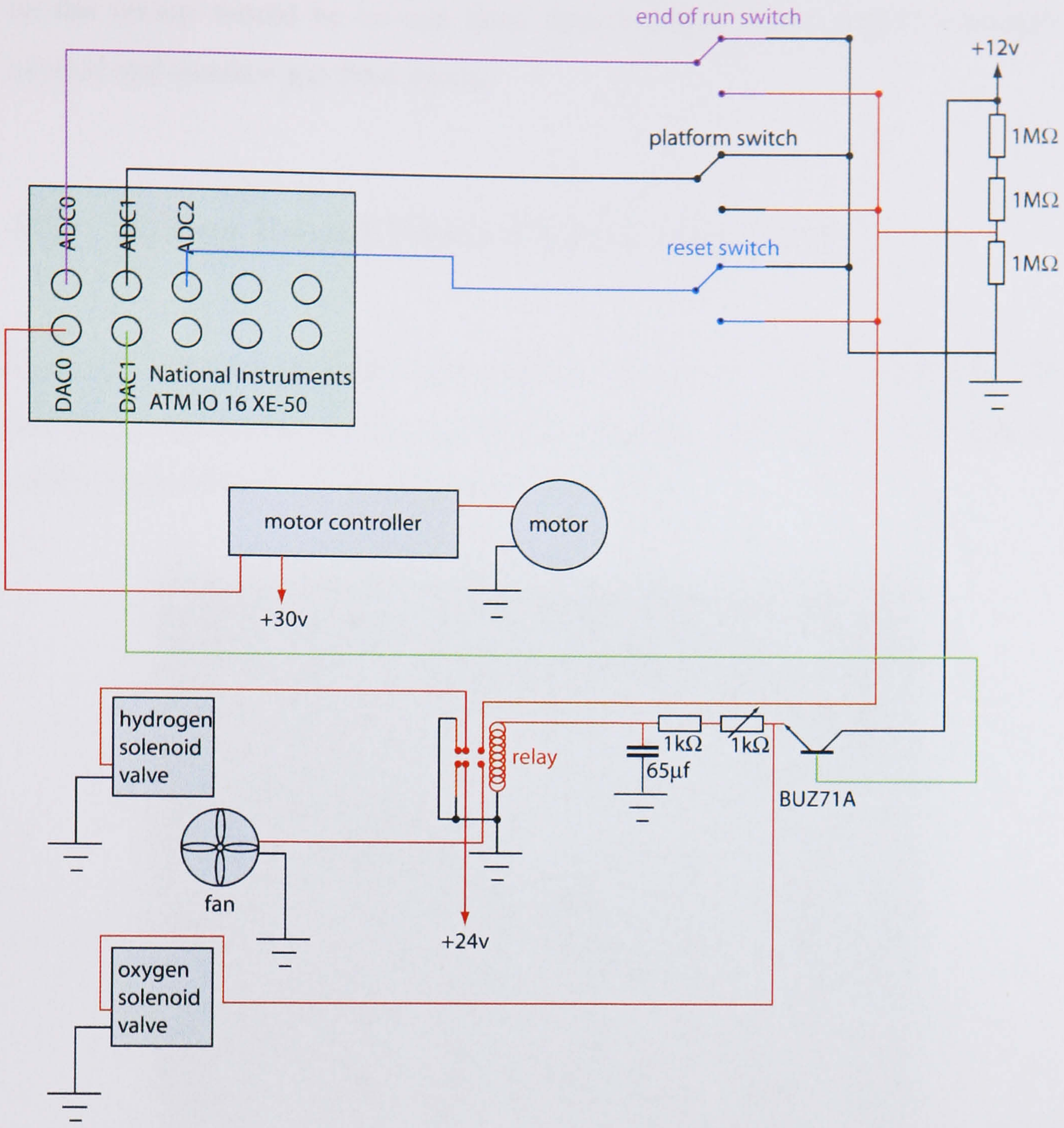

Figure 26: Schematic of control scheme for ribbon pulling machine.

After initial trials of the machine, during which heating times, pulling speeds and all other variables were set, it became apparent that only one heat and pull cycle was required to produce ribbons with a neck suitable for welding and the Labview code was then suitably altered to give this pattern of pulling. Using this system reproducible fibres could be produced although a warm up period of around five pulls was required during which time variations in length and thickness were seen as the temperature of parts of the machine altered, and were brought up to operating temperature. Also a consistent flow of gas is of importance, with the standard regulator valves occasionally giving different gas flow rates, mainly due to either pressure inside the gas tank or after the tank had been closed and then reopened. One possible improvement

to the set-up would be to use mass flow control valves which accurately control and monitor gas flow levels.

4.6. Pulling Round Fibres Using a Glass Lathe

Using a glass-working lathe a piece of silica rod is mounted horizontally with one large surface mix burner situated to one side. The glass is heated until white-hot and then the pulling program is initiated.

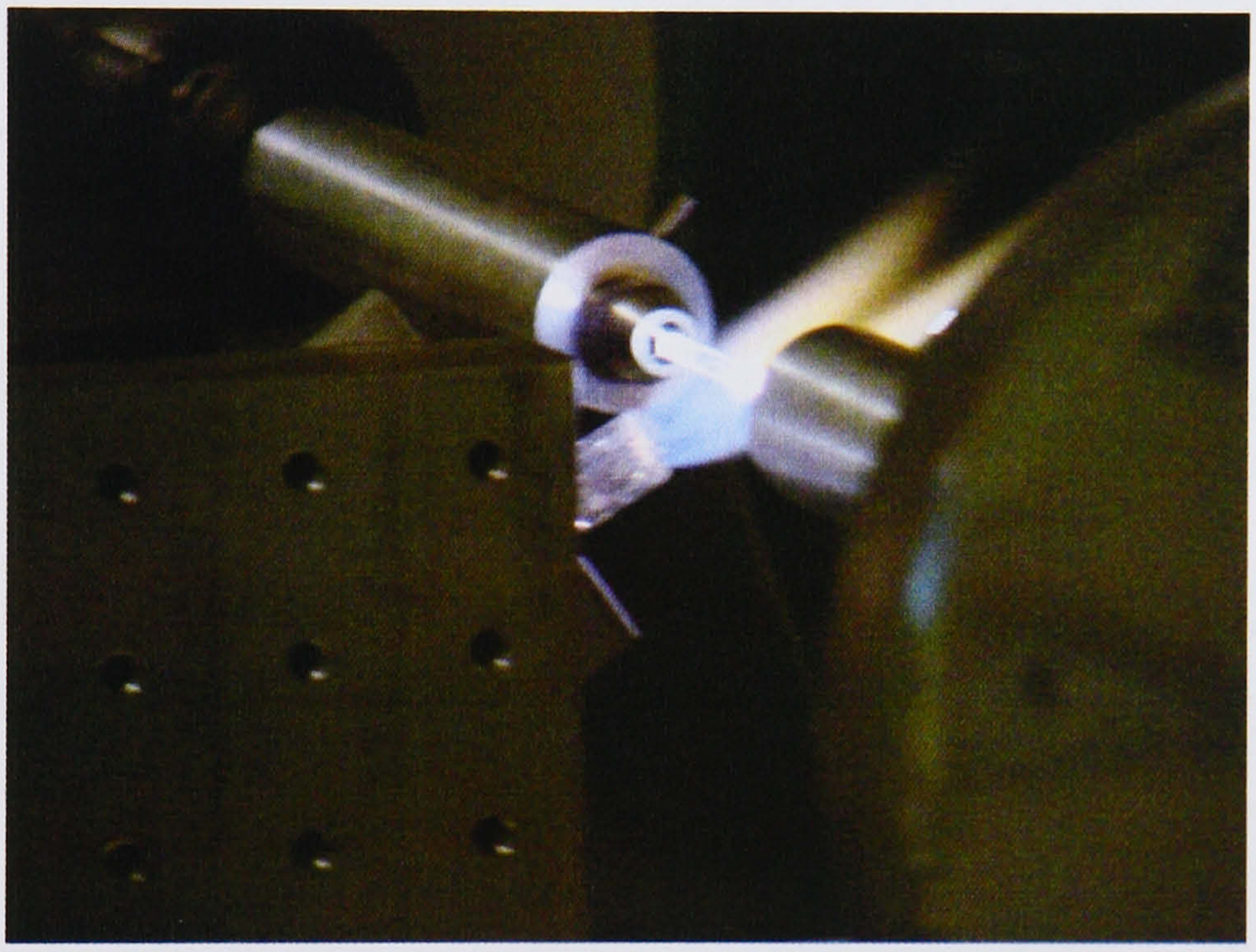

Figure 27: Silica rod is heated before pulling using a glass working lathe using a feed and pull system well suited to producing variable cross section fibres.

The fibre is pulled by the movable end of the lathe while at the same time the burner head moves to the opposite side, effectively feeding in material to the flame. By balancing the two speeds of movement it is possible to set-up the lathe such that the amount of glass pulled out of the flame is the same as that fed into the flame and equilibrium is produced. This equilibrium state is difficult to achieve but gives this technique two advantages, allowing fibres of any length to be produced and allowing fibres of different dimensions to be produced from the same size of rod. It also allows a number of programs for different fibre dimensions to be stored and then recalled later at need. This system may also prove relatively simple to use in implementing varying cross

section fibres due to its ability to vary both the feed and pull speeds. The use of a burner head that mixes the gases at the surface rather than within the supply pipes gives a smoother less turbulent flame with a more uniform shape. Also it improves safety, as it is impossible for the flame to flash back into the supply pipes.

One disadvantage of this method of fibre production is that the necks at each end are uneven, due to pulling from one side, while the initial section of fibre pulled tends to be a slightly different diameter than the rest, as the equilibrium point is being reached. However the suspensions that were made using these fibres did not use the necks. Instead the welding was carried out directly on the thinner part of the fibre, using a technique covered in Chapter 9.

4.7. CO_2 Laser Production

Work is now being done to set-up an alternative to flame pulling. This will be done using a CO_2 laser, which will give far greater control over application of heat. There is a precedent to using such techniques as they are widely used in production of optical fibres. It will give a more reproducible heating while also giving better control over heat distribution. Unlike using a flame there is no pollution to worry about and it does not produce water as a hydrogen/oxygen flame does.

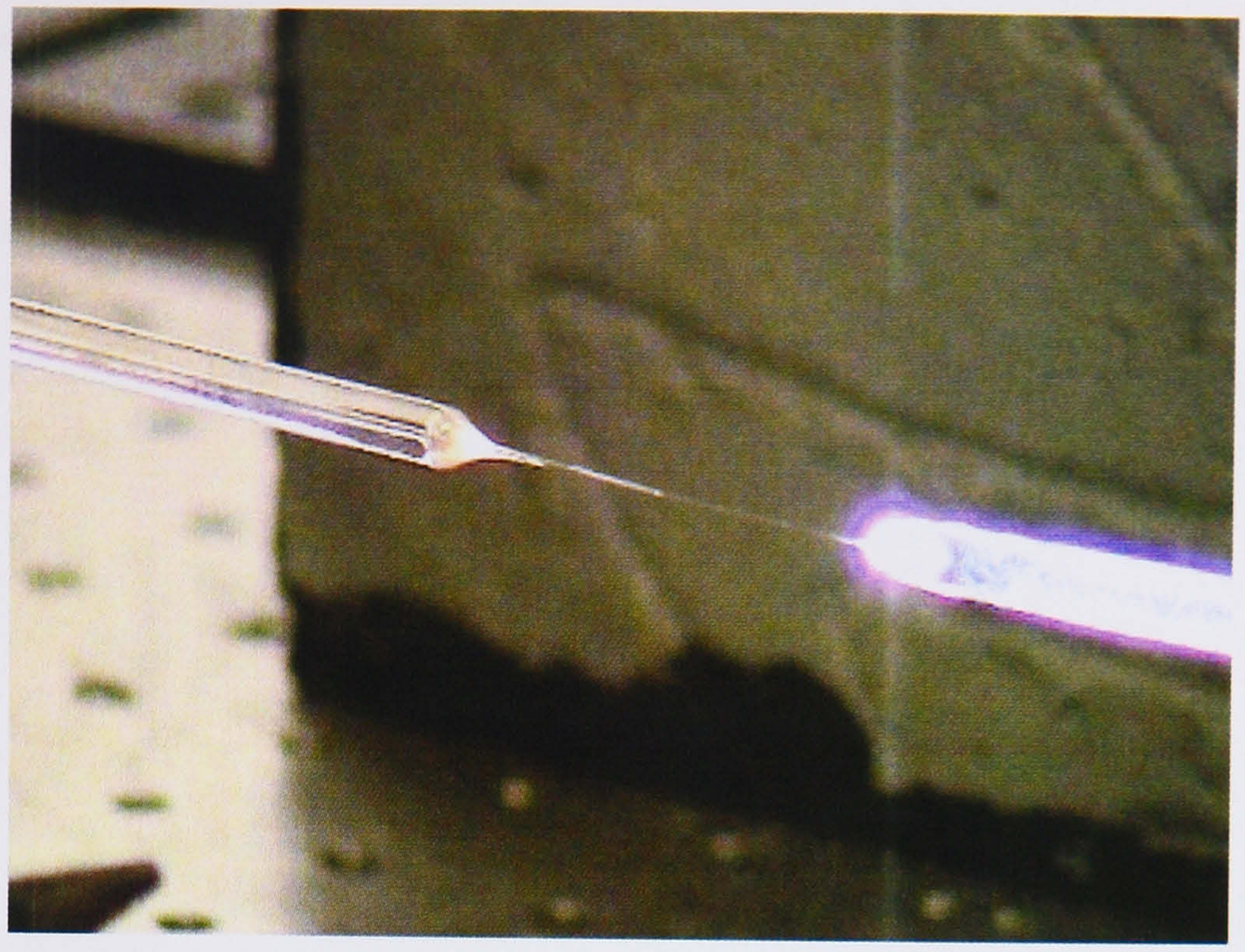

Figure 28: Round silica fibre being pulled using 140W CO_2 laser. Pulling fibres in this way should provide a self regulation of the fibre thickness to give highly reproducible results. The CO_2 laser will also be used to weld suspensions.

It should also be self-regulating in producing fibres of uniform thickness as for a reasonably thin sample the heating relates to the volume absorbing the radiation while cooling relates to the surface area. This means that a thicker piece of silica will have a higher heating to cooling ratio than a thinner section.

4.8. Conclusions

In this chapter it has been shown that, using simple hydrogen-oxygen flames, fused silica fibres, of suitable dimensions for use as suspension elements, may be pulled from stock material. It has been seen that a variety of designs of pulling machines were used to produce fibres, which are characterised elsewhere in this thesis.

The main aim of the design and construction of these machines was to allow the dimensions of fibres to be fixed using computer control of heating and pulling times.

Future work will concentrate on use of CO_2 lasers to produce fibres. It is expected that this will improve control of fibre dimensions and give greater uniformity to the fibres.

Chapter 5

Measurement of Violin Mode Loss

5.1. Introduction

In this chapter we investigate both the violin modes and cantilever bending modes of a rectangular cross section fibre, mounted as part of a monolithic suspension. These both form anharmonic series following the beam equation [62]. The violin modes are those where the fibre is held in tension, with the first three modes of oscillation shown in Figure 29. The cantilever bending modes are those where the fibre is held only at one end with the other free or unloaded.

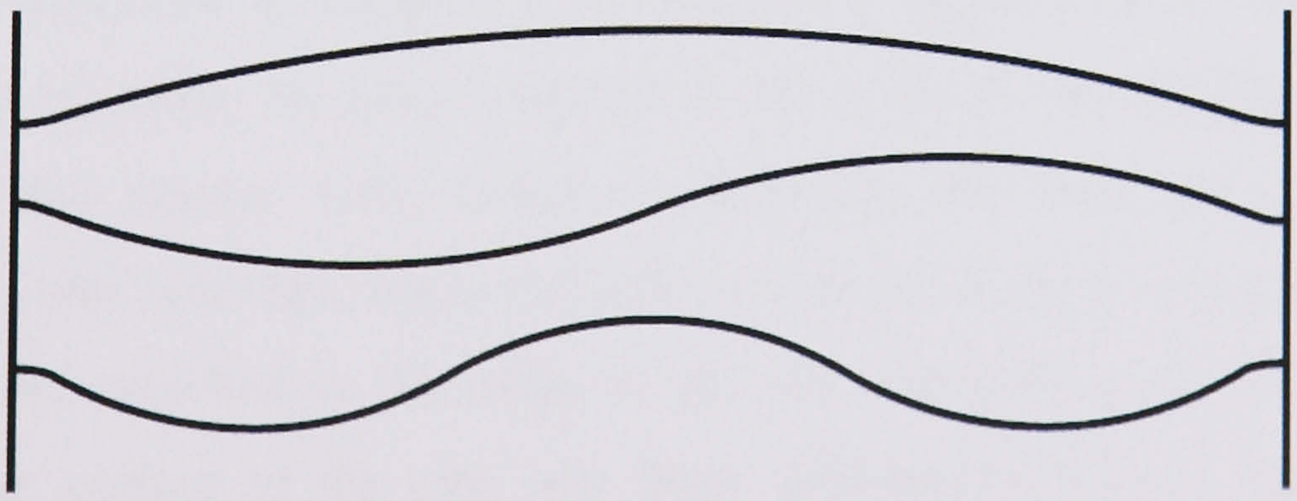

Figure 29: Violin modes of a fibre held at both ends. From top to bottom the first three modes of oscillation are shown.

In the cantilever bending modes the primary sources of loss we expect will be structural and thermoelastic as the energy is all stored in the bending of the material, resulting in a low Q. This therefore limits the effects of gas and recoil damping whose loss is at a much lower level. As we are able to measure modes over two decades of frequency, a range that includes the thermoelastic loss peak, we shall be able to look at the dependence of these loss mechanisms on frequency and will attempt to reconcile this to the theoretical calculation of loss.

With the violin modes of a fibre held in tension, other effects come into play. As the tension and hence dilution factor increases, the suspension Q increases to the point where other loss mechanisms such as recoil of the support and gas damping, become of higher importance.

5.2. Experimental Measurement of Violin Mode Q

The suspension used was a monolithic fused silica double pendulum, shown in Figure 30. The purpose of the upper stage of suspension was to create a low loss suspension point for the test fibre, whose energy is isolated from the dissipative support through the inertia of the intermediate mass, as discussed in Section 5.8 of this chapter.

The top plate and masses, made of Heraeus HOQ quality silica, were machined by grinding a 3mm diameter pin into the surface using the technique described in Chapter 9, to a depth of approximately 7mm. In an attempt to minimise the torque applied by the mass on the welding point, the centre of the masses were found by balancing the mass on a pin. The balancing point was then made the edge of the pin when it was ground, such that the fibre attached to this edge of the pin would be at the centre of the mass. The surface of the pins was flame polished to remove large surface defects. Figure 31 shows the lower mass after having had the pin ground into it.

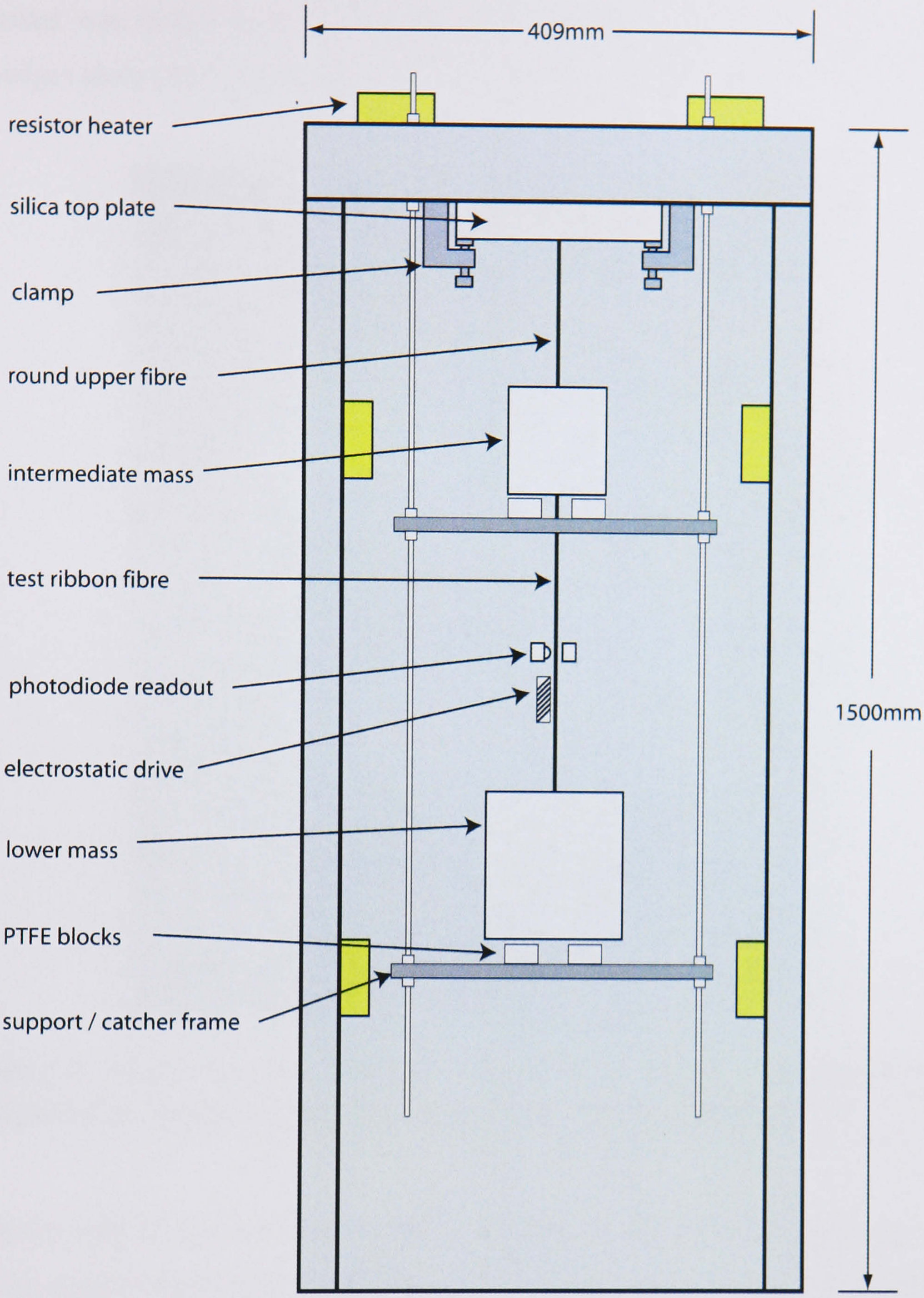

Figure 30: Experimental setup of violin mode loss measurement showing the support frame, monolithic fused silica suspension and catcher frame.

The support frame was machined from a 400kg stainless steel tube to produce a structure as shown in Figure 33. Appendix F gives a description of the design of this frame along with the predicted performance, though it is of interest here to note the key points. The surface of the tube was machined to produce a vacuum compatible finish. After this a door was cut in one side to give access once inside the tank. This was designed to be hinged and when

closed was bolted back into place using bolts down both sides and brass wedges along the bottom edge in order to maintain rigidity.

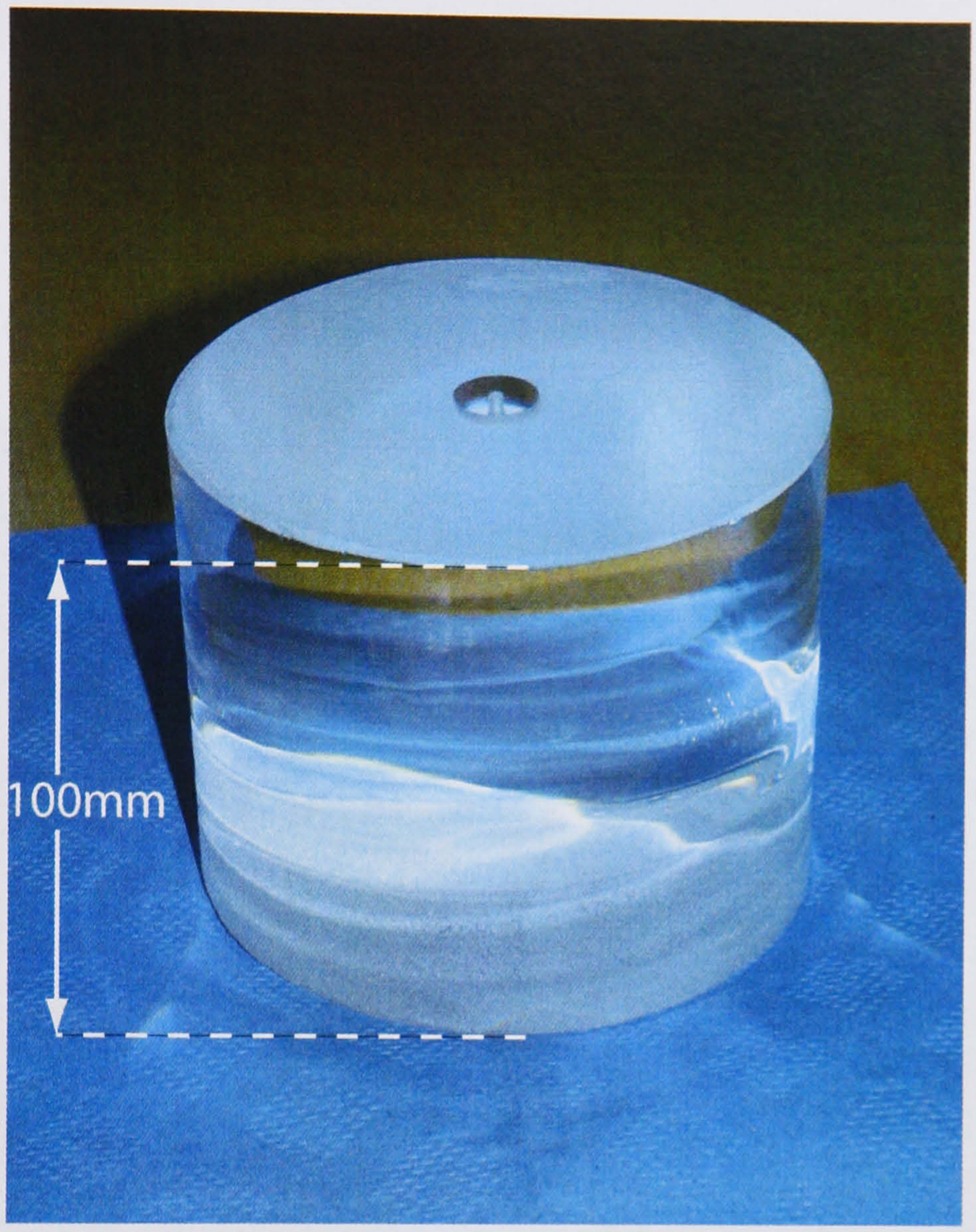

Figure 31: 2.4kg HOQ grade fused silica lower mass with attachment pin ground into top surface by machining using a brass grinding tool and carborundum grit.

On the side of the tube that would be in front of the turbo vacuum pump, a large circular opening was machined in order to improve pumping of the inner part of the structure where the suspension would be. The structure was cleaned using acetone and then methanol using clean cloths on the flat surfaces and pipe cleaners in the holes and threads. After this it was baked in air for a period of three days. It was then craned into the vacuum tank while still hot to reduce the amount of water adsorbed on the surface. After moving the support structure into the tank it was braced against the tank sides.

A top plate 50mm thick was made with a clamping surface machined into the bottom side. The clamping surface consisted of a circular inset with small

rectangular feet designed to minimise the contact area with the silica top plate while maintaining the stiffness of the clamp. A circular clamping ring, also using small rectangular contact points, was then used to clamp the silica top plate onto this. The bolts pushing this ring up onto the mass were tightened by hand, which produced satisfactory clamping of the plate without damaging its surface. A torque wrench could have been used had a more even application of force been necessary.

Figure 32: Isolation mass, upper fibre and upper clamp.

The design allowed the top plate to be craned out of the tank, allowing the suspension to be made outwith the support structure. The masses rested on PTFE blocks in a cradle made from threaded rod and aluminium crosspieces. The cradle could then be lowered once inside the tank and would double as a catcher for the masses.

The silica fibres used were produced from Suprasil 3 stock (Heraeus). The upper isolation mass was suspended from a round fibre, produced by hand. This was welded in place and can be seen in Figure 32, which also shows detail of the upper silica plate's clamp. Two ribbon fibres (400mm by 1.3mm by 0.15mm approximately) were to be analysed, with both being produced using the method described in Chapter 4. These should have similar properties to the fibre used in the pendulum mode loss experiment as they came from the same batch of stock material and were produced using the same settings for heating and pulling time. Any variation in cross section between these fibres is likely therefore to come from the consistency of gas supply used to heat the fibre when pulling as described in Chapter 4.

Silica pins 7mm long and 3mm in diameter were taken from Suprasil 3 stock material and had flats ground onto one side as described in Chapter 9. The ribbon was then welded at each end to one of these pins, which in turn were then welded to the isolation mass at the top, and the tensioning mass at the bottom. The welded areas were then annealed using a diffuse gas flame to reduce the thermal stress in the welded region.

The completed suspension was then tested for strength by lowering the supporting cradle. Once the strength had been confirmed the cradle was moved back up to support the masses again and the suspension was craned into place in the vacuum tank, inside the main support structure with the top plate bolted down in place. This can be seen in Figure 33.

Also shown in this figure are the electrostatic drive, mounted behind the lower fibre, the heating resistors used to bake out the steel structure once under vacuum, mounted on the outside of the steel structure, and the brass plates used to create a flush closure between the door and the main body of the tank.

Figure 33: Completed suspension mounted in the support frame on the vacuum tank base. The catcher frame has been lowered and sits close to the underneath of the masses.

Violin modes of the silica fibre held in tension were excited using an electrostatic drive, shown in Figure 35. This method of excitation is discussed further in Appendix D but it is of interest to note some points about the operation here. The electrostatic drive used at first consisted of a PTFE rod with a double screw thread cut onto it and wound with the positive and negative wires separated by around 1mm. These wire were then connected through a vacuum feedthrough to a high voltage amplifier. The high voltage amplifier operated by taking a signal in from a signal generator and then gave an output of 1kV for a 1V input. The maximum output available was ± 5kV though in practise a voltage of around 2 to 3kV was used. As described in

Appendix D the method of operation was to apply an excitation signal at half the frequency at which we wished to drive the fibre. A range of frequencies was then manually scanned until a resonance of the fibre was found. Later a single copper wire placed 1mm from the fibre was used as a positive electrostatic drive surface instead of the more complex electrostatic drive. The earth connection from the high voltage amplifier was then made to the wall of the tank. This gave improved excitation of the higher order modes whose wavelength is short compared to the 1mm separation of the wires in the electrostatic drive described above.

The motion of the fibre was detected using a shadow sensor type readout. An infrared LED placed close to the fibre is used to cast a shadow onto two photodiodes placed close behind the fibre. The photodiodes are placed side by side and aligned at 45° to vertical, as shown in Figure 34, to give a linear response as the shadow crosses the central region. In practise this gives a range of approximately 3mm in which the detection of the fibre position behaves linearly. Any non-linear behaviour would appear in as harmonics in the signal from a mode as the output signal deviates from a true sine wave. Also this would be seen as a ringdown whose envelope was not an exponential decay. Neither of these were seen in the measurements made. The outputs of the two photodiodes were subtracted before being amplified and filtered.

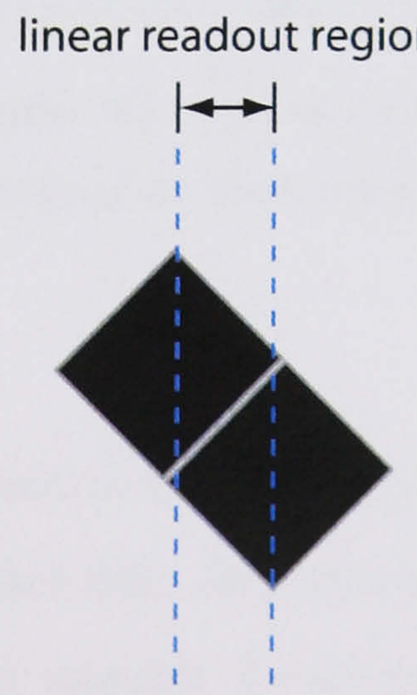

Figure 34: Schematic of the linear readout region of photodiodes used for displacement measurement of fibre

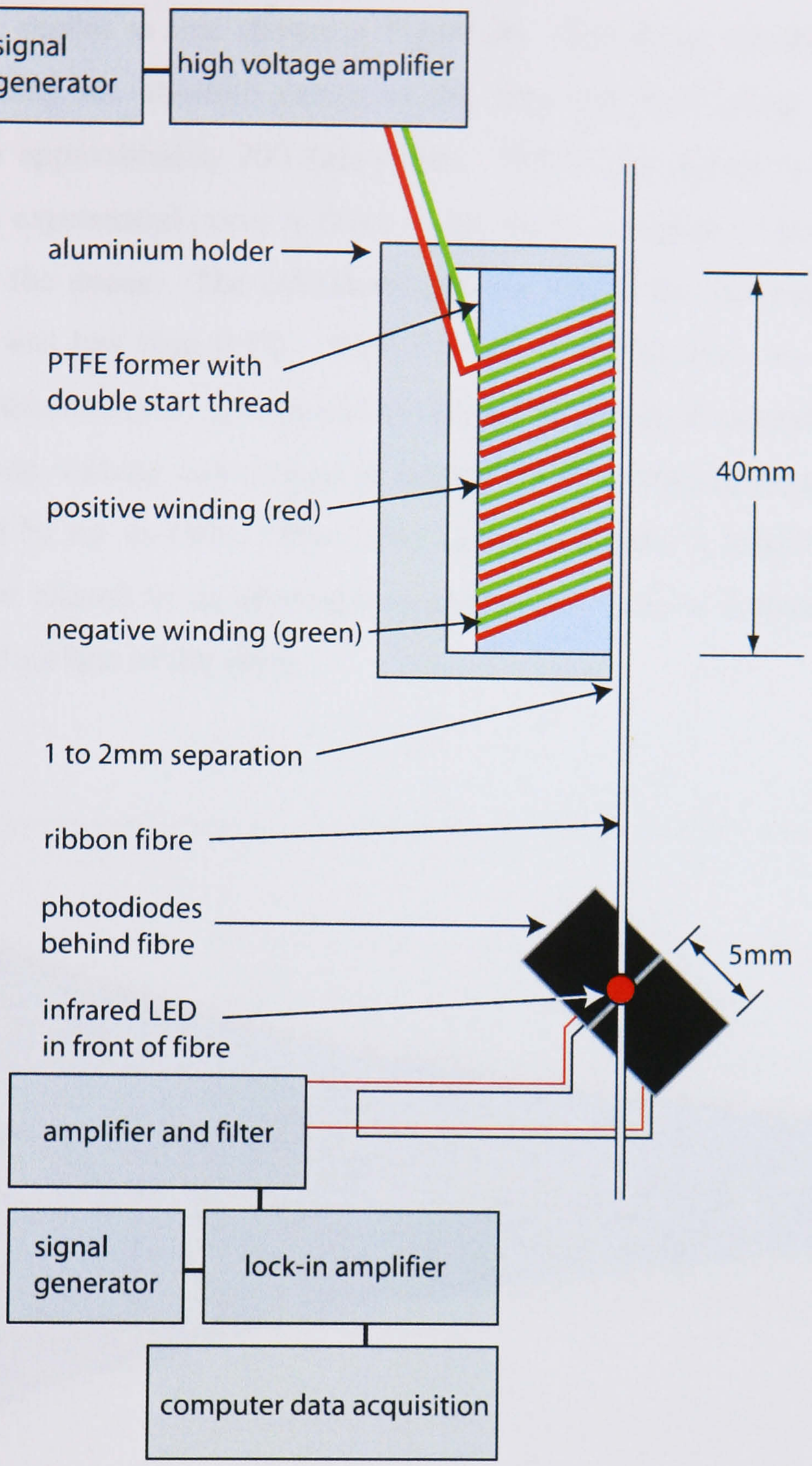

Figure 35: Schematic of electrostatic drive and shadow sensor readout. The photodiodes are placed approximately 3mm behind the fibre with the infrared LED placed 3mm in front of the fibre.

The frequencies of modes measured were between 1Hz and 2kHz, with the later being unsuitable for direct data acquisition using a computer. A lock-in amplifier was used to give a suitable frequency, around 0.1Hz, at which to acquire data, by beating the photodiode signal with a generated signal 0.1Hz away from it. Data were acquired on a computer using a LabVIEW based program using a National Instruments card. A decaying sinusoid should then

be recorded, similar to that shown in Figure 36. The decay envelope is then found by taking the absolute values of the data and then taking a running average over approximately 200 data points. This is also shown in Figure 36. After this an exponential curve is fitted to the decay envelope to find the time constant for the decay. The calculated error in this fit for the example data shown here was less than 0.1%. While this gives the accuracy to which we make the measurement of Q it should be noted that repeated measurements of the same mode without any change in experimental conditions gave Q values which varied by up to 10%. The cause of this variation is unknown but is thought to be related to an altering loss mechanism such as variations in the cracks on the surface of the silica.

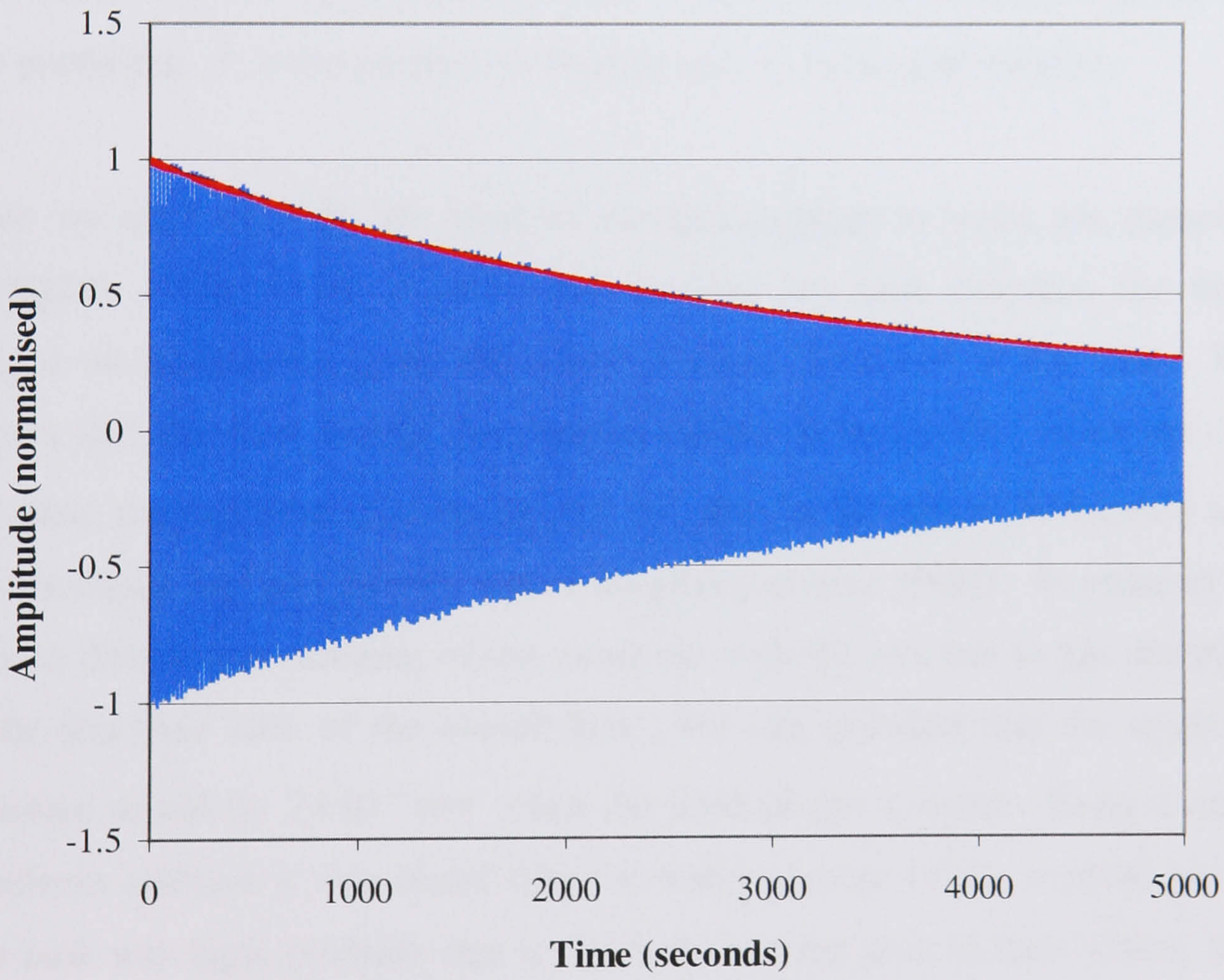

Figure 36: Example data from cantilever bending mode ringdown. The blue line shows the original data (normalised). The red line shows the envelope of the decay. The fit of an exponential to this red line gives an error of less than 0.1%.

5.3. Gas Damping Limit for Violin Modes

As derived in Appendix G, the equation for the Q of a gas-damped pendulum is given by:

$$Q = \sqrt{\frac{\pi}{2}} \frac{\omega m}{4AP} \sqrt{\frac{R_0 T}{M}} \tag{66}$$

where ω is the frequency of motion of the mode of oscillation, A is the surface area of the moving part of the pendulum, M is the average mass of one mole of the residual gas molecules, m is the mass of the moving part of the pendulum, P is the pressure in Pascals and R_0 is the gas constant.

Here we shall calculate the level of vacuum required to make gas damping negligible, while in the experimental sections we shall calculate the limit placed on measurable Q by the actual pressure measured in the tank. We expect that the most heavily gas damped mode will be the first where we can calculate the expected Q to be around 10^9 due to the effects of material and thermoelastic loss and dilution with a frequency around 300Hz. In order to be able to dismiss gas damping of this mode we wish the loss due to gas damping to be less than 10% of the overall loss. We can calculate that the required pressure would be 2×10^{-9} torr when the residual gas is water. Using a mass spectrum analyser it was found that the water content of the residual gas in our tank was high, probably due to the large surface area of steel within, and we may therefore assume the effects due to other molecules to be negligible. We may note however that the highest measured Qs were approximately ten times lower than this. Hence a pressure of 2×10^{-8} torr should ensure that gas damping is not the dominant loss mechanism. The Edwards inverted magnetron gauge used to measure pressure inside the tank was calibrated by the manufacturers for nitrogen with calibration being dependent on the residual gas type. A calibration for water was unobtainable and hence we

must assume some error due to this with a corresponding error in the calculation of limit placed on the measurable Q. A more suitable gauge may have been a hot cathode ion gauge for which calibration charts for water are readily available.

5.4. Calculation and Measurement of Violin Mode Frequencies

By applying the dynamic beam equation derived in Appendix A, and by applying the boundary conditions given for a beam fixed at both ends and under tension, we may find the frequencies of the violin modes from Equation 114 which is given again here [70]:

$$f_n = \frac{n}{2l}\sqrt{\frac{T}{\rho_l}}\left[1+\frac{2}{l}\sqrt{\frac{EI}{T}}+\frac{EI}{2T}\left(\frac{n\pi}{l}\right)^2\right]$$

Figure 37 shows the predicted and measured frequencies for the second suspension as a function of mode number for a fibre of dimensions 405mm by 1.3mm by 0.15mm, under tension of 23.5N with the density of silica being taken to be $2200 kgm^{-3}$. As will be seen in Section 5.7 the value for the Young's modulus of the fibre was found to different to that for bulk fused silica and hence this altered value of $5.4\times10^{10}\,\mathrm{Nm}^{-1}$ was used for this graph. The modes for the first suspension are not shown here as it was only possible to excite two of them. This problem we believe to stem from the size of the electrostatic drive, which was subsequently replaced by a single wire. It can be seen that while the frequencies are within 4% of those expected they do not accurately follow the expected curve. Also we note that the predicted frequencies are close to a harmonic series due to the high tension. The deviation from predicted frequency is due to irregularities in the cross section of the fibre, which mean we cannot closely model its behaviour as a beam of constant cross section. Indeed, when measured the fibre was found to have a

thicker section in the middle that may be the cause of the altered frequency distribution. The theoretical dilution factors shown later use the average thickness of the fibre and hence the same value for every mode. However to be absolutely accurate we should note that in fact the dilution level will be different for each mode as it is dependant on the thickness of the fibre at the points of bending which will vary in a non-homogeneous fibre.

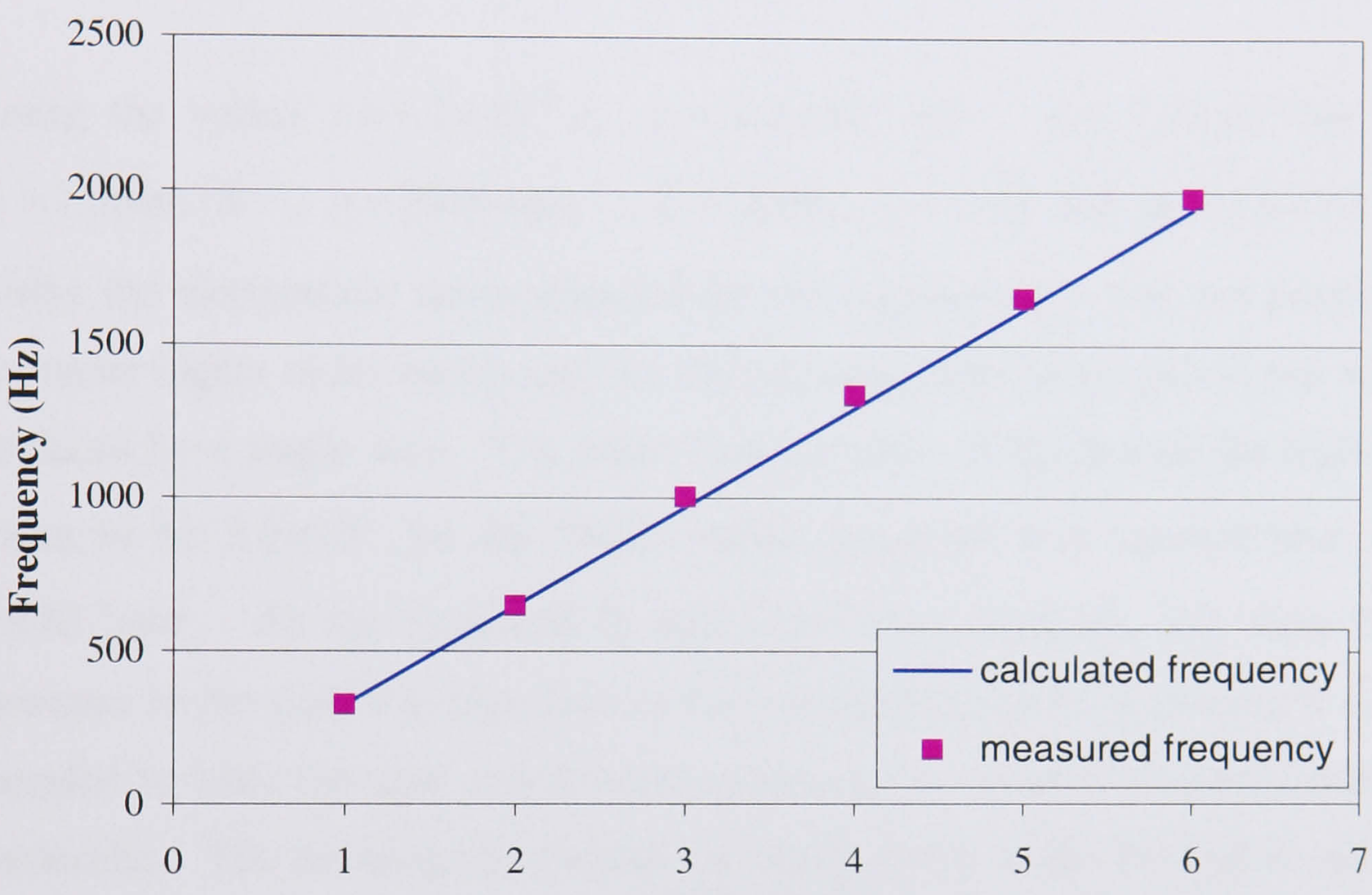

Figure 37: Measured frequencies of violin modes show a small deviation from predicted values, found using Equation 114, which are close to being a harmonic series. Deviations from predicted values, which are at the 1% level, are thought to be due to non-uniformities in fibre shape. Errors in measurement of frequencies are at the 0. 1% level.

5.5. Measurement of Violin Mode Loss

The Qs of the two modes measured in the first suspension are shown in Figure 38. As noted above the random error in measurement of Q is below 0.1% though a variation between subsequent measurements of up to 10% was seen due to a systematic effect, which may be related to the cracks in the surface of the silica altering and this has been taken here to be the overall error in the

measurement. The theoretical line shown is calculated using the equation shown below, derived from Equations 45, 48, 54 and 55.

$$Q = D\left[\phi_0 + \left(\frac{\alpha ET}{\rho C}\right)\left(\frac{\omega\frac{\rho C t^2}{\pi^2 k}}{1+\left(\omega\frac{\rho C t^2}{\pi^2 k}\right)^2}\right)\right] \qquad (67$$

using the values $t = 1.7\times10^{-4} m$, $\alpha = 4.2\times10^{-7} mK^{-1}$, $E = 5.2\times10^{10} Nm^{-1}$, $k = 1.38 \mathrm{Jm^{-1}K^{-1}}$, $\rho = 2200\,\mathrm{kgm^{-3}}$, T = 300K, D = 240 and $\phi_0 = 1.9\times10^{-7}$. Using the electrostatic drive prepared for this experiment it was not possible to excite higher order modes and for the second pendulum measured this was replaced by a single wire. The initial measurements of Q showed the highest value to be 5.3×10^7 for the 594Hz mode, measured at a vacuum level of $1\times10^{-6} torr$. As the measured Q was lower than expected, and since the pressure in the tank was high enough for gas damping to be a concern it was decided to bake the tank and internal suspension to remove unwanted water molecules. The resulting Qs showed an improvement in the first mode but a lowering of the second. Use of a mass spectrometer showed that as a result of the heating some large mass molecules had been released, later being found to originate from some wiring internal to the tank, and it is presumed that the deposition of these upon parts of the fibre caused the lowering of the Q of the second mode, while the improvement in the first mode is likely to have arisen from an improved vacuum level.

An attempt was made to use liquid nitrogen to cool the tank while taking ringdown measurements, in order to reduce the residual gas pressure further by using a polystyrene trough mounted around the base of the vacuum tank. However it was found that the differential cooling of the tank by the nitrogen gave rise to tilting of the support structure, which in turn gave rise to motion of the pendulum. This method of improving the vacuum may prove effective in future measurements if it is possible to remove the problem of differential cooling.

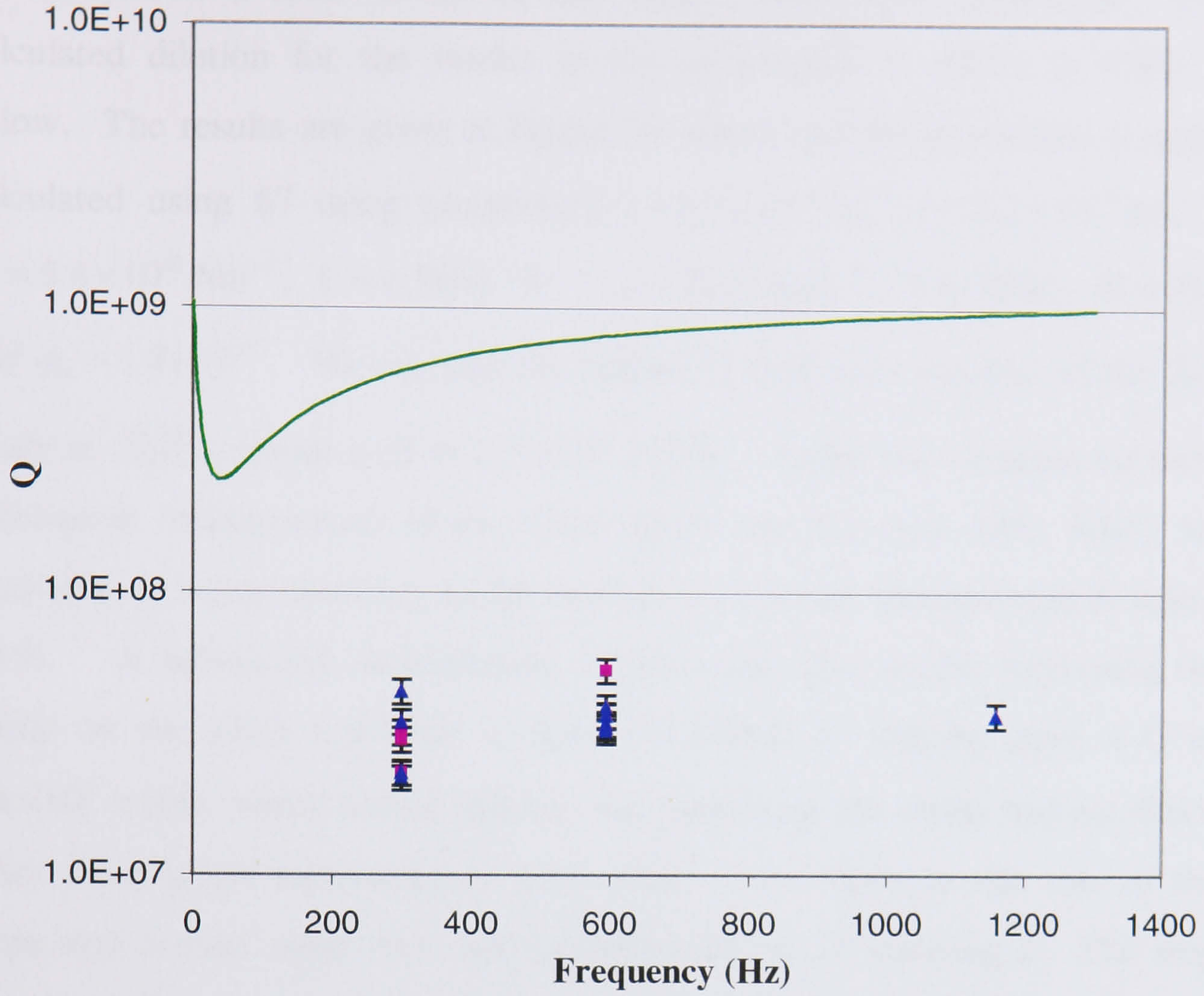

Figure 38: Violin mode Q of first suspension. Green line gives the theoretical Q. Pink points show initial Q measurements. Blue points show Q after baking tank. The theoretical line was calculated using Equation 67 with parameters given in the text. Errors shown are ±10% as discussed in the text.

The measurement of the second suspension was performed with all measurements taken below 2×10^{-7} torr. In this case the water content of the vacuum system was removed by pumping for substantially longer lengths of time (of the order of weeks). This did however lengthen the time necessary between subsequent measurements if the tank was to be opened. Again this vacuum level was not sufficiently low to get below the limit for the gas damping to be negligible for the lowest modes. Indeed for the first mode we calculate that the limit to the measurable Q for this vacuum level is $(1.3\pm0.5)\times10^{8}$ which matches with the experimental measurement and would imply that the main source of damping was due to the residual gas. However due to the frequency relationship between gas damping and Q we find that the higher modes are less affected by gas damping, and that by the third mode it

will contribute less than 20% of the damping measured. With the electrostatic drive replaced a total of six of the violin modes were measured. The calculated dilution for the modes in this experiment is shown in Table 1 below. The results are given in Figure 39 where the theoretical line is again calculated using 67 using parameters $t = 1.5\times10^{-4} m$, $\alpha = 4.2\times10^{-7} mK^{-1}$, $E = 5.4\times10^{10} Nm^{-1}$, $k = 1.38 \mathrm{Jm^{-1}K^{-1}}$, $\rho = 2200\ \mathrm{kgm^{-3}}$, T = 300K, D = 181 and $\phi_0 = 1.8\times10^{-7}$. We see that the highest Q measured was that of the first mode at 324Hz giving a Q of $1.5\times10^{8} \pm 10\%$. Again the variation between subsequent measurements of the violin mode was less than 10%, which we shall take to be the accuracy as the random error in the measurement is below 0.1%. A subsequent measurement of this mode after further tightening the clamp on the silica top plate to look for effects of slipping gave a Q of $1.4\times10^{8} \pm 10\%$ which would indicate that tightening the clamp had no effect. After these initial measurements were made it was thought that one of the stops near a mass might have moved sufficiently to be damping it. The stop was moved and the first mode re-measured, giving a lower value of $7.8\times10^{7} \pm 10\%$.

Mode Number	1	2	3	4	5	6
Frequency (Hz)	324	648	1005	1337	1654	1982
Theoretical Dilution	181	174	164	151	138	125
Measured Dilution ± 10%	27	13	13	24	21	26

Table 1: Measured and theoretical dilution factors for second suspension

At this point it was noticed that the Q values of the first mode appeared to be creeping lower and it was thought this might be the result of a crack opening, possibly at one of the welds. In order to check this, the tank was opened once again and the welded points at the top and bottom of the fibre were reheated until the glass glowed white hot. The welds between the pins were heated again also and care was taken to check that the weld was continuous across the whole area. The Q measured after this had not significantly altered, with some modes improving a small amount while others decreased slightly. This

effect may be expected if the shape of the welds was altered during heating or perhaps due to an altered distribution of thermal stress within the weld.

The theoretical lines shown in these graphs use the material loss values found in the next section and clearly show that the measured Q is substantially lower than that predicted from calculated dilution factors, with the first mode achieving a dilution factor of 26.9. Further discussion of this point will be appear in Section 5.8 below where we shall investigate the potential effects of recoil of the support as the excess loss mechanism.

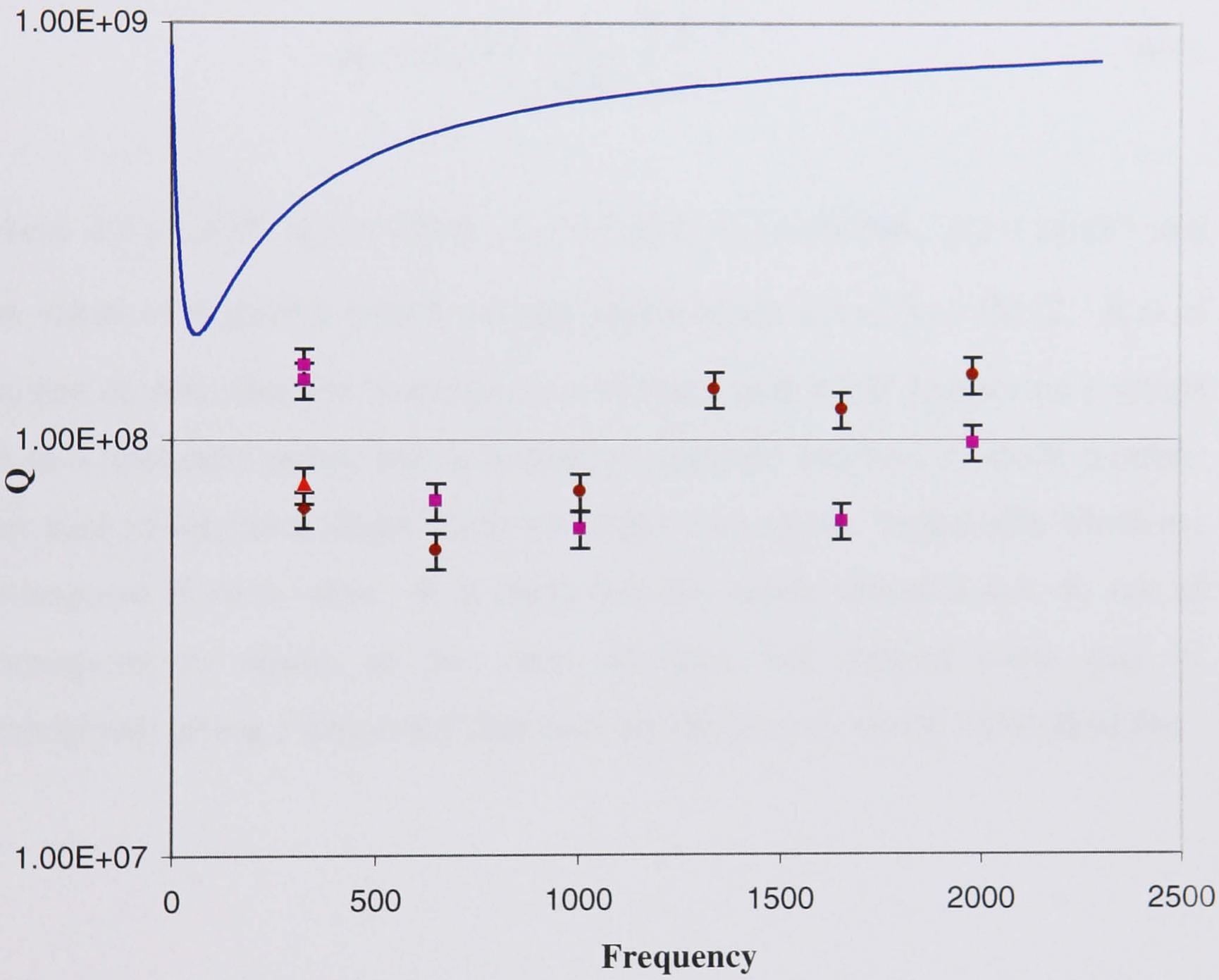

Figure 39: Measurements of the Qs of violin modes of the second suspension. The blue line shows the theoretical curve. Pink square points are initial Q measured. Red triangular point shows the Q after repositioning mass stops. Maroon diamond points show Q after reheating pins. Errors in measurements shown are ±10% as discussed. The theoretical line was calculated using Equation 67 using the values given in the text.

5.6. Calculation and Measurement of Cantilever Mode Frequencies

Having measured the loss of the fibres while under tension, the lower mass was then removed and the measurements repeated. The frequencies now found for the second suspension, plotted as a function of mode number in Figure 40, show a close fit to the predicted values found using the equation[63]:

$$\omega_n = (k_n l)^2 \left(\frac{a}{2\sqrt{3} l^2} \right) \left(\frac{E}{\rho} \right)^{\frac{1}{2}} \qquad (68)$$

where $k_1 l = 1.875$, $k_2 l = 4.694$, $k_3 l = 7.853$, $k_4 l = 10.996$, $k_5 l = 14.137$ and for values of n greater than 5 we may approximate $k_n l \approx (2n-1)\pi/2$. It is of interest to note that the frequency is not linear with mode number as it would be in a harmonic series, but is instead a quadratic function of mode number. For each violin mode shape there are in fact two modes measurable which are orthogonal to each other. It is likely that the points shown below do not all correspond to modes in the same direction but instead some may be orthogonal, giving a frequency that does not lie directly on the theoretical line.

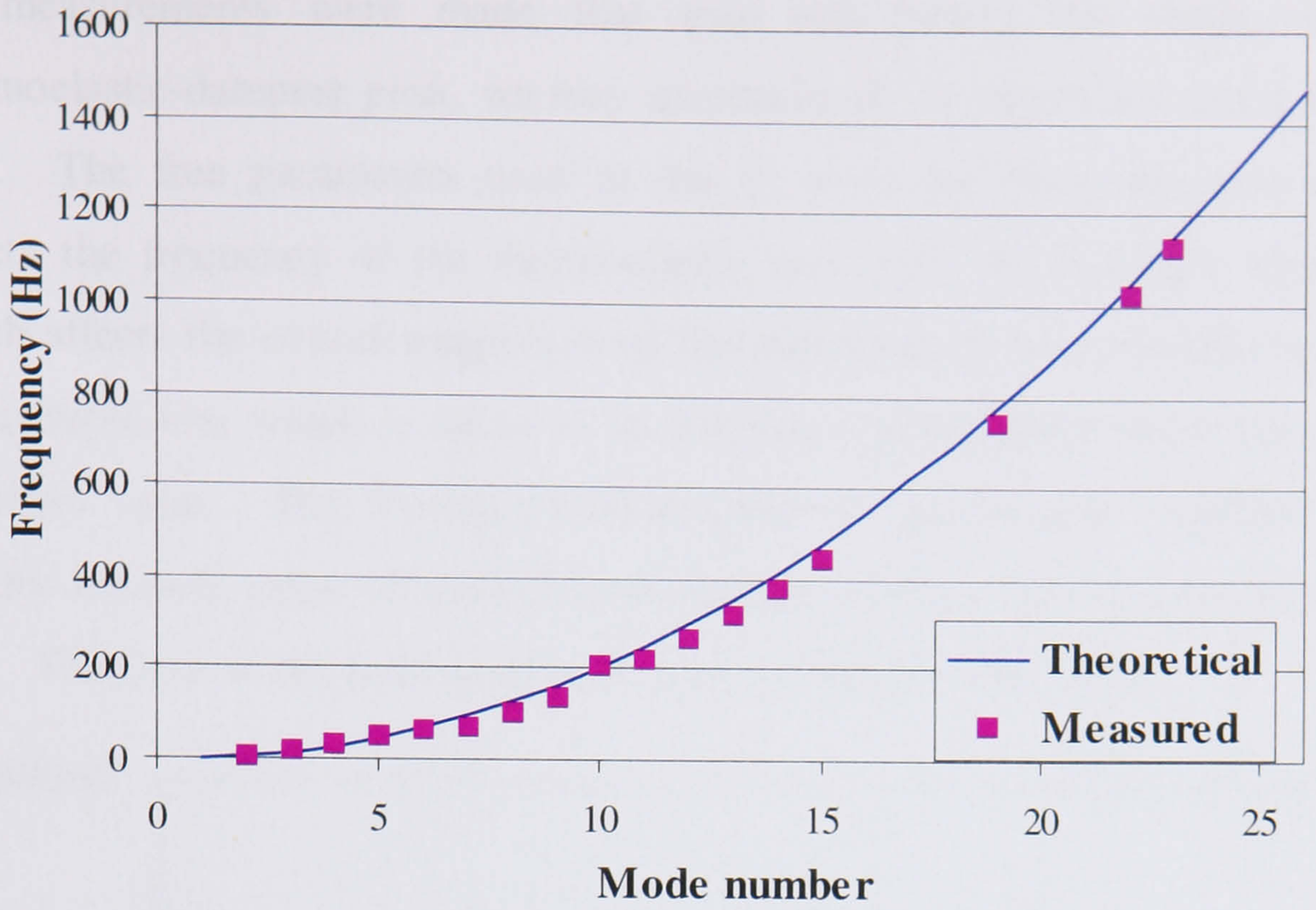

Figure 40: Frequency of cantilever bending modes as a function of mode number. Again the non-uniform nature of the fibre causes deviation from the predicted values found using Equation 68.

5.7. Measurement of Unloaded Cantilever Mode Loss of the Fibre

The loss of these modes was then measured in a similar way to that for the violin modes. Again only a small proportion of the modes were found in the first fibre and the measurements of these are shown in Figure 42. A total of 17 modes were found for the second suspension however and these measurements are shown in Figure 41 where the theoretical line given is a combination of structural loss, which we have taken to be frequency independent, and thermoelastic loss. Again the random error in the measurement of Q was below 0.1%. However the variation in Q between subsequent measurements was far larger at $\pm 5\%$. If this variation in loss was due to surface cracks altering then this might be expected to occur to a larger extent when under tension as we see here.

As measurements were made that map out clearly the shape of the thermoelastic-damping peak, we may accurately fit the theoretical curve to the data. The free parameters used in this fit were the fibre thickness which affects the frequency of the thermoelastic loss peak, the Young's modulus. which affects the overall magnitude of the thermoelastic loss contribution and the material loss which is taken to be frequency independent and hence gives an offset value. The Young's modulus may be significantly different from that for the bulk value of fused silica if there is an effect due to a surface layer [71]. The error in the least squares fit was calculated to be $\pm 1\%$.

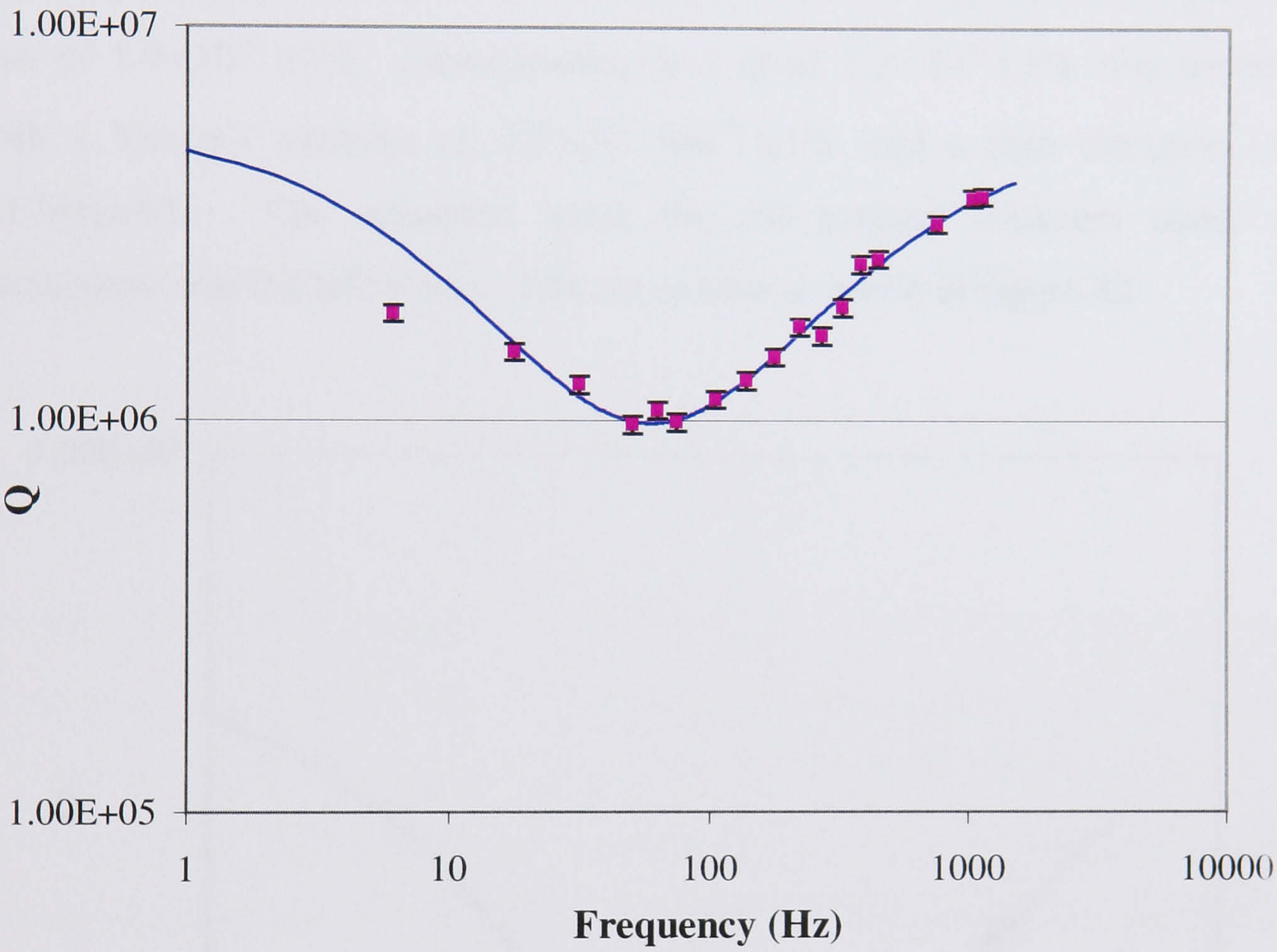

Figure 41: Cantilever bending mode losses of suspension 2. Line shows fit of thermoelastic and structural loss to data using Equation 67 with values given in caption of Figure 39 but using a dilution factor of D=1 as no lower mass was used.. The fitted values were $t = 1.5\times10^{-4}\,\mathrm{m}$, $E = 5.4\times10^{10}\,\mathrm{Nm}^{-1}$ and $\phi_0 = 1.8\times10^{-7}$ with a 1% error in the fit.

The fitted value for the thickness was 0.15mm±1% which we may compare to the average value measured using a micrometer of 0.17±0.01mm. The thermoelastic loss was found to be lower than predicted by using standard material parameters. The average fibre Young's modulus found by allowing

this to be a free parameter in the fit was $5.4\times10^{10}\,Nm^{-2}\pm1\%$. While this is significantly lower than $7.1\times10^{10}\,\mathrm{Nm}^{-2}$, the currently accepted value for bulk fused silica, similar values have been measured for round fused silica fibres of these dimensions by C.V. Boys who found a value of $5.2\times10^{10}\,\mathrm{Nm}^{-2}$ [71].

The fitted value for the material loss was $1.8\times10^{-7}\pm1\%$, which gives a Q of $5.6\times10^{6}\pm1\%$ for this Heraeus Suprasil 3 grade fused silica.

By using the same method to fit the data from the first suspension, a material loss of $1.9\times10^{-7}\pm1\%$, corresponding to a Q of $5.2\times10^{6}\pm1\%$ was found, with a Young's modulus of $5.0\times10^{10}\,Nm^{-2}\pm1\%$ and a fibre thickness of 0.17mm±1%. The measured value for the average thickness using a micrometer was 0.19±0.01mm. This set of data is shown in Figure 42.

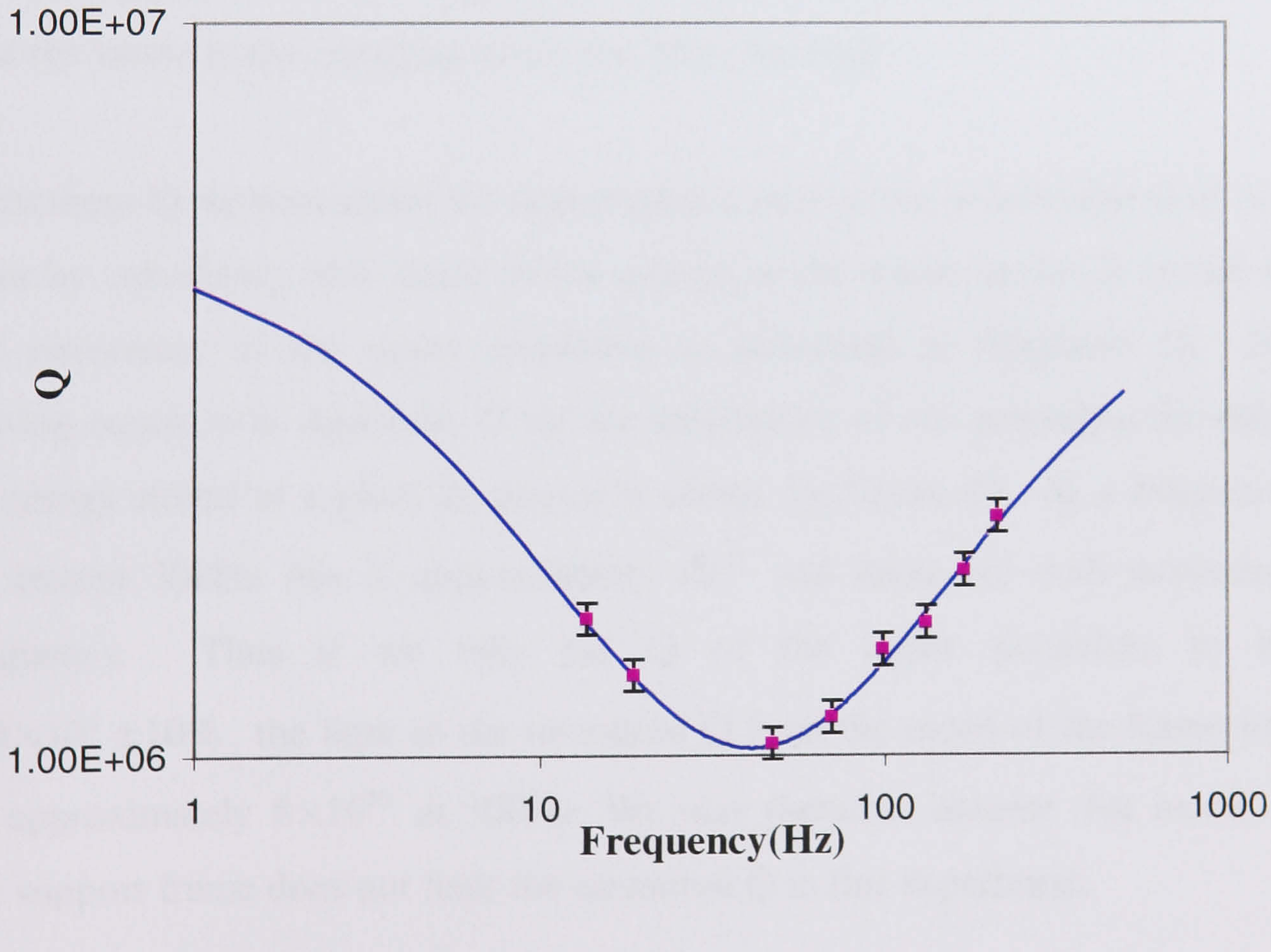

Figure 42: Cantilever bending modes of suspension 1. Line shows fit of thermoelastic and structural loss to data using Equation 67 with values given in caption of Figure 38 but using a dilution factor of D=1 as no lower mass was used. The parameters allowed to vary in fit were the fibre thickness and the Young's modulus. The fitted values were $t=1.7\times10^{-4}\,\mathrm{m}$, $E=5.2\times10^{10}\,\mathrm{Nm}^{-1}$ and $\phi_0=1.9\times10^{-7}$ with an error of 1% in the fit.

5.8. Measurement of Upper Suspension Stage

In order to have some measure of the effects of the isolation of the fibre a measurement was made of the Q of two modes of the upper suspension. With the lower part of the suspension removed, the shadow sensor was relocated to the isolation mass. A flat electrostatic drive plate was produced to fit under the mass and excite the tilting mode, while the pendulum mode was easily excited seismically by pushing on the outside of the vacuum tank. These two modes will give information on the combined loss effects of recoil of the frame and loss in the clamp.

The pendulum mode, with a frequency of 1.2Hz was found to have a Q of $7.8\times10^5 \pm 10\%$. The tilting mode, at 4.68Hz was found to have a Q of$1.9\times10^6 \pm 10\%$. Both values are significantly lower than those calculated for the support structure using FEA. The most likely explanation for this is that the losses in the clamping of the top plate are high.

With these Q measurements we may predict a limit to the measurable Q of our fibre by calculating how much of the energy in the violin modes is stored in the movement of the upper pendulum as described in Appendix D. By solving equation in Appendix D for the dimensions of our pendulum the ratio of energy stored at a given frequency is shown by Figure 43. At a frequency of around 300Hz this is approximately 10^{-5} and decreases with increasing frequency. Thus if we take the Q of the upper pendulum to be $7.8\times10^5 \pm 10\%$, the limit to the measured Q from the recoil of the frame will be approximately 8×10^{10} at 300Hz. We may therefore assume that recoil of the support frame does not limit the measured Q in this experiment.

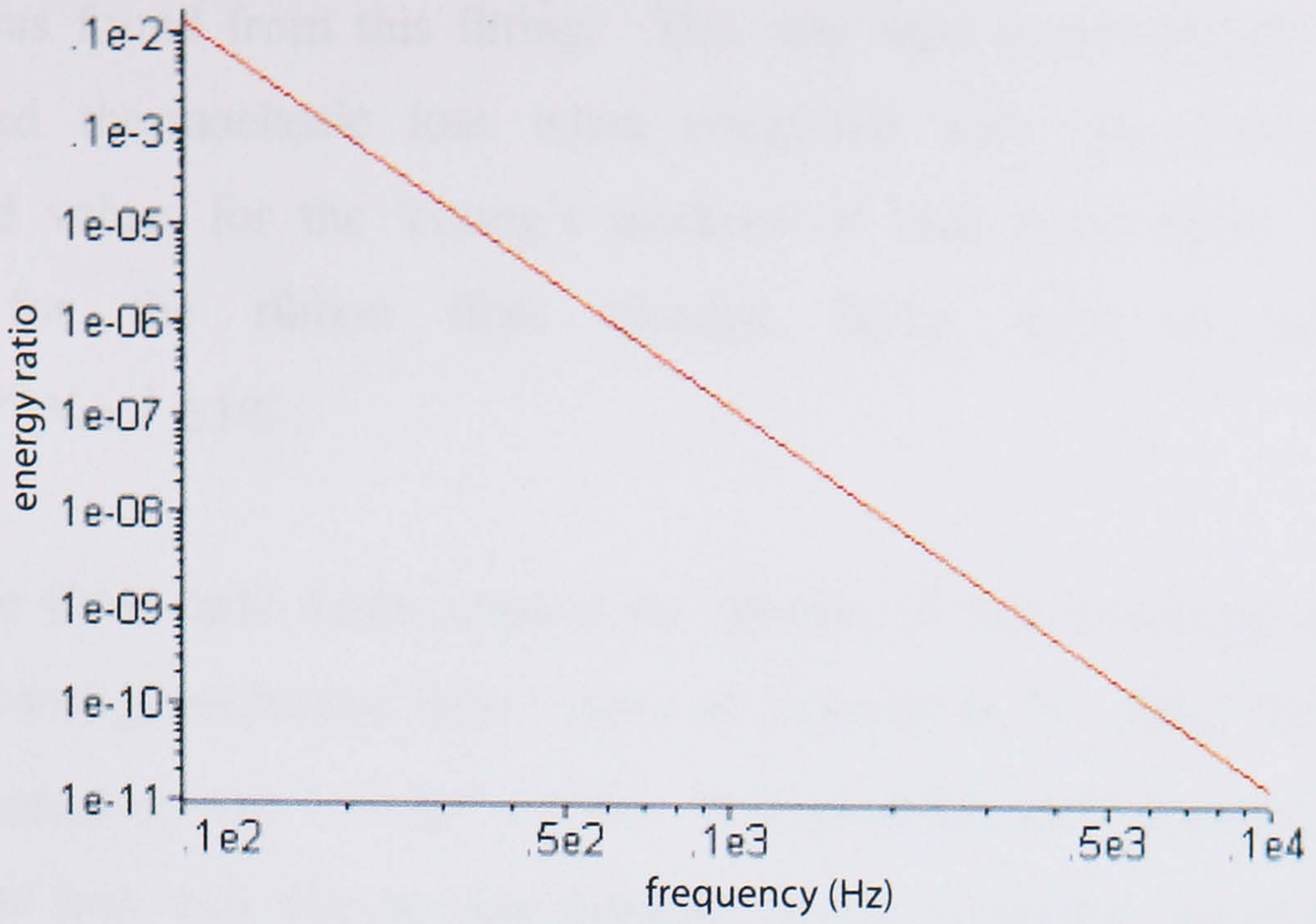

Figure 43: Ratio of energy stored in upper pendulum to energy stored in first violin mode as a function of frequency.

Other sources of loss, such as bad welding at the fibre suspension point may explain the low Q of the violin modes, compared to the theoretical predictions, as the tension in the violin fibre shortens the bending length of the fibre and concentrates more energy near the welds. This region will also differ from the rest of the fibre in both shape and stress, due to welding. The welding process can also be seen to leave a surface finish, which is not completely transparent but has some opacity that may be the result of deposition of vaporised silica on the surface of the fibre. Further investigation is needed in order to finally confirm whether or not a suspension may be constructed which achieves experimentally the theoretical dilution factor.

5.9. Conclusions

Monolithic fused silica suspensions were constructed using ribbon fibres with rectangular cross sections. Measurements were made of both the cantilever bending modes of fibres constrained at one end only, and the violin modes of fibres under tension. From these the material loss of the fibres was found to be $1.9\times10^{-7}\pm1\%$ and $1.8\times10^{-7}\pm1\%$, by fitting a model of thermoelastic and structural damping to the data. Interestingly a modified Young's modulus

value was found from this fitting. This was seen experimentally through a decreased thermoelastic loss when compared with that calculated using accepted values for the Young's modulus of bulk fused silica. The value found for the ribbon fibre through fitting was, as an average. $5.2\times10^{10}\,Nm^{-2}\pm1\%$.

With the fibres held under tension the dilution of loss as energy is stored in the loss-less gravitational field causes an increase in Q. Here the highest Q value measured was $1.5\times10^{8}\pm10\%$. It is plausible that, for the first mode, the main loss was due to gas damping in the imperfect vacuum. Higher frequency modes also did not achieve the calculated levels of dilution of loss despite the effects of gas damping being inversely proportional to frequency and hence becoming insignificant from around the fourth mode onwards. As this cannot be due to loss of energy through recoil of the frame, or damping due to collisions with residual gas molecules, the most likely explanation may be due to the bending energy being concentrated in a region of the fibre that has increased losses due to the welding process.

Chapter 6

Measurement of Pendulum Mode Loss

6.1. Introduction

In this chapter the loss associated with the pendulum mode of a monolithic fused silica pendulum is investigated. It is of interest to measure the losses of different modes of a pendulum as a function of the frequency of the mode and to observe how the loss mechanisms vary greatly. The resonant frequency of the pendulum measured here is significantly lower than those measured in the violin mode experiment at around 0.76Hz.

Unlike the measurement of violin mode quality factors we expect here that the loss measured may be heavily dependant on the stiffness of the support frame as discussed in Sections 6.2 and 6.3.5 of this chapter. The pendulum will also be more sensitive to seismic motion, which is also larger at lower frequencies. The loss associated with residual gas damping will however not present a

significant effect due to the large moving mass of the pendulum compared to the small mass of the fibre of a violin mode.

6.2. Experiment

The experimental set-up is shown in Figure 44. The main features of this design are to reduce recoil of the support structure by creating as rigid a base as possible within the lab space.

In order to investigate the effects of dilution and recoil in this experiment the Qs of two pendulums were measured, where both used the same fibre and upper plate but differed in lower mass. To insure that the effects of the welds were identical, the mass was changed by separating the small pin at the end of the fibre from that which was ground into the mass, a point at which losses will be negligible. We may then calculate the dilution factor of the 43.5g mass to be 137.7 and for the 445g mass to be 440, with the dilution being proportional to $\sqrt{T}$ as shown in equation 45. However we may expect an opposing effect on the Q due to the increased recoil of the support when a larger mass is swung. The effect of this will be proportional to $m\omega^2$ as can be seen from our discussion of recoil damping in Appendix D, and hence by using two masses it should be possible to examine what loss may be attributed to recoil and thereby find the value for the material loss as discussed in Section 6.3.5. The dilution factor is given by Equation 45, which is repeated below.

$$D = \frac{2l\sqrt{T}}{\sqrt{EI}}$$

The first component of the suspension support to be put in place was the concrete base. Figure 45 shows the design of a steel frame that was inserted into a hole in the concrete floor in the sub-basement of the building. The design of this is such that it forms a root like structure to key into the concrete while also giving horizontal mounting threads for the tank to give a high

stiffness horizontally. A steel bar running across in one direction also gives a high degree of stiffness in the direction in which the pendulum was swung. This structure was then filled with concrete, leaving two circular insets with threaded attachment points into one of which the vacuum tank was inserted. The second, larger, inset was designed for use with a bigger vacuum tank than was used for this experiment. The concrete base formed measured 1.8m by 1.8m by 1.4m. The tank was then secured to the base using v-shaped blocks of steel, which were tightened against its sides.

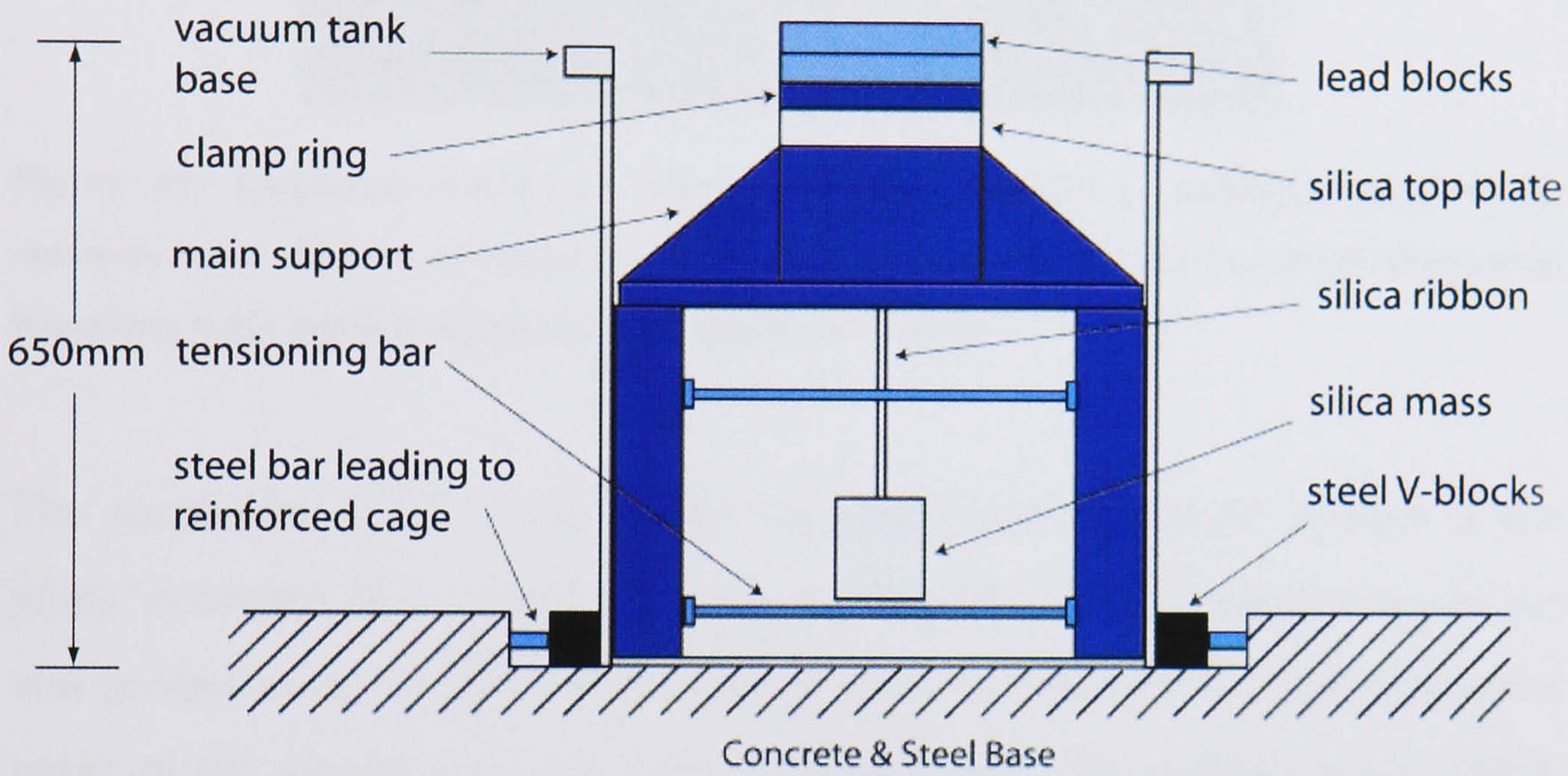

Figure 44: Schematic of pendulum mode measurement suspension and support frame. The stiffness of the support is increased by attaching the vacuum tank to a stiffened concrete and steel base.

The support structure internal to the vacuum tank was then assembled. This consisted of four aluminium legs of diameter 50mm surmounted by an aluminium top plate of thickness 16mm. On top of this a box shaped structure with reinforcing buttresses was mounted. This was designed again with recoil losses in mind as we wish to keep the lateral stiffness of the suspension point as high as possible. The aluminium legs were held firmly against the sides of the tank using threaded steel rods.

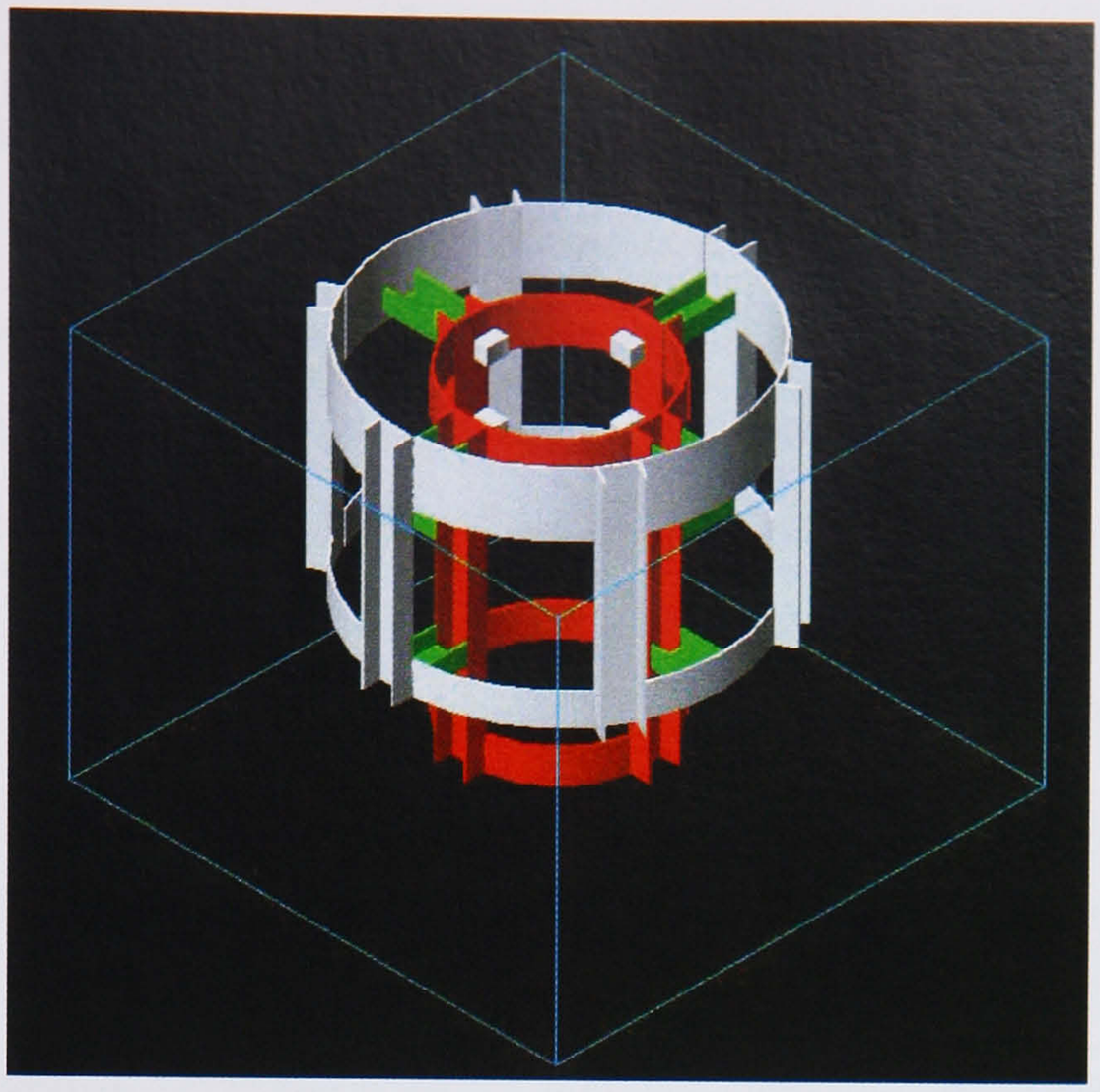

Figure 45: Rendered AutoCAD diagram of the reinforcing structure used in the concrete base. This was designed to key in well to the concrete and to provide horizontal mounting bolts against which the tank could be braced.

The suspension itself, a monolithic silica structure to reduce friction at the joints, consisted of a circular top plate into which a 3mm diameter circular pin was ground using the same process as described in chapter 9. The attachment point on the masses was also made in this manner. Two masses were chosen such that they would differ by approximately one order of magnitude. These weighed 445g and 43.5g and were a low quality HOQ graded silica. The lowest frequency internal mode of the small mass was calculated to be 26.7kHz using finite element analysis and so we may assume that little of the pendulum modes' energy will couple into the mass. Because of this it was acceptable to use lower quality silica for the masses, as these will contribute only a fraction of the damping. A rectangular fibre of cross section 1.12 ± 0.02 mm by 0.12 ± 0.02 mm and of length 40.5 ± 0.3 cm produced using the automated process described in chapter 4, was then welded to two small silica pins. The silica pins were prepared from 3mm diameter Suprasil 3 stock cut to a length of 5mm onto which one flat side was ground in order to allow the rectangular fibre to be welded without deformation. This welded area was then heated again with a hydrogen-oxygen flame until glowing red-hot in order to anneal the area. Although this will not have removed the

thermal stress from the suspension altogether, it will have annealed the area of the weld where the mechanical stress will be high in a similar way to that seen in chapter 9. These thicker pins attached to the fibre were then welded onto the pins ground into the top plate and mass. The completed suspension was then transferred to the vacuum tank by holding the top plate and lowering into the support structure from above. The top plate was then fixed in place by a steel ring that was bolted down to the support structure. Finally, to reduce the risk of losses from the glass vibrating against the metal clamping ring, lead blocks were piled on top of the clamp to force the metal down against the glass. A combination of two vacuum pumps was used for the vacuum system so that the fast pump down time of a turbo pump could be achieved while also having the vibration free pumping of the ion pump to use while taking data. With this system a vacuum of 1×10^{-7} torr was reached when performing measurements. The limit to the Q due to residual gas damping can then be calculated to be 3.2×10^{10} and is hence negligible for this experiment. An approximation is made in this calculation that the area of the mass used to calculate damping effects is the projected area of the diameter times the height. This does not take into account how momentum transfer between gas molecules and a spherical surface alters the damping. A similar issue arises when calculating the gas-damping limit for round fibres.

The vacuum tank used had view ports allowing a direct line of sight to the pendulum. This therefore meant that readout of the amplitude of the pendulum could be made without the need to install it within the tank. It was decided that a video based monitoring system would give some significant advantages over other measurement schemes would not drift over time and could be easily calibrated as described below. A CCTV camera was used to observe the moving ribbon fibre with the output signal being fed to an image acquisition card in a PC. A programme written using 'NI Vision' software was used to process the images. The suspension was then backlit through the back viewport in order to give a high contrast between the fibre and its background.

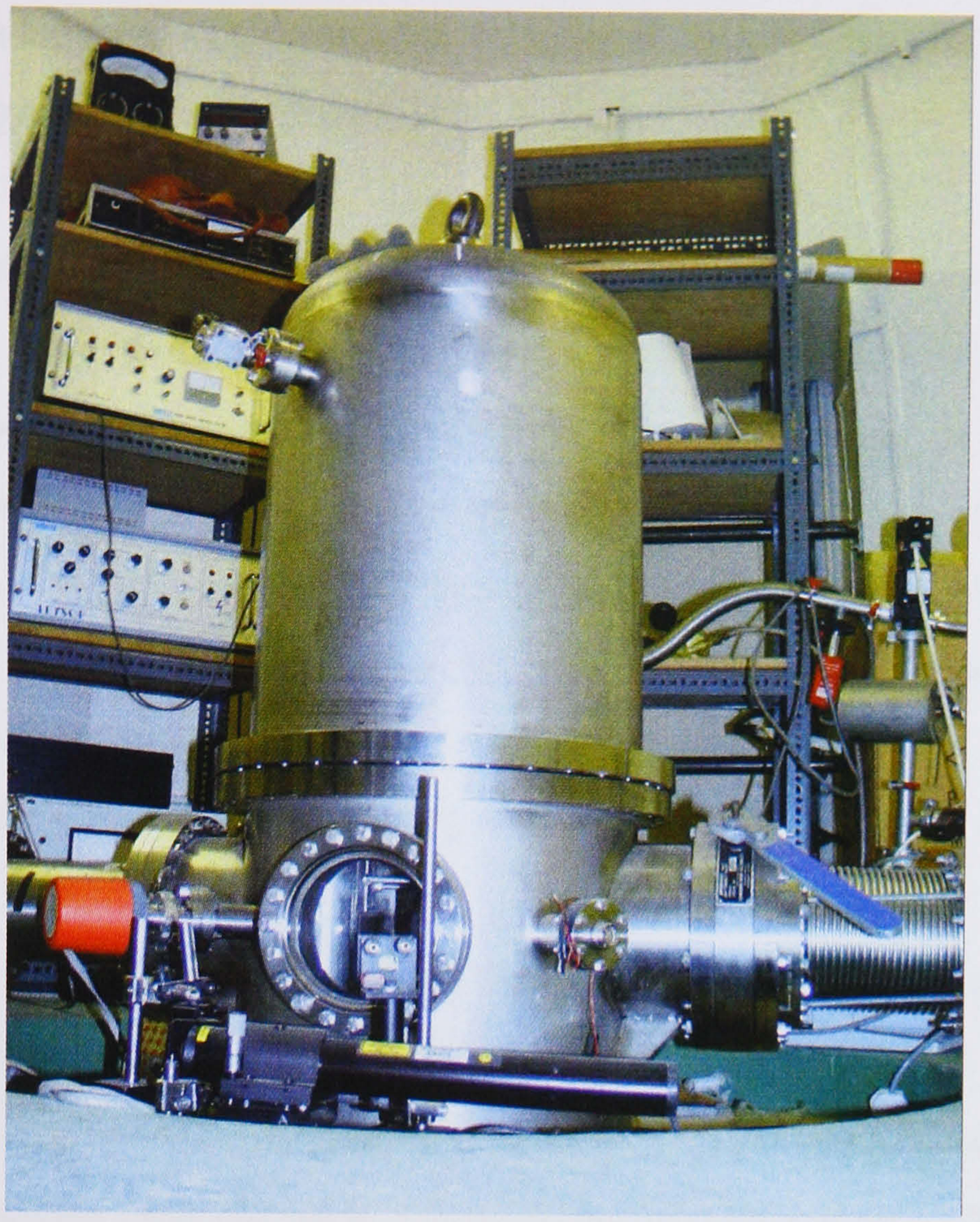

Figure 46: The vacuum tank shown above is installed on the inner circle of the reinforced concrete base using steel V-blocks which are tightened against it. The CCTV camera is not yet in place here, but was later installed in front of the view port. The right port is connected to a turbo pump while on the left side is an ion pump.

The refresh rate of the camera sets the data acquisition rate of 25Hz. Any drift in this refresh rate would give a timing error, which could give an incorrect loss measurement. However it was established that the camera uses a crystal oscillator to time its refresh rate and to confirm that no drift occurred the frequency of the pendulum mode was checked at regular intervals for any change that a timing error would give.

The spatial calibration of the camera, done by taking an image of a marked ruler placed at the same distance as the fibre from the camera, and counting the pixels taken up by each millimetre of space, showed that the camera was linear in the region of the image field used for the measurement. With the pendulum swinging across approximately 80 pixels at a frequency of 0.76Hz

and using an acquisition rate of 25Hz the resolution of the camera will be more than adequate. This can also be seen in the graphs of the ringdowns where no digitisation noise is seen.

For each image acquired, the analysis programme performs a set of tasks to identify the fibre from its background in the image. This then gives its horizontal position in terms of pixels with the output being written to file. The data are separated into sequentially numbered sections to allow it to be more easily managed and is time and date stamped. Using a MATLAB script it was then possible to perform an FFT on sections of the data to find the modes of the pendulum. These were then summed and plotted sequentially then fitted using an exponential decay.

Motion of the pendulum was induced by a mechanical actuator consisting of a sprung metal bar and an electric motor with an Archimedes spiral shaped cam as shown in Figure 47. The bar was adjustable such that it could be set to different positions from the mass, allowing the excitation level to be set. With the motor connected through a vacuum feedthrough it was then possible to mechanically excite the pendulum while under vacuum with a force difficult to achieve using an electrostatic drive.

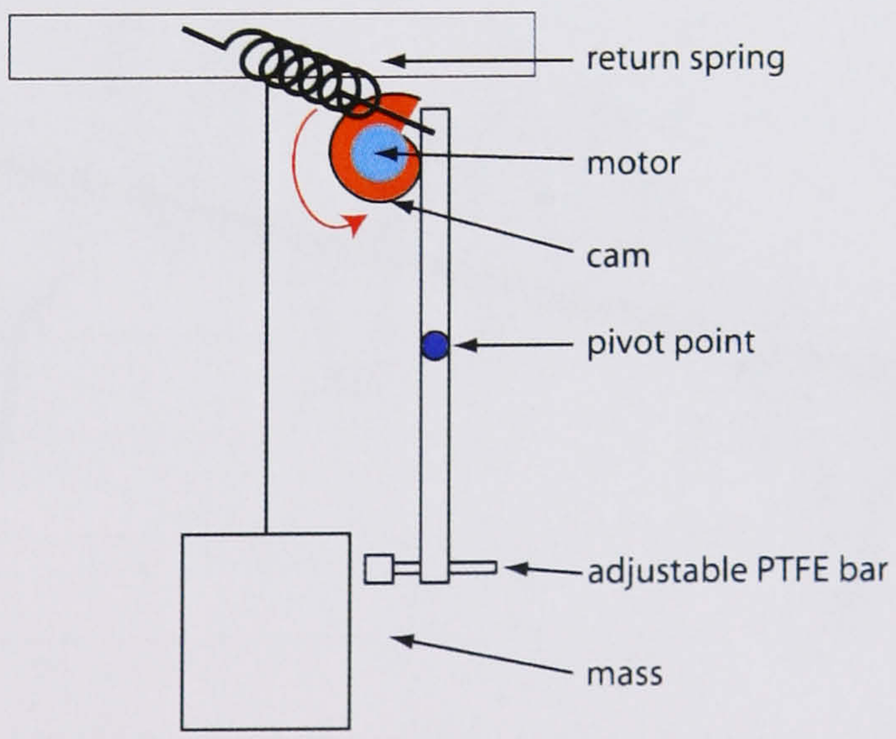

Figure 47: Schematic diagram of the pendulum mode actuator, based on a sprung lever and Archimedes spiral shaped cam, which was used to give a large, predetermined amplitude of swing to the pendulum.

A measurement to exclude the effects of the ground state motion of the pendulum due to seismic excitation was also made in order that we could be sure that our measurements were being made at amplitudes significantly above this level. This was done by opening the tank to air to damp the motion of the pendulum and then pumping down again to vacuum. When pumping out the air a small but measurable motion was induced in the pendulum as the air moved past, causing a displacement of the fibre measured to be approximately four pixels, this being 5% of the amplitude used in the measurements of Q. The motion was then monitored for a period of five days, during which time the amplitude decayed with a Q near identical to that found when measuring the Q using a larger amplitude. This can be see in Figure 48 below. We may infer from this that the ground state to which the pendulum will ringdown has an amplitude lower than this and thus shall not significantly affect our measured Q. In Figure 48 it can be seen that the amplitude recorded deviates from the fitted line, which for this fit gives an error of $\pm 19\%$. Even at this low amplitude we see no sign that the pendulum is being driven up.

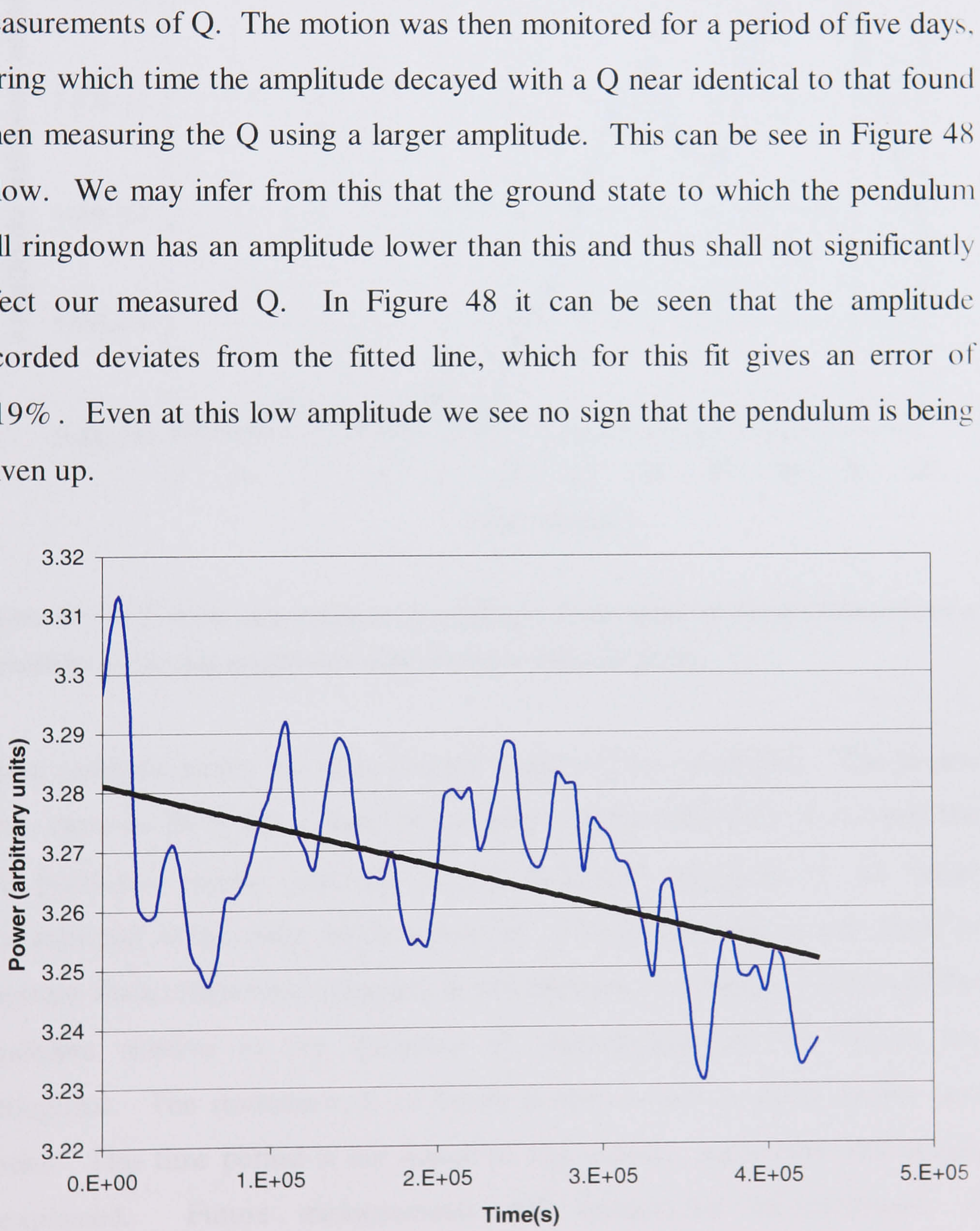

Figure 48: Measurement of motion of pendulum without initial excitation.

The excursions have a periodicity which was found, by performing an FFT on the recorded amplitude data, to have two main resonant peaks, one with a time period of 24.3 ± 0.7 hours and one with a time period of 22.0 ± 0.6 hours. Other smaller peaks were also seen.

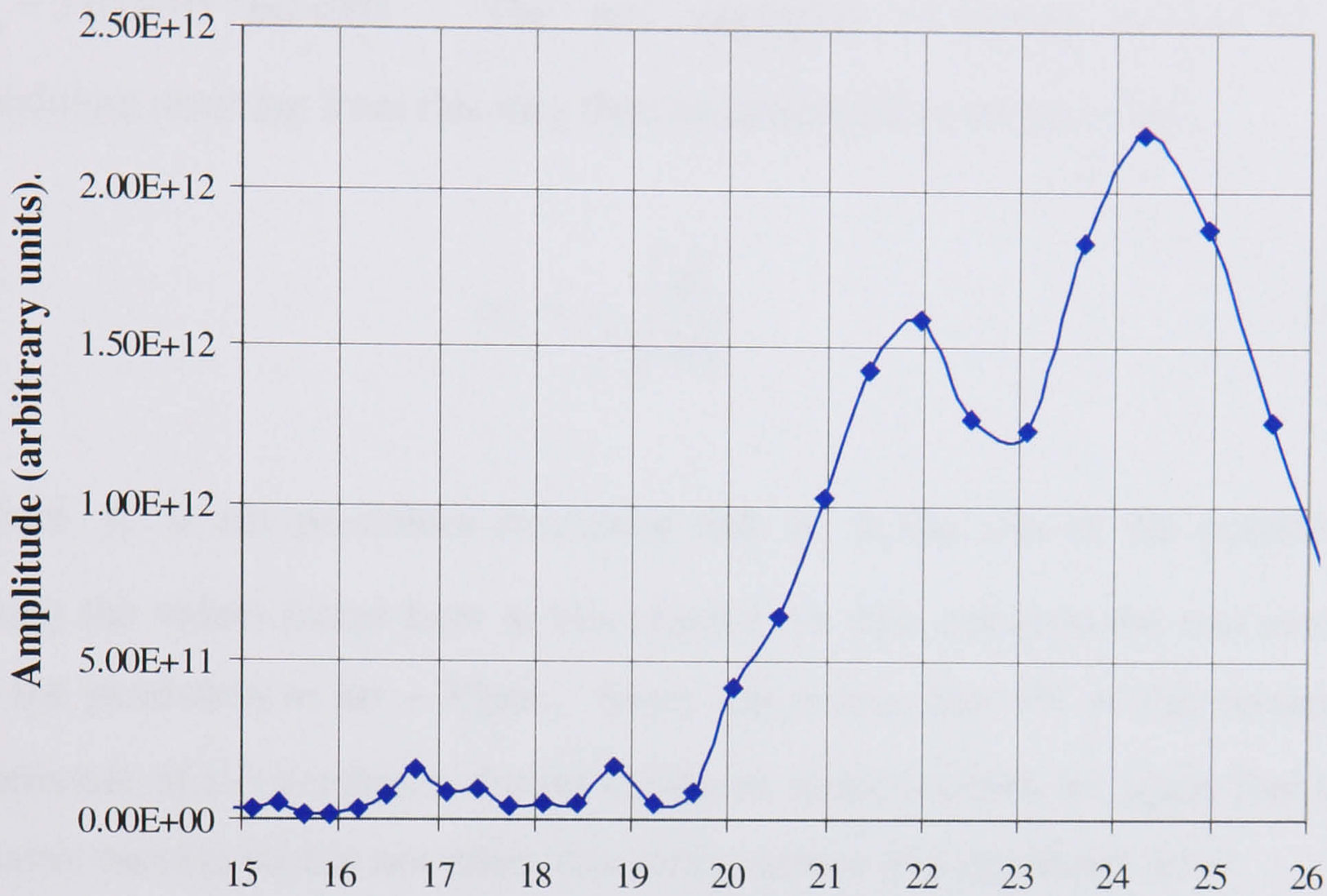

Figure 49: FFT of the measurement of amplitude of one mode of the pendulum shows a periodicity to varying amplitudes with two main resonant peaks.

These resonant peaks are seen in both modes of the pendulum. The largest peak, close to 24 hours, is seen to act with a phase difference of π upon the two pendulum modes, and thus as the measured amplitude of one mode increases that of the other mode decreases. This relationship is very likely to originate from temperature changes in the laboratory causing a rotation of the pendulum relative to the direction of measurement as the modes are orthogonal. The resonance at 22 hours is seen to act in phase on the two modes. This time period is not linked to any obvious mechanism and stands unexplained. Future measurements will incorporate measurements of temperature and ground tilt in order to identify the source of this periodicity.

While taking measurements of Q, the motion of the ground beside the tank in the horizontal direction was measured using a seismometer. This was done in order to ensure that the coupling of ground motion into pendulum motion was small enough to be considered negligible. At a frequency of 1Hz the amplitude spectral density of seismic motion was found to be $x_g = 2.61\times10^{-9} m/\sqrt{\text{Hz}}$. The rms amplitude of driven motion in the pendulum resulting from this may then be calculated as follows [72]:

$$x_p = x_g\sqrt{\frac{\pi f_0}{2\phi_p}} \tag{69}$$

where f_0 is the pendulum frequency and ϕ_p is the loss of the pendulum. Using the values found later in this chapter we then calculate the rms motion of the pendulum to be $\sim 35\mu\text{m}$. Since this is less than 1% of the maximum amplitude of the pendulum during ringdown measurements we again find that seismic motion should not affect this measurement at a significant level.

A third measurement made while taking data for the Q measurement was to look for charging of the mass. This was done using a wire internal to the tank and close to the moving fibre, which was then connected through an amplifier to a data acquisition system. Any charge on the mass would clearly show at the same frequency as that of the pendulum. The effect of charging on the mass may be to give another form of dissipation, with the charged pendulum producing a current in close by objects as it swings back and forth. This feature of the experiment was only implemented after an initial measurement of Q showed signs of possible charging of the mass, with the ringdown being separated into an initially high Q then changing to a lower Q over a short period of time. Although some charging of the mass was subsequently seen, the effect seen in this measurement, as discussed in the next section, is more likely to be attributable to energy coupling between modes due to a high amplitude as discussed below.

6.3. Results

6.3.1. Measurement Using 445g Mass and a High Amplitude

The first measurement made was using the larger, 445g, mass. The mechanical actuator was used to give an amplitude of around 5cm in the direction which the fibre was thinnest. However after a short period of time the motion of the fibre showed that in fact there were two modes with frequencies 0.7636Hz and 0.7691Hz which produced a beat period of 181.8s, which may be seen in Figure 50. The pendulum, during the course of one complete beat period, would move between a state where all motion was in the direction the pendulum was originally swung to a state where it moved in an elliptical motion and then back again.

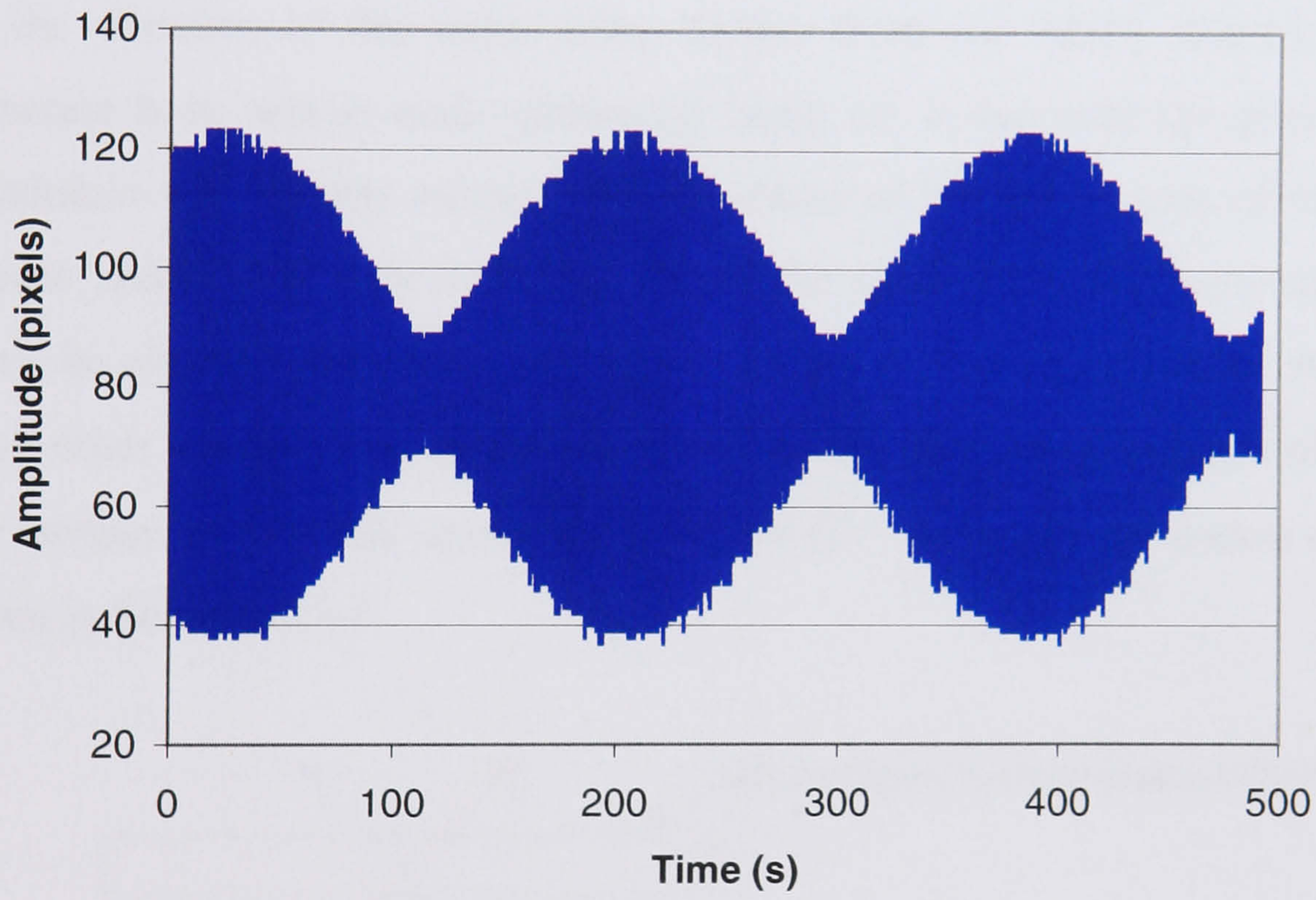

Figure 50: Section of data before analysis shows clearly the beat between the two modes. The minimum amplitude is non-zero as the pendulum was not swung exactly at 90° to the direction of measurement. The shape of motion is described below.

The ringdown of the sum of power in the two modes of the pendulum was seen, as mentioned previously, to have a higher Q to start with however when looking at the first mode over this period it was found that the amplitude actually increased, and as the alignment of this mode relative to the camera

made its measurement more sensitive than that of the other mode the overall effect was that this appeared as an increased Q. It is thought that this behaviour was caused by energy coupling from the second mode due to a high amplitude being used. After an initial period where energy moved into this mode it then began to decay, with this point corresponding to the change in Q of the summed energy. From this point on the two modes decayed with separate Q values, indicating that they were orthogonal and not strongly coupled below a certain threshold amplitude. The mode whose motion was most sensitively detected was found to have a Q of $9.6\times10^{7} \pm 26\%$ from this ringdown and a frequency of 0.7636Hz. The error quoted is from the fit of the exponential curve to ringdown. It is relatively high for this particular fit as a short period of data has been used to calculate the time constant. The Q of the 0.7691Hz mode was found to be $5.3\times10^{7} \pm 25\%$. This lower Q may be due to the direction of this mode being further from the stiffest direction of the concrete base, whose main reinforcing beam ran in line with the direction the pendulum was initially swung. The closeness of the frequencies of these two modes shows that they must experience the same dilution effects and hence must be almost symmetric. In order for these to still be orientated at 90° to each other the direction of the individual modes must be at an angle of 45° to the surface of the fibre as shown in Figure 51. A further discussion of this is given in Section 6.3.4.

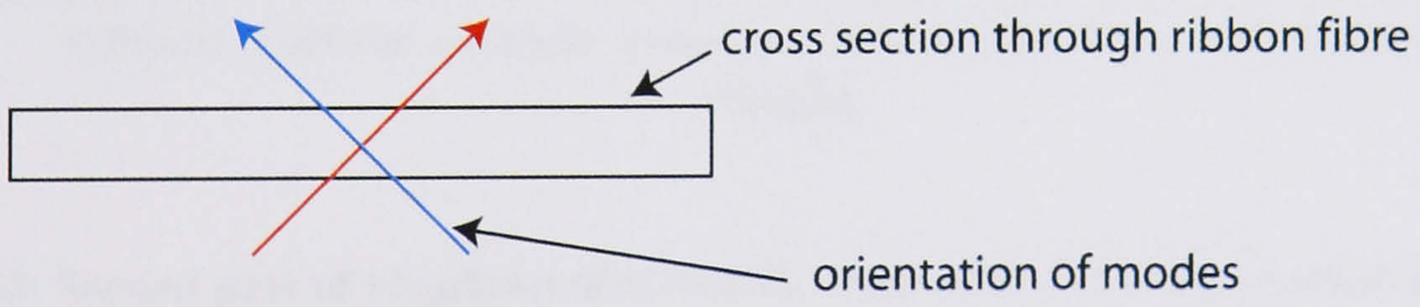

Figure 51: Orientation of the two modes of oscillation, with respect to the ribbon fibre. Modes must be at right angles to each other as they are not coupled below a threshold amplitude. The close frequency of the modes means that the restoring forces must be almost identical and hence they are orientated as shown above.

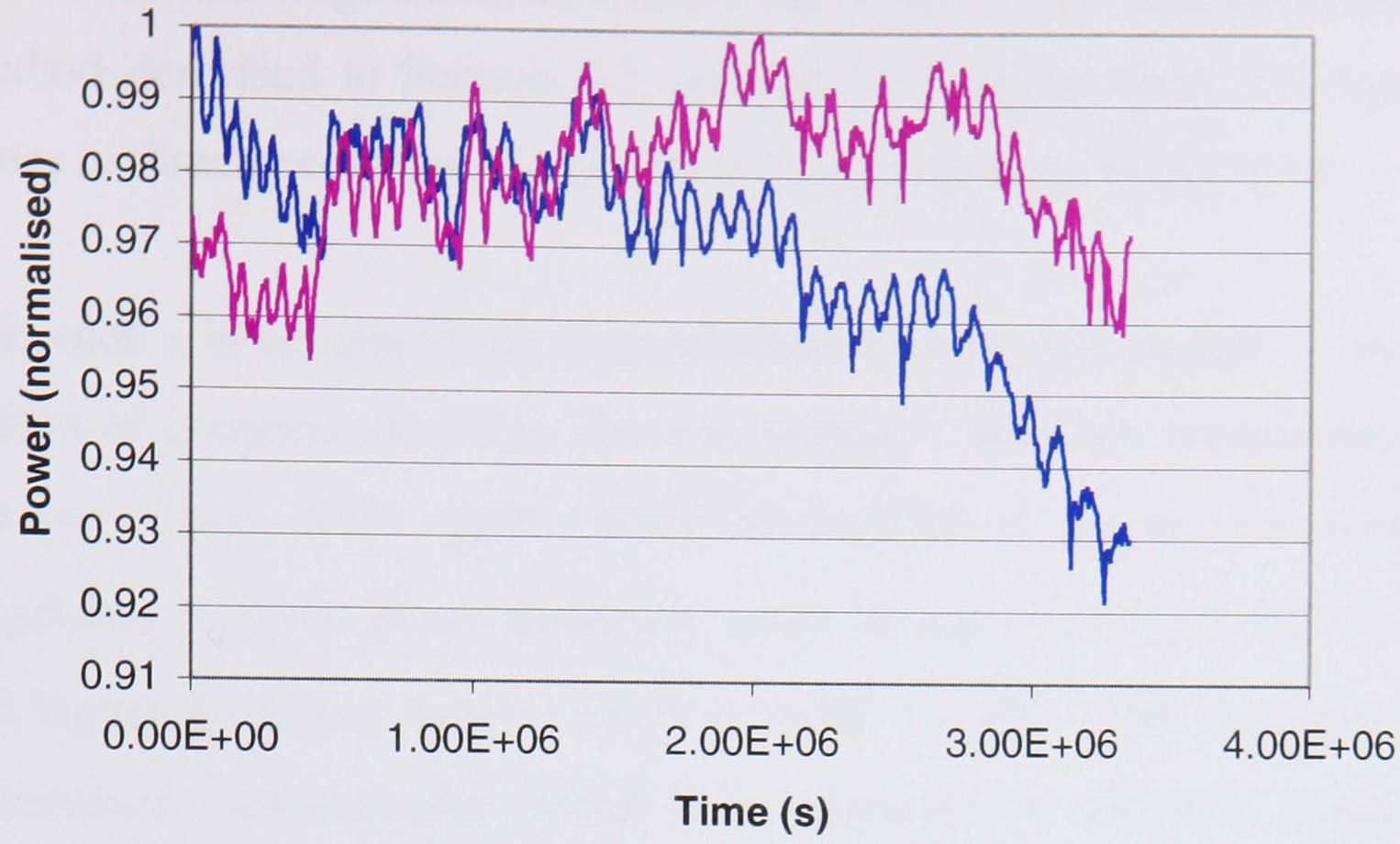

Figure 52: Ringdown of pendulum using 445g mass and high amplitude (around 5cm displacement). Blue line shows sum of power in the modes. Pink line shows 0.7636Hz mode.

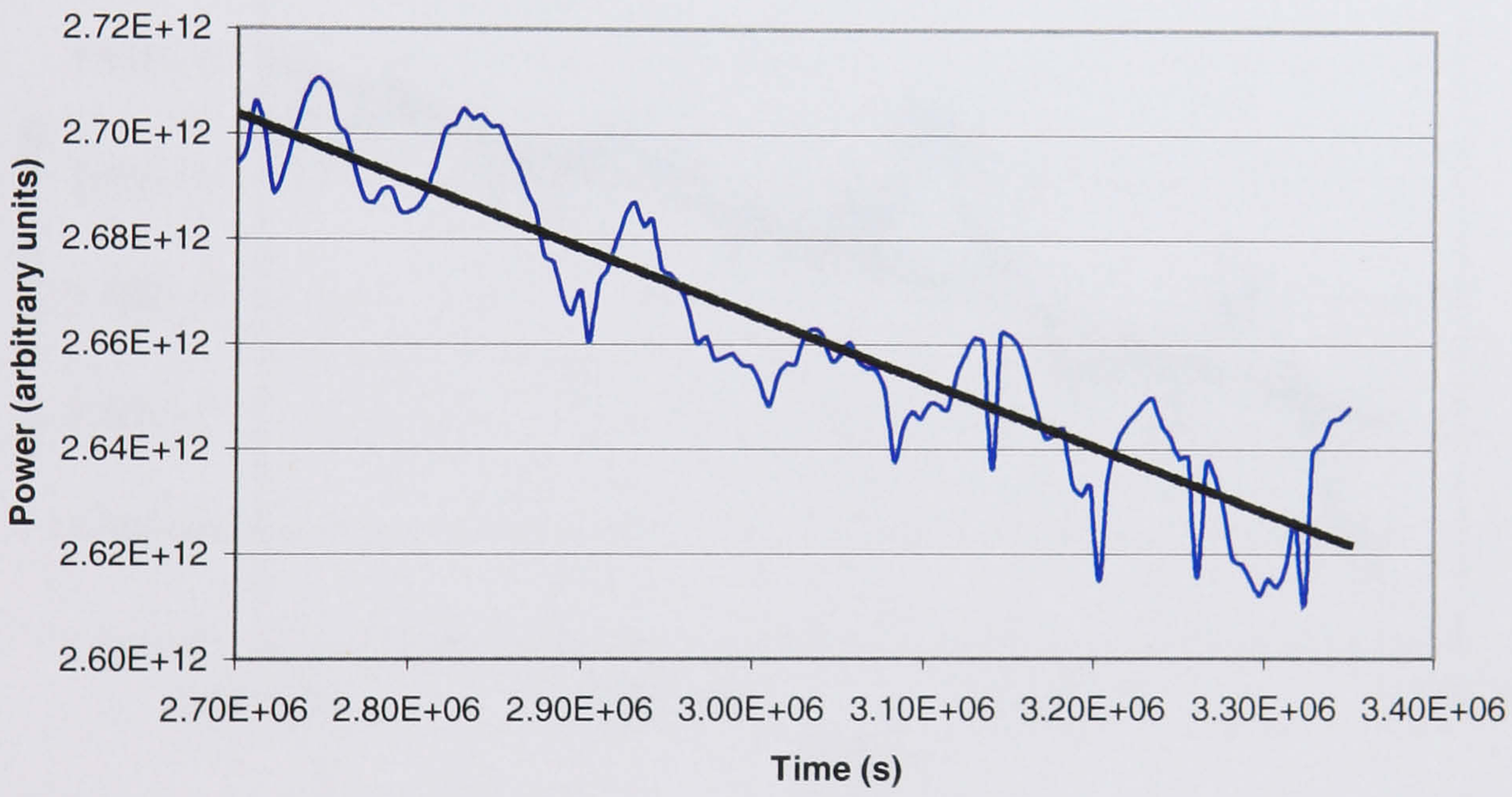

Figure 53: Second part of ringdown of 0.7636Hz mode with fitted exponential decay. A Q of 9.6×10^{7} was found from the fit. The error in the fit was ±26%

6.3.2. Measurement Using 445g Mass and Lower Amplitude

In the measurement made at high amplitude the change in Q, which occurs very rapidly, was also thought to be possibly due to charging of the mass which may give another form of energy dissipation as described in Section 6.2

above. At this stage therefore monitoring of the charge was started, using the method described in Section 6.2, and the first measurement was repeated in order to directly compare the Q with the level of charge on the mass.

This time a lower amplitude of approximately 5mm was chosen, to reduce the effects of coupling of energy between modes. With this measurement while the two modes were again evident no transfer of energy was seen in the ringdown, with the lower frequency mode having a Q of $1.3\times10^{8}\pm5.1\%$ and the higher frequency mode a Q of $4.0\times10^{7}\pm1.3\%$. The variation between subsequent measurements, which were performed at different amplitudes, is approximately 25% which is consistent with the error in the fitting used to find the time constant of the decay. This error is predominantly due to the excursions of amplitude due to periodic effects discussed in section 6.2.

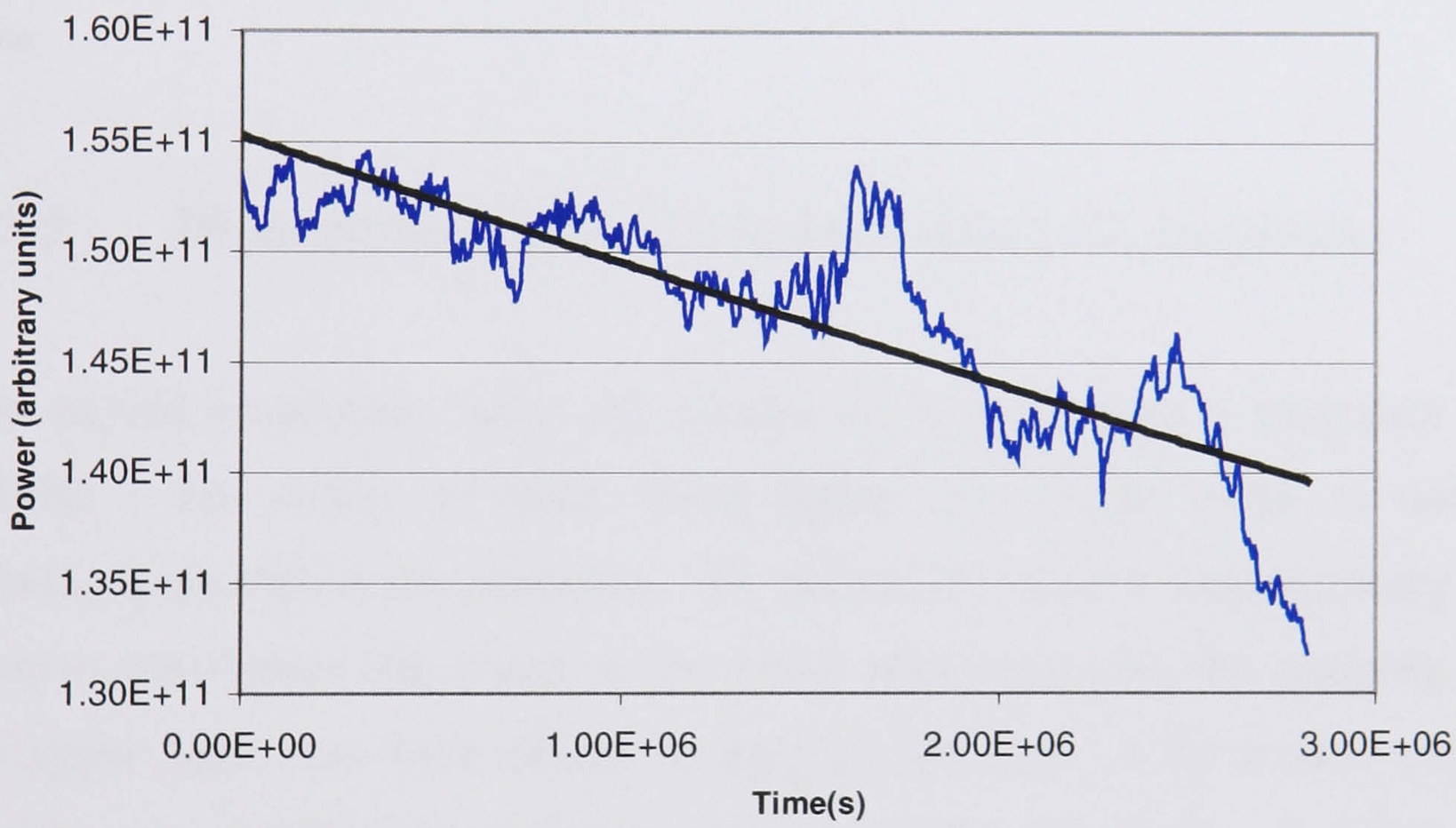

Figure 54: Ringdown of 0.7636Hz mode using lower amplitude (approximately 5mm displacement). Line shown is fit of exponential giving a Q of $1.3\times10^{8}\pm5.1\%$. The error quoted is that calculated for the fit of an exponential line to the data.

Measurement of the charge showed it to increase rapidly during pumping down of the vacuum system and then steadily over the course of the ringdown although without any large steps as described by V.Mitrofanov [73]. As there is no obvious correlation between the increasing charge and the measured Q

we assume that the level of charge on the mass was not sufficient to cause a significant source of damping.

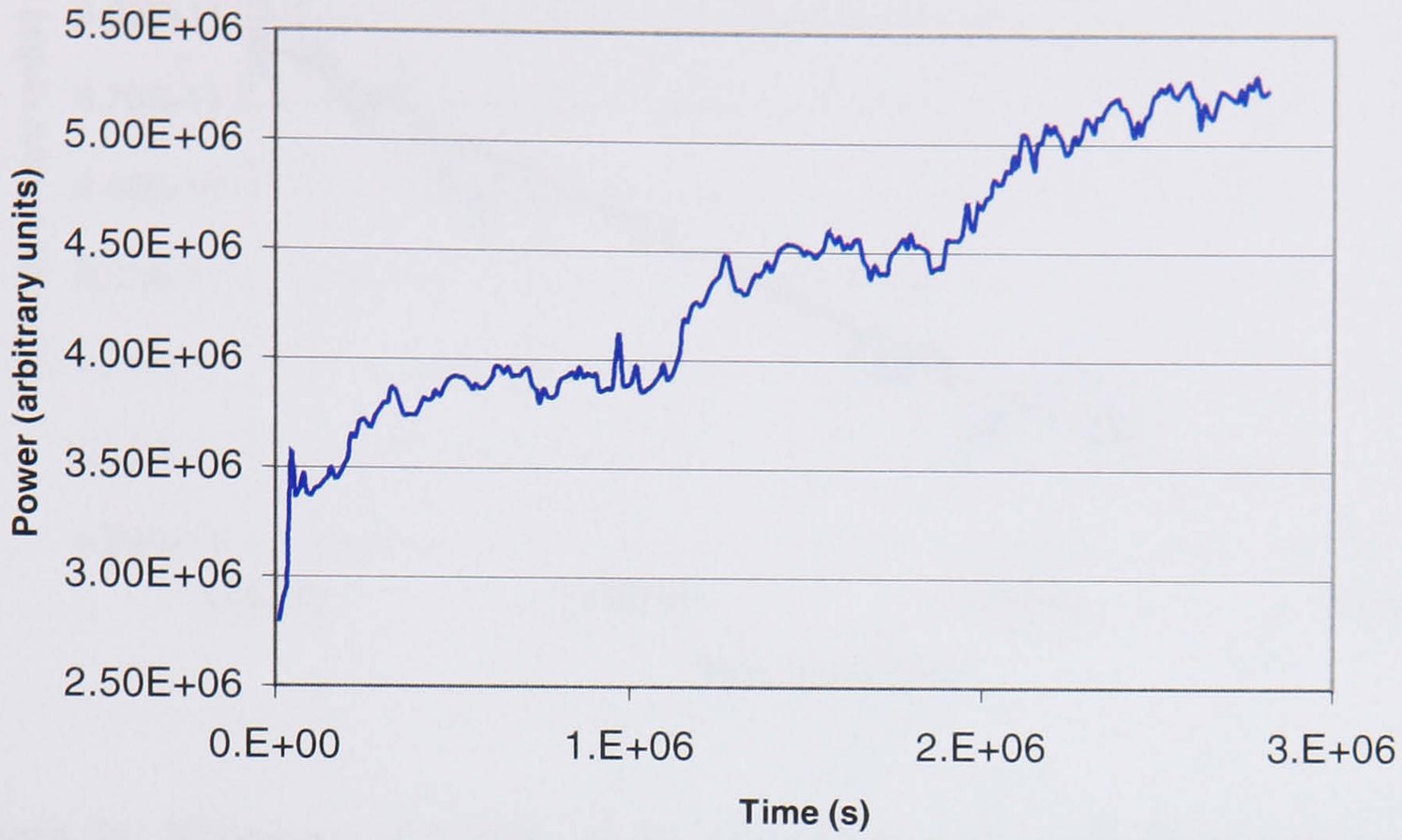

Figure 55: Measurement of charge on mass from lower amplitude ringdown of 445g mass

6.3.3. Measurement Using 43.5g Mass and Low Amplitude

The second suspension, using the smaller 43.5g mass gave a frequency of 1.18Hz. The centre of mass, being higher due to the shape of mass, effectively shortened the pendulum. To change the mass it was necessary to remove and replace the clamp so the losses associated with the clamping of the upper mass may have altered as may the direction of the modes which may be aligned differently with respect to the stiffened direction. A failure of the data acquisition computer meant that data were not taken continuously throughout the measurement; however, the data acquisition was restarted to give the ringdown shown in Figure 56 from which the Q could be found. The Q measured for the lower frequency mode was $1.4\times10^{8}\pm9.9\%$ while that of the higher frequency mode was found to be $6.3\times10^{7}\pm2.1\%$.

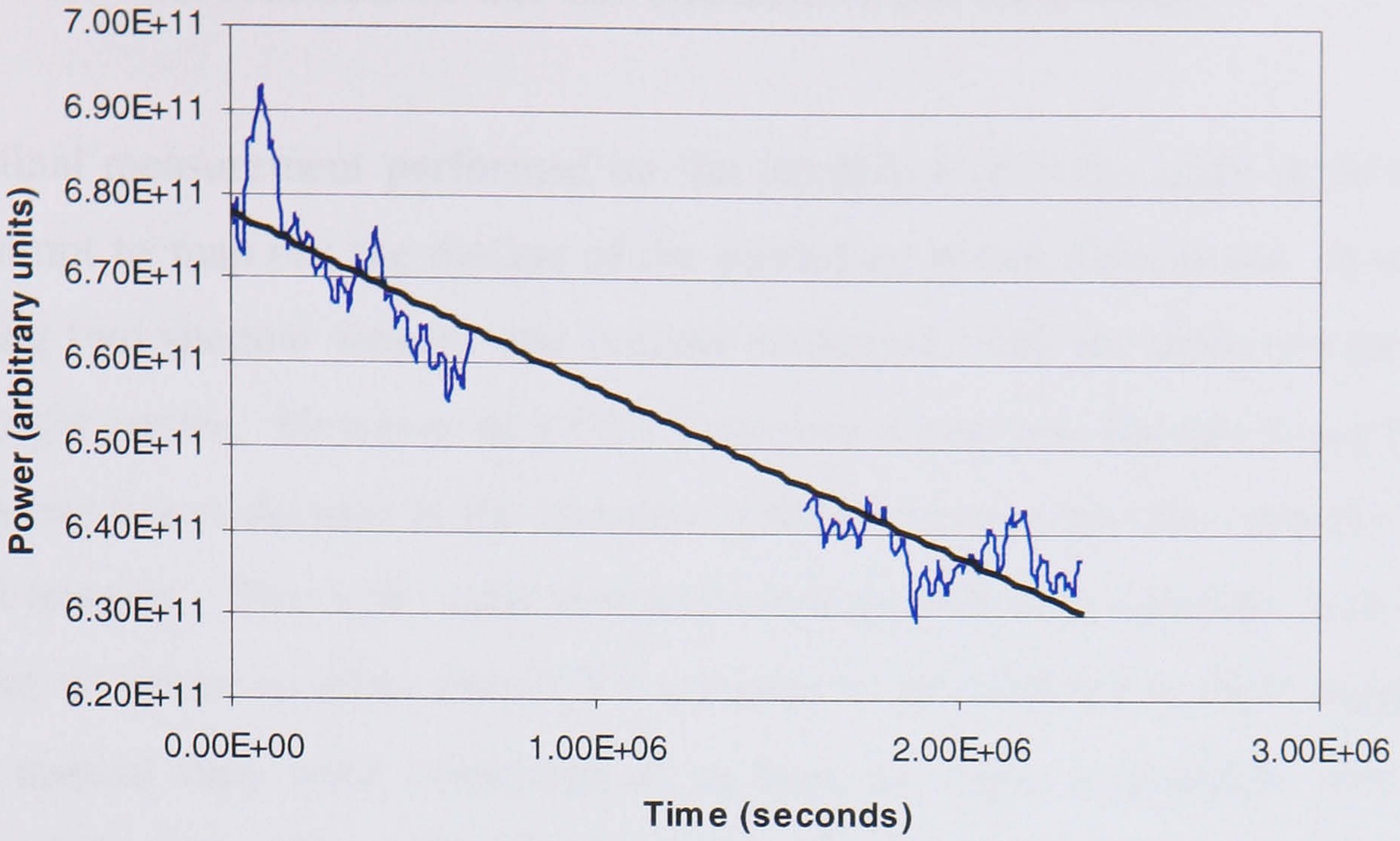

Figure 56: Ringdown of 1.18Hz mode using 43.5g mass with fitted exponential decay curve. A Q value of 1.4×10^{8} was found from the fit with an error of $\pm 9.9\%$.

Again the charge was monitored and, as shown in Figure 57, we can see that there is a smaller variation in charge levels although the mean is close to that seen previously and as such should not significantly affect the loss measured.

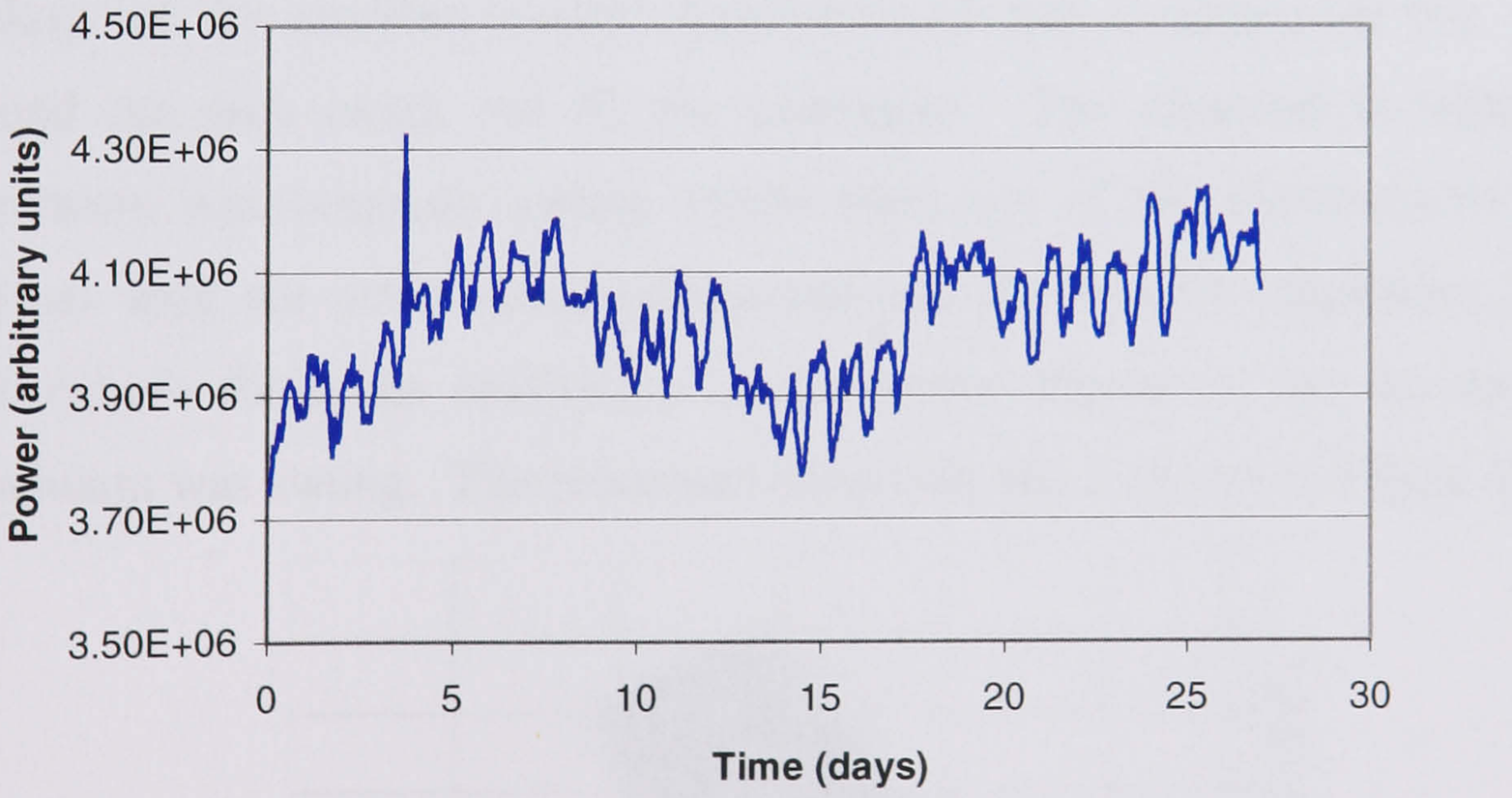

Figure 57: Measurement of charge for 1.18Hz mode using 43.5g lower mass

6.3.4. Detection of the 2D Motion of the Pendulum

A final measurement performed on the pendulum with the small mass was to attempt to map out the motion of the pendulum in two dimensions. A scheme using two shadow sensors was initially envisaged, with the detectors mounted at right angles. However as a CCTV camera set-up was already in use for 1D sensing it was decided in the interests of time to mount another camera to give 2D imaging. The tank, with viewports mounted directly opposite each other, gave no scope to allow the CCTV cameras to be mounted at right angles and so instead they were orientated at as large an angle as possible, this being approximately 30°, while looking through the same front viewport. The Labview software was re-written to allow data from two cameras to be simultaneously processed and recorded using two image acquisition boards. Data was then taken for a period of 1hour, with the pendulum exhibiting the same motion as described above. The values collected by one camera were used to define one axis of the motion. The data from the second camera was then modified by subtracting off the contribution calculated to be from motion along the first axis and by then projecting the resulting contribution onto the orthogonal axis. A calculation done in Maple predicted that if the modes were orthogonal the resulting motion should be such that a rectangular box would bound the area swept out by the pendulum. The direction in which the pendulum was originally swung would form one of the directions of linear motion with the other being orthogonal and the relative amplitudes giving information about the orientation of the modes relative to the direction the pendulum was swung. The processed data collected is shown in Figure 58.

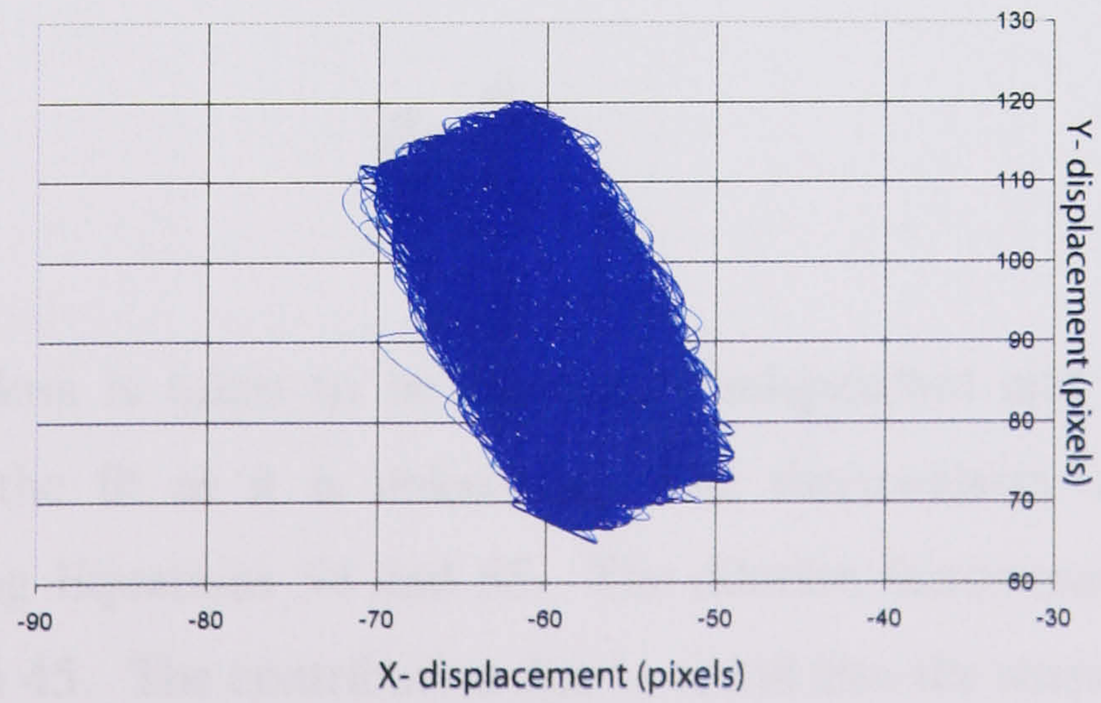

Figure 58: Measurement of 2D motion of pendulum using two CCTV cameras

The slight deviation from a rectangular area is likely to be due to errors in measurement of the angles between the camera and pendulum. Seismic excitation of the pendulum can also be seen with the pendulum moving outwith the rectangle. This would therefore appear compatible with our understanding of the orientation of modes. The pendulum moves within a bounded rectangle where one of the directions of linear motion is in line with the direction the pendulum was originally swung. The relative length of sides shows that more energy was put into one mode than the other, with this mode being more closely aligned with the direction the pendulum was swung. It is also of interest to note that the direction the pendulum was swung was aligned with the stiffened direction of the base and thus we expect that one mode is more closely aligned with this than the other, this being reflected in the Q values of the two modes.

6.3.5. Calculation of Material Loss and Recoil Loss Contributions

Using the measurements from the higher Q mode of the two suspensions we may fit the loss to the following model if we assume that the dominant damping effects are from material, thermoelastic and recoil losses:

$$\phi_{total} = (\phi_{mat} + \phi_{thermoelastic})D^{-1} + \beta m \omega^2 \tag{70}$$

where β is a coefficient dependant on the level of recoil loss in the frame and is given by:

$$\beta = \frac{\phi_{\sup}}{k_{\sup}} \tag{71}$$

The material loss is taken to be frequency independent and will be a free parameter in the fit as it is unknown. The thermoelastic contribution is calculated using Equations 54 and 55. The dilution factor used is calculated using Equation 45. The contribution due to recoil into the suspension frame is

discussed in Appendix D. Material characteristics such as Young's modulus were taken from measurements made in Chapter 5.

It is important to note that due to the pendulum having been removed from the clamp and then replaced after changing the lower mass the contribution to damping from the clamp may have altered between measurements, as may the direction of the modes relative to the stiffened beam. This will become manifest in an altered β term, with that corresponding to our fit being the average value for the two suspensions. The two free parameters in our fit are therefore β and ϕ_{mat}.

From this fit the material loss was found to be:

$$\phi_{mat} = 7\times10^{-7} \pm 10\%$$

where the error here comes from the fitting of the original data to calculate the Q values. It is not possible here to assess the error associated with this fit as we have two measured Q values and two unknown parameters we wish to fit. We may find the approximate stiffness of the frame in this direction from the fit if we assume that the loss in support material is around $\phi_{sup} = 10^{-3}$. This value for the loss in the support assumes that there is no friction between separate parts and comes from previously made measurements on steel such as the suspension wires used to suspend the masses in the first generation detectors[72]. This then gives:

$$k_{sup} = 1.6\times10^{6}\,\mathrm{Nm}^{-1} \pm 10\%$$

again assuming that the largest source of error is due to the fitting of the original data to find the Q values. It should be noted that the variation of clamping between subsequent measurements may in fact exceed this error but is unknown. With recoil damping at this level we find that the contributions to the total loss from the individual loss mechanisms are as shown in Table 2 below.

Pendulum	Material Loss	Recoil Loss	Thermoelastic Loss
445g	1.6×10^{-9} ±10% (20%)	6.2×10^{-9} ±10% (78%)	1.2×10^{-10} (2%)
43.5g	5.1×10^{-9} ±10% (71%)	1.4×10^{-9} ±10% (20%)	5.9×10^{-10} (9%)

Table 2: Contributions to total loss from material, recoil and thermoelastic sources.

It is of interest to note that the loss of the pendulum with the larger mass is significantly dominated by recoil of the support frame while that of the smaller pendulum is dominated by the material loss itself.

We may now look at the loss contributions for the lower Q modes in a similar way. Using the higher mass pendulum value we can once again find the coefficient β for the frame in this direction. This then gives a spring constant of:

$$k_{sup} = 4.3\times10^{5}\,\mathrm{Nm}^{-1} \pm 2.1\%$$

Using this, along with the previously calculated material loss, we may calculate what the expected Q of the higher frequency mode will be for the pendulum with the small mass. This is found to be $Q_{predicted} = 8.9\times10^{7}$ ±10% which we may compare to the $Q_{measured} = 6.3\times10^{7}$ measured for this mode. The difference between measured and predicted values may be due to altered conditions in the clamping, or orientation of the mode with respect to the stiffened base caused by removal of the suspension from the frame.

6.4. Conclusions

By making measurements of the pendulum mode of an all fused silica pendulum and varying the mass it has been possible to extract a value for the loss associated with the material and to identify the contribution to the loss from the recoil of the support frame. The loss associated with thermoelastic damping was calculated and included in calculation of the material loss while

the effects of gas damping were calculated and shown to be negligible. The effect of variation of charge on the mass was not seen to significantly alter the Q of the pendulum and was therefore not included in the calculation of material loss. The value of the material loss angle, calculated here to be 7×10^{-7} (radians) $\pm 25\%$ through use of a theoretical dilution factor, was higher than that found through measurement of the cantilever modes of the suspension measured in Chapter 5. This may be due to the theoretical dilution factor not being achieved by a fibre whose material loss is in fact lower, as is seen in the violin mode experiment, and hence similar reasons to those discussed in Chapter 5 may explain this effect, namely the concentration of energy in a shorter bending length whose loss may be higher due to the welding of this region. The pendulum Q values measured here are at present the highest to ever be measured for a linear pendulum [74, 75]. The time constants for the decay are 1.2 years for the smaller mass pendulum and 1.7 years for the larger mass pendulum..

Future work may improve our understanding of the losses associated with the support frame by directly measuring its stiffness and by improving the clamping ring of the support to reduce friction. Also further investigation into the modulation of amplitudes will be carried out using tilt meters and temperature monitors in the laboratory.

Chapter 7

Stress Dependence of Internal Loss

7.1. Introduction

Experimental data has shown that theoretical dilution factors are rarely achieved and that losses of suspensions are higher than expected (as seen in Chapters 5 and 6 of this thesis) when compared to the intrinsic loss of the material. Since large dilution factors increase the Q to very high levels it is to be expected that losses from recoil of the support structure or from residual gas damping will become more prominent compared to those of internal friction. However one other possible explanation would be a stress dependence of the internal friction. Other physical properties of silica have been seen to be stress dependent (Young's modulus [76] (though only a 2% change to our suspension stress levels) and density [77]) giving some cause to believe that the loss may also be affected. Also we have already seen that the

loss mechanism of thermoelastic damping has a stress dependence caused by the temperature dependence of the Young's modulus [65].

Measuring the vertical bounce mode of a suspension is a particularly suitable way in which to investigate any stress dependence for the following reasons. Firstly, since gravity does not provide a restoring force there is no dilution factor, eliminating this form of dynamic stress dependence. This will also keep the Q of the suspension to that of the material ($\sim 10^7$) rather than the high values a dilution factor gives ($\sim 10^9$), reducing the effects of residual gas or recoil damping. Secondly, because there is no bending taking place, the thermal gradients, which cause thermoelastic damping, will not occur and so this stress dependant loss mechanism will not be seen. It should be noted however that for this to be true the fibre must be considered uniform in cross section and with a Young's modulus that does not differ at the surface. Thus by varying the lowest mass of the suspension we can alter only the stress in the fibre without affecting other stress related loss mechanisms.

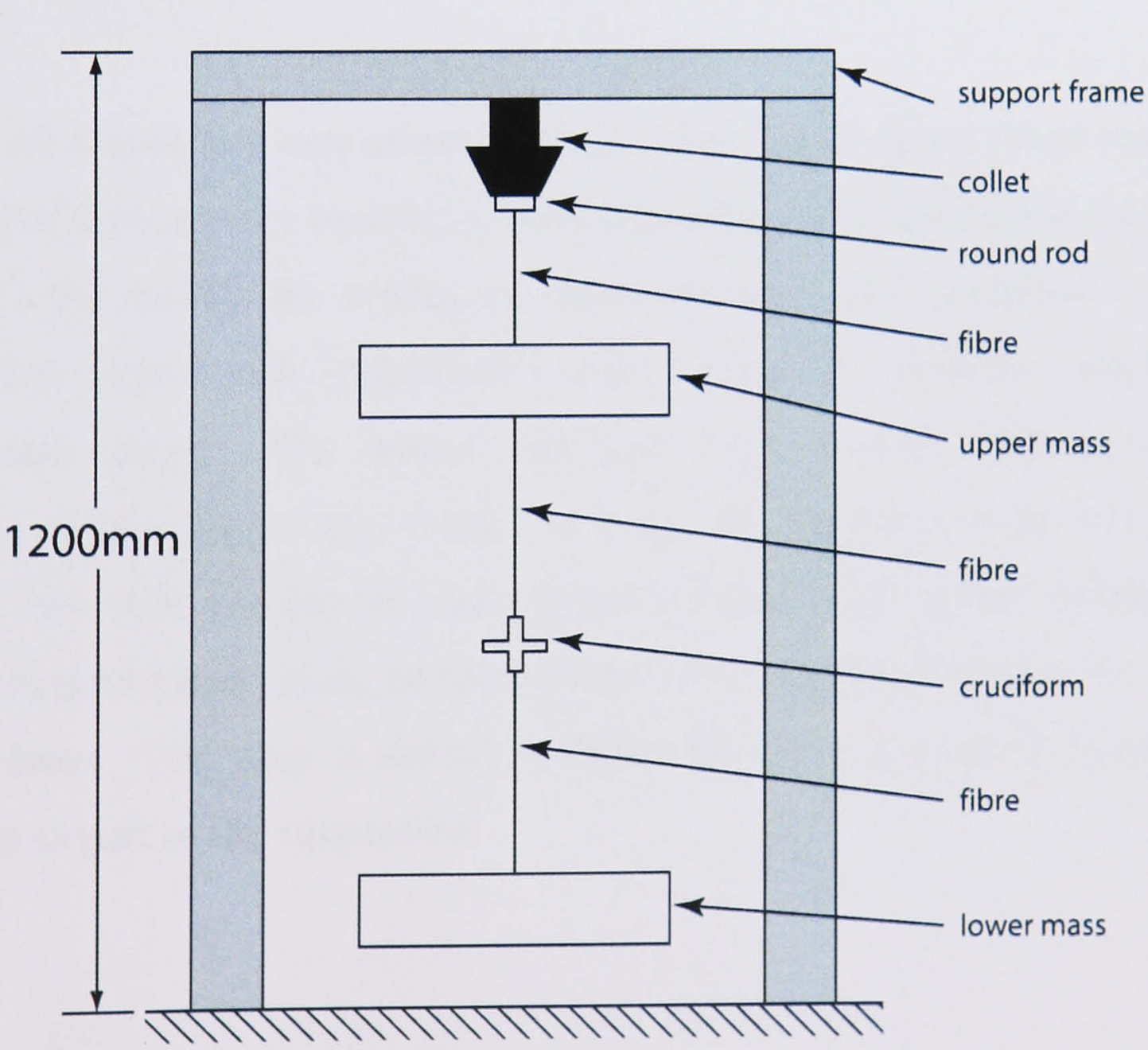

Figure 59: Diagram of the experimental setup for vertical bounce mode measurement Large masses used to hold the ends of the fibres essentially stationary while small cruciform bob provides a small momentum.

When considering the vertical bounce mode of a pendulum, such as that used in Chapter 5 to measure violin mode Qs, it is seen that if the lower mass is caused to oscillate vertically there is a large amount of moving mass, and hence momentum, connected to the support frame, causing a large amount of recoil damping. The large mass will be essential if we are to stress the fibre to a significant fraction of its strength. A solution that was proposed for this is seen in Figure 59. Here the mass that will oscillate is the central one, which is small in comparison to the upper isolation mass and lower mass. The lower mass is used purely to provide tension. The restoring force on the central mass then comes from both the fibre above and below the mass.

The experiment was set-up jointly with the California Institute of Technology and was carried out jointly with Dr Phil Willems.

7.2. Experiment

Figure 59 shows the experimental set-up. The upper mass, lower mass and round rod fixture were machined using a grinding tool and carborundum grit to give a pin suitable for welding to, similar to those used in chapter 7. These were then etched with hydrofluoric acid to clean the surfaces, which were rough and opaque. The central mass was constructed by welding together sections of silica rod to give a mass of 4.4g. Its cruciform shape was chosen to give two ends suitable for welding and a longer edge section suitable both for exciting vertically using an electrostatic drive and for detecting the motion of the mass. This mass is shown in Figure 60 where it is being welded into position as part of the suspension.

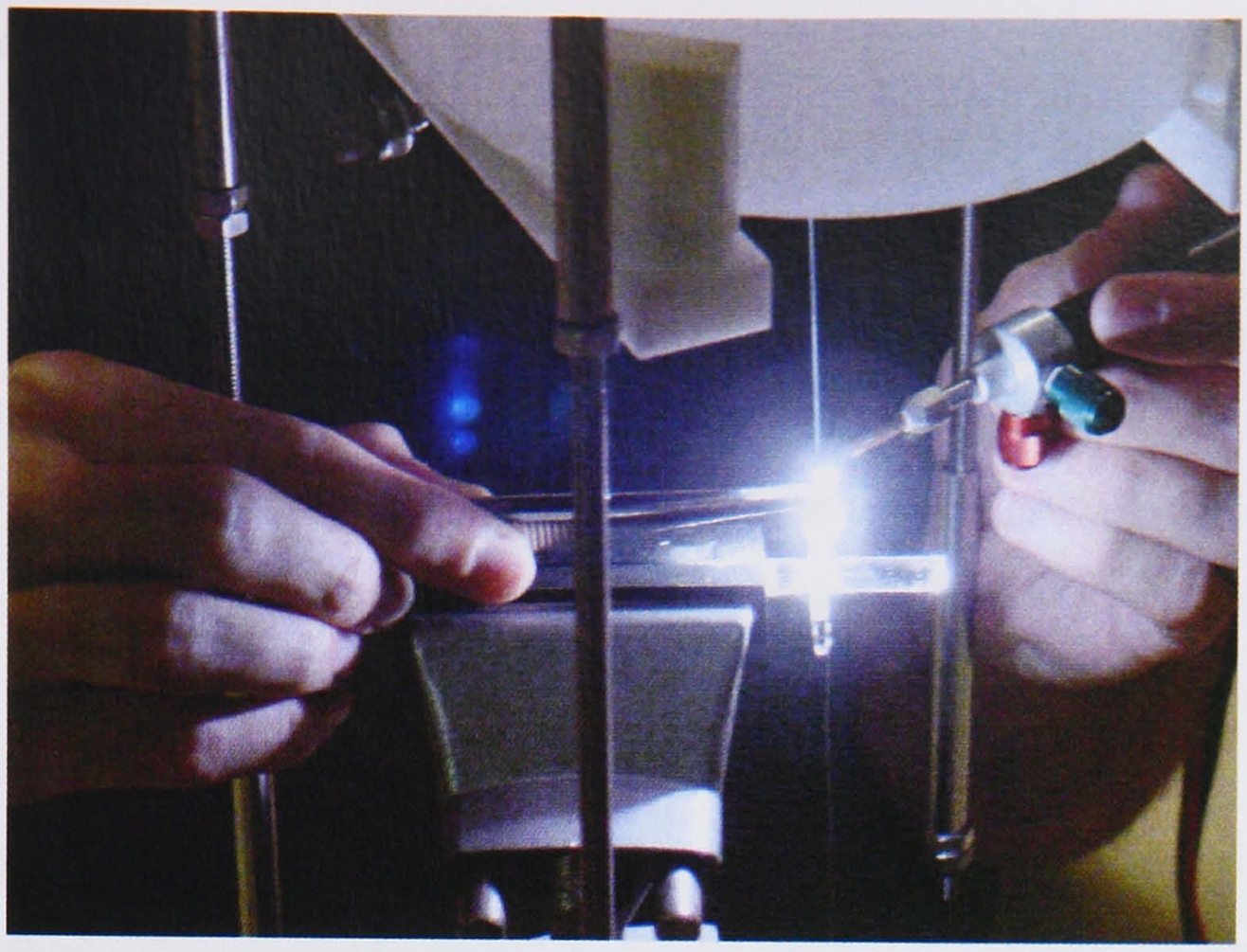

Figure 60: Welding the cruciform onto the suspension fibre using a hydrogen-oxygen gas torch.

The detection of displacement was done using a He-Ne laser and shadow sensor. The shadow sensor was used in a similar configuration to that seen in Figure 35 though using a split photodiode rather than two separate photodiodes. A laser was used here instead of an LED as the viewports in the vacuum tank gave a direct line of sight to the silica cruciform. This then allowed the photodiodes and laser to be mounted outside the tank, which was advantageous for easier alignment and reduces the number of in-vacuum components. The same sensor arrangement was used to measure other modes of the suspension.

The suspension frame was constructed using 3inch diameter round aluminium posts and an inch thick stainless steel top plate to give a highly rigid structure. The round rod, used as the top suspension point, was held in a sprung collet attached to the top plate. This form of collet gives an even distribution of force on the glass over a number of points allowing the glass to be more tightly held, reducing any loss due to suspension point friction. Fibres used in the suspension were 320μm diameter round fibres produced using the glass lathe method described in chapter 4. As with other suspensions investigated, a monolithic approach was taken to reduce friction between the fibres and mass. The welding was done using a technique described in Chapter 9 where

no neck section was used, but instead the fibre was welded directly to the side of a 3mm piece of silica rod, which in turn was welded to the pin of the mass. The area around the weld was then gently heated using a diffuse hydrogen flame to remove highly concentrated areas of thermal stress (this method cannot be compared with true annealing as the stress is not removed altogether) from points where the mechanical stress is likely to be high. These areas of high mechanical stress result from the fibre not being attached to exactly the centre of the mass, inducing a torque on the fibre which will be concentrated at the point where it attaches to the pin and being the cause of a number of initial failures of the suspension. In the final suspension care was taken to weld as close as possible to this central point though it is likely that some torque was still present. The completed suspension is shown in Figure 61, resting on a temporary support structure before being lowered into the vacuum chamber.

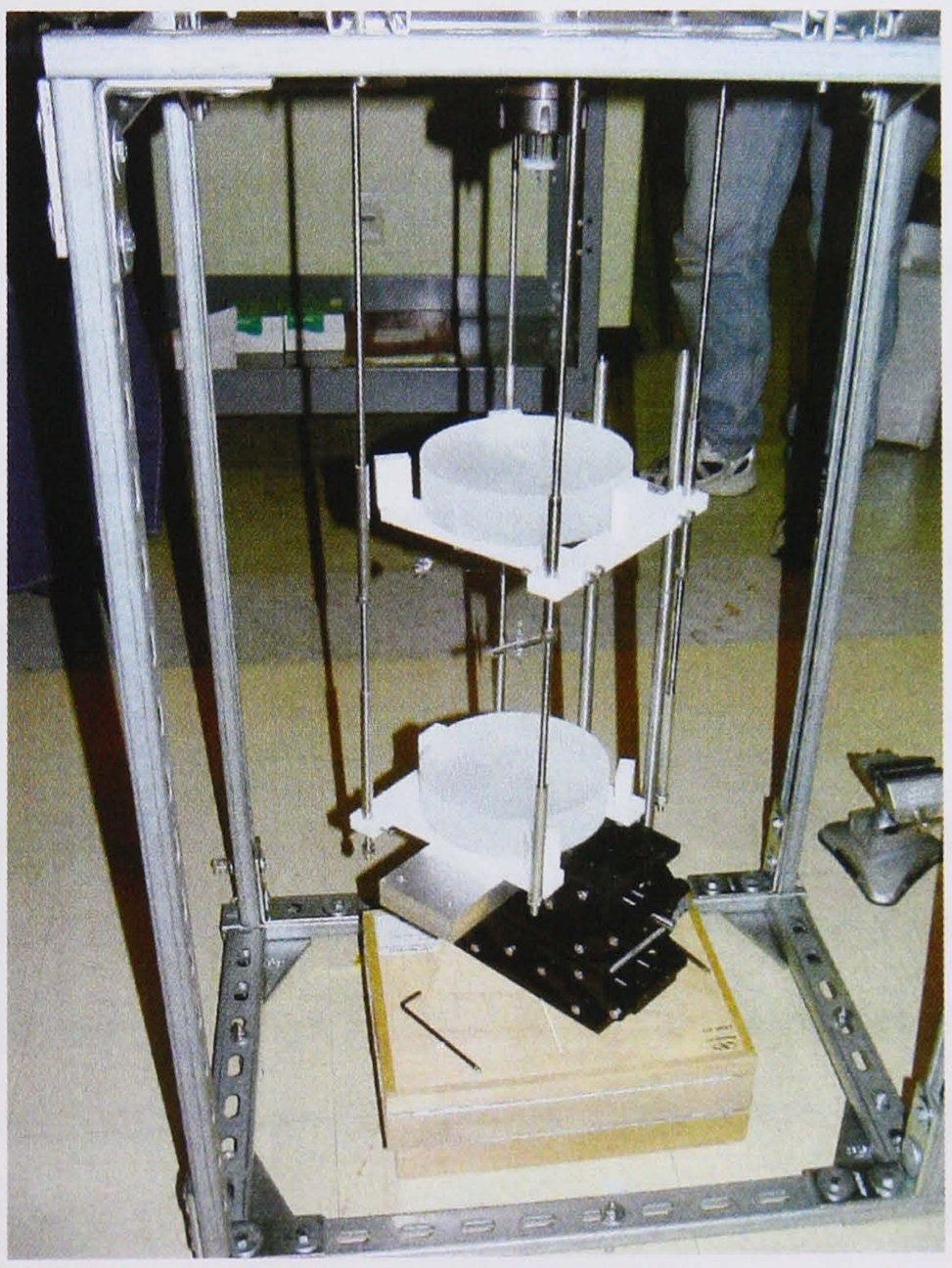

Figure 61: Suspension used for vertical bounce experiment

By considering the dynamics of the suspension as shown in Figure 62 we can calculate that if we cause the central mass to oscillate vertically, then the upper and lower masses (using the 1.7kg lower mass) will move by 0.13% of

this displacement, thus essentially fixing the position of the upper and lower ends of the test fibre though their inertia.

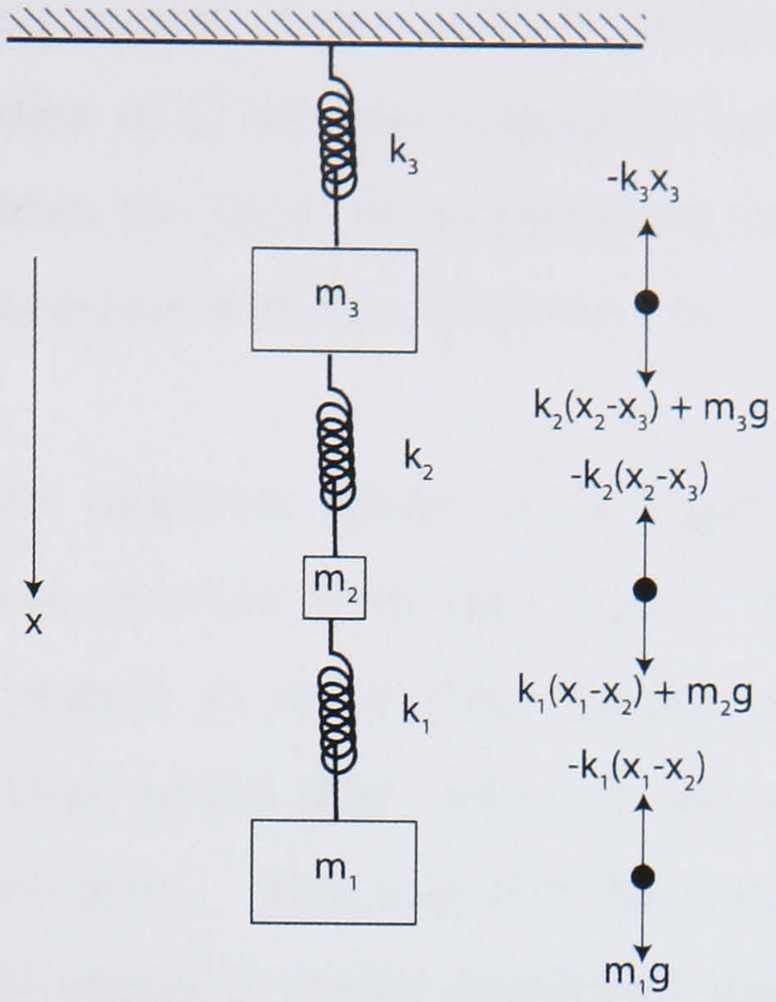

Figure 62: Diagrammatic representation of suspension

From this we can then calculate that the proportion of the energy of this mode stored in the upper fibre is 0.00147%, which gives a high degree of isolation even if we assume that the upper stage is lossy and achieves only a low Q ($\sim 10^5$). The calculated frequency of this mode of oscillation is 817Hz for the 1.7kg mass. This does not alter significantly when the smaller 105g mass is used and the predicted value is 821Hz.

In order to ensure that losses from residual gas damping were low enough to be considered negligible, measurements of the Q of the vertical bounce mode were made at different vacuum levels. The values found at pressures higher than 10^{-5} Torr and those made below this value were in agreement to within the limits of experimental error. All subsequent measurements were then made at pressures below 10^{-5} torr.

7.3. Results

The Q of the vertical bounce mode with the larger mass of 1.7kg giving a stress of 213MPa was found to be $1.2\times10^7 \pm 10\%$. With the lower mass of

105g and a stress of 12.8MPa a Q of $1.1\times10^{7}\pm10\%$ was measured. The working stress used in other parts of this thesis is between these two extremes, with the violin mode experiment using a stress of around 139MPa. The error here comes from variation of Q between subsequent measurements. We can therefore state that within the limits of measurement the loss of the vertical bounce mode of the suspension was stress independent.

The measurement of the cantilever modes of the upper fibre with the lower section of the pendulum removed were then made. These can be seen in Figure 63. It is of interest to study these modes as the energy is now concentrated at the surface of the fibre, with zero energy in the neutral axis where no bending takes place. This may then be compared to the vertical bounce mode where the energy is evenly distributed across the cross section. This may then give an indication of how the loss is distributed within the fibre.

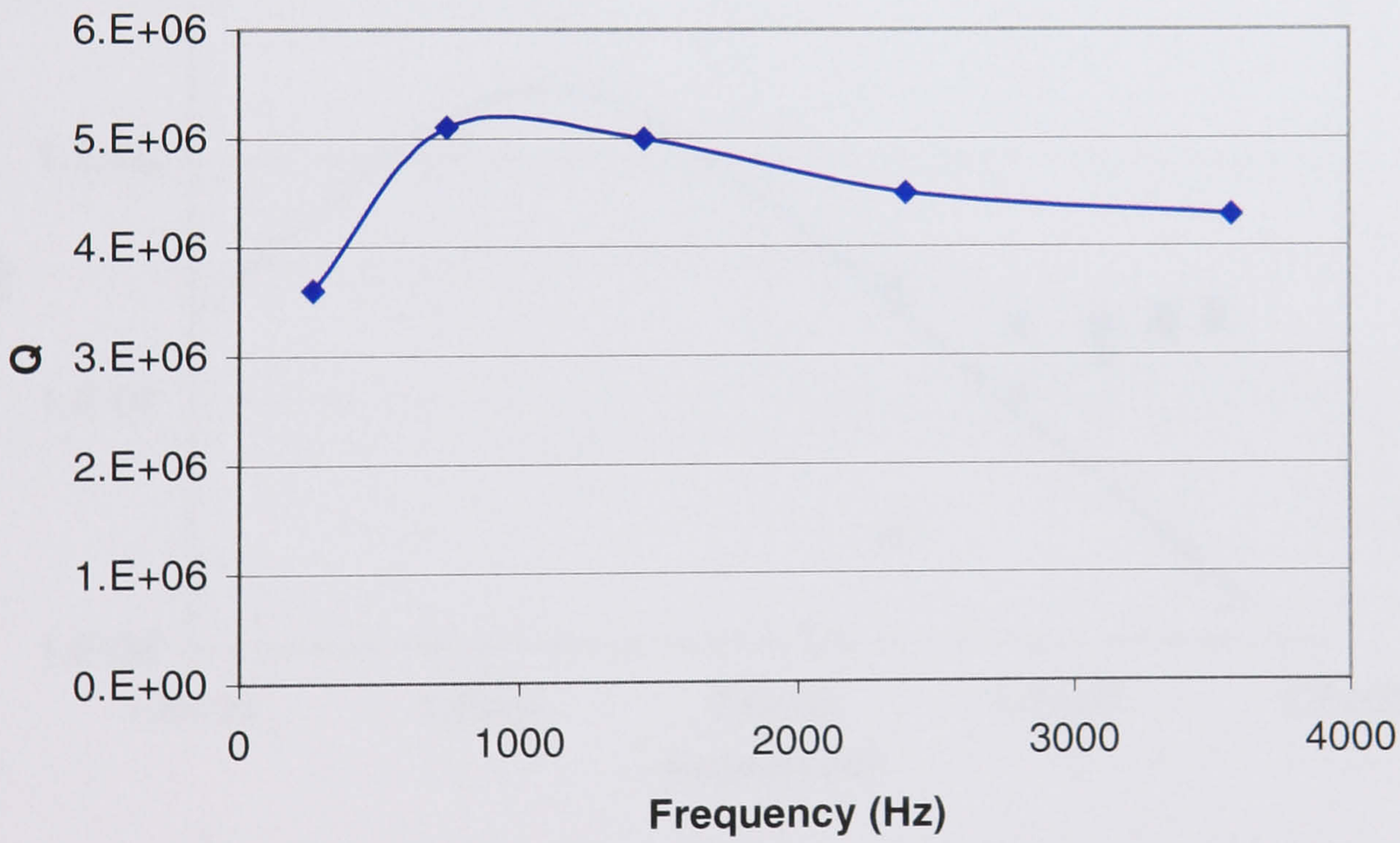

Figure 63: Q of cantilever bending modes of upper fibre

The decrease in Q at low frequency is due to thermoelastic damping while at higher frequencies there is a slight drop in Q. The closest mode in frequency to the vertical bounce mode was that at 740Hz which gave a Q of 5.1×10^{6}. As the Q of this mode is affected by thermoelastic damping it is not possible

to directly compare it with that of the vertical bounce mode. If we calculate the value of thermoelastic loss using standard material property values for silica we find that the contribution to this modes loss is $\phi_{T.E.} = 8.8 \times 10^{-8}$. If this is then subtracted from the measured loss we then find that the Q of the mode would be 9.3×10^{6}, much closer to that of the vertical bounce mode.

However using this calculated level of thermoelastic loss we find, as shown in Figure 64, that the material loss below 264Hz would appear to drop off towards zero. If, however, we use the Young's modulus value that was found in the violin measurements made in Chapter 5, we find a lower level of thermoelastic damping and higher level of internal frictional loss. This would then also increase the difference in loss due to internal friction between the cantilever bending mode at 740Hz and the vertical bounce mode.

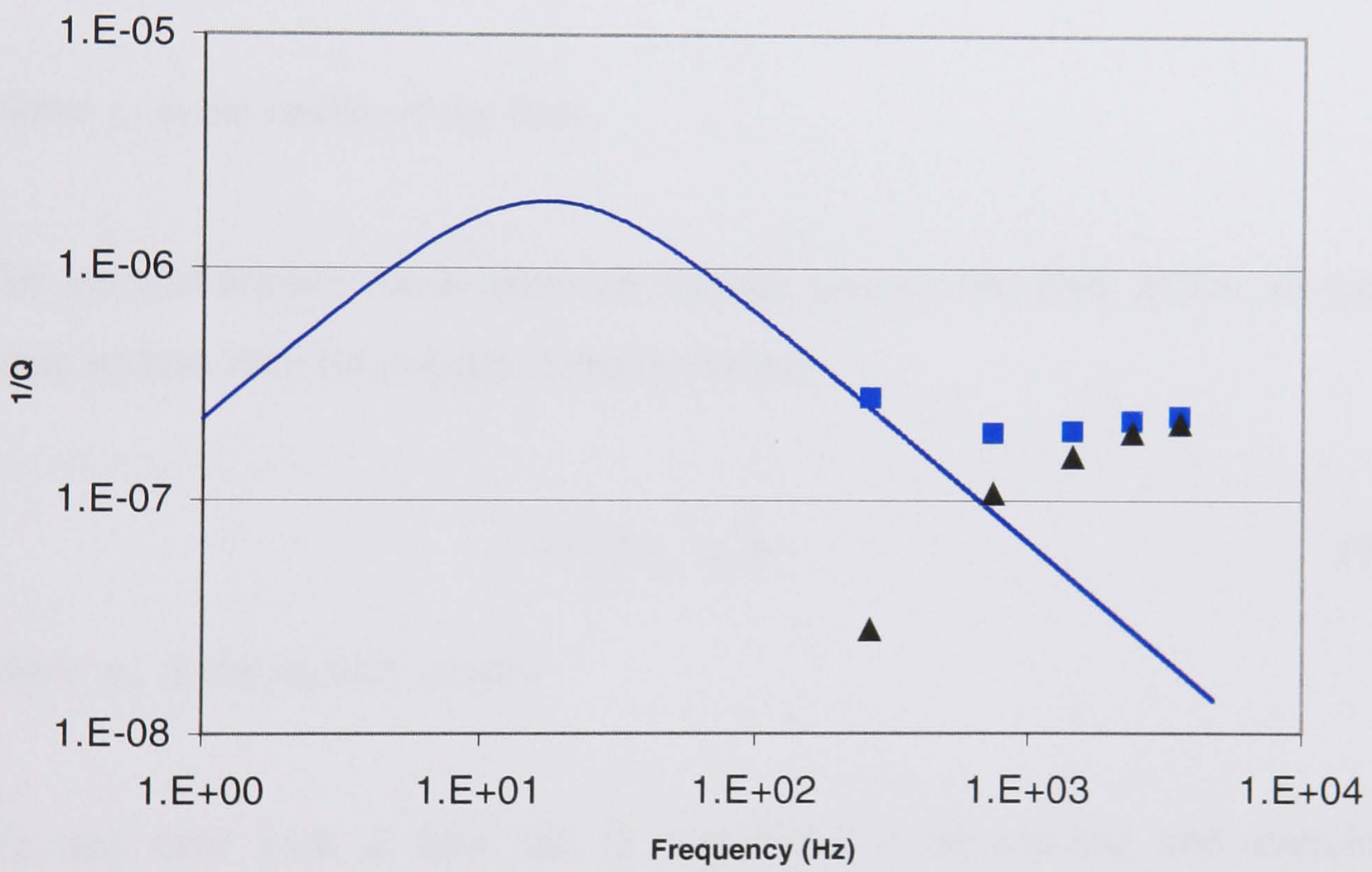

Figure 64: Thermoelastic Loss Contribution. Blue line shows predicted thermoelastic loss for a Young's modulus of 7.2×10^{10}. The square points show the measured loss of cantilever modes. The triangles show the resulting loss due to internal friction

This difference could be explained if the loss in the fibre was concentrated close to the surface layer while the bulk of the material was relatively low loss. It has been noted elsewhere that silica fibres have a loss approximately

proportional to their surface area to volume ratio [78] which would also be in agreement with this hypothesis.

The bending involved in the cantilever mode causes the highest deformation at the inside and outside of the bend while at the middle there is a neutral axis where no deformation takes place with the strain given by:

$$u_z = \frac{x}{R} \tag{72}$$

where R is the radius of curvature of the bent fibre and x is the transverse direction of the fibre. The energy stored in a bent fibre can then be given by:

$$U = \frac{1}{2}\int_{x^2+y^2 \le r_0^2} E u_z^{\,2} dxdy = \frac{\pi}{8}\frac{E}{R^2} r_0^{\,4} \tag{73}$$

where r_0 is the radius of the fibre.

The vertical bounce mode however equally stresses the fibre across its entire cross section with the energy stored given by:

$$U = \frac{1}{2} E u_0^{\,2} r_0^{\,2} \pi \tag{74}$$

where u_0 is the uniform strain.

We may now look at how the Q expected for the bending and stretching modes act for a highly lossy layer with thickness given by $\delta << r_0$. For the bending mode the loss of energy per oscillation is proportional to the following:

$$\Delta U \propto \frac{1}{2}\iint \phi E u_z^{\,2} dxdy = \frac{\pi}{2}\frac{E}{R^2} r_0^{\,3} \phi\delta \tag{75}$$

integrating over the region $(r_0 - \delta)^2 \le x^2 + y^2 \le r_0^{\,2}$. This then gives a Q value proportional to the following:

$$Q = \frac{2\pi U}{\Delta U} \propto \frac{r_0 \pi}{2\phi\delta} \tag{76}$$

For the stretching mode the loss of energy per oscillation is given by:

$$\Delta U \propto \frac{1}{2}\iint \phi E u_0{}^2 dxdy = r_0 \pi \phi E u_0{}^2 \delta \tag{77}$$

integrated over the region $(r_0 - \delta)^2 \le x^2 + y^2 \le r_0{}^2$. This gives a Q value proportional to the following:

$$Q \propto \frac{r_0 \pi}{\phi\delta} \tag{78}$$

Thus if the loss were concentrated in a thin lossy layer at the surface, the cantilever modes would have a measured loss a factor of 2 greater. While this factor is considerably larger than that found if a Young's modulus of 7.2×10^{10} is used, this would be possible if a value of 5.4×10^{10} is used, as measured in Chapter 5. Using this value for the Young's modulus we the have a calculated thermoelastic loss of 4.4×10^{-8}. If this is then subtracted from the measured loss the Q of the cantilever mode would be 6.4×10^{6}, giving a factor of 1.9 ± 0.3 higher loss than for the vertical bounce mode, in agreement to within measurement limits with a model where loss is concentrated in the surface layer of the fibres.

7.4. Conclusion

The vertical bounce mode of a silica fibre, which has no dilution of loss, was investigated under two different tensions. The losses seen showed no stress related mechanical loss mechanisms, with the suspension losses measuring $1.2\times10^{7}\pm10\%$ at a stress of 213MPa and $1.1\times10^{7}\pm10\%$ at a stress of 12.8MPa. The low dilution factors seen in other measurements, such as the violin mode and pendulum mode experiments in this thesis, must therefore be attributed to other loss mechanisms as described in the discussions in those chapters. We have also seen evidence that the majority of loss measured comes from a lossy surface layer, with the bulk of the material contributing relatively little loss.

Chapter 8

Strength Testing of Ribbon Fibres

8.1. Introduction

We have so far discussed the advantages of using fused silica suspension elements due to the materials low level of internal friction. There is however another property of this material which is equally surprising. Fused silica is one of the strongest materials known, with breaking strengths of up to 14 GPa [79] having been recorded. The high failure rate we might typically expect from glass is due to its brittle nature and imperfections in the surface due to abrasion may propagate quickly under stress.

From equation 45 and 64 we see that a great deal may be gained in improving the dilution factor and lowering the vertical bounce frequency by increasing the working load on the fibres by decreasing their cross section or increasing the tension. Indeed a typical suspension for advanced LIGO, which will require the 40kg to put a force of 98N on each of its suspension fibres whose cross sectional area is around $1.7\times10^{-7}\,\mathrm{m}^2$ resulting in a working stress of 700MPa. While this is of the same order of working stress as the GEO600 suspensions the increased surface area of the fibres makes them more susceptible to surface defects which may limit the strength. In this chapter we shall investigate the breaking strength of ribbon fibres of the same design as those analysed throughout this thesis.

8.2. Failure of Fibres

Before looking at the measured values of fibre strengths it is of interest to discuss briefly the effects that will cause a lowering of the breaking stress of fibres.

8.2.1. Surface Crack Propagation

In a defect free piece of silica the primary cause for failure will be due to propagation of minute cracks on the surface[79, 80]. These cracks cause regions of high stress at their lowest point and hence give a limit to the fibre strength that is related to their size. Any abrasion of the surface of the fibre will cause surface damage and a decrease in the strength of the fibre. In practise the level of abrasion needed to weaken a fibre substantially is little more than a brief touch of a piece of tissue paper.

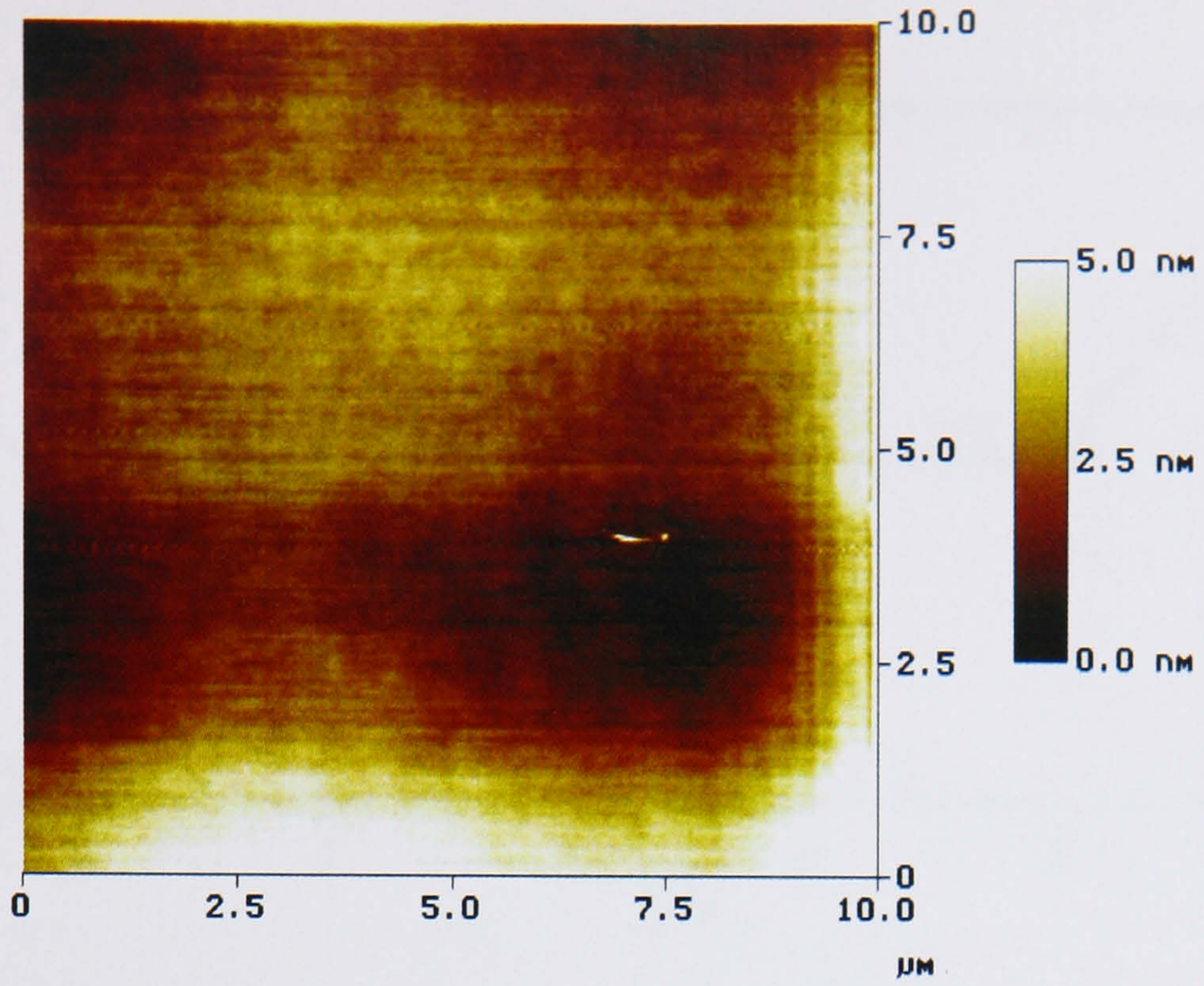

Figure 65: Atomic force microscope (AFM) image of the surface of a fused silica fibre

In Figure 65 we see the surface flatness of a fibre, measured using an atomic force microscope (AFM) scan. As the fibre has not been mounted perfectly flat there is a slope across the sample from the top left up to the bottom right. The variation in height across the sample is around 15*nm* and gives an indication of how flat this side of our ribbon really is. In Figure 66 we see a cross sectional view through the sample, which, assuming the AFM is capable of resolving the cracks (the resolution of the AFM is approximately 0.1nm), shows the surface roughness of the silica. These cracks have a depth of around 0.3nm which is small compared to the aged silica, measured by Kurkjian[79], again using AFM, where the surface roughness is of the order of 15nm .

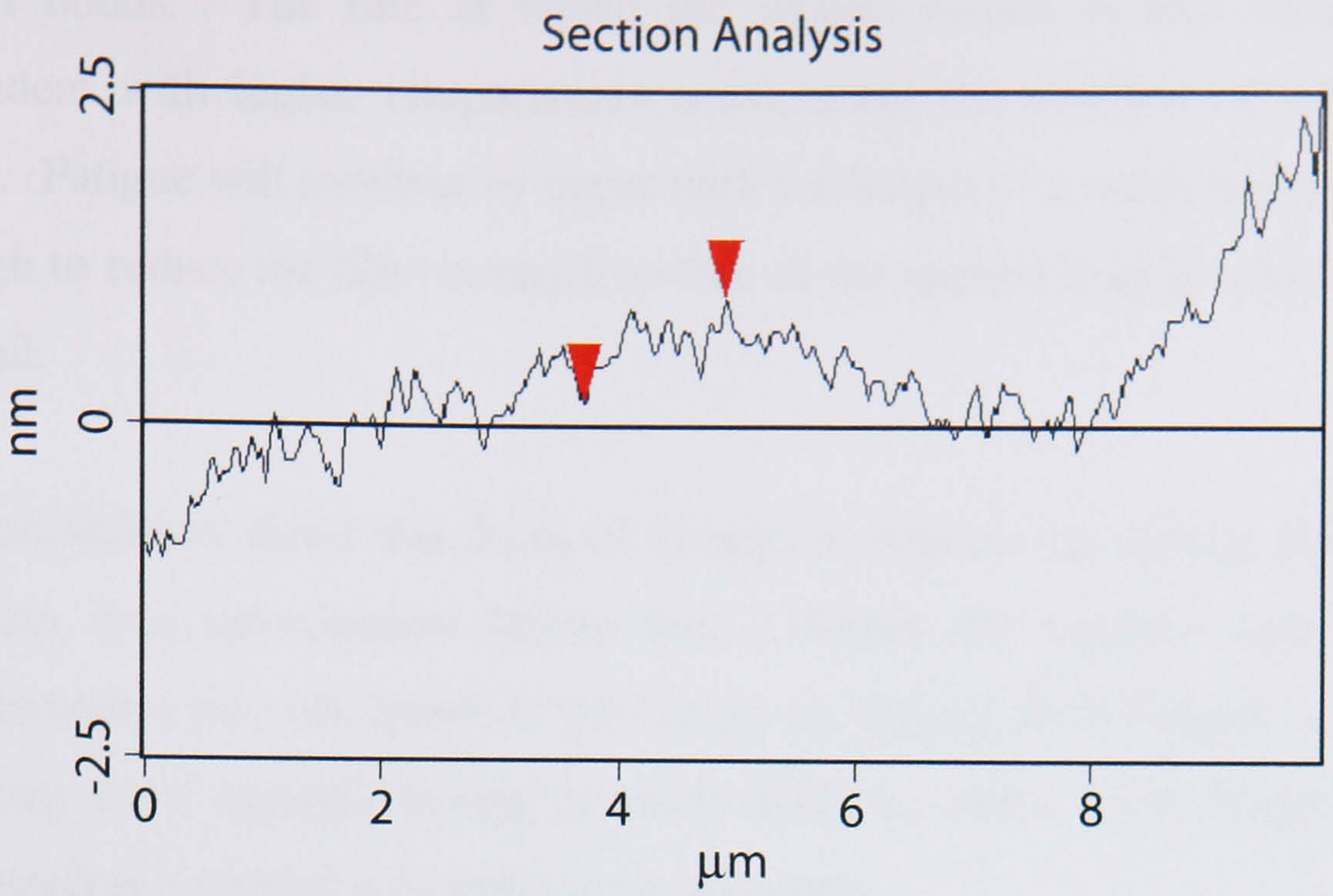

Figure 66: Cross sectional height of a fused silica fibre showing surface roughness. Taken from AFM image

The strength of a fibre may be given by the Griffith equation [79]:

$$\sigma = \frac{K}{Y\sqrt{c}} \tag{79}$$

where σ is the breaking stress of the fibre, K is a material constant known as the fracture toughness, Y is a constant related to the shape of the crack and c is the length of the crack. We may therefore expect the strength of the fibre shown in Figure 66 to be seven times that of the aged fibre measured by Kurkjian [79].

8.2.2. Fatigue Due to Water

If a fibre with cracks on its surface is put in tension with a sub critical load it will not break immediately. However fatigue will occur, whereby the strength decreases with time, when there is water present. The process that occurs is one where OH groups are formed on the surface, resulting in Si-OH bonds. These being weaker than the Si-O bonds, the surface cracks propagate slowly, with the rate of reduction in strength being related to the rate of formation of

Si-OH bonds. The rate at which the fatigue occurs is also temperature dependent with higher temperatures accelerating the reaction of silica with water. Fatigue will continue to occur until the length of a crack becomes large enough to reduce the fibre strength to that of the applied load at which point it will fail.

It is possible to avoid this form of fatigue in practise by storing fibres in a moisture free environment before use. Within the vacuum tanks of an interferometer we will therefore not expect to see any such fatigue. However any long term strength testing is more likely to suffer from fatigue if it is performed in a normal atmospheric environment.

8.2.3. Thermal Stress

When molten silica cools a temperature gradient is produced, with the outside cooling faster than the centre. As silica is a poor conductor of heat the thermal gradient can be high, causing a differential expansion of the material as it solidifies. The effect of this stress is seen most clearly when a fibre is welded. As it cools a region of high stress, close to the weld is formed. This region is the point at which the fibre will normally fail under load. Unfortunately the points close to the weld are also often where the highest concentration of stress occurs, for example when a mass tilts. With the fibres used in the GEO600 suspensions the thermal stress from the welds occurs in the neck region, which has a large enough cross section to spread the load. However, with planned advanced LIGO suspensions using no necks in their welds the problem of thermal stress becomes more important.

There will also be thermal stress in the fibres due to pulling and hence we may expect that even without welding the fibres thermal stress may contribute to low strengths.

Thermal stress may be annealed out of the material by heating it to its softening point and then cooling very slowly in order to minimise the

temperature gradient produced. For fibres this appears to be a promising idea, however in Chapter 9 we shall discuss the implications of using annealing on welded regions.

8.2.4. Impurities

When fibres are produced and the silica is molten it is possible for impurities to become introduced. Using stock material that has not been sufficiently cleaned, or particles being blown from the inside of the burners may sometimes be seen as glowing spots in the flame or as a colouring of the flame. Such impurities may become embedded in the fibre, producing a region where either the chemical make up is altered, causing a weakening or where high thermal stress is produced due to the differing expansion coefficients, leading to cracking of the surrounding silica. Such impurities may be the cause of widely varying strength measurements due to the random nature of this effect.

8.2.5. Experimental Techniques

In practise, when measuring breaking strengths care is taken to limit the effects of these modes of failure. Fibres are pulled from stock that has been carefully cleaned using isopropanol in order to avoid surface contamination. The fibres are then handled only by the tailstock in order to avoid abrasion of the surface. They are clamped only by the ends and are broken within an hour of being pulled in order to avoid aging. The inside of the burners is cleaned using small pieces of wire and the burners are run for long periods of time to remove debris from inside.

8.3. Experimental Measurement of Breaking Stress

In order to measure breaking strengths of fibres a rig is used to hold the fibre while one end is stretched using an electric motor. The maximum force

exerted on the fibre is measured using a piezo force meter. Initially the measurements were made using an existing system, shown in Figure 67. However it quickly became apparent that the drive system, using string, and the force meter, which only worked up to 50N, were inadequate for measuring the strength of these fibres while its length precluded measurements of fibres of 60cm length. Also, the universal joints to which the clamps were attached were thought to be a source of lateral force on the fibre. Thus a more rigid system was needed.

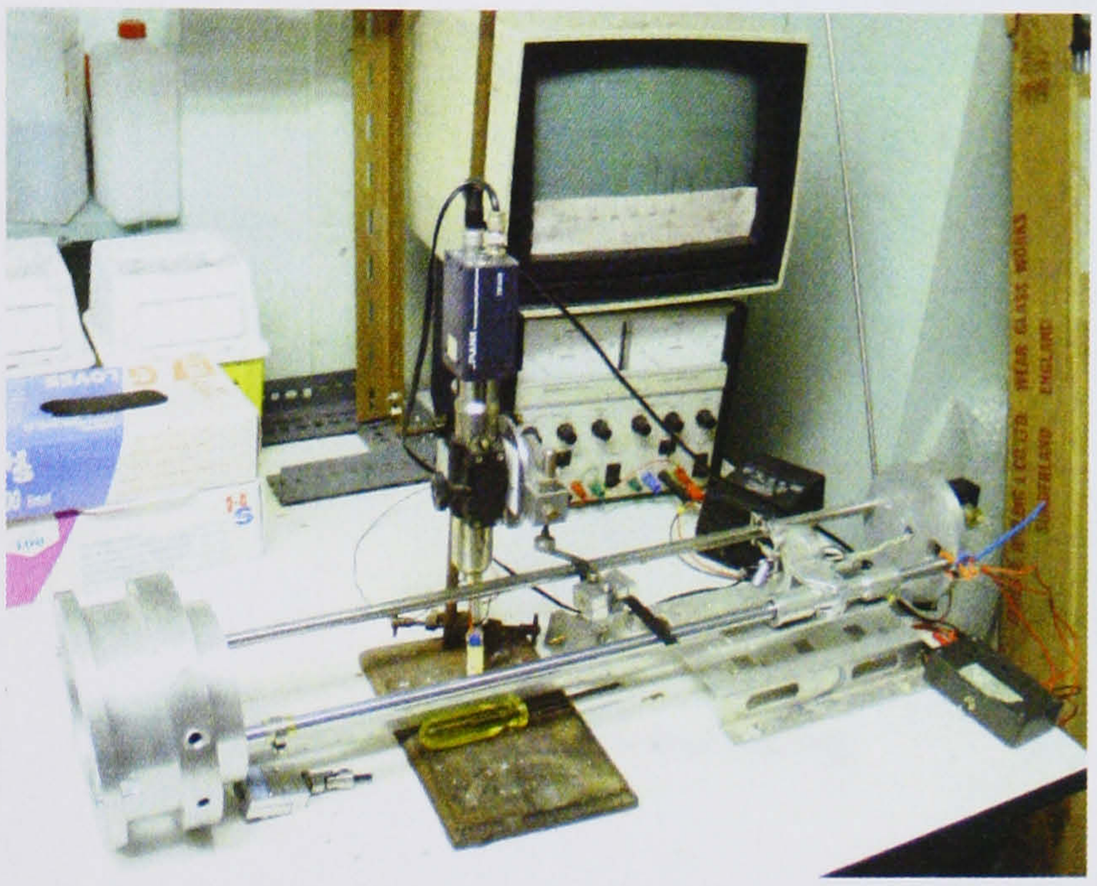

Figure 67: Previously used breaking stress measurement rig

8.3.1. Strength Testing Rig

The design of a the new system had to be based around the need for an inherently rigid frame and drive system. A 60W motor with a double reduction worm gearing was used to provide power, with the drive then coupled through a re-circulating ball race to give a smooth linear drive that would take a large longitudinal load. The clamps were allowed to travel longitudinally on hardened steel rods using linear bearing races in order to give a high rigidly in the transverse direction. The position of the motor could be moved in order to allow a wide range of lengths of fibre to be tested and a higher rated piezo force meter was also used.

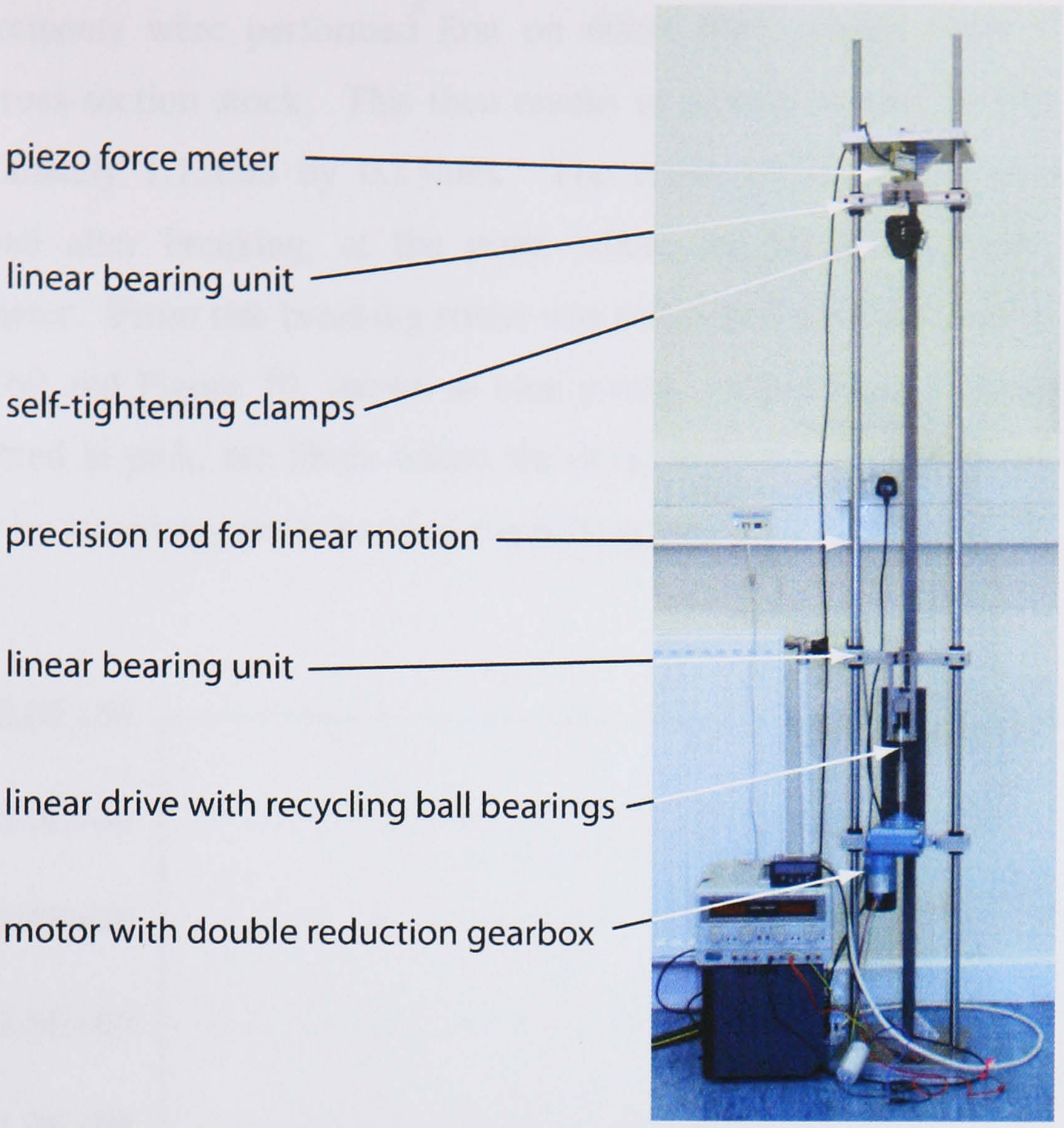

Figure 68: Strength testing rig

The clamping of the fibres in the rig required that they be carefully aligned in order to avoid transverse stress. This was done by using the edge of the clamps as a reference point at each end, allowing the fibre to be aligned to the same tolerance as the manufacture of the rig. The clamps used were self-tightening wedge clamps, into which the fibre was mounted by using epoxy resin. Without using the resin the tailstock would tend to snap easily as pressure was applied at a small number of points only. The epoxy, with a degree of elasticity, allowed this pressure to be applied more evenly and resulted in easy clamping of the fibres.

The final design of strength testing rig can be seen in Figure 68.

8.3.2. Results

Measurements were performed first on 60cm fibres pulled from 11mm by 1mm cross-section stock. This then results in a cross section for the fibre of approximately 1.13mm by 0.13mm. The cross sectional dimensions were measured after breaking, at the point where the break occurred, using a micrometer. From this breaking stress was calculated with the results given in Figure 69 and Figure 70, shown as blue points. Also shown in these graphs, highlighted in pink, are fibres where the cross section was deliberately altered slightly by increasing or decreasing the pulling speed.

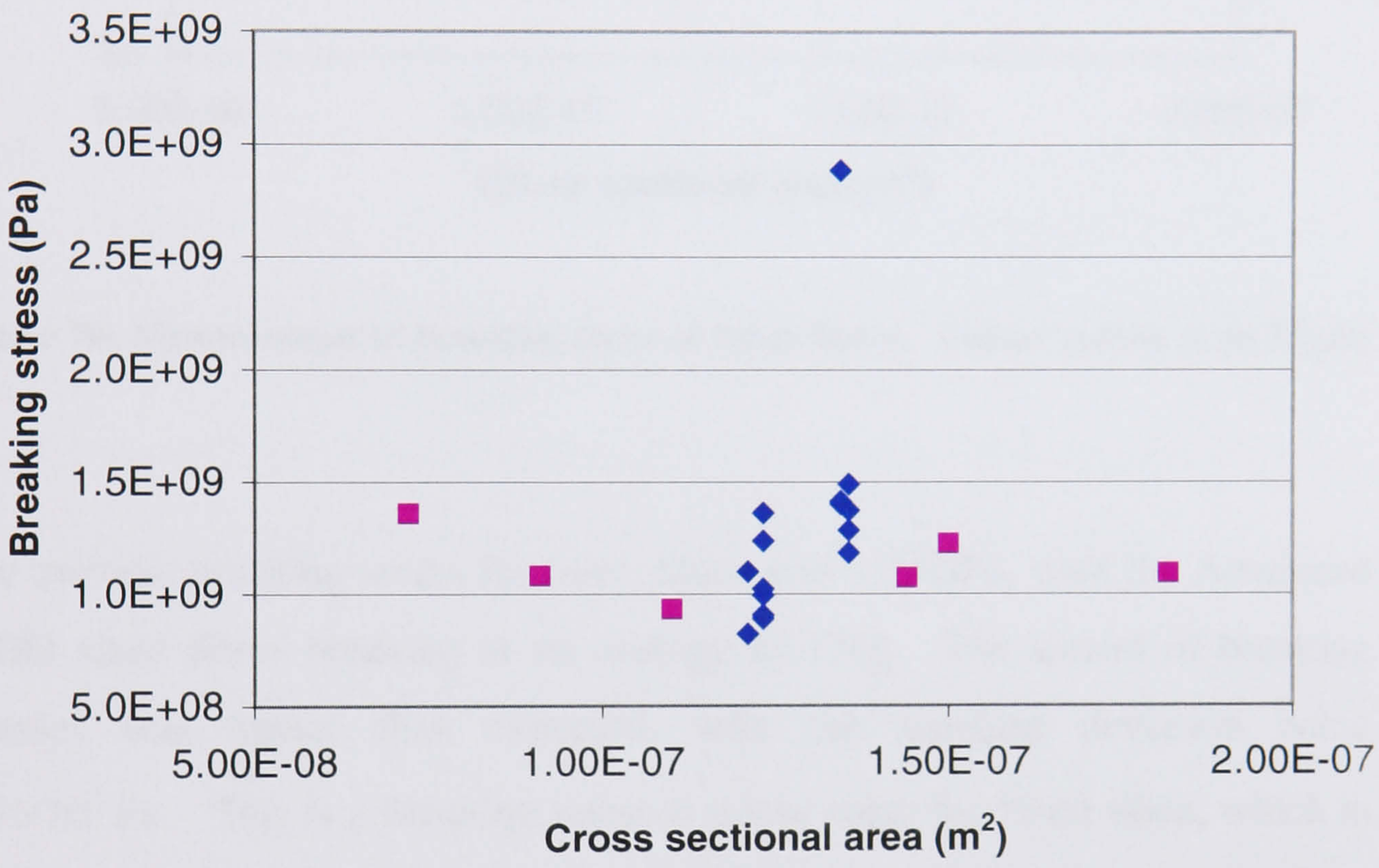

Figure 69: Measurement of breaking stress of 60cm fibres. Blue points show advanced LIGO sized fibres while pink points show fibres of larger or smaller cross section

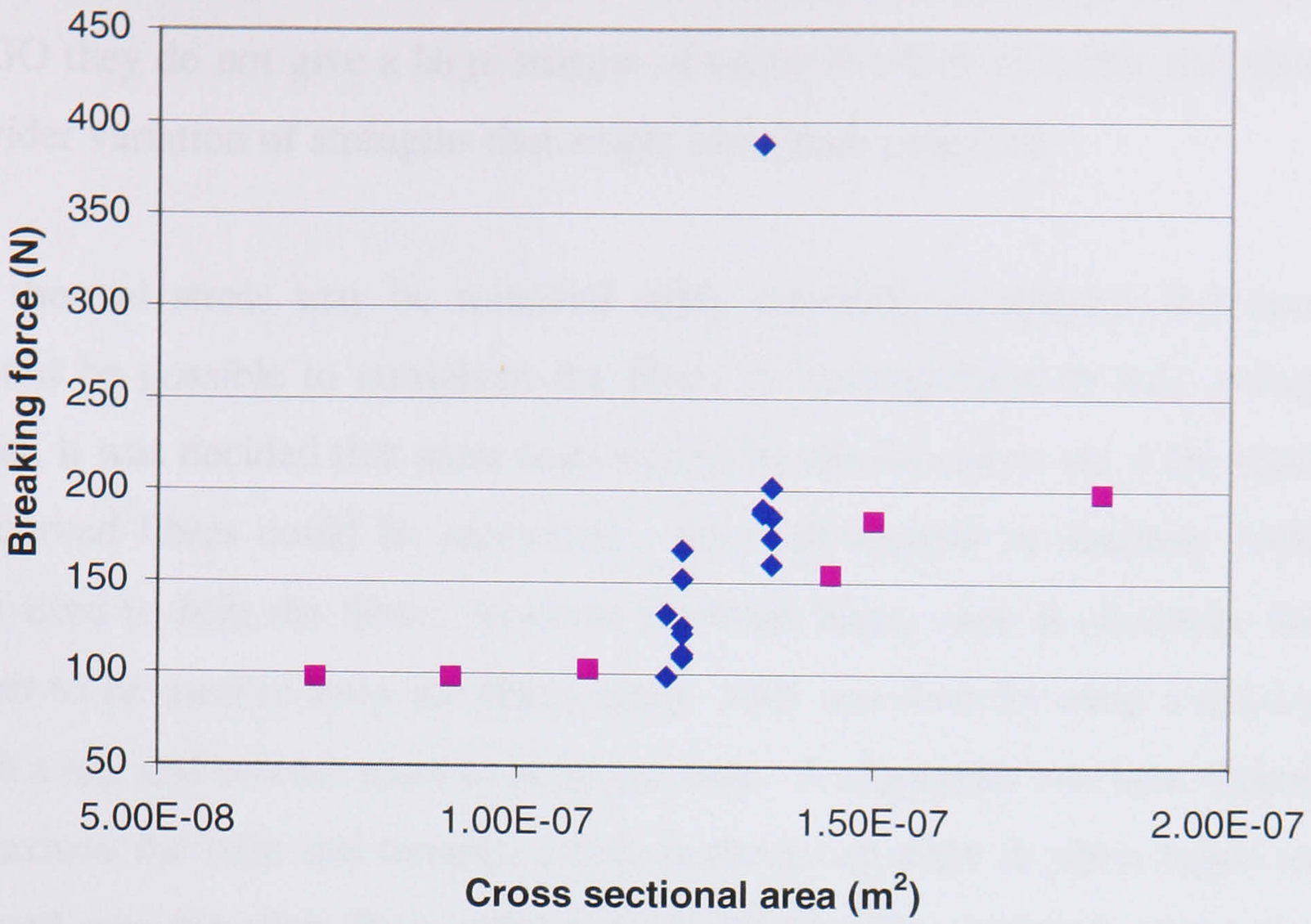

Figure 70: Measurement of breaking force of 60cm fibres. Colour coding as in Figure 69

The average breaking stress for these fibres was 1.24GPa, with the Advanced LIGO sized fibres breaking at an average of 17kg. The spread of breaking stresses was higher than expected, with the standard deviation being 9.9×10^{7} Pa. This is a breaking stress is a low value for fused silica, which in tests on round silica fibres has previously given average values of 3GPa. Initially it was thought that these low values were due to contamination from the flame, however after careful cleaning of the burners no improvement was seen. The stock material itself was also carefully prepared before use using isopropanol. For these reasons it is thought that the low strength comes instead from curvature of the fibre. As the fibre is pulled, differential cooling builds in thermal stresses, which may cause it to bend once cold in the plane of the flat surface of the fibre. This bending makes it difficult to exert a truly longitudinal stress on the fibre, and instead it is likely that one side of the fibre experiences a higher stress, resulting in a low strength being recorded.

The proposed working load for the suspension fibres for Advanced LIGO is 98N per fibre and hence 1Gpa for a fibre of $1\times10^{-7}\,m^{2}$ cross-section. While

none of the fibres broke at a stress lower than the working stress for Advanced LIGO they do not give a large margin of safety in which to work, and showed a wider variation of strengths than might have been expected.

As thermal stress may be removed using annealing techniques and since it should be possible to straighten the fibres by heating them to their softening point, it was decided that some tests should be carried out to see if the strength of curved fibres could be recovered. An oven capable of reaching 1300°C was used to heat the fibres, however the brick lining made it necessary for an insert to be used to keep the fibres clean. This was done by using a silica tube with a top and bottom plate to keep out dust. A silica pipe was then shaped to fit around the tube and through a hole in the lower plate to allow argon to be flowed over the silica fibres when heated. Due to the constraints of the size of the tube however it was not possible to use full size fibres. Instead it was decided that by pulling 15cm fibres from stock that was of half the thickness and half the width it would be possible to obtain fibres with approximately the same cross sectional area that would fit into the oven to be annealed.

Five shorter fibres were then produced by altering the pulling speed and flame temperature and were welded to a piece of silica rod at one end to allow them to be hung in the oven, as shown in Figure 71. Again the fibres appeared slightly bent across their midsection.

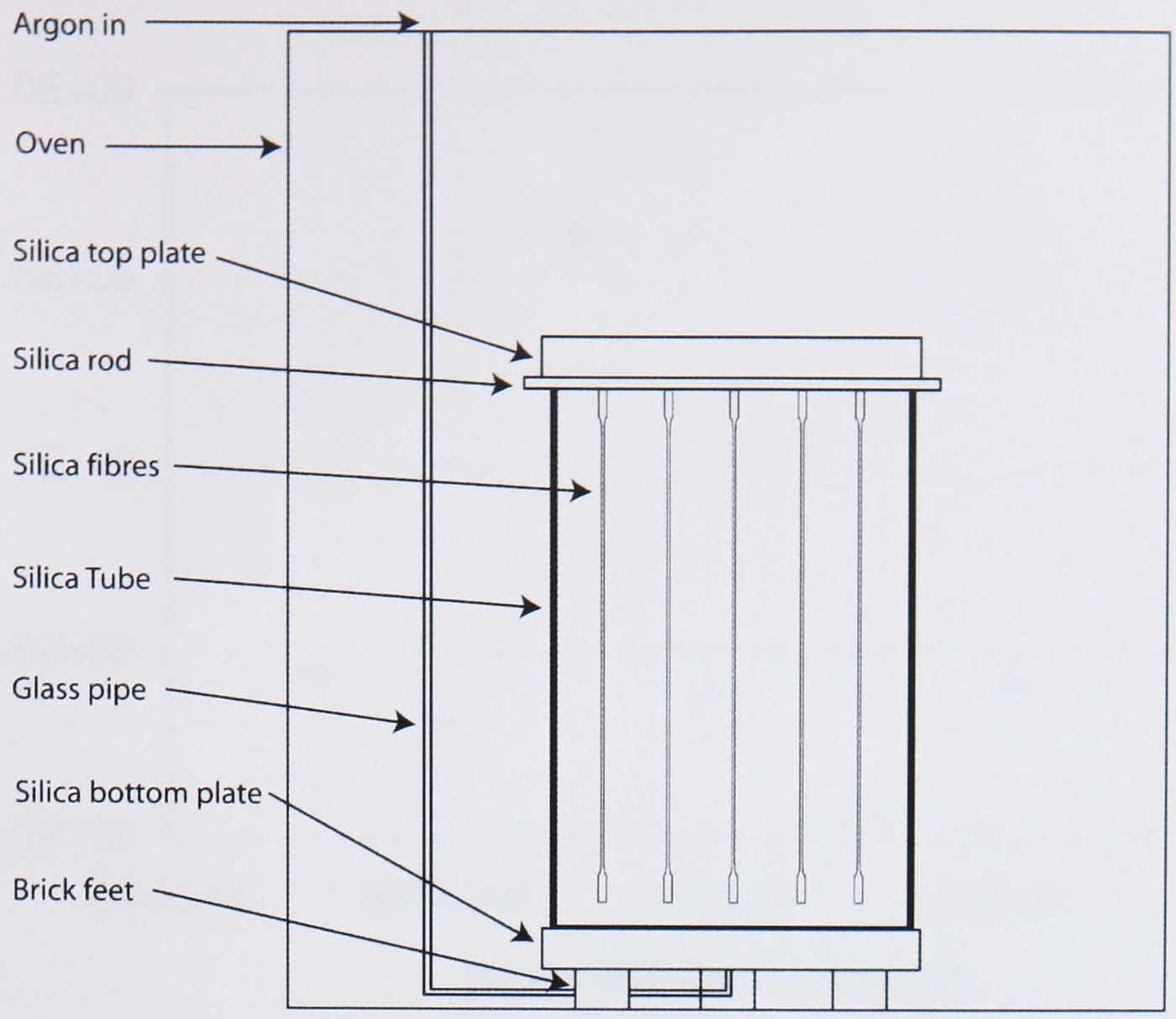

Figure 71: Experimental setup for annealing fibres

The fibres were annealed at a temperature of 1200°C for 24 hours and then brought back down to room temperature of a period of four days. After this they were removed from the oven and upon visual inspection appeared to have straightened without having lost their rectangular shape. The fibres were then strength tested with the results being shown in Figure 72 in blue.

In order to give a direct indication of how the strength was affected by this annealing some shorter fibres were produced but not annealed. These were then tested and gave an average breaking stress of 1.59GPa , which is close to the value found for the larger fibres. These points are shown in Figure 72 in pink.

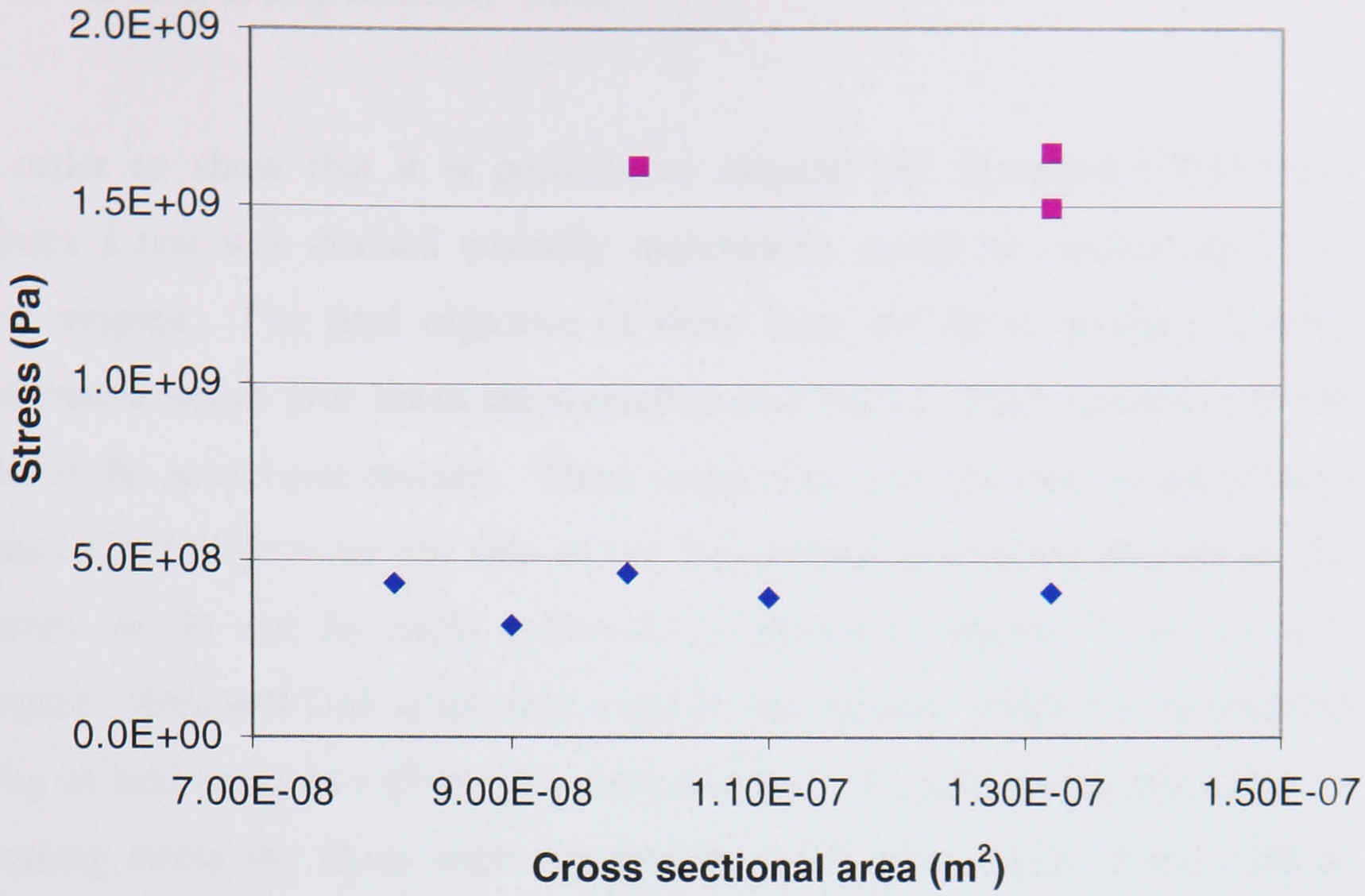

Figure 72: Measurement of breaking stress of 15cm fibres. Points in blue show fibres that were annealed in oven while pink points show fibres that were not annealed

It is clear that after our attempted annealing of the fibres they had in fact decreased in strength with the average breaking stress becoming $4.0\times10^{8}\,\mathrm{Pa}$ with the standard deviation being $3.68\times10^{7}\,\mathrm{Pa}$. As care was taken not to abrade the surface of the fibres during this process it is probable that some impurities were introduced onto the surface of the fibre whilst in the oven, despite our attempts to shield the fibres within the silica tube. It is of interest to note that the spread of results is smaller for the annealed fibres. This would indicate that the most likely cause of failure is due to surface damage from dust in the kiln, with all fibres being exposed to identical conditions during the annealing process. The wider distribution of results seen due to the curvature of the fibres will not be seen here as the annealed fibres had become straightened in the oven and hence the loading during testing should be close to being purely longitudinal.

8.4. 20kg Suspension Test

In order to show that it is possible to suspend the advanced LIGO sized masses a test was devised whereby suspensions would be mocked up using lead weights. The final objective of these tests will be to produce a 40kg suspension where four fibres are welded to ears such as those bonded onto the side of the actual test masses. These small silica ears are used as attachment points for the fibres on the side of the test masses as welding directly to the masses would not be easily achieved, as shown in Figure 75 in the next chapter. Here will look at the first stage of this process, which was to suspend 20kg of lead using two fibres that were clamped. As with the measurement of breaking stress the fibres were clamped by using epoxy resin on the ends in order to apply even pressure on the tail stock with the clamp. The fixture of the clamp to the bottom plate bearing the mass was movable in order to be able to adjust the tension on the fibres individually. With the bottom plate sitting on an adjustable lab-jack it was then possible to slowly put weight onto the fibres.

Figure 73: 20kg test suspension

The completed suspension shown in Figure 73 hung for eight weeks in air before breaking. The cause of the break was unknown but is likely to have either been the result of abrasion of the fibre surface or fatigue of the fibre due to water in the atmosphere.

8.5. Conclusions

The fibres that were not annealed showed a high variation in strengths. This was primarily thought to be due to non-uniform cooling of the fibres causing bending which in turn would create regions where the force was not applied equally across the fibre and thus a true measure of the longitudinal stress was not achieved. It is also possible that some contamination of the fibres led to lowered strengths though steps were taken to try to minimise this. Preliminary tests on fibres that were annealed at high temperature showed that the process used introduced some contamination of the samples, thus lowering the strength significantly.

We may conclude from these measurements that, while a maximum breaking stress of 2.89GPa was seen in one fibre, which was presumably the most defect free, there was inconsistency between fibres giving a wide spread of results and an average breaking stress of $(124 \pm 9.9) \times 10^7$ Pa. Clearly when a full monolithic suspension is produced it is necessary to have a high degree of confidence in the fibres being of high strength. For this reason more work is needed to identify a method for creating fibres whose strength is consistent.

The average strength of the fibres is already beyond the working stress required for the advanced LIGO suspensions, which is below 1Gpa, and a test suspension was created using two fibres to hang half the weight of an advanced LIGO test mass.

Chapter 9

Technology of Pendulum Construction

9.1. Introduction

Having now looked at the possible designs for Advanced LIGO suspensions it is worthwhile discussing the technology behind their construction. A completed monolithic suspension for GEO600, shown in Figure 74, displays something of the art of fused silica pendulum construction where the constituent parts are welded and bonded together. Here we shall look at the techniques employed in this welding and explain why the suspensions for advanced LIGO present an altogether different challenge.

9.2. GEO600 Suspensions

The monolithic suspensions for GEO600 have now been completed and installed at the site. As the only detector currently using such monolithic suspensions, GEO600 will pave the way for the upgrade to other detectors. It is therefore of interest to look at the methods used to create its suspensions.

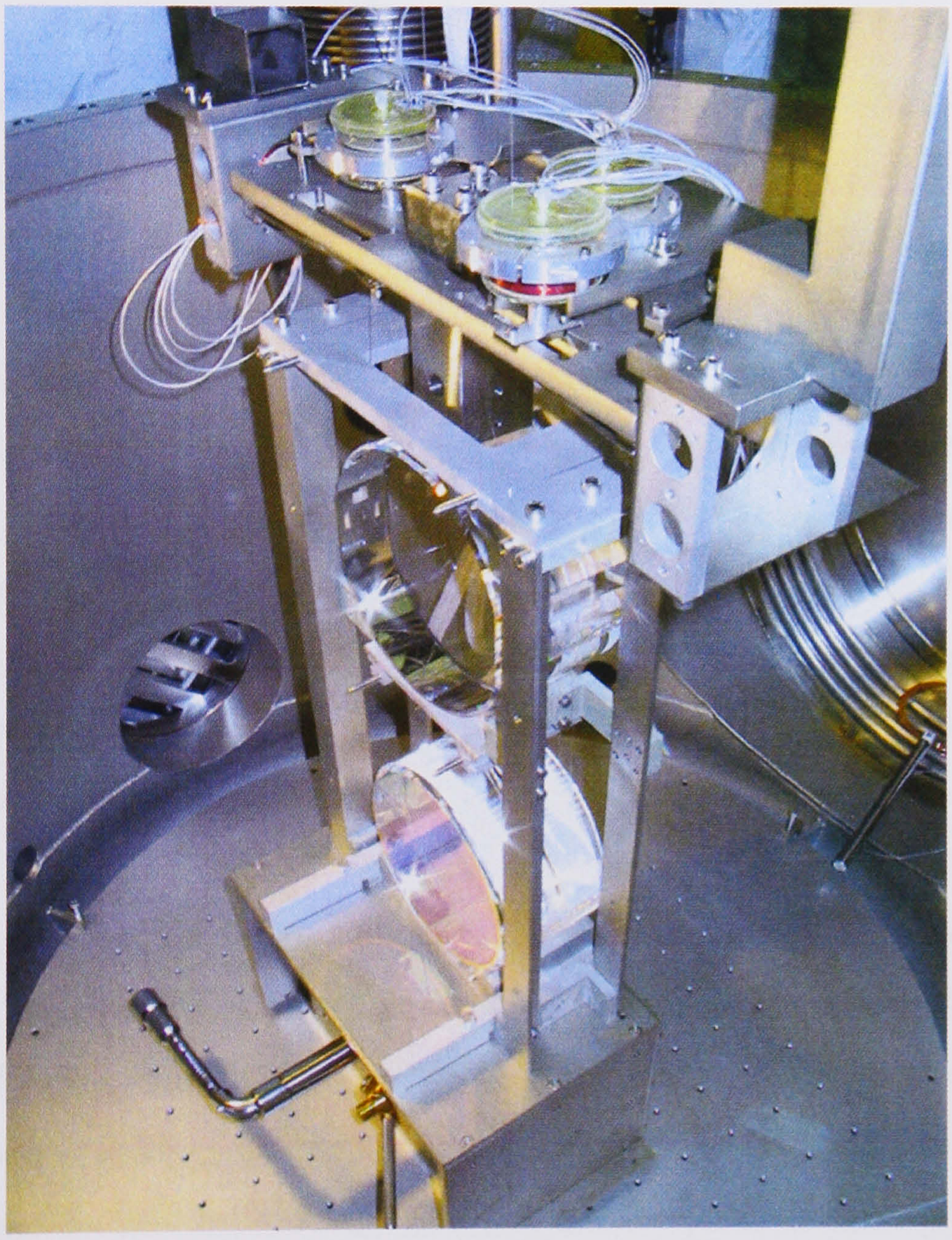

Figure 74: GEO600 triple suspension with monolithic lower section

The masses have small fused silica ears bonded to the sides using the process of hydroxide catalysis bonding [48]. These ears give the attachment points required to weld the fibres onto the mass, with welding directly to the mass being undesirable due to the thermal stress or mechanical loss this would produce. Round fibres are produced, using the automated method described

in Chapter 4, in large numbers in order that matched sets may be obtained. Each fibre is tested to four times its working load before use. They then have their vertical bounce frequency measured in order to match together fibres that are close in shape. Using a jig the fibres are cut at the neck to the same lengths and have Teflon applied at two points on their length. The Teflon is used to lower the Q of the violin modes in order to stop these becoming heavily excited. As it is applied well away from the ends of the fibre it will not affect the Q of the pendulum mode.

The fibres are now welded into place using an electrolytic hydrogen-oxygen burner. The test mass and intermediate mass are held in a jig and the fibres are welded using the thicker neck region onto the tips of the ears. Where necessary, extra silica may be let into the weld. During this process the ears are cooled at periodic intervals using a damp cloth. Once the fibres are in place a small amount of tension is applied by lowering the bottom mass. The welds are then reheated to their softening point in order to even out the tension on each fibre. Care is taken to ensure the whole width of the weld is melted, even at the centre of the neck, as the strength may be greatly affected by a weld that is not continuous, as may the loss. Figure 75 shows a completed weld to a bonded ear.

The main advantage of this design of suspension is that it is possible to achieve high strength suspensions without the need to anneal the welded regions. Despite thermal stresses affecting the welds the cross sectional area at these points is large, giving a lower working stress from the tension in the fibres. Also because no bending takes place at the point of the weld its shape does not affect the suspension.

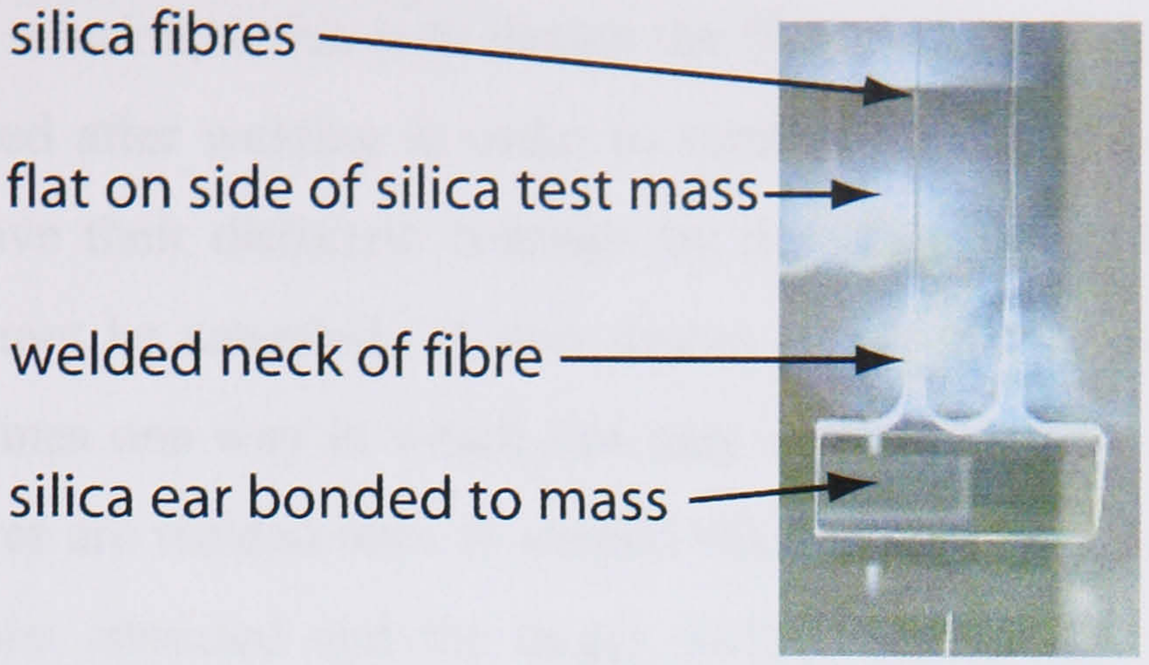

Figure 75: Fused silica ear silicate bonded onto a flat on the side of a GEO600 test mass. The fused silica fibres used to suspend the mass are welded onto the tips of the ear using the end or neck region of the fibre.

9.3. Advanced LIGO Suspensions

The suspensions for advanced LIGO will take the technology used in GEO600 and stretch it as far as possible in order to achieve the performance required. We know already that the suspensions will operate at a working stress three times higher than that used in GEO600 using fibres with a higher surface area to volume ratio due to the rectangular shape, in order to give high dilution factors.

The requirement of a high dilution factor also means that fibres must be welded without necks, as was the practise for GEO600, in order to give the fibre more compliance in the pendulum mode. This then leads to a number of difficulties in producing the suspension. Firstly the region that is welded has a small cross sectional area and is therefore more affected by thermal stress due to the increased load parts of it are under. Secondly any deformation of the welded region may affect the actual fibre, which will tend to become circular again. Thirdly the region where the weld occurs will also be the point where stresses are greatest if the masses tilt and are therefore more likely to fail than a gradually tapering neck. Yet despite these issues the suspensions must remain reliable when under load and indeed give some margin for safe working.

Our proposed solution to this is to design the fibre and ear section such that it may be annealed after welding in order to remove the thermal stress. As the masses will have their dielectric coatings by this stage, the whole completed suspension cannot be annealed. A new design of ear may solve this problem. Figure 76 outlines one way in which this may work in practise. In this figure we see the fibres are welded onto H-shaped silica blocks top and bottom. This assembly is then annealed and the larger surface area of the bottom of the block is used to weld onto the ears of the mass. The bar of the H-shaped block may then be removed. The advantages of this technique would be that it not only allows annealing of the fibre welds but also gives a prefabricated unit which may be strength tested without risking damage to the mass. While being attached to the mass the fibres will be held at exactly the correct separation by the bar giving more flexibility for the fibre separation which otherwise must be reasonably large.

An alternative method would be to use an adaptation of the technique of using pins to join fibres to masses, as discussed below. In this case the fibre is welded to a block, top and bottom and annealed separately from the other fibre of the pair. This then results in a situation similar to the welding done at GEO600 as each fibre is separate. While this does mean that it is more difficult to perform the welding to the mass, as the fibre ends may move independently, it does give the advantage that the fibres are welded separately.

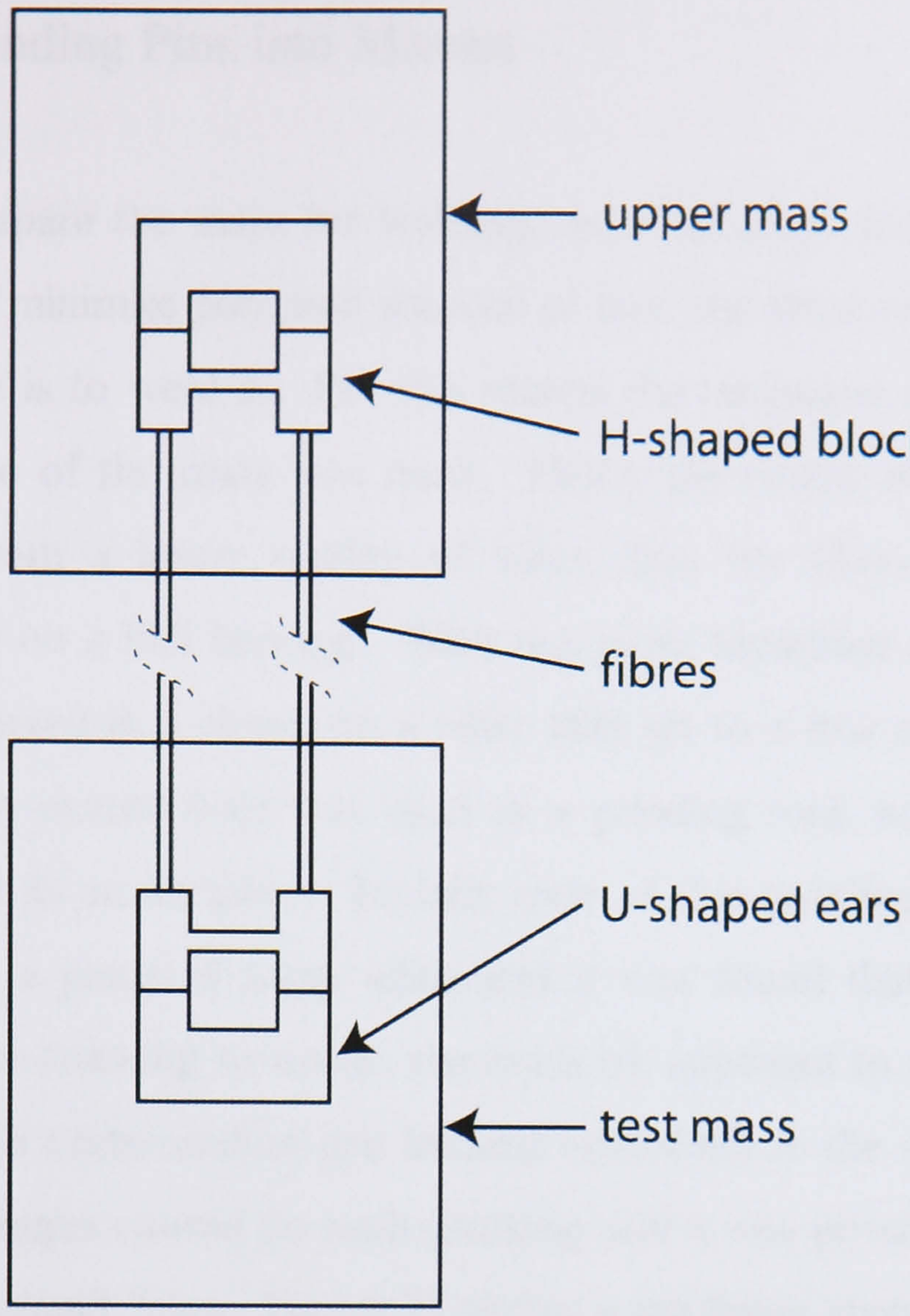

Figure 76: Suggested design for ear attachment points

Currently experimental work is being carried out on using CO_2 lasers to weld fibres. This gives the advantage that the fibre will be less likely to deform and some degree of annealing can be carried out. This annealing effect will be similar to the use of a diffuse flame discussed below, however here it will be a diffuse laser beam that is dithered over the region. Also a major advantage over flame welding is that, as long as the volume heated is small, the laser will heat the bulk of the block to the same temperature as the fibre.

9.4. Construction of Test Suspensions

Suspensions tested in this thesis were constructed using very similar techniques. In each case the fibres were attached to pins in the masses by welding and it is this process that we shall now discuss.

9.4.1. Grinding Pins into Masses

In order to prepare the mass for welding, an attachment point was required. As we wish to minimise potential sources of loss, the ideal way of attaching a mass to a fibre is to weld it. For this reason the technique of grinding a pin into the surface of the mass was used. Firstly the centre of the face of the mass, made from a lower quality of silica than the fibres, was found by balancing them on a ball bearing. With this point identified and marked they were then mounted in a clamp on a pillar drill set to a low speed. A round brass bit with a central hole was used as a grinding tool, with carborundum grit being used as an abrasive. Initially tests of this grinding technique were carried out on a piece of scrap silica and it was found that, while the first attempts caused cracking to occur, the brass bit appeared to smooth with use and some of the carborundum grit became embedded in the surface such that subsequent attempts caused no such cracking and it was possible to make pins of a depth of around 7mm. Figure 77 shows a pin being ground for the lower mass used in the violin mode experiment, while Figure 31 in Chapter 5 shows the mass after the pin has been produced.

Figure 77: Machining pin into mass using brass bit mounted in a pillar drill.

After machining the pin and cleaning with acetone and methanol, the surface of the pin was heated to its softening point to remove any surface defects and to look for any contamination of the surface, which would glow in the flame of the gas torch.

9.4.2. Producing Pins for Attachment of Fibres

The pins ground into the surface of the mass are too close to the surface to directly attach the fibre. For this reason small silica pins were produced which were welded onto the top and bottom of the fibres. This also allowed the mass in the pendulum mode measurement and the vertical bounce mode measurement to be changed easily to give different dilutions without altering the weld of the fibre to the pin.

The pins used in the vertical bounce mode experiment were simply made using short sections of round rod, approximately 7mm in length, as the round fibres were narrow enough to weld directly onto the side without any further machining. Those used in the pendulum mode experiment were similar, however since a rectangular cross section fibre was used the pins were machined using a grinding tool to create a flat surface on one side onto which the fibre could be welded without altering its shape significantly. Finally the pins used in the violin mode experiment were made by cutting small sections of silica slide to approximately 7mm by 3mm by 1mm. These then gave a flat surface onto which to weld the fibre while still being thick enough to easily weld onto the mass. The surface of the pins were heated to their softening point using a gas flame before use to remove surface defects.

9.4.3. Welding the Suspension

With the pin held in a vice and the fibre held in a retort stand the fibre was carefully lined up against the side of the pin with an overlap of around 3mm. When close enough the air pressure holds the fibre against the pin. The pin

was then heated, starting from the side opposite the fibre using a large flame. The flame was slowly brought closer to the fibre until it was tack welded onto the pin. At this point a smaller flame was used closer to the position of the fibre to heat the pin until a solid weld was formed. Generally no direct heating of the fibre was required as this quickly results in the fibre becoming misshapen and does not heat the bulk material of the pin to a high enough temperature. The rectangular cross section fibres would tend to become circular in the region where they were heated. The welded fibres show a whitening of the surface close to the weld, which may be a result of vaporised silica being deposited back on the surface of the fibre.

The thermal stress in the welded regions was then diffused over a larger length of fibre by working over the welded region using a diffuse hydrogen flame to heat the fibre until it glowed. While it is possible to achieve a strong enough weld for small suspensions, such as the 2.4kg mass used in the violin mode measurement, a higher stress would be difficult to achieve without fully annealing the weld.

The fibres, with pins attached were then welded onto the masses, which were held in catchers. This was relatively simple by comparison as the cross sectional area was large and required only that a large enough amount of heat be delivered without cracking the mass. A completed weld can be seen in Figure 78, where we may contrast it with the relatively simple welding of a fibre using a neck.

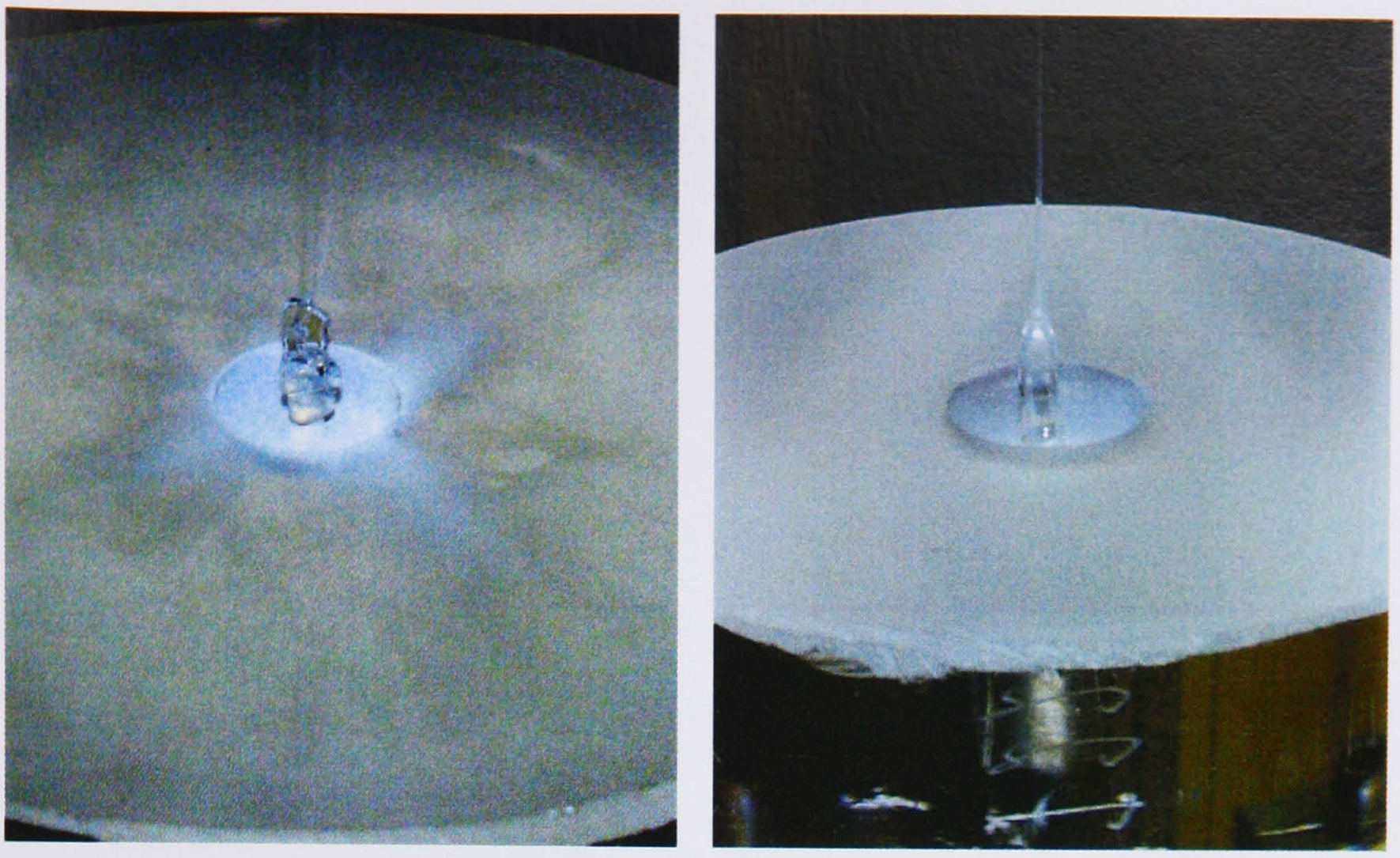

Figure 78: Image on left shows ribbon fibre welded to rectangular pin which in turn is welded onto pin ground from the mass. Image on right shows a round fibre with neck welded directly to the pin of a mass

After welding the suspensions were then transferred to the vacuum tanks where they were bolted rigidly in place. The difficulty of welding suspensions is such that it is usually easier to design the experiment in advance to allow the suspension to be created outwith the tank.

9.5. Conclusions

The construction of suspensions for Advanced LIGO is a major undertaking which will push the boundaries of technologies used to create suspensions for GEO600. In this chapter we have discussed possible solutions to the problem of welding without using the fibre neck, however more experimental work will be needed to develop a complete technique for producing strong welded regions.

Also discussed here are the techniques used to produce suspensions used elsewhere in this thesis. Many of these techniques have direct implications for producing the Advanced LIGO suspensions and provide an opportunity to test and practice welding fused silica suspensions.

Chapter 10

Conclusions

Reducing the effects of thermal noise at detection band frequencies is one of the most challenging areas of research for scientists pursuing direct detection of gravitational waves. With the construction of the suspensions for GEO600 a major step forward was taken in fabrication techniques for monolithic pendulums that we now seek to push to their limits for the Advanced LIGO upgrade. Key parts of the design are the ultra low loss suspension fibres that will bear the weight of the 40kg test masses. Work presented in this thesis is concentrated on the characterisation of these suspension fibres in preparation for the construction of the Advanced LIGO pendulums.

The mechanical loss of fused silica fibres was measured using three separate experiments, designed to look at different modes of oscillation of the fibres, these being the pendulum, vertical, violin and cantilever modes.

Measurement of the unloaded or cantilever bending modes of ribbon fibres were measured giving an average material loss of 1.85×10^{-7} and allowing a fit of the thermoelastic loss to give a value for the Young's modulus of 5.17×10^{10}. The violin modes of fibres held in tension gave Q values of up to 1.5×10^{8} which while amongst the highest values ever measured do not reach the theoretical dilution levels. Characterisation of other loss mechanisms has shown that these should not contribute at a high enough level to cause the dissipation to be this high. It is thought that this may be due to the tension concentrating the bending closer to a more dissipative end region of the fibre by shortening the bending length.

Measurement of the loss of the linear pendulum mode of two suspensions gave the highest Q values yet measured at 1.40×10^{8} and 1.27×10^{8}. Analysis of the results allowed the contribution of recoil loss to be calculated and a pendulum loss factor to be found for each, these being 1.97×10^{8} and 6.33×10^{8} respectively. Again the dilution calculated does not appear to reach the levels measured, assuming a similar material loss to that measured for the cantilever bending modes.

The results of the vertical bounce mode loss measurements show no sign of stress dependence of the mechanical loss of fused silica and further show evidence that the loss is concentrated in the surface layer of the fibre with little loss coming from the bulk.

While the material loss is already within the limits required for the Advanced LIGO suspensions, they must also achieve close to the theoretical dilution value in order to keep the suspension thermal noise from limiting sensitivity. Thus further research is needed to fully understand the excess loss mechanisms seen here.

Measurements of the strength of the fibres has shown that while breaking stress of up to 2.89GPa were achievable, the variation in strengths was considerable, with the average breaking stress being 1.24GPa. While this

value is above the working stress of the Advanced LIGO suspensions, which require below 1Gpa, it does not leave significant margin for safety. The spread of results was thought to be caused by the variation in shape of the fibres tested causing some of the loading to result in shear stresses.

Finally we have discussed the construction techniques proposed for the Advanced LIGO suspensions as well as the future plans to use a CO_2 laser to produce and weld the fibres in suspensions which should prove more reproducible and give more homogeneous fibres.

Appendix A

The Beam Equation

A.1 Introduction

The beam equation is the equation of motion for a solid beam whose length is large compared to its thickness and may be used to closely model the behaviour of a uniform fibre. We also require two other conditions to be met, these being that the displacement, u, is small and that the gradient, $\frac{\partial u}{\partial x}$, is small at each point along the beam.

A.2 Derivation of the Beam Equation

If we consider a beam that is bending and look at the forces at one point, as shown in Figure 79 we see that to describe an acceleration of the right hand section we must define a shearing force T and that to describe the rotation of

the right hand section we must define a torque on the left edge of this section G. For there to be no discontinuity across this point, the left hand section must experience an equal and opposite force and torque.

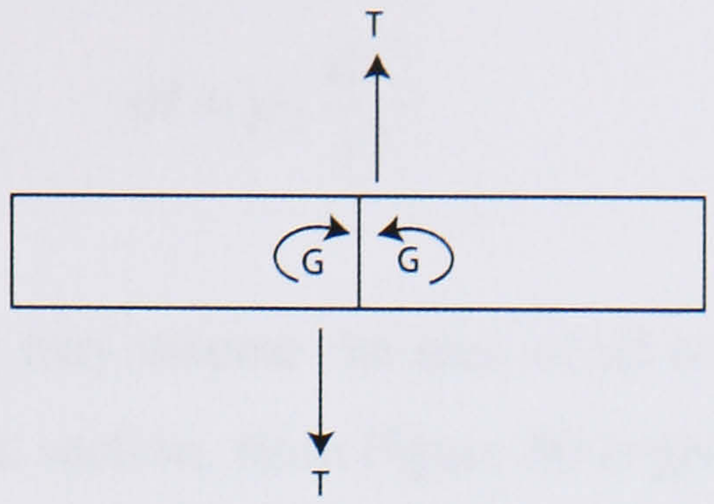

Figure 79: Forces on one point of a beam

If we consider the forces acting on one small section of the beam, dx as it is deflected. The section will experience both shearing forces and torques as shown in Figure 80.

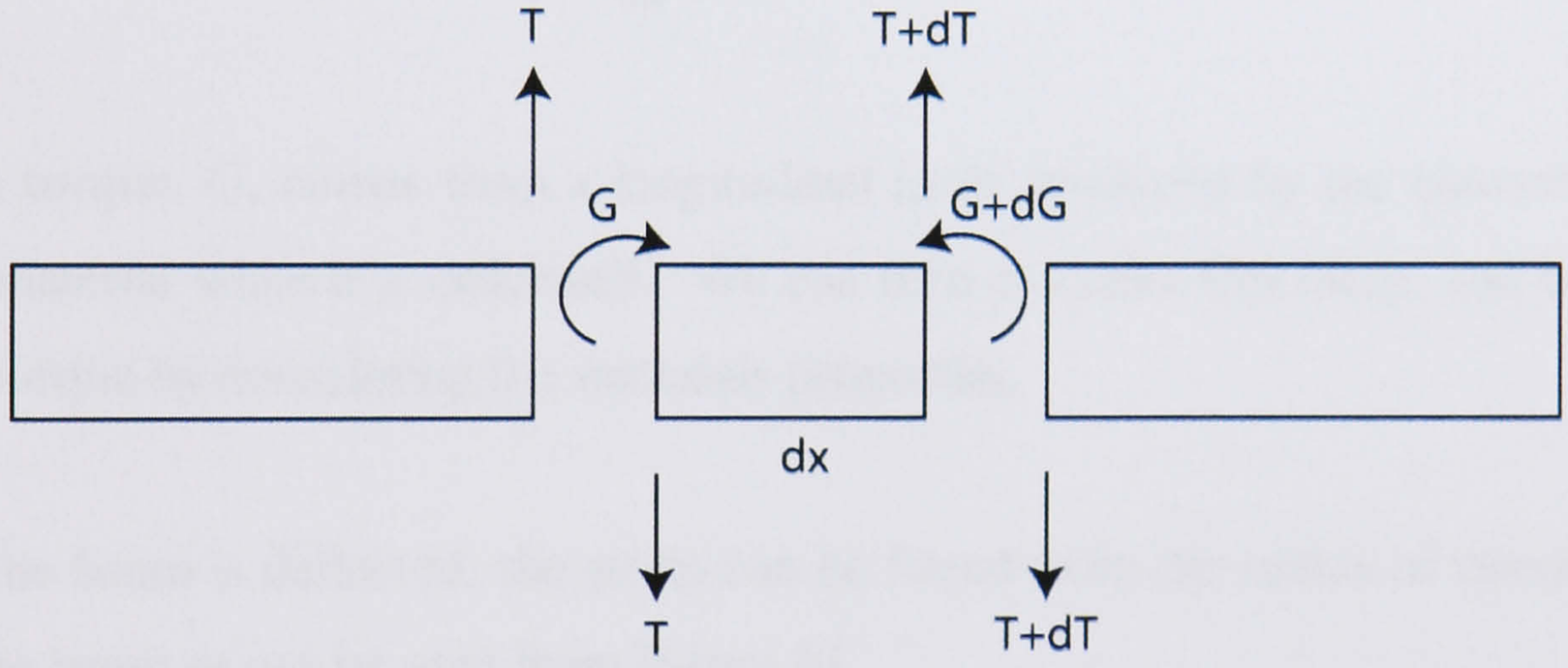

Figure 80: Forces experienced by element dx of beam

Any unbalanced forces acting on this section, such as the shearing force will produce an acceleration.

$$\sum F = -T + T + dT = \frac{\partial T}{\partial x} dx = \partial m \cdot a = \rho_L \cdot dx \cdot a \tag{80}$$

$$\frac{\partial T}{\partial x} = \rho_L a \tag{81}$$

where ρ_L is the linear mass density. The moment of inertia of this section is given by:

$$\partial I = \rho_L \frac{dx^3}{12} \tag{82}$$

and is so small that we may assume the sum of all torques on the element is zero. The torque on this section, from Figure 80 is given by $-G + G + dG$. If we consider the moment of the shearing force about the left hand end of the section we find that there is another torque equal to $(T + dT)dx$ produced. For these torques to sum to zero we have:

$$-G + G + dG + (T + dT)dx \approx dG + Tdx = 0 \tag{83}$$

$$\frac{\partial G}{\partial x} = -T \tag{84}$$

This torque, G, comes from a longitudinal force produced by the elasticity of the material when it is deformed. We can then calculate this force, and hence the torque by considering the materials properties.

As the beam is deflected, the strain can be found from the radius of curvature of the beam as can be seen from Figure 81.

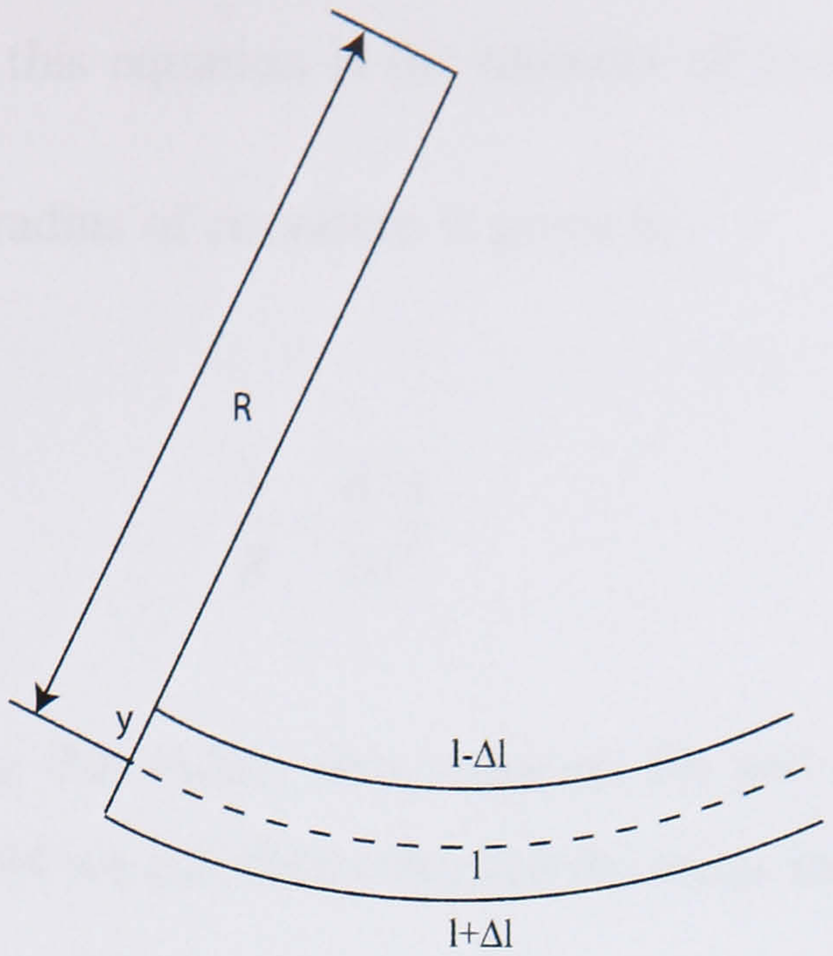

Figure 81: Longitudinal strain in beam

Where the ratio of stretched to unstretched length is given by:

$$\frac{l-\Delta l}{l}=1-\frac{\Delta l}{l}=\frac{R-y}{R}=1-\frac{y}{R} \tag{85}$$

where y is the distance from the middle line on the bending plane. The strain is found to be:

$$\varepsilon_x=\frac{\Delta l}{l}=\frac{y}{R} \tag{86}$$

From this strain, using the materials Young's modulus, E, we can find the force produced through the following surface integral over the beam cross section.

$$F=\frac{E}{R}\iint y\,dS \tag{87}$$

Hence the torque is given by multiplying the force by the distance from the x axis:

$$G=\frac{E}{R}\iint y^2\,dS \tag{88}$$

The term $\iint y^2 dS$ in this equation is the moment of inertia I. If the gradient $\frac{\partial y}{\partial x}$ is small then the radius of curvature is given by:

$$\frac{1}{R} = \frac{\partial^2 y}{\partial x^2} \tag{89}$$

Hence by substituting this radius into equation 88 and then substituting this torque into equation 84 we can then calculate the shear force:

$$T = -\frac{\partial G}{\partial x} = -EI\frac{\partial^3 y}{\partial x^3} \tag{90}$$

and from this we find that the equation of motion for the beam is

$$-EI\frac{\partial^4 y}{\partial x^4} = \rho_L a \tag{91}$$

We may take this one step further by looking at the case where there is tension in the beam. Here we find another longitudinal force, which from Figure 82 has a lateral component.

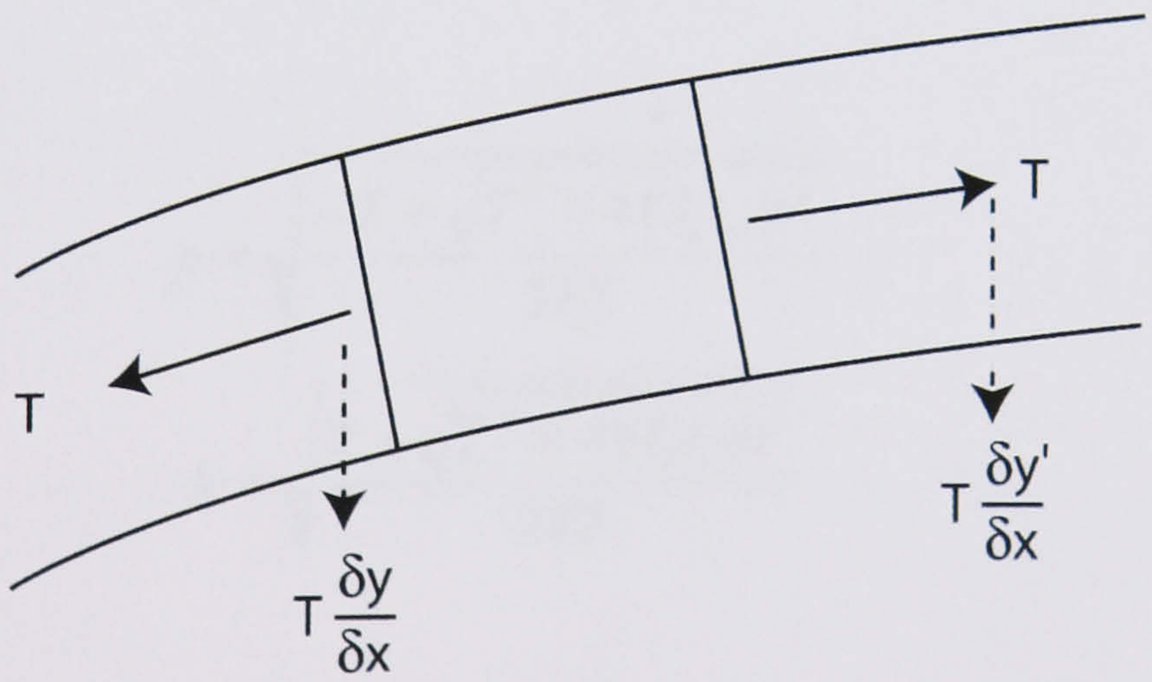

Figure 82: Lateral force produced by tension on element dx

Hence the total lateral force on the element from the tension is:

$$T\left[\frac{\partial y'}{\partial x}-\frac{\partial y}{\partial x}\right]=T\Delta\left(\frac{\partial y}{\partial x}\right)=T\frac{\partial^2 y}{\partial x^2}dx \tag{92}$$

From this we may then write the completed form of the beam equation as:

$$-EI\frac{\partial^4 y}{\partial x^4}+\frac{\partial^2 y}{\partial x^2}T=\rho_L\frac{\partial^2 y}{\partial t^2} \tag{93}$$

We may then assume that the motion is SHM and hence:

$$Y(x,t)=Y(x)e^{i\omega t} \tag{94}$$

and we may write:

$$-EI\frac{\partial^4 y}{\partial x^4}+T\frac{\partial^2 y}{\partial x^2}+\rho_L\omega^2 y=0 \tag{95}$$

solutions will then be of the form:

$$y(x)=ae^{-kx}+be^{k(x-l)}+c\sin(px)+d\cos(px) \tag{96}$$

where :

$$p=\sqrt{\frac{-T+\sqrt{T^2+4EI\rho_L\omega^2}}{2EI}} \tag{97}$$

$$k=\sqrt{\frac{T+\sqrt{T^2+4EI\rho_L\omega^2}}{2EI}} \tag{98}$$

By then applying boundary conditions we may find specific solutions.

A.3 Calculation of Violin Mode Frequencies

The fibre in our violin mode loss measurement may be considered to be held fixed at both ends due to the inertia of the masses. We may then write the boundary conditions for the solution to the beam equation as follows:

$$\begin{aligned} Y(0) &= 0 \\ Y'(0) &= 0 \\ Y(l) &= 0 \\ Y'(l) &= 0 \end{aligned} \tag{99}$$

These conditions correspond to a system of four linear equations:

$$\begin{aligned} a + d &= 0 \\ -ka + pc &= 0 \\ b + c\sin\ pl + d\cos pl &= 0 \\ kb + pc\cos pl - pd\sin\ pl &= 0 \end{aligned} \tag{100}$$

There is a non-trivial solution for the coefficients a, b, c and d only where the determinant of the characteristic matrix M is zero:

$$M = \begin{bmatrix} 1 & 0 & 0 & 1 \\ -k & 0 & p & 0 \\ 0 & 1 & \sin\ pl & \cos pl \\ 0 & k & p\cos pl & -p\sin\ pl \end{bmatrix} \tag{101}$$

$$\det(M) = 2kp\cos pl + \left(p^2 - k^2\right)\sin\ pl = 0 \tag{102}$$

hence:

$$\tan pl = \frac{2kp}{k^2 - p^2} \tag{103}$$

If we now introduce the two parameters of speed, c, and bending length, λ, we may rewrite this as:

$$\tan pl = 2\frac{\lambda}{c}\omega \tag{104}$$

where

$$c = \sqrt{\frac{T}{\rho_L}} \tag{105}$$

$$\lambda = \sqrt{\frac{EI}{T}}$$

The speed, c, is given by the well known expression for transverse waves in a string under tension. λ is equal to $1/k$ in the limit $\omega \to 0$ and the reason why it is known as the bending length is described in Appendix B. If we then consider the shape of the function on the right of this equation we see that we have a linear function of ω with a gradient that for most practical cases is small ($<10^{-6}$). If we then plot the two sides of this function, as is shown in Figure 83 we see the crossing points where our solution lies.

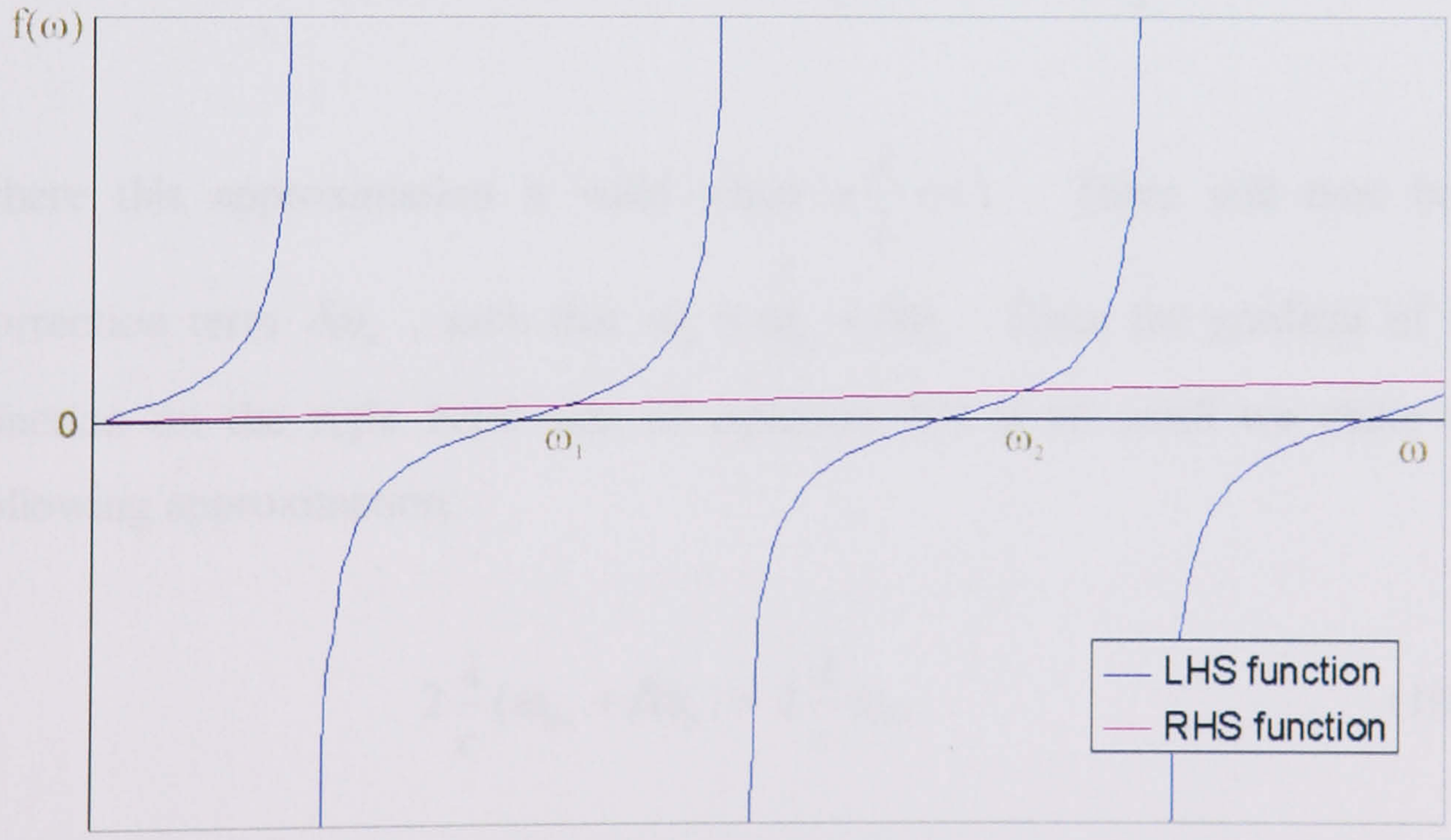

Figure 83: Left and right hand functions of equation 104. The gradient of the right hand side is exaggerated to make it visible above the x-axis.

If we then look at a closer view of one of these crossing points, as shown in Figure 84, we find that an approximate value for ω may be found by setting $\tan pl = 0$, giving a value ω_{0n}.

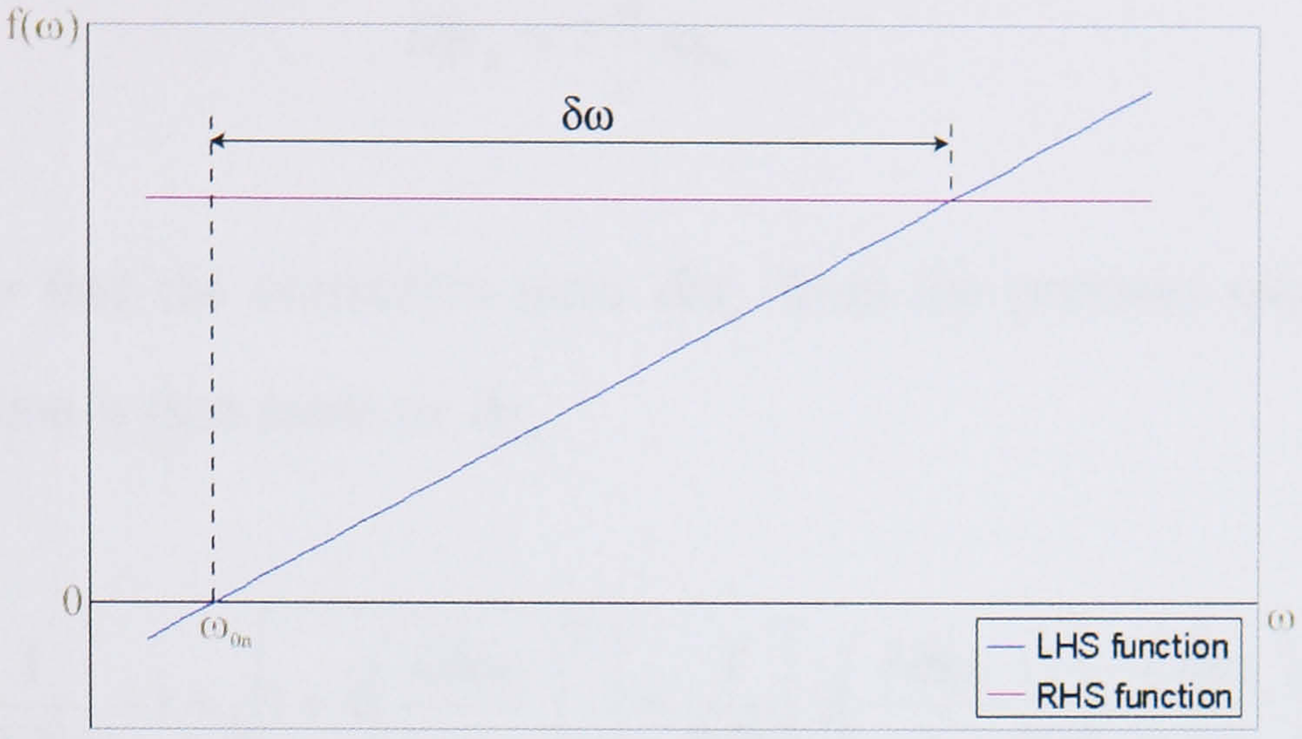

Figure 84: Left and right hand functions of equation 104, plotted close to cross over point

An exact solution to $\tan pl = 0$ may be found and gives

$$\omega_{0n} = n\pi\frac{c}{l}\sqrt{1+\left(n\pi\frac{\lambda}{l}\right)^2} \cong n\pi\frac{c}{l}\left[1+\frac{1}{2}\left(n\pi\frac{\lambda}{l}\right)^2\right] \tag{106}$$

where this approximation is valid when $n\frac{\lambda}{l} << 1$. There will then be a correction term $\delta\omega_n$, such that $\omega_n = \omega_{0n} + \delta\omega_n$. Since the gradient of the function on the right hand side of equation 104 is so small we make the following approximation:

$$2\frac{\lambda}{c}(\omega_{0n} + \delta\omega_n) \approx 2\frac{\lambda}{c}\omega_{0n} \tag{107}$$

and as the tangent function is being evaluated close to zero we may make the following approximation:

$$\tan l\delta p_n \approx l\delta p_n \tag{108}$$

We may then write:

$$l\delta p_n = 2\frac{\lambda}{c}\omega_{0n} \tag{109}$$

In order to find the correction term $\delta\omega_n$ from the previous expression, an approximation is then made to δp_n:

$$\delta p_n{}^2 = \frac{1}{2\lambda^2}\left[-1+\sqrt{1+4\left(\frac{\lambda\delta\omega_n}{c}\right)^2}\right] \approx \frac{1}{2\lambda^2}\left[2\left(\frac{\lambda\delta\omega_n}{c}\right)^2\right] = \left(\frac{\delta\omega_n}{c}\right)^2 \tag{110}$$

giving the correction term:

$$\delta\omega_n = 2\frac{\lambda}{l}\omega_{0n} \tag{111}$$

where, taking only the dominant term of the expression for ω_{0n} we have:

$$\partial\omega_n = 2n\pi\frac{c\lambda}{l^2} \tag{112}$$

This then gives the full expression for ω_n as [70]:

$$\omega_n = n\pi\frac{c}{l}\left[1+2\frac{\lambda}{l}+\frac{1}{2}\left(n\pi\frac{\lambda}{l}\right)^2\right] \tag{113}$$

And the frequencies of the modes are then given by:

$$f_n = \frac{n}{2l}\sqrt{\frac{T}{\rho_l}}\left[1+\frac{2}{l}\sqrt{\frac{EI}{T}}+\frac{EI}{2T}\left(\frac{n\pi}{l}\right)^2\right] \tag{114}$$

Appendix B

A Model for a Bending Fibre

B.1 Introduction

In Appendix A we derived both the beam equation and a solution to the beam equation using the boundary conditions for a fibre held in tension. In this appendix we shall now consider the case of a fibre held fixed at one end with the other free to move and shall look at a model that may be used for the bending.

B.2 Exact Calculation Using The Beam Equation

If the free end of the beam is displaced it produces a restoring force and torque which may be calculated using the beam equation. The equation of the beam we shall use here is of the form:

$$-EI\frac{\partial^4 y}{\partial x^4}+T\frac{\partial^2 y}{\partial x^2}=0 \qquad (115)$$

With respect to the beam equation found in Appendix B, the inertial term has been considered negligible at low ω. The general solution we shall use is of the form:

$$Y(x) = Ae^{-\frac{x}{\lambda}} + Bx + Ce^{-\frac{(l-x)}{\lambda}} + D \tag{116}$$

since we wish only to look at the first cantilever mode. Here λ is the bending length of the fibre and may be written as

$$\lambda = \sqrt{\frac{EI}{T}} \tag{117}$$

The boundary conditions are then:

$$\begin{aligned} Y(0) &= 0 \\ Y'(0) &= 0 \\ Y(L) &= \delta \\ Y'(L) &= \beta \end{aligned} \tag{118}$$

where δ is the displacement and β is the rotation of the end of the fibre. From this the coefficients A, B,C and D may be found to be:

$$A = \frac{\delta - \lambda\beta}{\frac{L}{\lambda} - 2} \tag{119}$$

$$B = \frac{A}{\lambda} \tag{120}$$

$$C = \frac{-\delta + (L - \lambda)\beta}{\frac{L}{\lambda} - 2} \tag{121}$$

$$D = -A \tag{122}$$

Giving the solution:

$$Y(x)=\frac{1}{\left(\frac{L}{\lambda}-2\right)}\left[(\delta-\lambda\beta)\left(e^{-\frac{x}{\lambda}}-1+\frac{x}{\lambda}\right)+(-\delta+(L-\lambda)\beta)e^{-\frac{L-x}{\lambda}}\right] \tag{123}$$

This bending is shown in Figure 85.

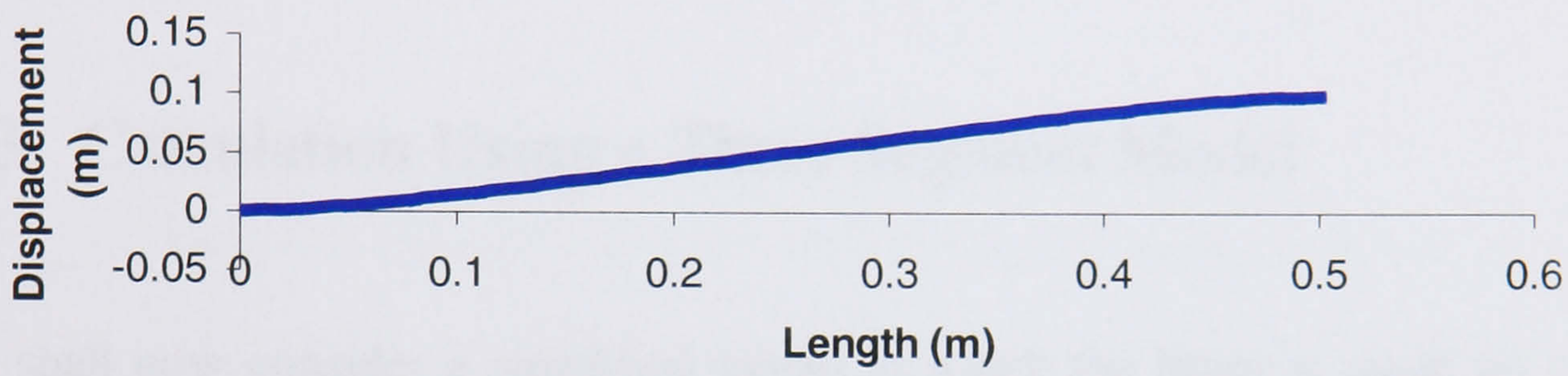

Figure 85: Beam whose displacement has been calculated using the beam equation for values $\lambda = 0.05\text{m}$, L=0.5m, $\delta = 0.1$ and $\beta = 0.001$.

We may then calculate the force generated by shearing of the beam. From Appendix B we see that this comes from both the elasticity of the material and the tension in the beam:

$$F = EIY'''(L)-TY'(L) \tag{124}$$

which may then be given as:

$$F = T\left(\lambda^2 Y'''(L)-\beta\right) \tag{125}$$

Upon substitution of our solution for $Y(x)$ we then obtain:

$$F = T\left[-\frac{\delta-\lambda\beta}{L-2\lambda}\right] \tag{126}$$

The torque at this point is given by:

$$\tau = -EIY''(L) \tag{127}$$

Since the tension cannot produce a torque at this point the only term here comes from the elasticity of the fibre. Upon substitution of our solution for $Y(x)$ we obtain:

$$\tau = -\frac{T\lambda}{L-2\lambda}[-\delta + (L-\lambda)\beta] \tag{128}$$

B.3 Calculation Using a Three Segment Model

We shall now consider a simplified model in which the beam is made up of three straight sections. The top section does not bend relative to the fixed point at the top while the bottom section does not bend relative to any mass attached to it. The central section of the fibre is then given as the total length minus twice the bending length:

$$L^{+} = L - 2\lambda \tag{129}$$

It is fundamental to notice that the tension is applied to the ends of this central section, not the ends of the whole fibre. We then give the displacements and angles of each section as shown in Figure 86.

The horizontal force due to the tension applied at the lower hinge is found as follows:

$$F = -T\alpha = -T\frac{\xi}{L^{+}} = -T\frac{\delta - \lambda\beta}{L-2\lambda} \tag{130}$$

in agreement with the exact calculation given above.

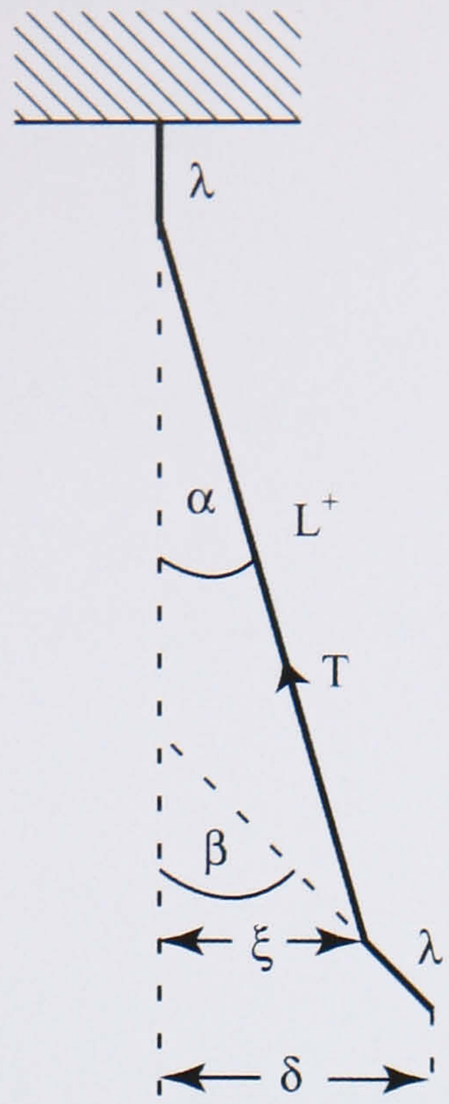

Figure 86: Equivalent model to a bending fibre using segments

If we then consider the moment the tension in the middle section of the fibre produces about the end we calculate the torque to be:

$$\tau = -T(\beta - \alpha)\lambda = -\frac{T\lambda}{L - 2\lambda}[-\delta + (L - \lambda)\beta] \tag{131}$$

which again is in agreement with the torque calculated using the beam equation. We therefore conclude that this model may be used when calculating the torque and force generated at the end of a displaced beam.

Appendix C

Potential Energy in a Deformed Beam

The potential energy of a deformed beam may be expressed by the transverse displacement and angle of the end of the beam as follows:

$$V = \frac{1}{2}k_{11}\delta^2 + \frac{1}{2}k_{22}\alpha^2 + k_{12}\delta\alpha \tag{132}$$

In this appendix the coefficients, k_{11}, k_{12} and k_{22}, are calculated to give the full expression for the potential energy.

We begin by using the beam equation with the low frequency approximation taken:

$$EI\frac{\partial^4 Y}{\partial x^4} - T\frac{\partial^2 Y}{\partial x^2} = 0 \tag{133}$$

If we now substitute in the bending length:

$$\lambda = \sqrt{\frac{EI}{T}} \tag{134}$$

we have:

$$\lambda^2 Y^{(iv)} - Y^{(ii)} = 0 \tag{135}$$

We may then look for a solution of the form seen in Appendix B equation 116 with the boundary conditions:

$$\begin{aligned} Y(0) &= 0 \\ Y'(0) &= 0 \\ Y(L) &= \delta \\ Y'(L) &= \alpha \end{aligned} \tag{136}$$

This then gives the solution seen in Appendix B, equation 123, which we rewrite as:

$$Y(x) = \frac{\delta - \lambda\alpha}{L - 2\lambda}\left[x + \lambda\left(e^{-\frac{x}{\lambda}} - 1\right)\right] + \lambda\frac{\alpha(L-\lambda) - \delta}{L - 2\lambda}e^{-\frac{l=x}{\lambda}} \tag{137}$$

The potential energy is stored in the beam in both the bending and the stretching. We shall now proceed by calculating the contribution from the bending term. The bending potential energy is defined as:

$$V_B = \frac{1}{2}EI\int_0^L (Y'')^2\,dx \tag{138}$$

Substituting in equation 137 and evaluating the integral we find:

$$V_B = \frac{1}{2}T\frac{\lambda}{(L-2\lambda)^2}\left[\delta^2 - L\delta\alpha + \left(\frac{L^2}{2} - \lambda L + \lambda^2\right)\alpha^2\right] \tag{139}$$

Next we shall calculate the energy stored in the stretching of the beam as work is done against the longitudinal tension in the beam, T. The expression for the potential energy is:

$$V_S = \frac{1}{2}T\int_0^L (Y')^2\,dx \tag{140}$$

Again we substitute in equation 137 and evaluate the integral to give:

$$V_S = \frac{T}{2\left(L-2\lambda^2\right)}\left[\delta^2(L-3\lambda)+\alpha^2\lambda\left[\tfrac{L^2}{2}-2\lambda L+\lambda^2\right]+\delta\alpha\lambda(L-4\lambda)\right] \qquad (141)$$

Combining these two components gives the total potential energy stored in the deformed beam to be:

$$V = V_B + V_S = \frac{T}{2[L-2\lambda]}\left[\delta^2+\alpha^2\lambda(L-\lambda)-2\delta\alpha\lambda\right] \qquad (142)$$

from which we find that the coefficients we seek are given by:

$$\begin{aligned} k_{11} &= \frac{T}{L-2\lambda} \\ k_{12} &= -\frac{T\lambda}{L-2\lambda} \\ k_{22} &= \frac{T\lambda(L-\lambda)}{L-2\lambda} \end{aligned} \qquad (143)$$

Appendix D

Calculation of the Effects of Recoil Loss

D.1 Introduction

When attempting to measure the loss of a material or suspension it is important to identify and limit all other forms of loss. Here we shall look at how losses from recoil of support structures can affect measured Q values in both the pendulum mode and violin mode measurements. The recoil associated with the measurement of the vertical bounce mode is dealt with in Chapter 7 as this is a relatively simple calculation.

D.2 Pendulum Mode Measurements

Here we shall discover why recoil of the support is a major limiting factor to measuring high Q values for the pendulum mode of a suspension and hence why the stiffness of the frame is of great importance.

We may model our system as a mass attached to two springs. The first represents the spring constant of the pendulum, which is mostly dominated by the effects of gravity on the mass. The second represents a support that is not perfectly rigid but instead has some stiffness associated with it.

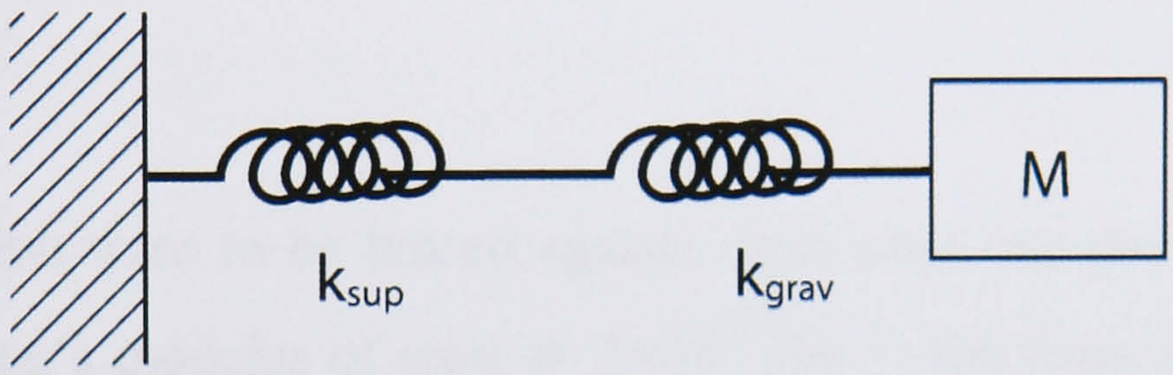

Figure 87: Model of suspension of finite stiffness

Adding the springs in series gives a system spring constant:

$$K_{sys} = \frac{k_{grav}}{1 + \frac{k_{grav}}{k_{sup}}} \tag{144}$$

where the spring constant of the pendulum is given by:

$$k_{grav} = \frac{mg}{l} = m\omega^2 \tag{145}$$

If we now add in the loss in the form of complex spring constants we may write:

$$K_{sys}e^{i\theta} = \frac{k_{grav}e^{i\phi_p}}{1 + \frac{k_{grav}e^{i\phi_p}}{k_{sup}e^{i\psi}}} \tag{146}$$

This may then be simplified to give the approximation for the loss of the system:

$$\theta \approx \phi_p + \frac{k_{grav}}{k_{\sup}}\psi \tag{147}$$

when $k_{grav} << k_{\sup}$.

If we now consider some numbers for our pendulum we may calculate how stiff the support must be in order for it not to limit the measured Q of the suspension. Taking the mass as 0.445kg and length as 0.405m we calculate the spring constant of the pendulum to be $10.8 Nm^{-1}$. If we wish to be capable of measuring a pendulum with a Q of 10^{10} then we would wish to make the loss from the support around an order of magnitude lower than this to make it negligible. Assuming that the support is made from steel with a Q of around 10^3 this would then require the spring constant of the support to be $1.08\times10^9 Nm^{-1}$.

If the suspension were to be braced against rigid walls one meter apart then using the Young's modulus of steel at $2\times10^{11} Nm^{-2}$, the cross section of the beams would need to be $53 cm^2$

While this calculation may give a feel for the dimensions of support needed it is interesting to note that here we have assumed the support beams to be fixed rigidly while in an experimental situation this is not the case. In fact it may be argued that by stiffening the support structure one simply moves the point of dissipation further down, for example into the concrete base whose material loss is high, or further into the foundations of the building where the stiffness may be lower than that of our concrete base. Also we have taken no account of couplings between bracing points or between the top of our suspension and the support. Finally we may note that the use here of horizontal bracing bars will also increase their stiffness compared to the table style of support used in Chapter 6.

However if we consider instead that the values of Q measured in the pendulum mode experiment are around 1.4×10^8 we may calculate how low

the stiffness of support would need to be to limit the measured Q. For a similar 1m horizontally mounted bar rigidly fixed at each end the cross section must now be only 0.28cm by 0.28cm.

As it is clearly difficult to calculate the exact values of recoil we may expect, the experiment documented in Chapter 6 instead uses two measurements made with different pendulum spring constants in order to calculate what loss may be attributable to recoil. This is done by fitting the measured loss for the pendulums to the equation:

$$\phi_{total} = (\phi_{mat} + \phi_{thermoelastic})D^{-1} + \beta m \omega^2 \tag{148}$$

D.3 Violin Mode Measurements

The calculation of the effects of recoil in the measurement of violin mode loss is substantially complicated by the use of an isolation stage in the suspension. The calculation is therefore split into three stages. Firstly we must calculate the force produced by the end of the fibre due to the bending of the violin modes. Secondly the dynamics of the upper isolation pendulum must be considered in order to find its resonant modes. Finally by uniting these two calculations we will calculate the fractional energy stored in the bending of the upper fibre.

D.3.1 Force Produced at End of Lower Fibre

We shall start by finding the force produced at the end of the fibre for some given displacement at the centre as shown in Figure 88. This may be calculated from a purely geometrical argument as follows:

$$F = T_x = TY'(x = 0) \tag{149}$$

assuming the restoring force comes mostly from the tension. We then evaluate the gradient of the fibre at the end to find:

$$F = T\frac{\pi}{L}Y_M \cos\left(\frac{\pi}{L}x\right)\Big|_{x=0} = T\frac{\pi}{L}Y_M \tag{150}$$

where Y_M is the displacement at the centre of the fibre. This force is exactly half that required to give the centre of mass of the fibre the required acceleration, the other half coming from the lower end of the fibre.

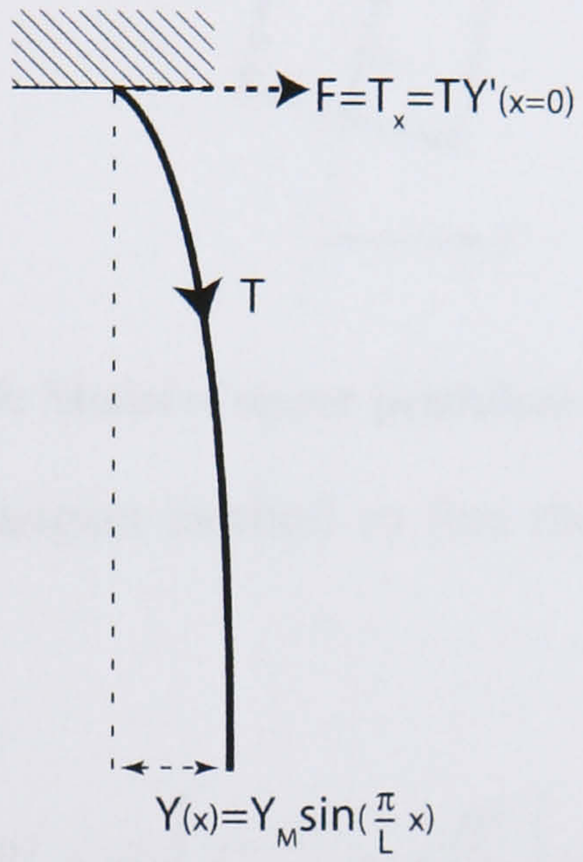

Figure 88: Force produced at the end of the lower fibre

D.3.2 Dynamics of Upper Pendulum

We now consider an extended object, such as our mass, suspended from a fibre whose behaviour may be modelled, as described in Appendix C, as three straight sections. This is shown in Figure 89 where we may also note that the upper section of fibre, which does not move relative to the suspension point, has been brought into the rigid section above.

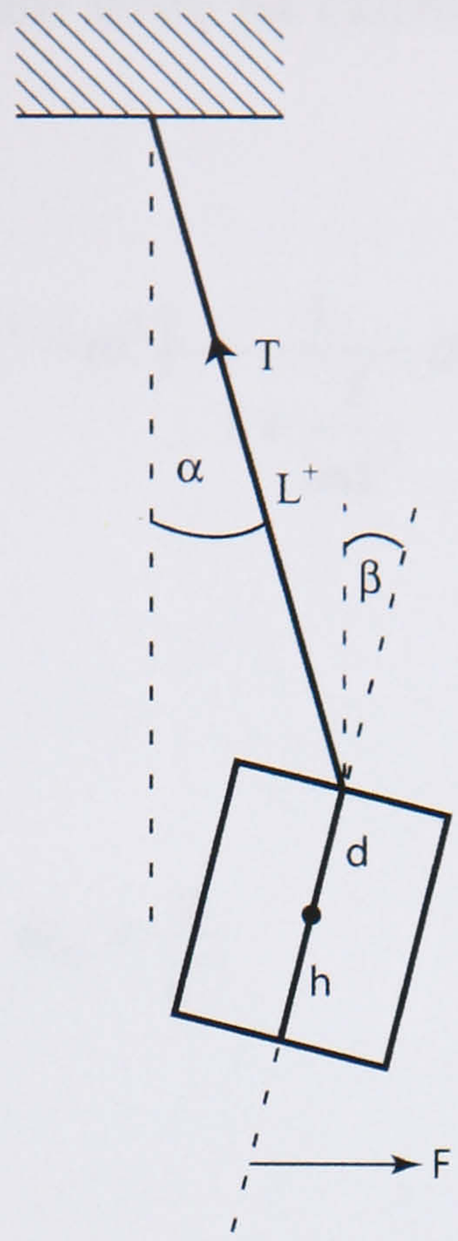

Figure 89: Model of upper pendulum motion

We may then use the Lagrangian method to find the equations of motion for this system:

$$L_g = \frac{1}{2}m\left[d\dot{\beta} + L^+\dot{\alpha}\right]^2 + \frac{1}{2}I\beta^2 + mg\left[L^+\frac{\alpha^2}{2} + d\frac{\beta^2}{2}\right] + F\left[(d+h)\beta + L^+\alpha\right] \quad (151)$$

This then gives the equations of motion in the frequency domain as:

$$\left(g - L^+\omega^2\right)\alpha - d\omega^2\beta = \frac{F}{m} \quad (152)$$

$$-L^+\omega^2\alpha + \left(g - d\omega^2 - \frac{I}{md}\omega^2\right)\beta = \frac{F}{m}\frac{d+h}{d} \quad (153)$$

From this we may find the case when no external force is applied. giving a characteristic equation:

$$\left(\omega_{01}{}^2-\omega^2\right)\left(\omega_{02}{}^2-\omega^2\right)-\frac{1}{1+\frac{I}{md^2}}\omega^4=0 \tag{154}$$

where ω_{01} is given by:

$$\omega_{01}=\frac{g}{L^+} \tag{155}$$

and ω_{02} is given by:

$$\omega_{02}=\frac{g}{d+\frac{I}{md}} \tag{156}$$

and from this we find solutions for ω (this is done numerically in chapter5). Having found the values of ω the Q of each mode may be expressed as:

$$Q=\frac{\Re(\omega)}{2\Im(\omega)} \tag{157}$$

where the complex form of ω comes from use of a complex Young's modulus.

D.3.3 Calculation of Energy Storage Ratio

We may now estimate the isolation provided by the intermediate mass using the equations 152 and 153 given above. We may rearrange these to find α and β as:

$$\alpha = \frac{F}{L^{+}\omega^2}\left[\frac{hd}{I} - \frac{1}{m}\right] \tag{158}$$

$$\beta = -\frac{Fh}{I\omega^2} \tag{159}$$

Next the energy stored in the bending of the upper fibre is estimated through the potential energy of a deformed beam:

$$E_{upper} = \frac{1}{2}k_{11}\delta^2 + \frac{1}{2}k_{12}\delta\beta + \frac{1}{2}k_{22}\beta^2 \tag{160}$$

where:

$$\begin{aligned} k_{11} &= \frac{T}{L-2\lambda} \\ k_{12} &= -\frac{T\lambda}{L-2\lambda} \\ k_{22} &= \frac{T\lambda(L-\lambda)}{L-2\lambda} \end{aligned} \tag{161}$$

as derived in Appendix C. We may then write the energy stored as:

$$E_{upper} = \frac{1}{2}\left(\frac{Fh}{I\omega^2}\right)^2\left[\left(\frac{I}{mh} - \Delta\right)^2 k_{11} + k_{22} + 2k_{12}\left(\frac{I}{mh} - \Delta\right)\right] \tag{162}$$

where:

$$\Delta = d - \lambda \tag{163}$$

The energy stored in the stretching of the lower fibre may be given by:

$$E_{lower} = \frac{1}{2} T \int_0^L (Y')^2 \, dx = \frac{1}{2} \frac{T\pi^2}{2L} Y_M{}^2 = \frac{F^2 L}{4T} \tag{164}$$

Thus we may rewrite the energy stored in the upper fibre as a function of the energy stored in the lower fibre:

$$E_{upper} = E_{lower} \times D_{isolation} \tag{165}$$

where:

$$D_{isolation} = 2\frac{T}{L}\left(\frac{h}{I\omega^2}\right)^2 \left[\left(\frac{I}{mh} - \Delta\right)^2 k_{11} + k_{22} + 2k_{12}\left(\frac{I}{mh} - \Delta\right)\right] \tag{166}$$

A plot of this function using parameters for our experimental setup is shown in Figure 43.

Appendix E

A Note on the Method of Operation of an Electrostatic Drive

The application of a force upon a body without contact is achieved here through use of an electrostatic drive. These are commonly used in experiments to measure material loss to impart energy without damaging the surface of delicate parts such as fused silica fibres. We shall consider here the method of operation of these.

A material placed in a magnetic field will become polarised spontaneously, as electron clouds shift and cause the atoms to take on the form of dipoles. The force the field exerts upon the dipole, where the separation distance between positive and negative charge is ∂x, is then given as

$$F = -qE(x) + qE(x + \partial x) \tag{167}$$

which may be rewritten to give:

$$F = q\frac{dE}{dx}\partial x = P\frac{dE}{dx} \tag{168}$$

where P is the polarisation. Therefore while the material becomes polarised by using a steady field, in order for this field to exert a force the field must have a gradient. A usual way in which to operate an electrostatic drive is to apply an offset voltage that polarises the material and then modulate this with a frequency at which the material is to be excited. In this case the sign of polarisation of the material remains constant while the gradient of the field fluctuates negative and positive, pushing and pulling the material. This is indeed the manner in which the electrostatic drive was operated in the measurements made in Chapter 7. This is not necessarily convenient experimentally as the signal from the electrostatic drive may couple through directly to the readout causing a large signal at the excitation frequency. which is not dependant upon the motion of the object.

However an alternative operating mode of an electrostatic drive is to not use any offset voltage but instead to apply a varying voltage at half the frequency of that at which the material is to be excited. In this case we see that when the voltage goes from positive to negative the polarisation changes direction in the material. As in most materials the polarisation is directly proportional to the field we may write:

$$P = AE \tag{169}$$

where A is some constant. Hence we find that:

$$F = AE\frac{dE}{dx} \tag{170}$$

and so for an applied voltage which is of the form of a sine wave the force produced oscillates at a frequency twice that applied. In practise this allows one to observe only the excitation of the fibre through the optical readout while using the electrostatic drive without the signal becoming masked by coupling since the frequency at which the voltage is applied is half that of the excitation.

Appendix F

Discussion of the Design of the Support Frame for Violin Mode Loss Measurements

The design of the support frame for the violin mode loss measurements, made in Chapter 5, was to improve upon an existing experimental set-up that is shown in Figure 90. The previous frame was not only too small to allow measurement of fibres greater than around 20cm but may also have been contributing to the overall loss through recoil due to lack of rigidity, showing as low Q values for the first mode. A new system capable of measuring 60cm fibres with masses of up to 10kg was required to work toward the Advanced LIGO design specifications and would be required to achieve a rigidity that would allow recoil losses to be assumed negligible. A new vacuum tank using a rotary and turbo molecular pumps gave an internal space 2m high in which the support could sit directly on the floor to reduce recoil.

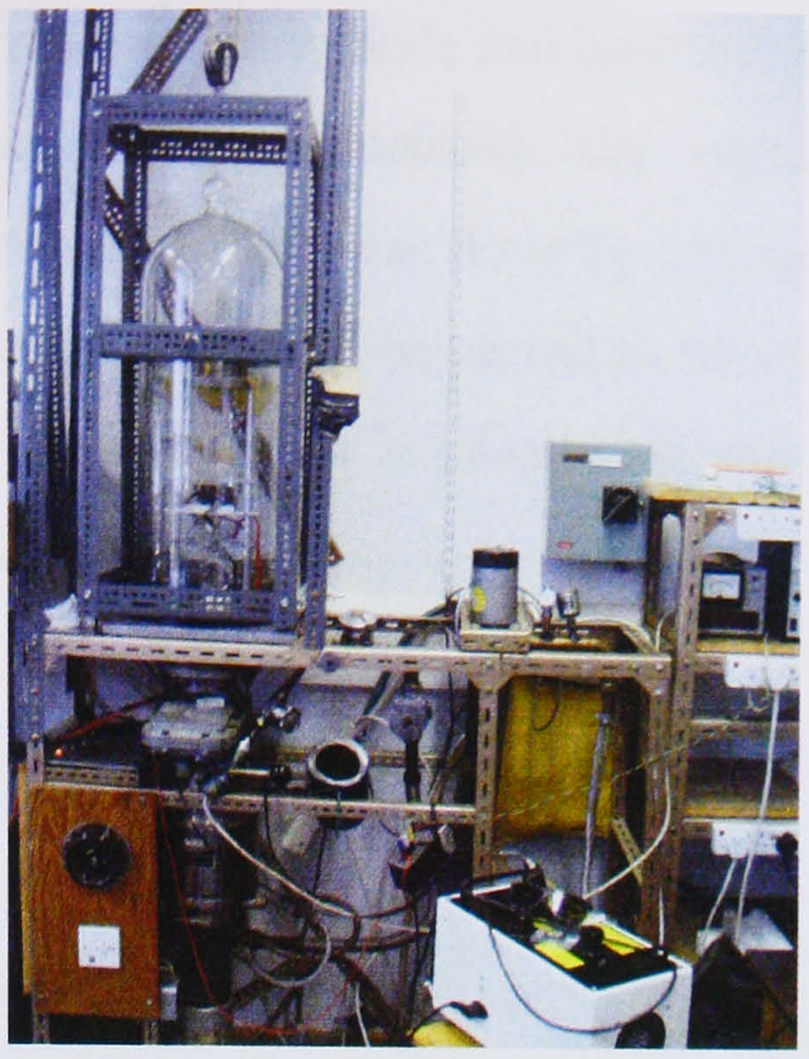

Figure 90: Previously used experimental set-up for violin mode experiments. A glass bell-jar houses an aluminium frame and double stage pendulum. This is mounted on a dexian frame and is pumped using an oil diffusion pump

The frame was designed to be made from a 400kg piece of stock cast stainless steel pipe which would not only provide rigidity but would be vacuum compatible and reduce manufacture time. The top plate from which the suspension would be hung would simply be made sufficiently thick to reduce flexure. It was decided that 5cm thickness would provide an adequate stiffness for this top plate. In order to give a vacuum compatible surface 1cm was to be machined from the wall of the tube, inside and out, by turning on a lathe, reducing the overall weight to around 200kg and setting the overall dimensions for the design. This then gave a wall thickness of 2cm.

Using the solidworks package the tube design was created to allow ease of use and a highly rigid frame. The first concern was to allow the suspension to be created outside the vacuum tank. Monolithic suspensions are difficult to produce when working in confined spaces and so the suspension would be craned into and out of the support frame rather than created within it. To do this the top plate would be unbolted and the masses would sit on a thin frame beneath which could be lowered when inside the tank to provide a catcher for the masses.

The need to align the readout photodiode and electrostatic drive relative to the fibre meant that access to the suspension was required after it had been installed in the vacuum tank. This was done by cutting a door in the side of the tube which was hinged and could be closed to increase the rigidity. Figure 91 shows the body without the door in place while Figure 92 shows the body and door when closed.

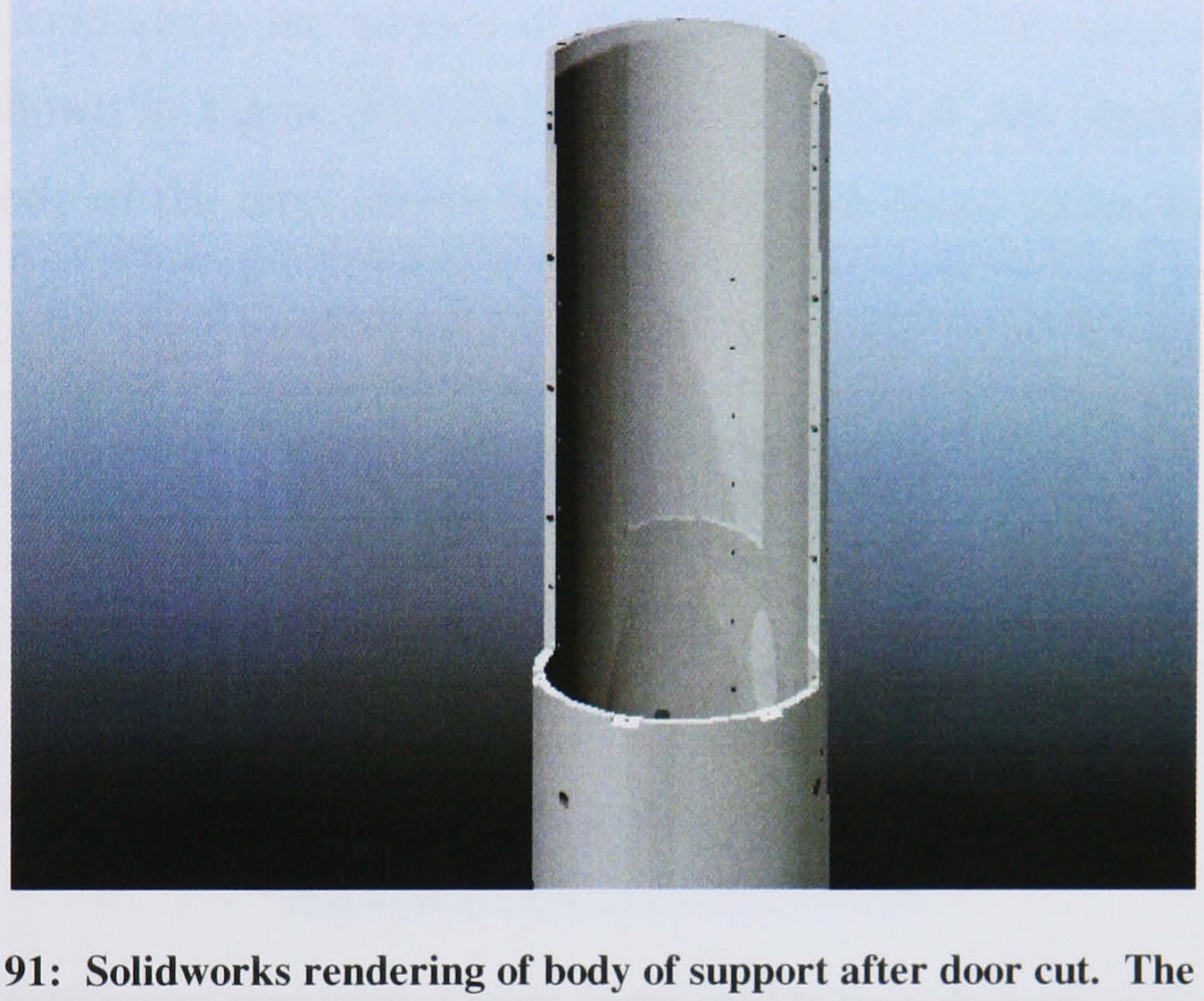

Figure 91: Solidworks rendering of body of support after door cut. The mating surfaces were then to be milled to give a clean surface finish and a known gap size that would be filled using brass plates.

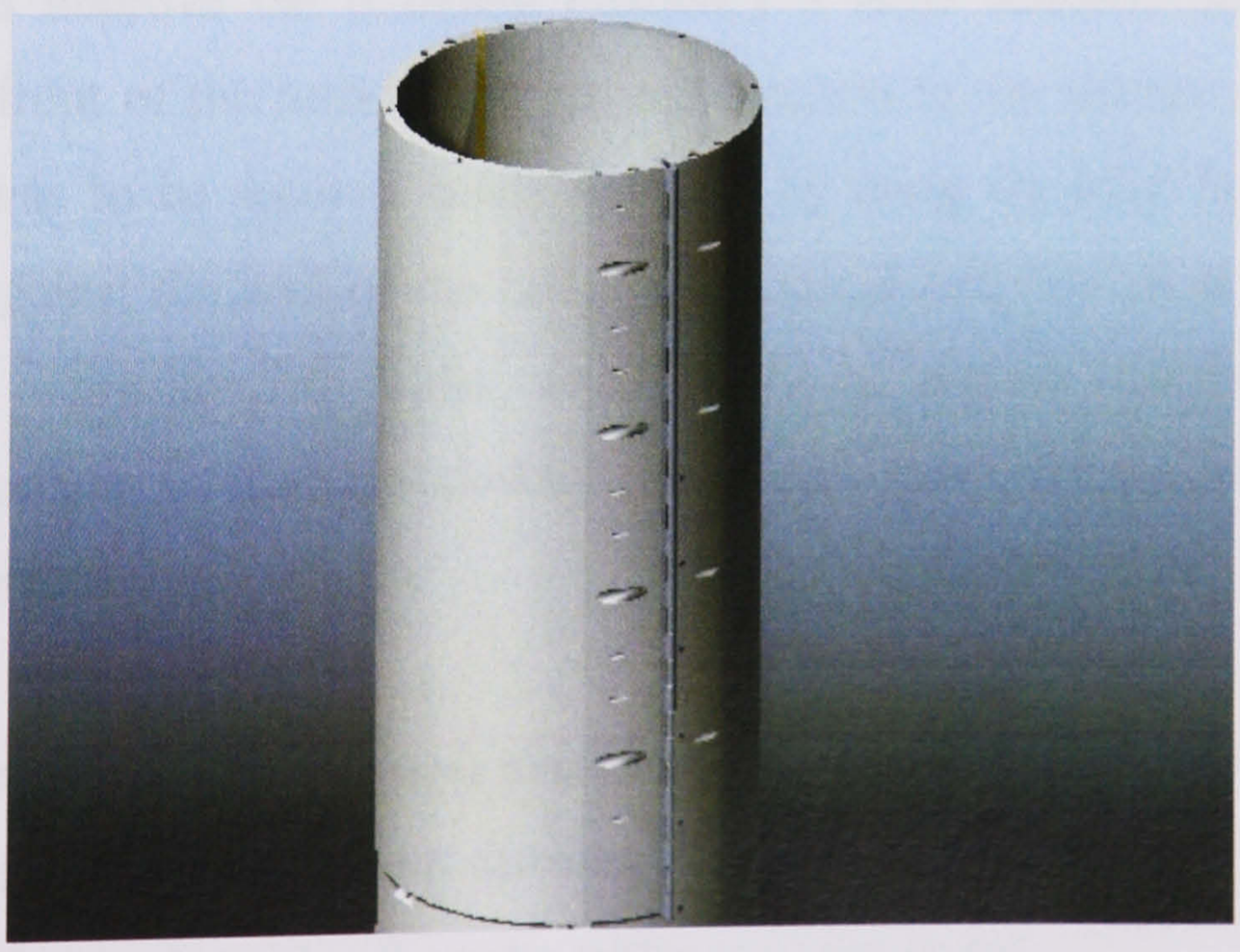

Figure 92: Solidworks rendering of the body of the frame with door attached by hinge. The four bolt holes can be seen as can the mounting holes for the top plate.

In order to secure this back in place when closed, four bolt holes were drilled down each side with corresponding M8 holes being tapped into the body behind them. Another four M8 tapped holes were made on top of the door onto which the top plate could be bolted. The material removed by the saw blade when cutting the door out was replaced using brass plates that bolted down either side between the door and the body. The gap due to material being cut from along the bottom of the door was filled by using three brass wedges, shown in Figure 93, which could be screwed into slopes machined into the body of the tube, shown in Figure 94, and driven up hard against the door.

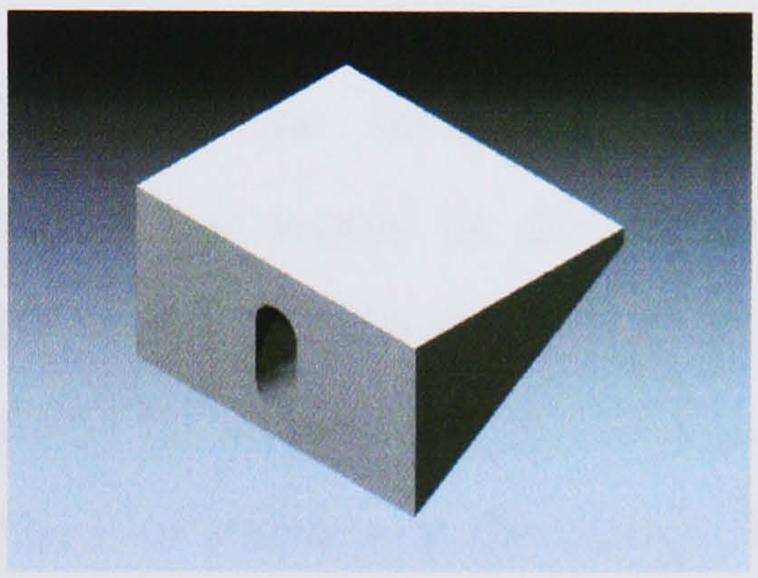

Figure 93: Solidworks rendering of brass wedge used to force door upwards against the top plate.

In order to improve the pumping efficiency a large diameter hole was cut directly in front of the turbo pump giving it access to the interior of the tube. The tube was to be secured inside the tank by using six M16 bolts to push outwards against the wall of the tank. The tapped holes for these are seen in Figure 94. Smaller M6 holes were drilled at regular intervals to give mounting points for the electrostatic drive and other components such as heating resistors.

The bottom of the tube was also machined to give three small rectangular feet on which it would sit without rocking. The small height of these, at only 1mm, would not adversely affect the stiffness of the frame.

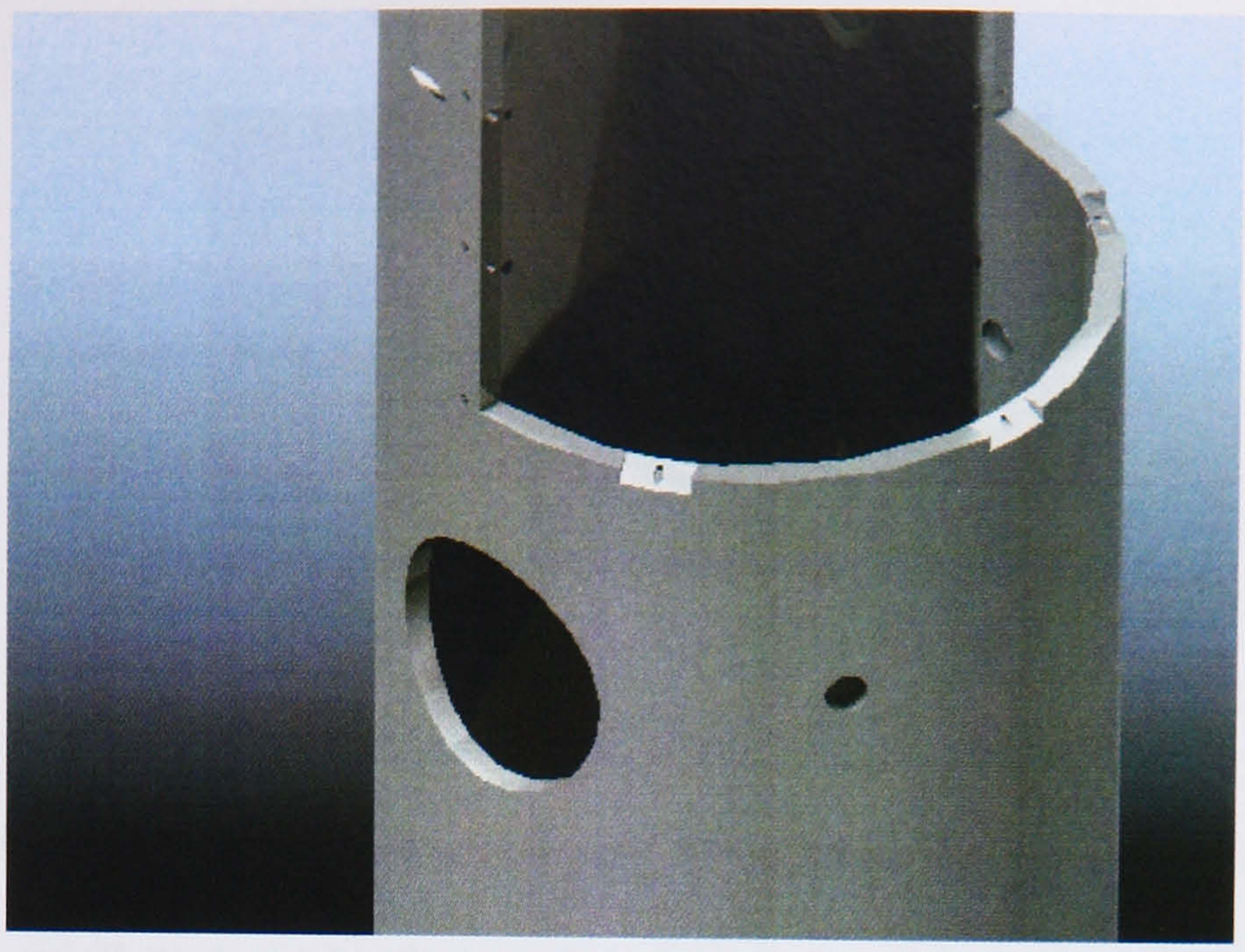

Figure 94: Solidworks rendering of body showing close up detail of the wedge cuts, vacuum pump hole and bolt holes to secure against vacuum tank walls.

The design of the clamp for the silica top plate was another area of importance. One source of loss would be due to slip-stick processes if the plate was not held tightly enough. Also if any part of the clamp could vibrate against the plate this would be another source of loss. There would also be recoil losses due to any lack of stiffness at the clamp. For these reasons it was decided to use a clamp in which the mass would be held by small blocks, to minimise contact area, mounted as far from the suspension point as possible. The height of the blocks would be only 1mm to increase their stiffness. The blocks were machined onto the face of the top plate, as shown in Figure 95 and onto a ring, shown in Figure 96.

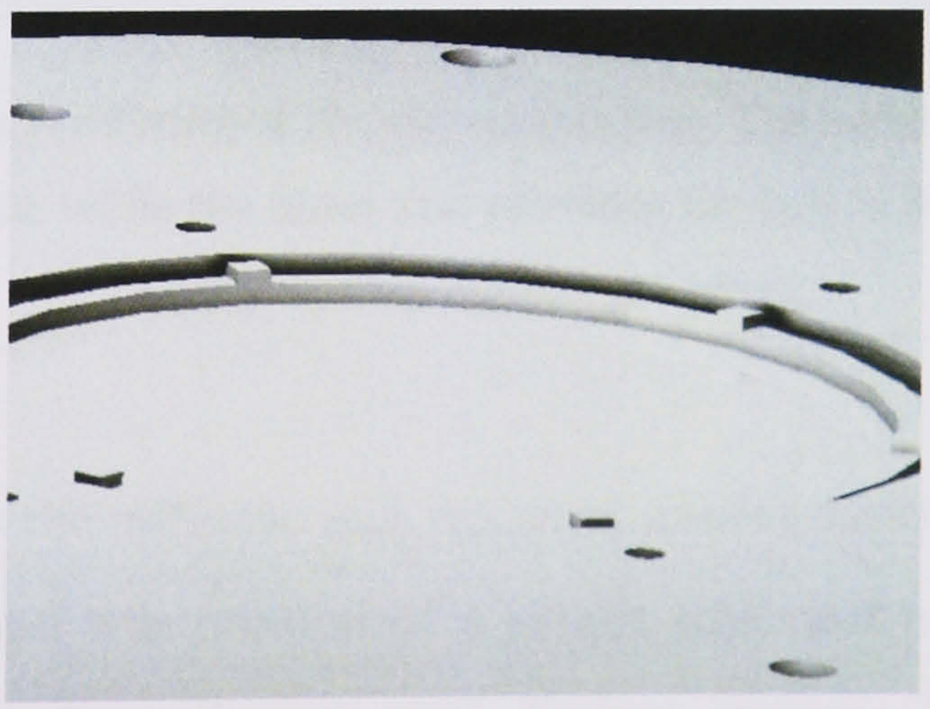

Figure 95: Close up detail of the underside clamping surface of the top plate showing the rectangular feet as well as the mounting holes for the catcher frame and the bolt holes to attach to the main body of the tube.

Figure 96: Solidworks rendering of the clamping ring. The six small rectangular feet used to clamp the glass can be seen.

The ring would be used to clamp the glass from underneath, mounted in a stiff circular housing, shown in Figure 97, and would be flexible enough to allow the blocks to be forced up onto the glass, using six M6 bolts, to give good contact.

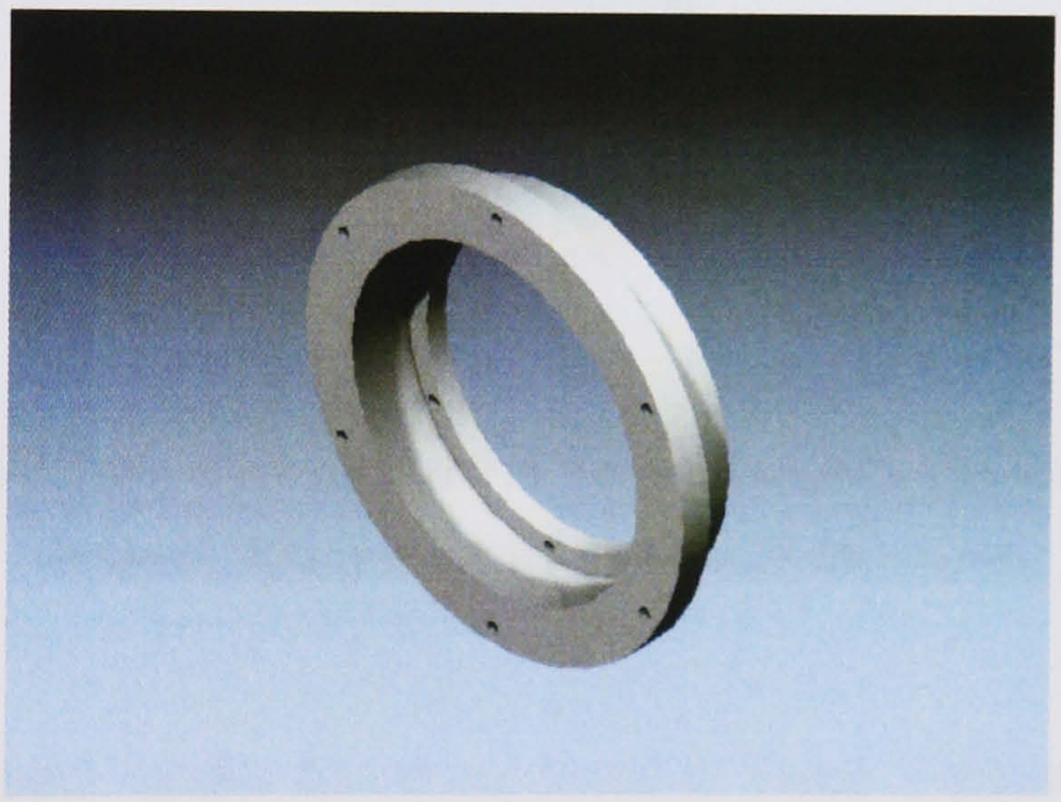

Figure 97: Solidworks rendering of the clamp housing. The outer edge would be bolted against the top plate while the inner rim provides the bolt holes used to force the clamping ring against the glass.

In order to evaluate the stiffness and resonant modes expected from this frame a finite element model was created of a simple tube and top plate. The finite element analysis can be split into two distinct stages. Firstly a list of the resonant modes was found. This was followed by an analysis of the stiffness of the structure both under lateral and rotational load.

This model of the tube was meshed to create a series of nodes that represent the support. A closer packing of nodes produces a closer approximation and in this model a total of 1602 nodes were used to make up 800 block elements. Figure 98 shows the mesh including the top plate and with the bottom surface constrained for displacement and rotation in all directions.

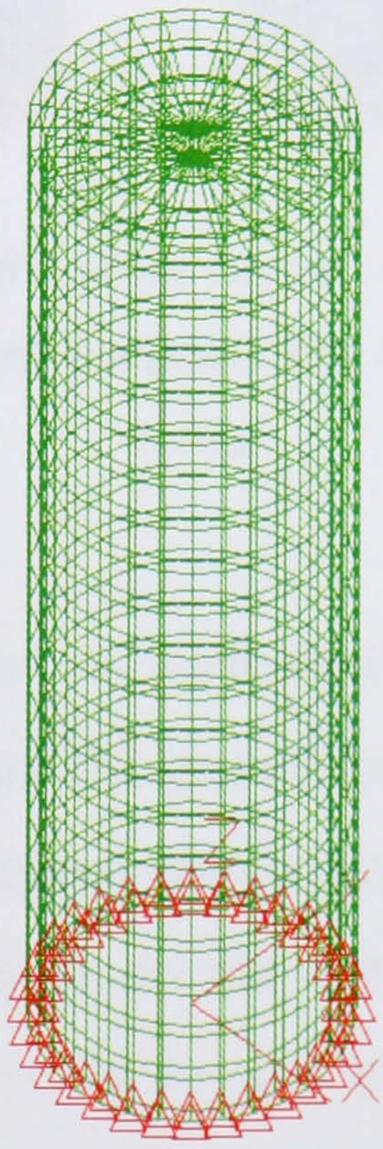

Figure 98: Meshed finite element model of the support structure with top plate. The bottom surface is constrained in all directions

The first six resonant modes found are listed in Table 3 below with the images of the first four modes being given in Figure 99.

Table 3: Resonant modes of the support structure found using finite element analysis

Mode Name	First Bending	First Compressed	Twisting	Second Bending	Vertical	Second Compressed
Frequency	126Hz	427Hz	492Hz	607Hz	729Hz	750Hz

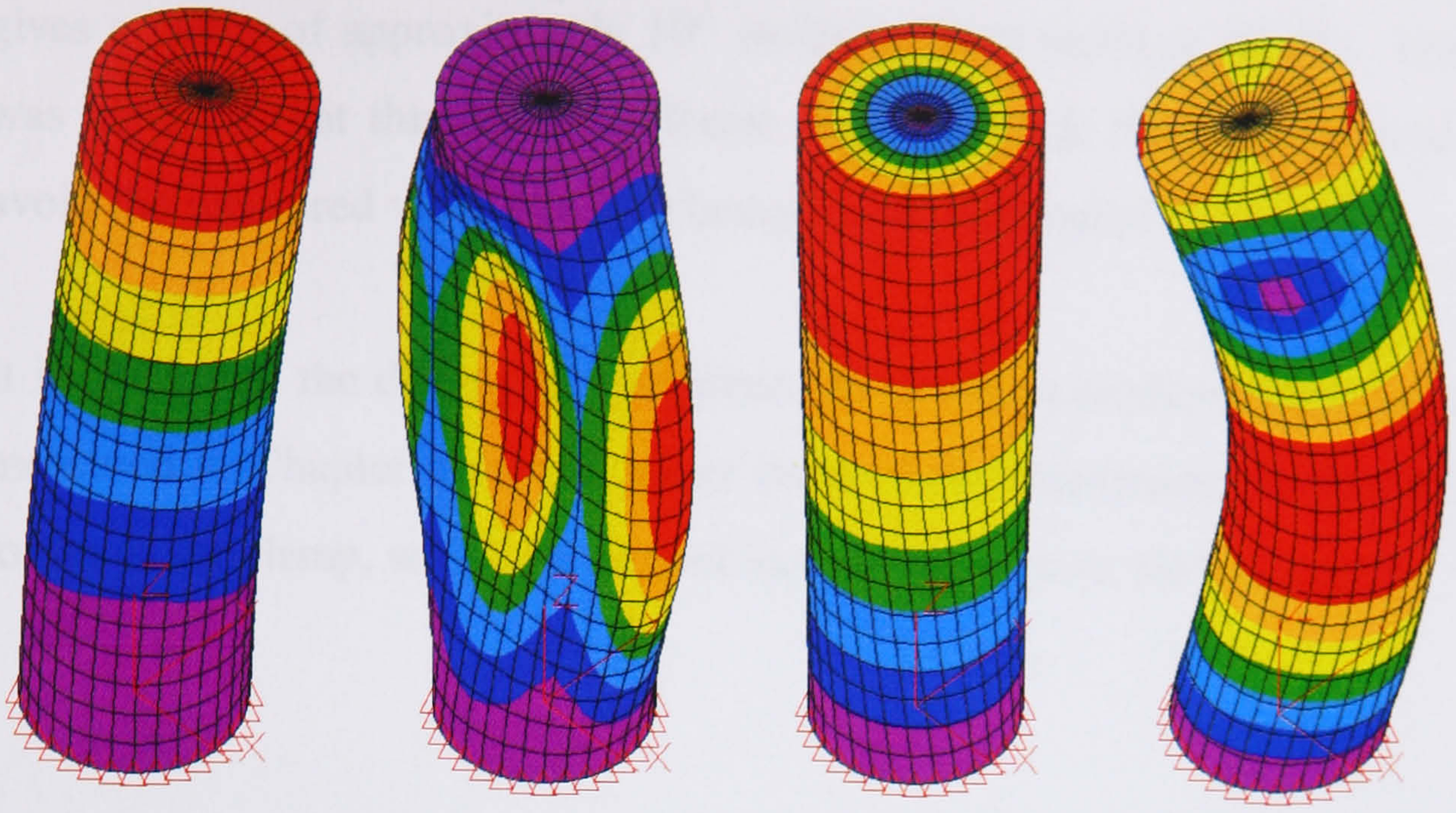

Figure 99: First four resonant modes of the support structure found using finite element analysis (frequency increasing left to right). The relative displacement is shown by colour.

Next the finite element analysis was performed for applied sinusoidal forces at the centre of the top plate where the suspension is to be mounted. For a given force and frequency the maximum displacements and stresses of the nodes were calculated. To accurately model the effects of a suspension we chose to look at two motions, one where the force is purely lateral and one where it is applied as a torque, causing the top plate to rotate. This was done at an applied frequency of 500Hz with a force of 1N applied at the centre of the underneath of the top plate. From the displacements the spring constants of the structure at the centre of the top plate were found to be:

$$k = 2.7\times10^{9}\ {}^{N}\!/_{m} \qquad k_{\theta} = 1.13\times10^{8}\ \frac{Nm}{rad}$$

A Maple model using the beam equation was produced to find the force and torque produced at the end of a bending fibre for the pendulum mode with 1joule of energy stored in it, and from this the amount of energy stored in the recoil of the support was found. The Q of a recoil-limited fibre was then calculated to be 2.3×10^{7} if the Q of the steel structure is taken as 10^{3}. This calculation does not take into account the isolation mass used which we know

gives a factor of approximately 10^5 isolation from recoil at 300Hz. Hence it was assumed that this design of frame should provide the stiffness needed to avoid the measured violin mode Q being recoil loss limited.

It is likely that the discrepancy between the Q values predicted here and those measured in Chapter 5 for the upper stage of the suspension are the result of losses at the clamp, which we did not include in the finite element model.

Appendix G

Residual Gas Damping of a Pendulum

When performing measurements of the loss of a pendulum it is important to be able to calculate the amount of damping that results from momentum transfer with residual gas molecules in the vacuum chamber. This will allow us to ensure that the vacuum level is sufficiently good to consider this effect negligible.

If we consider a suspended flat plate, whose suspension fibres have negligible mass and surface area compared to the plate, swinging through the vacuum with a speed $\dot{x}(t)$ in the x direction, there is a backward frictional force that acts upon this plate due to collisions with residual gas molecules. It will be shown that this force is velocity dependant and hence may be written:

$$F_{friction} = -b\dot{x} \tag{171}$$

where b is a coefficient dependant on the vacuum conditions. The equation of motion of the plate may then be given as:

$$F = m_p \ddot{x} = -kx - b\dot{x} \tag{172}$$

where m_p is the mass of the plate. Taking the solution to be that of a damped harmonic oscillator:

$$x = e^{-\frac{t}{\tau}} e^{i\omega t} \tag{173}$$

we may substitute this into the equation of motion to give:

$$m_p\left(-\frac{1}{\tau} + i\omega\right)^2 = -k - b\left(\frac{1}{\tau} + i\omega\right) \tag{174}$$

Equating the imaginary parts we find that the decay time is given by:

$$\tau = \frac{2m_p}{b} \tag{175}$$

and hence:

$$Q = \frac{\omega m_p}{b} \tag{176}$$

The coefficient of gas damping, b, may be calculated by consideration of the rate and velocity of impacts [81]. As the plate moves there will be a number of collisions front and back upon it. The resulting force will be the difference between the force acting upon the front and back surfaces. Impacts upon the front surface will be at a speed $v + \dot{x}$, where v is the x component of the speed of some gas molecule, while those occurring on the back face will be at $v - \dot{x}$. If the molecules reflect elastically from the surface then the

momentum exchange will be twice $mv_{collision}$, where m is the mass of one gas molecule and $v_{collision}$ is the relative speed of the molecule and the plate.

The velocity of the gas molecules will follow a Maxwell-Boltzmann distribution, which gives the velocity distribution in one dimension to be:

$$dn = n\left(\frac{m}{2\pi kT}\right)^{\frac{1}{2}} e^{-\frac{mv^2}{2kT}} dv \tag{177}$$

where k is Boltzmann's constant, n is the number density of the molecules and dn is the number density with speeds in the range v to $v+dv$.

The number of molecules hitting the front and back faces is also dependent on the velocity of the plate relative to the molecules, with the rate of collisions per unit area on the front face being given by $(v+\dot{x})dn$ and the rate of collisions on the back face being given by $(v-\dot{x})dn$.

We may now calculate the pressure difference between the two sides of the plate. This is given by the rate of change of momentum of the plate in the x direction per unit of surface area:

$$P_{diff} = n\left(\frac{2m^3}{\pi kT}\right)^{\frac{1}{2}} \int_0^\infty e^{-\frac{mv^2}{2kT}} \left((v+\dot{x})^2 - (v-\dot{x})^2\right) dv \tag{178}$$

which simplifies, using the relations $P = nR_0T$ and $m = \frac{Mk}{R_0}$ to :

$$P_{diff} = 4\sqrt{\frac{2}{\pi}}\dot{x}P\sqrt{\frac{M^3}{R_0{}^3T^3}} \int_0^\infty e^{-\frac{mv^2}{2kT}} v dv \tag{179}$$

where P is the pressure of residual gas (in SI units), R_0 is the universal gas constant, T is the absolute temperature and M is the mass of one mole of gas.

This may then be evaluated using the integral:

$$\int_0^\infty e^{Bz^2} z dz = \frac{1}{2B} \tag{180}$$

giving the result:

$$P_{diff} = 4\sqrt{\frac{2}{\pi}} \dot{x} P \sqrt{\frac{M}{R_0 T}} \tag{181}$$

which when exerted over a surface, A, gives a velocity dependant frictional force:

$$F_{friction} = -4\sqrt{\frac{2}{\pi}} AP \sqrt{\frac{M}{R_0 T}} \dot{x} = -b\dot{x} \tag{182}$$

hence giving a value for Q for a gas damped pendulum to be:

$$Q = \sqrt{\frac{\pi}{2}} \frac{\omega m_p}{4AP} \sqrt{\frac{R_0 T}{M}} \tag{183}$$

Bibliography

1. A. Einstein, Annalen der Physik. **49**: p. 769.

2. R.A.Hulse and J.H.Taylor, Astrophysical Journal. **195**(L51).

3. J.H.Taylor and J.M.Weisberg, Astrophysical Journal. **253**: p. 908-920.

4. J.Weber, Physical Review. **117**: p. 306.

5. B.Willke, P.Aufmuth, C.Aulbert, S.Babak, R.Balasubramanian, B.W.Barr, S.Berukoff, S.Bose, G.Cagnoli, M.M.Casey, D.Churches, D.Clubley, C. N.Colacino, D.R.M.Crooks, C.Cutler, K.Danzmann, R.Davies, R.Dupuis, E.Elliffe, C.Fallnich, A.Freise, S.Goßler, A.Grant, H.Grote, G.Heinzel, A.Heptonstall, M.Heurs, M.Hewitson, J.Hough, O.Jennrich, K.Kawabe, K.K¨otter, V.Leonhardt, H.Luck, M.Malec, P.W.McNamara, S.A.McIntosh, K.Mossavi, S.Mohanty, S.Mukherjee, S.Nagano, G.P.Newton, B.J.Owen, D.Palmer, M.A.Papa, M.V.Plissi, V.Quetschke, D.I.Robertson, N.A.Robertson, S.Rowan, A.Rudiger, B.S.Sathyaprakash, R.Schilling, B.F.Schutz, R.Senior, A.M.Sintes, K.D.Skeldon, P.Sneddon, F.Stief, K.A.Strain, I.Taylor, C.I.Torrie, A.Vecchio, H.Ward, U.Weiland, H.Welling, P.Williams, W.Winkler, G.Woan and I.Zawischa, Classical and Quantum Gravity, 2002. **19**: p. 1377.

6. A. Lazzarini. *LIGO Project Status Update*. in *Proceedings of the XXXIVth Rencontres de Moriond*. 1999.

7. L.S. Collaboration, *Advanced LIGO Systems Design*. P.Fritschel, Editor.

8. P.Saulson, *Fundamentals of Interferometric Gravitational Wave Detectors*. 1994: World Scientific.

9. E.Chaisson and S.McMillan, *Astronomy Today*. 2002: Prentice-Hall Inc.

10. B.F. Schutz. *The Detection of Gravitational Waves*. in *Proceedings of the 1995 Houches School on Astrophysical Sources of Gravitational Radiation*. 1996: Springer Berlin.

11. J.A. Lobo. *Sources of Gravitational Waves*. in *General Relativity, Proceedings of the 46th Scottish Universities Summer School in Physics, Aberdeen*. 1995.

12. B.F. Schutz, Nature, 1986. **323**: p. 310.

13. K.S. Thorne. *Gravitational Waves*. in *Proceedings of the 1994 Snowmass Summer Study on Particle and Nuclear Astrophysics and Cosmology*: Word Scientific, Singapore.

14. R.V. Wagoner, Astrophysical Journal, 1984. **278**: p. 345.

15. J.Hough, H.Walther, B.F.Schutz, J.Ehlers, H.Welling, I.F.Corbett and V.Kose, *Proposal for a Joint German-British Interferometric Gravitational Wave Detector*, in *Max-Planck-Institut fur Quantenoptik Report 147 and GWD/137/JH(89)*. 1989.

16. A.b.K.T. from, *Science Section of LIGO-II Proposal, LIGO-P000024-00-R*. 2000.

17. F.B.E.a.H.D. Wahlquist, General Relativity and Gravitation, 1975. **6**(5): p. 439-447.

18. B.Bertotti, R.Ambrosini, J.W.Armstrong, S.W.Asmar, G.Comoretto, G.Giampieri, L.Iess, Y.Koyama, A.Messeri, A.Vecchio and H. D.Wahlquist, Astronomy and Astrophysics, 1995. **296**: p. 13-25.

19. M. Tinto, Classical and Quantum Gravity, 2002. **19**: p. 1767–1773.

20. P.Astone, *Resonant Mass Detectors: Present Status.* Classical and Quantum Gravity, 2002. **19**: p. 1227-1235.

21. P.Astone, M.Bassan, P.Bonifazi, P.Carelli, M.G. Castellano, G.Cavallari, E.Coccia, C.Cosmelli, S.D'Antonio, V.Fafone, G.Federici, Y.Minekov, G.Modestino, I.Modena, A.Moleti, G.Pizzella, G.V.Pallettino, L.Quintieri, A.Rocchi, F.Ronga, R.Terenzi, G.Torrioli and M.Visco, *The EXPLORER gravitational wave antenna: recent improvements and performances.* Classical and Quantum Gravity, 2002. **19**: p. 1905-1910.

22. O.D.Aguiar, L.A.Andrade, L.C. Filho, C.A.Costa, J.C.N.d. Araújo, E.C.d.R. Neto, S.T.d. Souza, A.C.Fauth, C.Frajuca, G.Frossati, S.R.Furtado, V.G.S.Furtado, N.S.Magalhães, R.M.M. Jr, E.S.Matos, M.T.Meliani, J.L.Melo, O.D. Miranda, N.F.O. Jr, K.L. Ribeiro, K.B.M.Salles, C.Stellati and W.F.V. Jr, *The status of the Brazilian spherical detector.* Classical and Quantum Gravity, 2002. **19**: p. 1949-1953.

23. A.de.Waard, L.Gottardi and G.Frossati, Classical and Quantum Gravity, 2002. **19**: p. 1935–1942.

24. R. Weiss, *M.I.T. Quarterly Progress Report No. 105.* 1972.

25. D.Shoemaker, R.Schilling, L.Schnupp, W.Winkler, K.Maischberger and A. Rudiger, Physics Review D, 1988. **38**.

26. R.W.P.Drever, G.M.Ford, J.Hough, I.M.Kerr, A.J.Munley, J.R.Pugh, N.A.Robertson and H.Ward. *A Gravity-Wave Detector Using Optical Cavity Sensing.* in *Proceedings of the 9th International Conference on*

General Relativity and Gravitation. 1980. Jena: VEB Deutscher Verlag der Wiussenschaften, Berlin.

27. N.A. Robertson. *Detection of Gravitational Waves*. in *General Relativity, Proceedings of the 46th Scottish Universities Summer School in Physics*. 1995. Aberdeen.

28. D.I.Robertson, E.Morrison, J.Hough, S.Killbourn, B.J.Meers, G.P.Newton, N.A.Robertson, K.A.Strain and H.Ward. Review of Scientic Instruments, 1995. **66**(9): p. 4447.

29. M. Casey, *Developments Towards Autonomous Operation of Laser Interferometric Gravitational Wave Detectors*, in *Department of Physics and Astronomy*. 1999, University of Glasgow: Glasgow.

30. B.J. Meers, Physical Review D, 1988. **38**: p. 2317.

31. R.W.P. Drever, *Gravitational Radiation*, ed. T.P. N. Dereulle. 1983: North Holland Publishing Company.

32. B.Willke, P.Aufmuth, C. Aulbert, S. Babak, R. Balasubramanian, B.W. Barr, S. Berukoff, G. Cagnoli, C.A. Cantley, M.M. Casey, S. Chelkowski, D. Churches, C.N. Colacino, D.R.M. Crooks, C. Cutler, K. Danzmann, R. Davies, R.J. Dupuis, E. Elliffe, C. Fallnich, A. Freise, S. Goßler, A. Grant, H. Grote, S. Grunewald, J. Harms, G. Heinzel, I.S. Heng, A. Hepstonstall, M. Heurs, M. Hewitson, S. Hild, J. Hough, R. Ingley, Y. Itoh, O. Jennrich, R. Jones, S.H. Hutter, K. Kawabe, C. Killow, K. Kötter, B. Krishnan, V. Leonhardt, H. Lück, B. Machenschalk, M. Malec, R.A. Mercer, C. Messenger, S. Mohanty, K. Mossavi, S. Mukherjee, S. Nagano, G.P. Newton, M.A. Papa, M. Perreur-Lloyd, M. Pitkin, M.V. Plissi, V. Quetschke, V. Re, S. Reid, L. Ribichini, D.I. Robertson, N.A. Robertson, S. Rowan, A. Rüdiger, B.S. Sathyaprakash, R. Schilling, R. Schnabel, B.F. Schutz, F. Seifert, A.M. Sintes, J.R. Smith, P.H. Sneddon, K.A. Strain, I. Taylor, C.I. Torrie, C. Ungarelli, A. Vecchio, H. Ward, U. Weiland, H. Welling, P.

Williams, W. Winkler, G. Woan and I. Zawischa, *Status of GEO600.* Classical and Quantum Gravity, 2004. **21**: p. S417-S423.

33. F.Acernese, P.Amico, N.Arnaud, D.Babusci, R.Barillé, F.Barone, L.Barsotti, M.Barsuglia, F.Beauville, M.A.Bizouard, C.Boccara, F.Bondu, L.Bosi, C.Bradaschia, L.Bracci, S.Braccini, A.Brillet, V.Brisson, L.Brocco, D.Buskulic, G.Calamai, E.Calloni, E.Campagna, F.Cavalier, G.Cella, E.Chassande-Mottin, F.Cleva, T.Cokelaer, G.Conforto, C.Corda, J-P.Coulon, E.Cuoco, V.Dattilo, M.Davier, R.D. Rosa, L.D. Fiore, A.D. Virgilio, B. .Dujardin, A.Eleuteri, D.Enard, I.Ferrante, F.Fidecaro, I.Fiori, R.Flaminio, J-D.Fournier, S.Frasca, F.Frasconi, L.Gammaitoni, A.Gennai, A.Giazotto, G.Giordano, G.Guidi, H.Heitmann, P.Hello, P.Heusse, L.Holloway, S.Kreckelberg, P.L. Penna, V.Loriette, M.Loupias, G.Losurdo, J-M.Mackowski, E.Majorana, C.N.Man, F.Marion, F.Martelli, A.Masserot, L.Massonnet, M.Mazzoni, L.Milano, J.Moreau, F.Moreau, N.Morgado, F.Mornet, B.Mours, J.Pacheco, A.Pai, C.Palomba, F.Paoletti, R.Passaquieti, D.Passuello, B.Perniola, L.Pinard, R.Poggiani, M.Punturo, P.Puppo, K.Qipiani, J.Ramonet, P.Rapagnani, V.Reita, A.Remillieux, F.Ricci, I.Ricciardi, G.Russo, S.Solimeno, R.Stanga, A.Zoncelli, M.Tonelli, E.Tournefier, F.Travasso, H.Trinquet, M.Varvella, D.Verkindt, F.Vetrano, O.Veziant, A.Viceré, J-Y.Vinet, H.Vocca and M.Yvert, *Status of VIRGO.* Classical and Quantum Gravity, 2004. **21**: p. S385–S394.

34. *European Gravitational Observatory*.

35. t.T.C. Ryutaro Takahashi, *Status of TAMA300.* Classical and Quantum Gravity, 2004. **21**: p. S403-408.

36. S.Miyoki, T.Uchiyama, K.Yamamoto, H.Hayakawa, K.Kasahara, H.Ishitsuka, M.Ohashi, K.Kuroda, D.Tatsumi, S.Telada, M.Ando, T.Tomaru, T.Suzuki, N.Sato, T.Haruyama, Y.Higashi, Y.Saito, A.Yamamoto, T.Shintomi, A.Araya, S.Takemoto, T.Higashi,

H.Momose, J.Akamatsu and W.Morii, *Status of the CLIO project.* Classical and Quantum Gravity, 2004. **21**: p. S1173-S1181.

37. D.E.McClelland, S.M.Scott, M.B.Gray, D.A.Shaddock, B.J.Slagmolen, A.Searle, D.G.Blair, L.Ju, J.Winterflood, F.Benabid, M.Baker, J.Munch, P.J.Veitch, M.W.Hamilton, M.Ostermeyer, D.Mudge, D.Ottaway and C.Hollitt, Classical and Quantum Gravity. 2001. **18**: p. 4121-4126.

38. J.Hough. *LISA - the Current Situation.* in *Rencontres de Moriond.* 1999.

39. B.Meers and K.Strain, *Modulation, signal and quantum noise in interferometers.* physical review A, 1991. **44**(7): p. 4696.

40. Y. Chen, *Sagnac Interferometer as a Speed-Meter-Type, Quantum-Nondemolition Gravitational-Wave Detector.* Physics Review D. 2003. **67**: p. 122004.

41. H.J.Kimble, Y.Levin, A.B.Matsko, K.S.Thorne and S.P.Vyatchanin, *Conversion of conventional interferometers into quantum nondemolition interferometers by modifying their input and/or output optics.* Physics Review D, 2002. **65**: p. 022002.

42. M.E.Husman, C.I.Torrie, M.V.Plissi, N.A.Robertson, K.A.Strain and J.Hough, *Modeling of multistage pendulums: Triple pendulum suspension for GEO 600.* Review of Scientic Instruments, 2000. **71**(6): p. 2546.

43. P.Saulson, Physics Review D, 1984. **30**: p. 732.

44. V.B.Braginsky, M.L.Gorodetsky and S.P.Vyatchanin, Physics Letters A, 2000. **271**: p. 303-307.

45. A.RUDIGER, R.SCHILLING, L.SCHNUPP, W.WINKLER, H.BILLING and K.MAISCHBERGER, *A mode selector to suppress*

fluctuations in laser-beam geometry. OPTICA ACTA, 1981. **28**(5): p. 641-658.

46. E.Gustafson, *LSC white paper on detector research and development.* 1999.

47. K.D.Skeldon, K.A.Strain, A.I.Grant and J.Hough, Review of Scientic Instruments, 1996. **67**: p. 2443.

48. D.H.Gwo, *Ultra precision and reliable bonding method.* 2001: United States.

49. P.H. Sneddon, S. Bull, G. Cagnoli, D.R.M. Crooks, E.J. Elliffe, J.E. Faller, M.M. Fejer, J. Hough and S. Rowan, *The intrinsic mechanical loss factor of hydroxy-catalysis bonds for use in the mirror suspensions of gravitational wave detectors.* Classical and Quantum Gravity, 2003. **20**: p. 5025-5037.

50. J.Hough, K.A.Strain, S.Rowan, H.Ward, G.Woan and G.Cagnoli, *Investigations in Gravitational Radiation: Glasgow Rolling Grant Proposal 2004-2009.* 2004, Institute for Gravitational Research: Glasgow.

51. S.Kawamura, J.Hazel and F.Raab, *Suspension Preliminary Design.* 1996, LIGO Scientific Collaboration.

52. S. Kawamura, *Status and plans for future generations of ground-based interferometric gravitational wave antennas.* Classical and Quantum Gravity, 2003. **20**: p. S127–S134.

53. B.Jancovici, *Statistical Physics and Thermodynamics.* 1973: McGraw-Hill Book Company Limited.

54. K.Kuroda, M.Ohashi, S.Miyoki, D.Tatsumi, S.Sato, H.Ishizuka, M.K.Fujimoto, S.Kawamura, T. R, T.Yamazaki, K.Arai, M.Fukushima, K.Waseda, S.Telada, A.Ueda, T.Shintomi, A.Yamamoto, T.Suzuki, Y.Saito, T.Haruyama, N.Sato, K.Tsubono,

K.Kawabe, M.Ando, K.I.Ueda, H.Yoneda, M.Musha, N.Mio, S.Moriwaki, A.Araya, N.Kanda and M.E.Tobar, *Large-scale cryogenic gravitational wave telescope.* International Journal of Modern Physics D, 1999. **8**: p. 557-579.

55. R.Brown, Ann. Phys. Chem., 1828. **14**: p. 294.

56. A.Einstein, *Investigations on the Theory of Brownian Movement.* 1956, New York: Dover.

57. H.B.Callen and T.A.Welton, Physical Review, 1951. **83**: p. 34.

58. H.B.Callen and R.F.Greene, Physical Review, 1952. **86**: p. 702.

59. P.Saulson, *Thermal Noise in Mechanical Experiments.* Physical Review D, 1990. **42**(8): p. 2437-2445.

60. S.Rowan, R.Hutchins, A.McLaren, N.A.Robertson, S.M.Twyford and J.Hough, Physics Letters A, 1997. **227**: p. 153-158.

61. C. Zener, *Elasticity and Anelasticity in Metals.* 1948: University of Chicago Press.

62. P.Willems, V.Sannibale, J.Weel and V.Mitrofanov, *Investigations of the dynamics and mechanical dissipation of a fused silica suspension.* Physics Letters A, 2002. **297**: p. 37-48.

63. N.W.McLachlan, *Theory of Vibrations.* 1951, New York: Dover.

64. A.S.Nowick and B.S.Berry, *Anelastic Relaxation in Crystalline Solids* 1972: Academic Press.

65. G.Cagnoli and P.Willems, Physics Review B, 2002. **65**: p. 174.

66. M.M.Fejer, S.Rowan, G.Cagnoli, D.R.M.Crooks, A.Gretarsson, G.M.Harry, J.Hough, S.D.Penn, P.H.Sneddon and S.P.Vyatchanin, *Thermoelastic dissipation in inhomogeneous media: loss measurements and displacement noise in coated test masses for*

interferometric gravitational wave detectors. Accepted for publication. Physics Review D, 2004.

67. N.A. Robertson, G. Cagnoli, D.R.M. Crooks, E.J. Elliffe, J. Faller, P. Fritschel, S. Gossler, A. Grant, A. Heptonstall, J. Hough, H. Lueck, R. Mittleman, M. Perreur-Lloyd, M.V. Plissi, S. Rowan, D.H. Shoemaker, P. Sneddon, K.A. Strain, C.I. Torrie, H. Ward and P. Willems, *Quadruple suspension design for Advanced LIGO.* Classical and Quantum Gravity, 2002. **19**: p. 4043-4058.

68. G.Cagnoli, J.Hough, D.DeBra, M.M.Fejer, E.Gustafson, S.Rowan and V.Mitrofanov, Physics Letters A, 2000. **272**: p. 39-45.

69. P. Willems, *Dumbbell-shaped fibers for gravitational wave detectors.* Physics Letters A, 2002. **300**: p. 162-168.

70. G. Gonzalez and P.Saulson, *Brownian Motion of a Mass Suspended By An Anelastic Wire.* J. Acoust. Soc. Am., 1994. **96**(1): p. 207-212.

71. J.Strong, *Procedures in Experimental Physics*: Prentice-Hall Inc (New York).

72. S.Twyford, *Developments towards low loss suspensions for laser interferometric gravitational wave detectors.* 1998, University of Glasgow.

73. V.P.Mitrofanov, L.G.Prokhorov and K.V.Tokmakov, *Variation of electric charge on prototype of fused silica test mass of gravitational wave antenna.* Physics Letters A, 2002. **300**: p. 370-374.

74. V.B.Braginsky, V.P.Mitrofanov and O.A.Okhrimenko, Physics Letters A, 1993. **175**: p. 82.

75. G.Cagnoli, L.Gammaitoni, J.Hough, J.Kovalik, S.McIntosh, M.Punturo and S.Rowan, *Very High Q Measurements on a Fused Silica Monolithic Pendulum for Use in Enhanced Gravity Wave Detectors.* Physical Review Letters, 2000. **85**(12): p. 2442-2445.

76. J.T.Krausse, L.R.Testardi and R.N. Thurston, Phys. Chem. Glasses, 1979. **20**: p. 135.

77. C.Meade and R.Jeanloz, Physics Review B, 1987. **35**: p. 236.

78. A.M.Gretarsson and G.M.Harry, *Dissipation of mechanical energy in fused silica fibers.* Review of scientific instruments, 1999. **70**: p. 4081-4087.

79. C.Kurkjian, R.Frantz and H.Yuce, in *Optics and Photonics News.* 1997.

80. C.Kurkjian, J.Krausse and M.Matthewson, *Strength and Fatigue of Silica Optical Fibres.* Journal of Lightwave Technology, 1989. **7**(9): p 1360.

81. R.G.Christian, *The Theory of Oscillating-Vane Vacuum Gauges*, in *Vacuum*. 1966. p. 175-178.